Thermal remote sensing of glacial landscape dynamics

Dissertation

zur Erlangung des akademischen Grades

Doktor der Naturwissenschaften (Dr. rer. nat.)

am Fachbereich Geowissenschaften

der Freien Universität Berlin

angefertigt am Deutschen GeoForschungsZentrum Potsdam

von

Deniz Tobias Gök

Berlin, 18. Juni 2024

Erstgutachter:	**Prof. Dr. Dirk Scherler** Freie Universität Berlin, Deutsches GeoForschungsZentrum
Zweitgutachter:	**Prof. Dr. Bodo Bookhagen** Universität Potsdam
Tag der Disputation:	27.09.2024

Eidesstattliche Erklärung

Hiermit erkläre ich, dass ich die vorliegende Dissertation eigenständig und ohne unzulässige Hilfe erstellt habe. Bei der Erstellung dieser Dissertation wurden keine anderen als die im Text und Literaturverzeichnis angegebenen Hilfsmittel und Quellen verwendet. Beiträge von Koautoren zu veröffentlichten oder zur Veröffentlichung vorbereiteten Manuskripten sind im Vorwort („Preface“) dieser Arbeit erläutert. Ich versichere, dass die eingereichte elektronische Version mit der schriftlichen Version der Dissertation übereinstimmt. Ein Promotionsverfahren an einer anderen Hochschule oder einem anderen Fachbereich wurde zu einem früheren Zeitpunkt nicht beantragt.

Berlin, 17.06.2024

.....

Deniz Gök

Summary

High-mountain landscapes are becoming increasingly dynamic under climate change, with environmental changes impacting ecosystems and societies in and near mountains. The mountain cryosphere responds to rising atmospheric temperatures with declining snow and ice cover and thawing permafrost. The snow and ice cover decline modifies the surface energy balance, allowing increased heat transfer from the atmosphere into the ground and affecting mountain permafrost. Coupled with reduced mechanical ice support by retreating glaciers, high mountain landscapes destabilise and respond with increased bedrock erosion and sediment production. Mountain glaciers become increasingly covered by supraglacial debris of variable thickness that modifies their response to climate change by altered melt rates. Observations of increased rockfall activity, catastrophic slope failures, and cascading hazards related to climate change highlight the need for large-scale monitoring and detection techniques to analyse recent landscape changes and identify regions at risk of warming-related natural hazards.

In this thesis, I evaluate the potential and limitations of thermal infrared remote sensing to detect and analyse glacial landscape dynamics based on land surface temperature (LST) observations acquired from an unpiloted aerial vehicle (UAV) and multidecadal time series (1984-2022) of combined Landsat sensors. In the first study, I measured a significant portion of the diurnal temperature cycle of a debris-covered glacier section in Switzerland using UAV-acquired very high-resolution LST data and estimated spatially distributed debris thickness using two distinct approaches. The results showed that the nonlinearity in the relationship between LST and debris thickness varies throughout the day, which is relevant for interpreting satellite-derived debris thickness estimates at fixed acquisition times. Sub-daily LST measurements further allow quantifying surface energy balance components that satellite-based approaches cannot capture. Consequently, UAV-derived debris thickness maps can be used to calibrate and correct satellite-derived estimates, bridging the gap between spatial and temporal scales. Despite the relatively large RMSE in debris thickness estimates, this study is the first to discuss the limits and opportunities of UAV-derived LST to study the evolution of debris-covered glaciers. While UAV-derived LST can provide insights into glacial landscape changes over short time scales and relatively small spatial extent, detecting and monitoring longer-term changes at mountain range scale require long LST records and high spatial resolution to account for the steep altitudinal temperature gradients. In Chapter 3, I access patterns and trends in Landsat-derived LST data across the Swiss Alps using a harmonic model including a linear trend component. Comparison with LST time series from 119 weather stations revealed good accuracy of Landsat LST and LST trends. However, LST trends are biased due to orbital changes that cause variations in acquisition times, affecting the temporal coherence of LST measurements. Analysis of high temporal resolution

LST from alpine weather stations shows that the linear change in Landsat acquisition time can explain a trend of 0.045 K y^{-1}. However, the LST trend bias varies with topography, and I used modelled incoming shortwave radiation as a proxy to estimate the spatial variability of the LST trend bias. The corrected LST trends suggest that the highest LST warming rates are found in regions where mean annual land surface temperature is between -5 and 0°C and snow cover loss and permafrost thaw are expected to be large. In Chapter 4, I used several land cover datasets and created binary masks to compare the distributions of LST trends and their elevational differences for selected land cover and land cover change categories across the European Alps. Despite significant uncertainties in some of the binary masks, mean LST trends significantly vary with land cover and land cover changes, with a spatially averaged mean LST trend of 0.09 Kyr^{-1}. The analysis further shows that warming rates of regions with significant snow cover loss increase with elevation, while other land cover types do not show such patterns.

The studies in this thesis are the first to access LST and LST trends at unprecedented high spatial resolution, contributing to a better understanding of the climate sensitivity of glacial landscape dynamics and identifying regions prone to warming-related natural hazards.

Zusammenfassung

Hochgebirgslandschaften werden unter dem Einfluss des Klimawandels zunehmend dynamisch, wobei die Umweltveränderungen sowohl Ökosysteme als auch Gesellschaften in und in der Nähe von Gebirgen beeinflussen. Die Kryosphäre in den Bergen reagiert auf die steigenden atmosphärischen Temperaturen mit einem Rückgang von Schnee- und Eisbedeckung sowie dem Auftauen von Permafrost. Der Verlust von Schnee und Eis verändert den Oberflächenenergiehaushalt und ermöglicht einen verstärkten Wärmetransfer von der Atmosphäre in den Boden, wodurch der Permafrost zunehmend auftaut. Durch die erhöhten Bodentemperaturen und den Rückgang der Gletscher, die eine mechanische Stütze von Felswänden darstellen, werden hochalpine Landschaften zunehmend instabil und reagieren mit erhöhten Erosionsraten und Sedimentproduktion. Gebirgsgletscher sind zunehmend von supraglazialem Schutt bedeckt, was zu veränderten Schmelzraten gegenüber schuttfreien Gletschern führt. Beobachtungen von erhöhter Felssturzaktivität, katastrophalen Hangrutschungen und Kettenreaktionen von Naturgefahren im Zusammenhang mit dem Klimawandel unterstreichen die Notwendigkeit von Beobachtungs- und Detektionsmöglichkeiten zur Analyse von Landschaftsveränderungen und zur Identifizierung von Regionen, die anfällig für erwärmungsbedingte Naturgefahren gefährdet sind.

In dieser Dissertation bewerte ich das Potenzial und die Grenzen der thermalen Infrarot-Fernerkundung basierend auf der Landoberflächentemperatur (engl. Land Surface Temperature, LST) zur Analyse und Detektion von glazialen Landschaftsveränderungen. Hierfür nutze ich LST Messungen von einem unbemannten Luftfahrzeug (engl. unpiloted aerial vehicle, UAV) und einer LST Zeitserie (1984-2022) der kombinierten Landsat 5, 7 und 8-Sensoren.

In der ersten Studie habe ich mit Hilfe eines UAV, einen wesentlichen Teil des Tagestemperaturverlaufs der Oberfläche eines schuttbedeckten Gletscherabschnitts in der Schweiz gemessen. Auf Basis der hochaufgelösten LST Messungen habe ich zwei verschiedene Ansätze verfolgt, um die räumlich verteilte Schuttmächtigkeit abzuschätzen. Die Ergebnisse zeigten, dass die Nichtlinearität in der Beziehung zwischen LST und Schuttdicke im Laufe des Tages variiert, was relevant für die Interpretation satellitengestützter Schuttmächtigkeitsabschätzungen zu festen Überflugzeiten ist. LST Messungen des Tagestemperaturverlaufs ermöglichen es zudem, Komponenten des Oberflächenenergiehaushalts zu quantifizieren, die satellitengestützte Ansätze nicht erfassen können. Folglich können UAV-basierte Schuttmächtigkeitskarten verwendet werden, um satellitengestützte Abschätzungen zu kalibrieren und zu korrigieren und so die Lücke zwischen räumlichen und zeitlichen Skalen zu überbrücken. Trotz eines relativ großen Fehlers (RMSE) bei der Schuttmächtigkeitsabschätzung diskutiert diese Studie erstmals die Grenzen und Möglichkeiten von UAV-gestützten LST-Messungen zur Untersuchung der Entwicklung von schuttbedeckten

Gletschern. Während UAV-gestützte LST-Messungen Einblicke in Veränderungen der Gletscherlandschaften über kurze Zeitskalen und relativ kleine räumliche Ausdehnung bieten können, erfordert die Erfassung und Beobachtung langfristiger Veränderungen auf größeren Flächen, wie ganzen Gebirge, langjährige LST-Datensätze mit hoher räumlicher Auflösung.

In Kapitel 3 habe ich Muster und Trends in den aus Landsat abgeleiteten LST-Daten im Bereich der Schweizer Alpen unter Verwendung eines harmonischen Modells mit linearer Trendkomponente untersucht. Der Vergleich mit LST-Zeitreihen von 119 Wetterstationen zeigte eine gute Genauigkeit der Landsat LST und der LST-Trends. Allerdings sind die LST-Trends durch Orbitveränderungen verzerrt, die zu Variationen in den Aufnahmezeiten führen, und damit die zeitliche Kohärenz der LST-Messungen beeinträchtigen. Die Analyse von LST-Daten mit hoher zeitlicher Auflösung von alpinen Wetterstationen zeigt, dass ein Trend von 0,045 K/Jahr durch die lineare Veränderung der Landsat-Aufnahmezeiten erklärt werden kann. Die LST-Trendverzerrung variiert jedoch mit der Topographie, und ich habe die einfallende kurzwellige Strahlung modellierte und als Proxy verwendet, um die räumliche Variabilität der LST-Trendverzerrung abzuschätzen. Die korrigierten LST-Trends legen nahe, dass die höchsten Erwärmungsraten in Regionen mit einer mittleren jährlichen Landoberflächentemperatur zwischen -5 und 0°C zu finden sind, wo ein signifikanter Verlust an Schneebedeckung und Permafrost zu erwarten ist. In Kapitel 4 habe ich mehrere Hilfsdatensätze verwendet und binäre Masken erstellt, um die Verteilung der LST-Trends und ihre Höhenunterschiede für ausgewählte Landbedeckungs- und Landbedeckungsänderungskategorien in den Europäischen Alpen zu vergleichen. Trotz großer Unsicherheiten in einigen der binären Masken variieren die mittleren LST-Trends signifikant mit der Landbedeckung und den Veränderungen der Landbedeckung, mit einem räumlich gemittelten LST-Trend von 0,09 K/Jahr. Die Analyse zeigt weiterhin, dass die Erwärmungsraten in Regionen mit signifikantem Schneeverlust mit der Höhe zunehmen, während andere Landbedeckungstypen solche Muster nicht zeigen.

Die Studien in dieser Dissertation sind die ersten, die LST und LST-Trends in beispiellos hoher räumlicher Auflösung quantifizieren und so zu einem besseren Verständnis der klimasensitiven Dynamik von glazialen Landschaften beitragen. LST Trends können behilflich sein, Regionen zu identifizieren, die anfällig für erwärmungsbedingte Naturgefahren sind.

Preface

This PhD thesis was conducted at the German Research Centre for Geosciences (GFZ) and the Freie Universität Berlin as part of the project "Climate sensitivity of glacial landscape dynamics" (COLD). The COLD project (2018-2023) was funded by the European Research Council under the European Union's Horizon 2020 Research and Innovation program (grant no. 759639), led by Dr. Dirk Scherler.

The thesis consists of five chapters. The introduction provides the scientific background, addresses research gaps, and outlines the key objectives of the research. Chapters 1-3 contain scientific research articles that are either published, in review or prepared as manuscripts for submission to international peer-reviewed journals. Data publications for Chapters 1 and 2 are available through GFZ Data Services. Chapter 5 presents the overall conclusions drawn from the research articles with respect to the overarching objective of the thesis. Supplementary materials for each scientific article are included at the end of the thesis as Appendix A-C.

I used generative artificial intelligence (ChatGPT) during the writing process only to check spelling and grammar and improve readability. The tool did not create scientific content. After using the tool, I reviewed and edited the content and took full responsibility for the publications and manuscripts. Below, I provide further information about each chapter, including publication status, author contributions, and data availability.

Chapter 1: The introduction presents an overview of the climate sensitivity of high alpine landscapes, outlining the processes involved in the degradation of the mountain cryosphere and the subsequent landscape responses. It also introduces the basics of thermal infrared remote sensing and emphasizes the role of the land surface temperature in the surface energy balance. Finally, it highlights the research gaps and sets out the objectives of the thesis.

Chapter 2: The study "*High-resolution debris cover mapping using UAV-derived thermal imagery: limits and opportunities*" examines the potential for mapping diurnal variations in land surface temperature and creating supraglacial debris thickness maps from UAV data. The study was published in *The Cryosphere* (not-for-profit international scientific journal of the European Geosciences Union) in 2023. The study was designed by Deniz Gök and Dirk Scherler. Deniz Gök performed the analysis with support from Dirk Scherler. Deniz Gök developed the hardware set-up and conducted UAV flights. Leif Anderson conducted debris thickness measurements. Deniz Gök wrote the original version of the manuscript. Dirk Scherler and Leif Anderson commented on the initial manuscript and helped improve this version. The source code and input files of the surface energy balance model, and the debris thickness data are available through GFZ Data Services.

Chapter 3: The study "*Land surface temperature trends derived from Landsat imagery in the Swiss Alps*" focuses on analyzing land surface temperature trends derived from combined Landsat 5, 7, and 8 Collection 2 data across the Swiss Alps. It includes ground-truth validation, identification of a bias in Landsat LST trends due to orbital changes, assessment of its magnitude and spatial variation, and presents an approach to correct for it. The study is currently in review at *The Cryosphere*. The model results are accessible via GFZ Data Services. The study was designed by Deniz Gök and Dirk Scherler. Deniz performed the analysis with support from Dirk Scherler. Deniz Gök wrote the original draft of the manuscript. Dirk Scherler and Hendrik Wulf reviewed and edited the initial manuscript and helped improve this version.

Chapter 4: In the study "*Landsat derived land surface temperature trends and land cover changes in the European Alps*", I analyze LST trends across the European Alps and present LST warming rates for distinct land cover types and selected land cover changes. The study further evaluates the suitability of the harmonic model used for the respective land covers and land cover changes and is prepared as a manuscript with contributions from all co-authors for near future publication. The study was designed by Deniz Gök and Dirk Scherler. Deniz Gök performed the analysis with support from Dirk Scherler. Hendrik Wulf provided data on snow cover frequency. Deniz Gök wrote the original draft of the manuscript. Dirk Scherler and Hendrik Wulf reviewed and edited the original manuscript.

Chapter 5: The final Chapter provides a synthesis of the work outlined above and summarizes the overall conclusions drawn from the conducted studies concerning the research objectives.

List of Figures

List of Tables

List of Abbreviations

ASTER	Advanced spaceborne thermal emission and reflection radiometer
AVHRR	Advanced very high resolution radiometer
AWS	Automated weather station
COLD	Climate-sensitivity of glacial landscape dynamics (ERC project name)
DEM	Digital elevation model
DZAA	Depth of zero annual amplitude
ELA	Equilibrium line altitude
ETM+	Enhanced Thematic Mapper
FFC	Flat field correction
GCP	Ground control point
GEE	Google Earth Engine
GFC	Global Forest change
LC	Land cover
LST	Land surface temperature
MALST	Mean annual land surface temperature
MODIS	Moderate-resolution imaging spectroradiometer
NDIV	Normalized difference vegetation index
NDSI	Normalized difference snow index
RGI	Randolph glacier inventory
RMSE	Root mean squared error
SC	Single-channel
SEB	Surface energy balance
SEBM	Surface energy balance model
TIR	Thermal infrared remote sensing
TIRS	Thermal Infrared Sensor
TM	Thematic Mapper
TNG	Tsijiore Nouve Glacier
UAV	Unpiloted aerial vehicle
VIIRS	Visible Infrared Imaging Radiometer Suite

List of Publications

Research articles:

- Gök, D., Scherler, D., & Anderson, L. S. (2023). High-resolution debris-cover mapping using UAV-derived thermal imagery: limits and opportunities. The Cryosphere, 17(3), 1165–1184. https://doi.org/10.5194/tc-17-1165-2023
  *This article is licensed under a Creative Commons Attribution 4.0 license.

- Gök, Deniz T., Scherler, Dirk, and Wulf, Hendrik (2024). Land surface temperature trends derived from Landsat imagery in the Swiss Alps, EGUsphere [preprint], https://doi.org/10.5194/egusphere-2024-1228
  *This article is licensed under a Creative Commons Attribution 4.0 license.

Data publications:

- Gök, Deniz; Scherler, Dirk; Anderson, Leif S. (2022): High-resolution debris cover mapping using UAV-derived thermal imagery. GFZ Data Services. https://doi.org/10.5880/GFZ.3.3.2022.003

- Gök, Deniz; Scherler, Dirk; Wulf, Hendrik (2024): Landsat-derived spatiotemporal variations of land surface temperature. GFZ Data Services. https://doi.org/10.5880/GFZ.3.3.2023.005

Manuscript in preparation for publication:

- Gök, Deniz T., Scherler, Dirk, and Wulf, Hendrik (in prep.). Landsat derived land surface temperature trends and land cover changes in the European Alps

Table of contents

1 Introduction

1.1 Climate change in mountains

High-mountain landscapes are particularly sensitive to climate change and respond to increasing atmospheric temperatures by extensive degradation of the mountain cryosphere, including snow cover (Dedieu et al., 2014; Rumpf et al., 2022), glaciers (Zemp et al., 2015; Rounce et al., 2023), and permafrost. (Gruber and Haeberli, 2007; Biskaborn et al., 2019). Observations from most mountain ranges on Earth document the warming-related decline of the cryosphere in recent decades (Adler et al., 2022), with existent regional variability (Farinotti et al., 2020). These landscape transformations induce environmental shifts that can affect sea level rise (Radić and Hock, 2011; Zemp et al., 2020), water resources (Barnett et al., 2005), biodiversity (Elsen and Tingley, 2015), and landscape stability (Stoffel and Huggel, 2012; Krautblatter and Leith, 2015) and therefore poses significant challenges to ecosystems and societies (IPCC, 2022). Furthermore, warming rates in mountain landscapes are significantly higher than the global average (Beniston et al., 1997; Díaz and Bradley, 1997; Begert and Frei, 2018) and elevation-based differences in warming (Mountain Research Initiative EDW Working Group, 2015) further indicate that certain regions within mountainous landscapes are more susceptible to strong changes than others (Rottler et al., 2019; Pepin et al., 2022). As roughly 15% of the global population lives in or near mountains (Thornton et al., 2022), understanding mountain responses to global warming is crucial for developing and implementing effective climate change adaptation strategies (McDowell et al., 2021). In recent decades the research on climate change impacts on mountainous landscapes has gained much attention in the scientific community (Huss et al., 2017; Adler et al., 2018, Haeberli and Beniston, 2021) and the public media as downstream communities are increasingly threatened by changes in meltwater supply (Viviroli et al., 2020; Kraaijenbrink et al., 2021) and natural hazards (Clague et al., 2012) such as catastrophic slope failures (Stoffel and Huggel, 2012).

The evolution of the mountain cryosphere is closely linked to snow cover and its influence on glaciers and ground temperatures. In regions where snow accumulates over extended periods, it transforms into ice and subsequently to the formation of glaciers. At a glacier's equilibrium line altitude (ELA), the mean annual accumulation of snow is balanced by the mean annual ablation or melting. When atmospheric temperatures rise, precipitation shifts from snow to rain (Dedieu et al., 2014), reducing the snow supply to glacier accumulation zones. Additionally, less snow cover on glacier ablation zones leads to increased absorption of solar radiation, accelerating melting (Zhang et al., 2021). These changes cause the ELA to move to higher elevations. Observations show that the extent and duration of snow cover are declining in most mountain regions globally (Brown and Mote,

2009; Smith and Bookhagen, 2018; Pulliainen et al., 2020; Notarnicola, 2020). At lower elevations, especially near the 0°C isotherm, even small increases in atmospheric temperatures lead to enhanced melting of snow and ice (Dedieu et al., 2014; Beniston et al., 2018; Seidel and Free, 2003; Pepin and Lundquist, 2008). For instance, the European Alps have experienced a significant upward shift in the seasonal snow line in recent decades (IPCC, 2022), allowing flora and fauna to expand into newly snow-free areas (Rumpf et al., 2021). The rapid worldwide recession of glaciers in response to atmospheric warming has made them a prominent indicator of climate change (Zemp et al., 2015; Hock and Huss, 2021; Hugonnet et al., 2021). The increased melt rates of snow and ice further affect the hydrology of snow-dominated and glacier-fed river basins by altering the quantity and seasonality of river discharges (Kaser et al., 2010; Pellicciotti et al., 2014; Bliss et al., 2014).

The extent and duration of snow cover strongly control ground temperatures and the distribution and depth of permafrost (Zhang, 2005). In particular, its high albedo and insulating properties modulate the heat transfer from the atmosphere into the ground. The near-surface ground temperature, measured a few centimetres below the surface, varies in response to changes in air temperature and snow cover (Etzelmüller et al., 2023). This temperature variation propagates into depth until it reaches the depth of zero annual amplitude (DZAA), at which no more annual temperature fluctuations occur (Smith et al., 2022). Near-surface ground temperatures below snow-free surfaces primarily respond to the annual air temperature cycle (Haberkorn et al., 2021). Where snow cover occurs, ground temperatures are influenced by the presence and timing of snow (Zhang, 2005), which depends on many factors related to the local climate, topography, and surface characteristics (Hasler et al., 2015; Kenner and Magnusson, 2016; Haeberli et al., 2023). Borehole measurements in mountain regions worldwide have shown that permafrost temperatures near the DZAA increased between 1 to 3 °C since the 1980s. In the European Alps, observations of permafrost temperatures over the past 20 years at a depth of 20 meters, which is approximately the DZAA, indicate warming trends ranging from 0.02 to 0.08 K yr^{-1} (Etzelmüller et al., 2020).

Permafrost warming rates typically correlate with atmospheric warming rates in snow-free conditions. However, a stronger temperature response can indicate the impact of long-term snow cover decline on ground temperatures and, thus, permafrost (Etzelmüller et al., 2023). Reliable trend analysis requires long-term records over multiple decades from borehole temperature measurements, which are rare and challenging to implement in high-mountain environments. Given the importance of identifying regions at risk of warming-related natural hazards, spatially distributed information on permafrost warming is crucial. Permafrost temperatures have been derived in Arctic regions by modelling the heat transfer from the atmosphere into the ground using satellite-derived land surface temperature and land cover data (Bartsch et al., 2023). While effective for large areas, this method is less applicable in mountainous landscapes. The steep temperature gradients in these regions require higher spatial resolution than what is typically provided by common satellite sensors.

Thawing permafrost and changing ice cover substantially affect bedrock erosion and sediment production, influencing the stability of high-alpine landscapes. These erosional processes are sensitive to temperature and are expected to shift with climate change. For instance, subglacial erosion at the base of glaciers relies on sliding velocity, which is tied to the glacier's mass balance and thus to snow, input, and melt. (Hallet, 1996). Deglaciation can lead to glacial debuttressing in periglacial environments. This reduction in mechanical slope support weakens hillslopes and can trigger rock failures due to strength relaxation (Ballantyne et al., 2002). Following deglaciation, the exposure of bedrock to the atmosphere can induce a 'thermal shock' due to large-amplitude cyclic surface heating and cooling (Grämiger et al., 2018), resulting in increased rock fall activity due to thermo-mechanical stress changes (Hartmayer et al., 2020; Draebing, 2021). Since glaciers and hillslopes are coupled (Scherler et al., 2011; Scherler and Egholm, 2020), hillslopes are expected to respond with enhanced erosion to retreating and thinning ice. For steep bare bedrock faces without continuous ice accumulation, bedrock fractures form and propagate by frost-related weathering processes (Gruber and Haeberli, 2007), such as the volumetric expansion and segregation of ice (Hallet et al., 1991; Matsuoka and Murton, 2008) that reduce the bulk rock mass strength (Harris et al., 2009) and increase the likelihood of slope failures.

While some of these processes are well understood, others remain poorly constrained. Understanding their interplay across various time scales is essential for predicting changes in erosion rates (Herman et al., 2021) and identifying regions prone to hazardous slope failures. Observations support the connection between warming and increased rockfall activity (Gruber et al., 2004), catastrophic slope failures (Evans and Clague, 1999; Huggel, 2009), and cascading hazards (Shugar et al., 2021). Rockfall activity increases with rising temperatures (Stoffel et al., 2021) and in response to exceptional heatwaves, such as the hot summer of 2003 in the European Alps (Ravenel et al., 2017). Most observations document the removal of fractured bedrock by relatively small-scale hillslope failures. However, in recent years, several deep-seated and large mass wasting events, including the Fluchthorn rockslide (Figure 1.1 c) (Krautblatter et al., 2023), the Piz Scerscen rock avalanche and the Piz Cengalo event (Walter et al., 2020) have been reported, posing significant hazards to local communities.

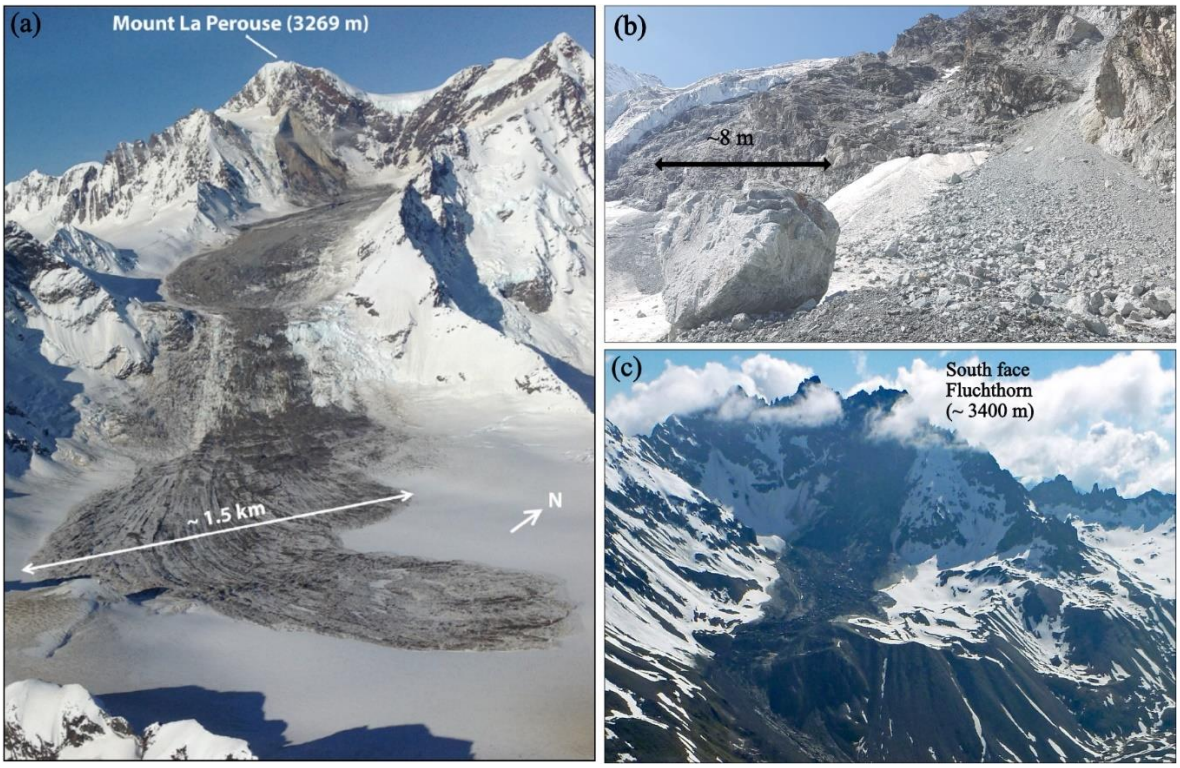

Figure 1.1. Examples of landscape destabilization showing (a) a rock avalanche from Mount La Perousa, Alaska (Coe et al., 2018) deposited on a snow field. Foto taken by Marten Geertsema. (b) Rock fall with large boulder onto the surface of Tsijiore-Nouve Glacier, Switzerland. Foto taken by Katharina Wetterauer. (c) The south face of the Fluchthorn rock slope failure was detached in June 2023, Austria (picture from Land Tirol).

Rock falls and rock avalanches from steep headwalls that deposit onto glaciers (Figure 1.1 a,b) form a cover of loose debris. Even if temporally buried in the ice, englacially transported debris emerges again in the glacier ablation zones (Benn and Evans, 2014). During warming phases, when the ELA shifts upward in elevation, the ablation areas expand and further expose englacial debris. For example, supraglacial debris cover on the Mer de Glace Glacier in the French Alps significantly increased between 1984 and 2022, especially near the confluence and eastern margin of the lower glacier zone (Figure 1.2). Debris cover thickness varies spatially, influencing melt rates as a function of debris thickness (Østrem, 1959). A debris cover thickness of more than ~ 2 cm reduces melt rates as the ice underneath the layer of debris is thermally isolated (Figure 1.3a). For thinner debris cover, the increased solar absorption, by decreased albedo, causes enhanced melt rates (Nicholson and Benn, 2006; Steiner et al., 2021). Consequently, heavily debris-covered glaciers (Figure 1.3 d) can persist longer at higher ambient temperatures, thus, at lower elevations than debris-free glaciers (Scherler et al., 2011). For glaciers with spatially heterogeneous debris thickness, the differential melt can result in complex feedbacks of surface processes that remain poorly constrained (Reznichenko et al., 2010).

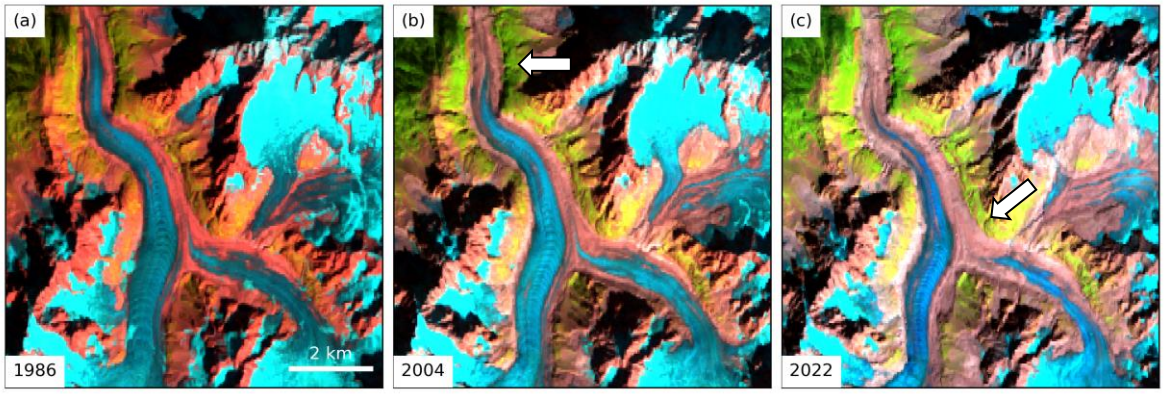

Figure 1.2. Landsat summer scenes of Mer de Glace Glacier in the French Alps showing glacier retreat and expansion of supraglacial debris cover over the years (a) 1987, (b) 2004 and (c) 2022. The satellite images show false color composites using the shortwave infrared 1, near-infrared and red bands as red, green and blue channels.

Globally, approximately 7% of glacier surfaces are covered by debris (Scherler et al., 2018; Herreid and Pellicciotti, 2020), and this coverage is expected to increase in the near future (Fleischer et al., 2021). Changes in debris cover extent within recent decades can be observed using satellite imagery, and several studies document changes in the extent of debris cover evolution (Shukla et al., 2009; Bhambri et al., 2011; Glasser et al., 2016; Gibson et al., 2017; Tielidze et al., 2020). For debris cover thickness, several methods have been tested to quantify its spatial distribution, including the extrapolation from in-situ measurements (Nicholson and Mertes, 2017), ground-penetrating radar campaigns (McCarthy et al., 2017), thermal infrared remote sensing (e.g. Mihalcea et al., 2008; Foster et al., 2012; Rounce et al., 2021; Steward et al., 2021) or estimating thickness by analyzing melt rates using change detection of digital elevation models (Rounce et al., 2018). While many of these methods are not applicable at large scales, the remote sensing approaches are, in part, limited due to the coarse spatial resolution of thermal infrared imagery and large model uncertainties. However, accounting for debris cover effects in glacier melt models is relevant for the prediction of future melt water supply for downstream communities reliant on these resources (Kraaijenbrink et al., 2017).

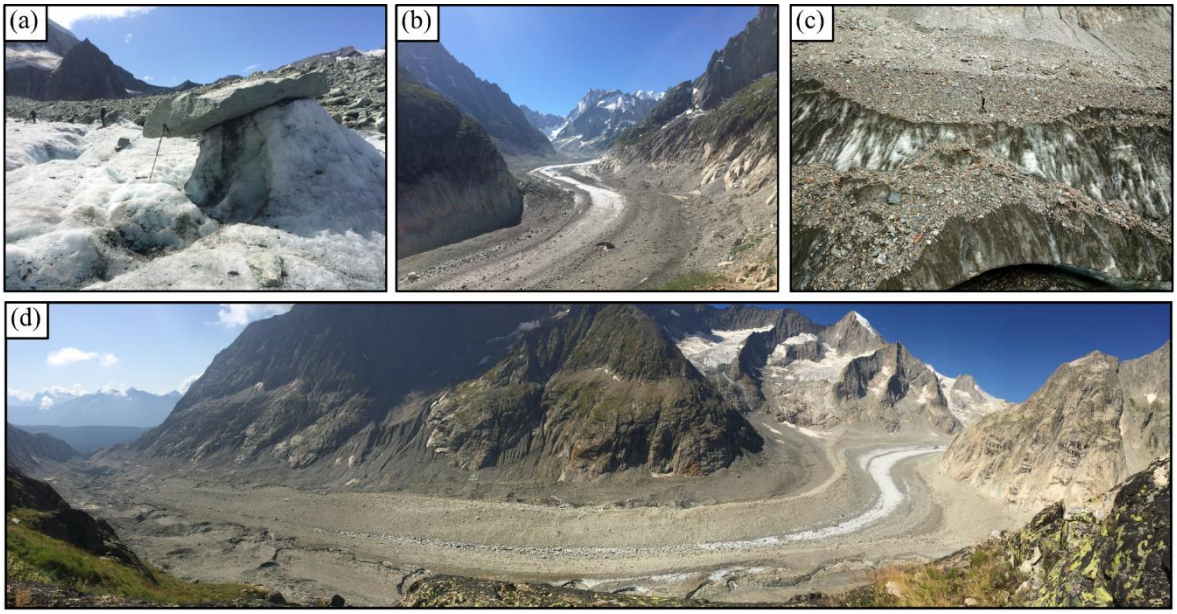

Figure 1.3. Debris-cover of the Oberaletsch Glacier in Switzerland shows (a) a glacier table isolating the ice underneath a single large boulder, (b) heterogeneous debris cover ranging from debris-free to heavily debris-covered areas with steep headwalls in the backgrounds, (c) a large ice cliff with very thin debris cover that increases ice cliff backwasting and (d) panorama view of the lower section of the Oberaletsch Glacier.

On the long-term evolution of glacial landscapes, the effect of supraglacial debris cover may have even further implications. Debris-free glaciers worldwide are generally thinning and retreating in response to climate change (Bolch et al., 2012; Hock et al., 2019; Hock and Huss, 2021). The response of debris-covered glaciers, on the other hand, varies widely, with some advancing, others remaining stable, and some retreating (Scherler et al., 2011; Benn et al., 2012; Gardelle et al., 2012; Kirkbride and Deline, 2013; Benn and Evans, 2014). If, during warming phases, supraglacial debris cover increases, glacier retreat may be partially suppressed, which, in consequence, challenges current interpretations of paleoclimate reconstructions from dated glacial moraine deposits (e.g., Ivy-Ochs et al., 2009).

Glacial landscape dynamics are determined by a complex interplay between glaciers, snow cover, and permafrost, with potential feedbacks occurring as steep hillslopes respond to atmospheric warming through rock falls and rock avalanches. While air temperature may be one of the key drivers for these changes, the earth's surface is the boundary through which heat is transferred from the atmosphere into the ground. Consequently, glacial landscape changes may manifest in long-term land surface temperature (LST) variations. Analyzing LST in these landscapes is thus key to better understand and predict climate change's impact on high mountain landscapes.

1.2 Land surface temperature

The land surface temperature (LST) is the temperature at the interface between the atmosphere and the earth's surface. It is the temperature you would feel if you touched it and is often referred to as the "skin temperature". The World Meteorological Organization has included the LST in the Global Climate Observing System as an Essential Climate Variable, among other surface temperature metrics such as sea surface temperature, lake surface temperature, ice surface temperature, marine air temperature and near-surface air temperature (Merchant et al., 2013; Bojinski et al., 2014). As an indicator for both climate change and land surface processes, LST has been applied in various research fields related to, e.g. global warming (Bechtel, 2015; Schneider and Hook, 2010; Sobrino et al., 2020), surface energy balance (Friedl, 2002), evapotranspiration (Anderson et al., 2007), the urban heat island effect (Dousset and Gourmelon, 2003), heat waves (Hulley et al., 2020), the agricultural sector (Jackson et al., 1981; Holzman et al., 2015; Heinemann et al., 2020) or the prediction of risk areas for vector-borne diseases (Neteler et al., 2011).

LST is usually derived from thermal sensors that measure the directional thermal infrared radiation (TIR) emitted from independent homogeneous and isothermal components within a sensor's field of view (Norman and Becker, 1995). The thermal emission of the ground, or the surface cover, depends primarily on the interaction with the incident solar radiation (Mildrexler et al., 2018), which makes LST a good indicator of the energy partitioning at the boundary between atmosphere and the land surface and is, therefore, a fundamental component of the surface energy balance (see Section 1.3). The LST is sensitive to climate and weather patterns and is a useful independent metric of surface temperature that can be measured with large spatial coverage and at various spatial and temporal resolutions (Hulley et al., 2019).

The most commonly used indicator of climate change is the temporal trend of the near-surface air temperature (T_a), which is usually measured by an in-situ thermometer from weather stations at a height of 2 meters above the ground (Trewin, 2010). However, the spatial coverage of weather stations is limited, and both availability and record length of T_a observations significantly vary from region to region. These data gaps increase the uncertainties of estimated regional warming trends (Stooksbury et al., 1999), and predictive climate models often require gridded temperature data. Although T_a and LST are correlated, they are not the same and differ in magnitude, response to atmospheric and surface conditions, and diurnal phase (Jin and Dickinson, 2010; Good, 2016). LST is more closely related to the biophysical properties of the land surface and responds to variations in land cover type, vegetation density, or soil moisture content.

LST can be derived from TIR remote sensing data and is usually acquired from ground-based, airborne and space-based platforms (Kuenzer and Dech, 2013). Typical satellite-based TIR sensors used for LST retrieval are the Moderate Resolution Imaging Spectroradiometer (MODIS) onboard

the Terra and Aqua satellites, the Advanced Very-High-Resolution Radiometer (AVHRR) observations from the continuous series of NOAA satellites, Landsat's Thematic Mapper (TM), Enhanced Thematic Mapper Plus (ETM+) and Thermal Infrared Sensor (TIRS), the Along Track Scanning Radiometer (ATSR) on board the ERS-1 and ERS-2 , the Advanced Spaceborne Thermal Emission and Reflection Radiometer (ASTER) on board of the Terra satellite or the Visible Infrared Imaging Radiometer Suite (VIIRS) on board NOAA-20 and NOAA-21. Differences across sensors in various factors such as spatial and temporal resolution, swath width, coverage, acquisition time, viewing angle, and spectral response to infrared radiation must be considered when comparing derived LST products between sensors. Only a few sensors exist that cover a sufficiently long time series for climate change studies (Table 1.1).

Table 1.1. Commonly used satellite sensors with long-term thermal infrared measurements.

Sensor/ satellite	Spatial coverage	Time span	Swath widths	Spatial resolution	Temporal resolution
MODIS Terra	Global	1999 - present	2330 km	1000 m	1 day
MODIS Aqua	Global	2002 - present	2330 km	1000 m	1 day
AVHRR	Global	1978 - present	2400–3000 km	1000 m	1 day
Landsat 5 (TM)	Global	1984 - 2013	185 km	120 m	16 days
Landsat 7 (ETM+)	Global	1999 - present	185 km	60 m	16 days
Landsat 8 (TIRS)	Global	2013 - present	185 km	100 m	16 days

*Landsat Collection 2 TM, ETM+ and TIRS are resampled to 30m resolution to match the optical bands

TIR observations from the Landsat family have a very long combined record, high spatial resolution, narrow swath width, and global coverage, but only low temporal resolution and the TIR data is acquired by different sensors. The recently released Landsat Collection 2 (C2), with improved radiometric calibration and geolocation information (Crawford et al., 2023), is optimized for processing Landsat data through time. The Landsat C2 - Level 2 archive contains consistently generated LST products derived using a single-channel (SC) algorithm (Malakar et al., 2018) that operates on a single TIR band (Jiménez-Muñoz and Sobrino, 2003). The SC algorithm uses the Plank function to retrieve LST and involves corrections for atmospheric and emissivity effects. The clear-sky top of atmosphere radiance received by the sensor is the aggregated radiance of (1) the radiation emitted by the surface, (2) the reflected proportion of the downward atmospheric radiance by the surface and (3) the upward proportion atmospheric path radiance. Mathematically expressed, the at-sensor radiance (L_{sat}) for a given wavelength (λ), here in the longwave infrared domain, and the viewing angle of the sensor (θ) is expressed as:

$$L_{sat,\lambda}(\theta) = \left[\varepsilon_\lambda B_\lambda(T_s) + (1-\varepsilon_\lambda)L_\lambda^{\downarrow}\right]\tau_\lambda(\theta) + L_\lambda^{\uparrow} \quad \text{Eq. 1.1,}$$

where ε_λ is the surface spectral emissivity, $B_\lambda(T_s)$ is the Planck function with T_s being the surface temperature, $L_\lambda^\downarrow$ is the atmospheric downward radiance, τ is the atmospheric transmissivity, and $L_\lambda^\uparrow$ is the atmospheric path radiance. For the atmospheric correction of Landsat TIR data, atmospheric emissions and attenuations are estimated using a radiative transfer model and reanalysis data (Barsi et al., 2004). The emissivity correction is based on the Advanced Spaceborne Thermal Emission and Reflection Radiometer Global Emissivity Data Set version 3 (ASTER GED v3) with further adjustment for the land surface conditions at the time of the Landsat overpass (Hulley et al., 2015). In the last step, a look-up table of radiances for 0.01 K temperature intervals is generated using the Planck function (Eq. 1.2):

$$B_\lambda(T_s) = \frac{c_1}{\lambda^5 \left[\frac{c_2}{e^{\lambda T}} - 1\right]} \qquad \text{Eq. 1.2,}$$

where c_1 and c_2 are physical constants of 1.191×10^8 Wμm^4 sr^{-1} and 1.439×10^4 μm K, respectively. LST is then determined by interpolation with the previously corrected thermal surface emittance (Alley and Jentoft-Nilsen, 1999). The operational SC algorithm generates standardized LST from Landsat series (TM, ETM+ and TIRS), allowing for high-resolution LST time series analysis (Malakar et al., 2018)

In principle, the record length of LST products from sensors listed in Table 1.1 is long enough for climate change studies and environmental monitoring. However, some requirements must be fulfilled to derive a long-term LST trend from LST observations. Along with temporally consistent cloud masking, calibration, georeferencing and atmospheric correction, a key contributor to the temporal coherence of LST is the long-term stability in orbit (Kuenzer and Dech, 2013). Orbital drift significantly affects the long-term LST trends, as a change in the satellite's orbit changes the acquisition time and, thus, the LST towards higher or lower temperatures (Reiners et al., 2023). Many algorithms have been developed to correct the phenomenon of drifting AVHRR sensors (Gutman, 1999; Pinheiro et al., 2006; Sobrino et al., 2008; Ma et al., 2020; Julien and Sobrino, 2022). The sporadic and continuous variations of Landsat TM and ETM+ orbits are rarely addressed in the scientific literature (Zhang and Roy, 2016; Roy et al., 2020; Qiu et al., 2021), and the impact on LST has not yet been quantified. Most temporal analysis of LST relies on data from the MODIS sensor, as it has remained stable in orbit over the past 20 years (Hulley et al., 2018). However, the large swath width (varying viewing angles within a single scene) and coarse spatial resolution restrict the applicability of long-term LST trends for some regions, such as high mountain regions with large altitudinal gradients. As LST responds to changes in atmospheric temperatures and to surface processes, time series analysis of LST can provide insights into both (Muro et al., 2018). Several approaches have been proposed to analyze LST time series data and to account for the inter-annual trend, the intra-annual variation (seasonality) and abrupt LST changes due to land cover changes

(time series breaks). The most commonly applied method to derive long-term LST trends is a simple linear regression (Good et al., 2020) in conjunction with a statistical significance test such as the Student's *t*-test (Muro et al., 2018). An alternative approach is the non-parametric Mann-Kendall test combined with the Theil-Sen slope for a robust linear trend estimation (Sobrino et al., 2020). Both return the same results if the deviations from the trend line are normally distributed (Schneider et al., 2013**)** with zero mean. To account for the seasonality in the LST data, an annual temperature cycle model (Bechtel, 2015) can be combined with a linear trend (Fu and Weng, 2016). Abrupt changes in land cover can lead to step changes in the LST time series. Several methods have been proposed to identify break points in LST time series by iteratively fitting a piecewise linear trend and a seasonal model (Verbesselt et al., 2010; Li et al., 2022). While several methods exist to derive LST trends, interpreting the temporal changes in LST requires considering the surface energy balance.

1.3 Surface energy balance

The temperature of the earth's surface is an expression of the surface energy balance (SEB) between the atmosphere and the ground (Duveiller et al., 2018). The primary driver of the surface energy fluxes is the incoming solar radiation, which varies with latitude and in relation to diurnal and annual cycles. At the Earth's surface, the incoming radiative energy fluxes are balanced by energy partitioning into various components (Eq. 1.3) that directly influence the LST (Li et al., 2023). Factors such as biophysical surface properties (e.g., albedo, emissivity, and surface roughness), vegetation density, soil moisture, and atmospheric conditions control how much energy is absorbed, reflected, or emitted by the surface, thereby affecting the LST and other surface processes (Hartmann, 1994). SEB models exist with various levels of complexity to estimate spatially distributed surface energy fluxes at various time scales using remote sensing data (McShane et al., 2017). In Chapter 2, I use a distributed point SEB model at sub-daily time intervals (Brock et al., 2010) over a debris-covered glacier surface (Figure 1.4) while in Chapter 3, I only use only the incoming solar radiation component. The specific use case in Chapter 3 requires accounting for the rate of change in heat storage within a surface layer. The SEB (Eq. 1.3) at the earth's surface can be expressed as the sum of directional energy fluxes in units of Wm^{-2}:

$$S_{net} + L_{net} + H + LE + \Delta S + G = 0 \qquad \text{Eq. 1.3,}$$

where S_{net} and L_{net} are net shortwave and longwave radiation fluxes, H is the turbulent sensible heat flux, LE is the latent heat flux, ΔS is the rate of change of heat stored in a surface layer, and G is the conductive ground heat flux.

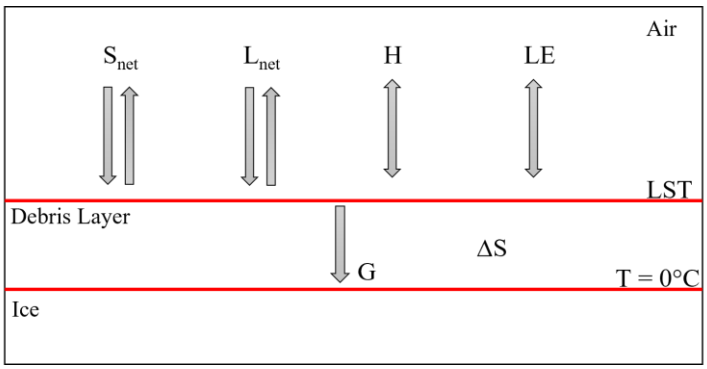

Figure 1.4. Schematic diagram of surface energy balance model showing directional energy fluxes at the boundary between the atmosphere and a debris-covered glacier, including the rate of change of heat storage (S) in a layer of supraglacial debris.

A key component of the SEB is the incoming shortwave radiation (S_{in}). At the top of the atmosphere, the incident energy flux is given by the solar constant of 1361.8 W m^{-2}. Modelling S_{in} under clear-sky conditions at the earth's surface (Eq. 1.4) typically involves reconstructing the solar zenith angle at a specific location and time and accounting for atmospheric attenuation effects. In a simplified version, S_{in} can be calculated as:

$$S_{in} = 1361.8 \cdot \cos\theta \cdot \tau_{total} \quad \text{Eq. 1.4,}$$

where θ is the solar zenith angle and τ_{total} the total atmospheric transmissivity. I implemented a Python version of the S_{in} model from the insol-package, written in the programming language R by Corripio et al. (2013) and is originally based on the work of Bird and Hulstrom (1981) and Iqbal (1983). The model calculates the solar zenith angle using the trigonometric relationship between the solar position in the sky and the local topography at given surface coordinates on Earth (Iqbal, 1983) derived from a digital elevation model. The attenuation by various atmospheric constituents is computed using a set of transmissivity equations that approximate scattering and absorption effects in the atmosphere (Bird and Hulstrom, 1981). The meteorological parameters, such as air temperature and relative humidity, were used from ERA-5 Land reanalysis data. The output of the insol-model (Corripio et al., 2013) are the spatially distributed direct and diffusive components of S_{in}. For more details of the S_{in} model and its applications in this thesis, see Chapter 1 and 2) and Appendix A-1. The incoming S_{in} is partially reflected and partially absorbed by the surface, with the proportion of reflected radiation determined by the surface albedo. Therefore, the net shortwave radiation (S_{net}) can be calculated as a function of the albedo:

$$S_{net} = S_{in} \cdot (1 - \alpha) \quad \text{Eq. 1.5,}$$

where α is the albedo. The absorbed shortwave radiation causes the surface to heat up and, in turn, emit longwave radiation at a rate that is proportional to the fourth power of the LST (Eq. 1.6). The outgoing longwave radiation (L_{out}) component in the SEB model is determined by the Stefan-Boltzmann-Law and requires knowledge of the surface cover specific emissivity:

$$L_{out} = \varepsilon_s \sigma {T_s}^4 \quad \text{Eq. 1.6,}$$

where ε_s is the emissivity of the surface, σ the Stefan-Boltzmann constant 5.67×10^{-8} W m^{-2} K$^{-4,}$ and T_s is the temperature of the surface - here LST. The incoming longwave radiation (L_{in}) is the downward directed proportion of longwave radiation emitted by the atmosphere and is equally calculated as L_{out} with emissivity and temperature of the atmosphere instead of the land surface. The net longwave radiation (L_{net}) results in the difference between incoming and outgoing longwave radiation ($L_{net} = L_{in} - L_{out}$).

The net radiation ($S_{net} + L_{net}$) at the surface is partitioned into the sensible heat flux, the latent heat flux, the ground heat flux and the rate of change of heat storage. The sensible heat flux involves heat transfer through air movement and is influenced by the temperature difference between the air and the surface, as well as the wind speed. Typically, during the day, the land surface is warmer than the air above it, resulting in the surface heating the air. The warmed air is then transported away from the surface by wind, transferring energy to the atmosphere through convection. The latent heat flux (LE) refers to the energy transfer associated with the phase change of water by evapotranspiration of the surface cover. Over rocky surfaces and during precipitation-free conditions, as in the studied case of a dry layer of supraglacial debris cover (chapter 2), the latent heat flux is assumed to be 0 and was neglected (Schauwecker et al., 2015). While there are several approaches to estimating the sensible heat flux (H) (Mohan et al., 2020), many remote sensing applications are based on the bulk aerodynamic approach using a bulk transfer coefficient (Glen, 1997; Nicholson and Benn, 2006):

$$H = \rho_0 \left(\frac{P}{P_0}\right) cAu(T_a - T_s) \quad \text{Eq. 1.7,}$$

where ρ_0 is the density of air at standard sea level pressure (1.28 kg m^{-3}), P is the air pressure at the location (Pa), P_0 the standard air pressure at sea level (1.013×10^5 Pa), c the specific heat capacity of air (1010 J Kg^{-1} K^{-1}), u the wind speed (m s^{-1}), A is a dimensionless transfer coefficient, T_a the air temperature (K), T_s the surface temperature (K) - here LST.

The rate of change of heat storage (ΔS) for sub-daily time intervals can be estimated by:

$$\Delta S = \rho_d c_d \frac{\partial \overline{T_d}}{\partial t} d \quad \text{Eq. 1.8,}$$

where ρ_d is the debris density (kg m^{-3}), c_d is the specific heat capacity of debris (J kg^{-1} K^{-1}), d is the debris thickness (m), and $\frac{\partial \overline{T_d}}{\partial t}$ the average rate of mean debris temperature change (K s^{-1}) with $\overline{T_d}$ as the mean debris temperature and t is the time. The conductive heat transfer into the ground (G), or here through a layer of debris, is termed the ground heat flux and calculated as:

$$G = -k_d \frac{(T_s - T_{di})}{d} \quad \text{Eq. 1.9,}$$

where T_s is the surface temperature (here LST), T_{di} is the temperature at the debris-ice interface, and k_d is the effective thermal conductivity (W m^{-1} K^{-1}). We assume a linear temperature gradient in the debris layer is equal to the difference between the LST and the temperature of the debris–ice interface, which is assumed to be at the melting point of 0 °C (Brock et al., 2010).

As LST is a fundamental variabile in the surface energy balance, LST measured from satellites or UAVs significantly contribute to quantifying the energy fluxes at the interface between the atmosphere and the ground at various spatial scales. While specific components like incoming solar radiation (S_{in}) can be computed with high accuracy under clear-sky conditions, other components remain challenging to estimate accurately due to significant uncertainties.

1.4 Research objective and questions

While high-mountain landscapes respond strongly to climate change, their remoteness and often limited accessibility require the development and advancement of remote sensing techniques to analyse recent landscape changes at various spatial scales. The main research objective of this thesis is to evaluate the potential and limitations of remotely sensed LST for detecting and analyzing glacial landscape dynamics using two distinct sensor systems. First, at the glacier-wide scale, I use high-resolution LST data derived from an unpiloted aerial vehicle (UAV) to quantify spatially distributed supraglacial debris thickness. Second, at mountain range scale, I use satellite-derived LST data from combined Landsat 5, 7, and 8 time series to assess patterns and trends in the LST of the European Alps. Based on these two sensor systems, I address, in three individual studies, the following research questions:

1) How can high-resolution LST from UAVs provide insights into the evolution of debris-covered glaciers?
2) How can the extensive Landsat Collection 2 LST archive be used to detect changes in glacial landscapes?
3) How do LST trends vary with changes in land cover and elevation?

In Chapter 2, I focus on high-resolution LST measurements obtained from a UAV to quantify spatially distributed supraglacial debris thickness. High-resolution mapping of debris thickness

potentially allows the monitoring of glacier-wide debris cover evolution, which can advance predictive glacier melt models in high mountain settings. Combining UAVs and thermal infrared sensors is a new field of research and has not been tested much in high mountainous terrain. I developed a hardware setup using a consumer-grade UAV and a thermal infrared sensor to measure a large fraction of the diurnal temperature cycle of a debris-covered glacier section in Switzerland. I further tested two approaches to derive spatially distributed debris cover thickness estimates. First, I estimated debris cover thickness by solving a surface energy balance model in conjunction with meteorological reanalysis data for debris thickness. This approach is independent of in-situ measurements and has so far only been tested with LST from coarse spatial resolution satellite data. Second, I used least squares regression of a rational curve using debris-thickness field measurements. I discuss the limits and opportunities of both approaches.

In Chapter 3, I access patterns and trends of combined Landsat 5, 7 and 8 LST data of the Swiss Alps using the cloud-computing platform Google Earth Engine. LST trends were derived by regression of a harmonic model including linear trend and validated with LST data from 119 weather stations distributed across the Swiss Alps. As the Landsat satellites experience orbit changes over the past almost 40 years of observations, LST trends are biased by a shift in LST acquisition time that varies with topography. In this chapter, I quantify the magnitude and spatial variability of the LST trend bias and propose a simple correction method using modelled changes in incoming shortwave radiation. Further attention is given to the effect of cryosphere changes on LST trends.

In Chapter 4, I analyze orbit drift-corrected LST trends across the European Alps and assess the effects of land cover and land cover changes on these trends. Since different land covers respond individually to climate change, LST trends vary accordingly. I use various land cover and land cover change maps from auxiliary datasets to extract and compare LST trends, highlighting their distributions and elevational differences. This analysis identifies regions experiencing the strongest surface warming with respect to changes in the mountain cryosphere. Additionally, I evaluate the suitability of the harmonic model for different land cover types.

In Chapter 5, I draw the conclusions from the individual studies with respect to the specific research questions and provide a synthesis of the work related to the overarching objective of the thesis.

2 High-resolution debris cover mapping using UAV-derived thermal imagery: limits and opportunities

Deniz Tobias Gök[1], Dirk Scherler[1,2], Leif Stefan Anderson[1,3]

[1]GFZ German Research Centre for Geosciences, Telegrafenberg, 14473 Potsdam, Germany
[2]Institute of Geological Sciences, Freie Universität Berlin, 12249 Berlin, Germany
[3]University of Utah, Salt Lake City, 000, United States

Published in: The Cryosphere, 17, 1165–1184, https://doi.org/10.5194/tc-17-1165-2023, 2023

Abstract

Debris-covered glaciers are widespread in high mountain ranges on Earth. However, the dynamic evolution of debris-covered glacier surfaces is not well understood, in part due to difficulties in mapping debris-cover thickness in high spatiotemporal resolution. In this study, we present land surface temperatures (LST) of supraglacial debris cover and its diurnal variability measured from an unpiloted aerial vehicle (UAV) at a high (15cm) spatial resolution. We test two common approaches to derive debris thickness maps by (1) solving a surface energy balance model (SEBM) in conjunction with meteorological reanalysis data and (2) least squares regression of a rational curve using debris thickness field measurements. In addition, we take advantage of the measured diurnal temperature cycle and estimate the rate of change of heat storage within the debris cover. Both approaches resulted in debris thickness estimates with an RMSE of 6 to 8 cm between observed and modelled debris thicknesses, depending on the time of the day. Although the rational curve approach requires in-situ field measurements, the approach is less sensitive to uncertainties in LST measurements compared to the SEBM approach. However, the requirement of debris thickness measurements can be an inhibiting factor that supports the SEB approach. Because LST varies throughout the day, the success of a rational function to express the relationship between LST and debris thickness also varies predictably with the time of day. During the warming phase of the debris cover, the LST depends strongly on the terrain aspect, rendering clear-sky morning flights that do not account for aspect-effects problematic. We find the rational curve approach with LST measured in the evening hours to yield the best result. Our sensitivity analysis of various parameters in the SEBM highlights the relevance of the effective thermal conductivity when LST is high. The residual and variable bias of UAV-derived LST during a flight requires calibration, which we achieve with bare ice surfaces. The model performance would benefit from more accurate LST measurements, which are challenging to achieve with uncooled sensors in high mountain landscapes.

2.1 Introduction

Debris-covered glaciers are common in many mountain ranges globally (Herreid and Pellicciotti, 2020; Scherler et al., 2018). Although debris cover is generally rather thin, usually less than a meter, it can profoundly influence surface melt rates, and thus the mass balance of glaciers (Rounce et al., 2021). Whereas thin debris cover (< 2 cm) accelerates melt rates, due to the lower albedo compared to clean ice, thick debris cover insulates the ice surface and reduces melt rates (e.g., Østrem, 1959; Nicholson and Benn, 2006). Consequently, glaciers with widespread and thick debris cover can persist longer at lower elevations than debris-free glaciers (Scherler et al., 2011a). Debris-free glaciers worldwide respond to climate change by thinning and retreating (Bolch et al., 2012; Hock et al., 2019; Hock and Huss, 2021). Debris-covered glaciers in contrast show a broad range of responses to climate change with some glaciers being stationary and some retreating.(Scherler et al., 2011b; Benn et al., 2012; Gardelle et al., 2012; Kirkbride and Deline, 2013; Benn and Evans, 2014). Therefore, regional to global scale predictions of glacier evolution in response to climate change need to account for debris cover (Rounce and McKinney, 2014; Pellicciotti et al., 2015).

Complex interactions between the various elements of debris-covered glaciers, including differential melt, the overall down glacier thickening of the debris layer, and the presence of ice cliffs and surface ponds remain not well understood (Benn et al., 2012; Anderson et al., 2021; Kirkbride, 1993; Irvine-Fynn et al., 2017; Miles et al., 2018; Anderson and Anderson, 2018). Processes responsible for the extent and thickness of debris cover are the rate of debris supply from bedrock hillslopes, the rate of ablation, which exposes englacially transported debris, and surface processes as well as ice dynamics (Hartmeyer et al., 2020a, 2020b; Kirkbride and Deline, 2013). As all these processes vary with time, supraglacial debris cover ought to change in time, too. Indeed, recent studies document changes in debris-cover thickness in various mountain ranges on Earth. Most studies, however, focus on changes in the extent of debris cover (Shukla et al., 2009; Bhambri et al., 2011; Glasser et al., 2016; Tielidze et al., 2020, Kaushik et al., 2022), whereas studies documenting changes in thickness are relatively rare (Stewart et al., 2021; Gibson et al., 2017). In addition, debris-thickness observations based on satellite imagery are at best limited to a relatively coarse spatial resolution of tens of meters. In particular, the abundance of supraglacial streams, ponds and ice cliffs can increase or decrease rapidly across the glacier surface (Anderson et al., 2021). A better understanding of transport and the emergence of supraglacial debris over short timescales requires the development of quantitative models. Therefore, comprehensive observations of debris-cover extent and thickness at high resolution are essential for understanding the dynamic evolution of debris-covered glacier surfaces.

Existing approaches to spatially quantify debris thickness comprise (1) the extrapolation of point or cross-section field data (McCarthy et al., 2017; Nicholson and Mertes, 2017), (2) the

exploitation of the relationship between the land surface temperature (LST) and debris thickness (Nakawo and Young, 1981), (3) the estimation of sub-debris melt by DEM differencing and converting melt rate to debris thickness based on the Østrem-curve (Rounce et al., 2018), (4) a combination of 2 and 3 (Rounce et al., 2021) and (4) the use of synthetic-aperture radar (Huang et al., 2017). It has been shown that the LST can be related to debris thickness by fitting empirical functions (e.g. linear, exponential, rational) using ground data (Mihalcea et al., 2008; McCarthy, 2019; Boxall et al., 2021; Gibson et al., 2017), exponential scaling assuming the lowest measured LST corresponds to 1 cm debris thickness (Kraaijenbrink et al., 2017), or solving a surface energy balance model for debris thickness with meteorological data input from either automated weather stations or reanalysis data (Zhang et al., 2011; Foster et al., 2012; Rounce and McKinney, 2014; Schauwecker et al., 2015; Stewart et al., 2021).

Most LST-based approaches to estimate debris-cover thickness have focussed on satellite imagery, whereas studies employing near-ground image acquisition in high resolution are less frequent. LST can be measured in high resolution using uncooled microbolometers applied either obliquely from the ground surface (Hopkinson et al., 2010; Aubry-Wake et al., 2015; Aubry-Wake et al., 2018) or in nadir mounted to an unpiloted aerial vehicle (UAV) (Kraaijenbrink et al., 2018). Debris thickness was recently mapped using oblique LST (Herreid, 2021), but the quantification of debris thickness from UAV thermal imagery has remained elusive. The possibility to measure the spatiotemporal variability of LST from the ground or UAV is a particular advantage, as most thermal infrared measurements from space do not have a sub-daily temporal resolution.

Here, we present UAV-derived LST and its diurnal variability to estimate debris thickness as it varies in space at various times of the day. To estimate debris thickness we, solve a surface energy balance model using ERA-5 reanalysis data and the measured LST. We take advantage of the diurnal measurements and consider the debris's change in heat storage as part of the surface energy balance model. We then compare the results with debris thickness maps derived from the empirical relationship of LST and in-situ measured debris thicknesses using a rational curve.

2.2 Study Area

Tsijiore-Nouve Glacier (TNG) (Figure 2.1) located in southwest Switzerland (46.01 °N, 7.46 °E) is around 5 km long with an average width of ~300 m. The surface area of TNG covers ~2.73 km². The glacier is characterized by an ice fall in the central part, separating the debris-covered and the debris-free part of the surface. The flow direction is north and shows a strong eastward knickpoint within the ablation zone. The lateral moraines are very steep and partly vegetated. The surface of TNG hosts steep ice cliffs (Figure 2.1b), supraglacial streams, debris-free bare ice parts, partly continuous as well as partly patchy debris-cover of heterogenic thicknesses and grain sizes. The glacier is easily accessible at day and night and therefore well suited for our study. The study focuses on a nearly

continuously debris-covered portion of TNG. A relatively small study area of 60000 m² allowed for 8 UAV flights covering the entire study area throughout the day.

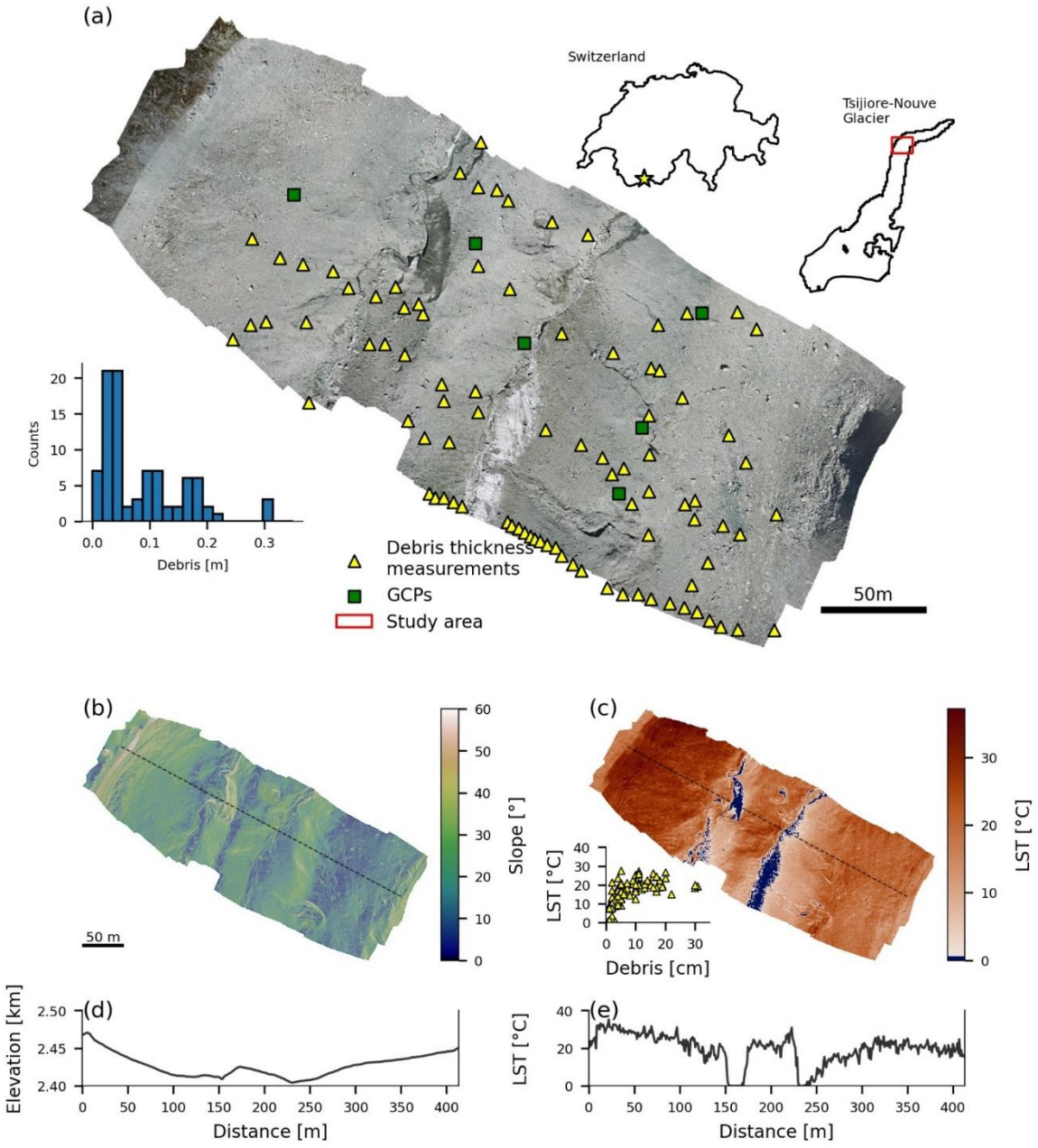

Figure 2.1. Overview of study area on Tsijiore-Nouve Glacier, Switzerland. (a) Orthomosaic from optical unpiloted aerial vehicle (UAV) data obtained on 30.08.2019. Yellow triangles indicate locations of debris thickness measurements, and green squares indicate ground control points. The histogram shows the distribution of the debris thicknesses measured in the field. (b) Slope map obtained from UAV-derived digital elevation model (15 cm resolution). (c) UAV-derived land surface temperature (LST) at 13h. Blue areas depict LST < 0.5 °C. The inset scatter plot shows in-situ debris thickness measurements versus LST. Black dashed lines in (b) and (c) indicate profiles shown in (d) (elevation) and (e) (LST).

2.3 Materials & Methods

2.3.1 Field Data

Field data were collected on 30.08.2019 on an area of approximately 60000 m^2 (Figure 2.1a), under blue sky conditions (isolated clouds in the late afternoon). Spatially distributed debris surface temperature was measured between 9 h and 22 h at 2-h intervals to capture the diurnal temperature cycle. Temperature measurements were done using a radiometric uncooled microbolometer (FLIR Tau2 longwave infrared thermal camera) mounted to a DJI Mavic Pro UAV. The UAV followed the same pre-defined path for all 8 flights at 80 m elevation above the glacier surface (terrain adjusted). Optical UAV imagery (12 MP) was recorded simultaneously with the thermal images. The thermal sensor operates within a temperature range of -40 °C to 160 °C, has a resolution of 640x512 pixels, which, given the flight altitude, yields a thermal image resolution of approximately 0.17m x 0.16 m, and measures longwave radiation within a range of 7.5 to 13.5 µm. Recording of the thermal infrared images was done in conjunction with the ThermalCapture 2.0 OEM (Teax Technology GmbH), allowing for the storage of images on an SD card. The recording was done with a reduced framerate (default 9 Hz). Each flight took between 12 and 15 minutes and captured around 600 thermal images. The setup is suitable for high-mountain UAV applications due to its very low size and weight. Prior to the UAV flights 6 ground control points (GCPs) were distributed across the area of interest (Figure 2.1a). The GCPs were made from aluminium foil to be clearly recognizable in the thermal images due to the very low emissivity.

Debris thickness measurements were made at 90 locations within the study area (Figure 2.1). Coordinates of measurement locations were documented using a Garmin Handheld GPS device (horizontal accuracy: ±3.6 m). The debris cover on the TNG is generally thin: measured thicknesses are below 30 cm, with a mean of 9 cm, a median of 5 cm, and a standard deviation of 10 cm. The debris cover close to lateral moraines consists of very large boulders (>0.5 m) that rendered measurements impractical and thus introduced a bias on the point measurements. Furthermore, it was not entirely clear where debris-covered ice transitioned to lateral moraines near the glacier margin.

2.3.2 Thermal drift and offset correction

Uncooled microbolometers are sensitive to environmental temperature fluctuations (Heinemann et al., 2020). Specifically, the sensor's detector focal plane array, the sensor housing, and the lens of uncooled microbolometers are sensitive to temperature changes. Accurate radiometric temperature measurements require a thermal equilibrium between the sensor's components and the environment. Unbalanced thermal conditions (e.g. the sensor cools down after UAV take-off, changing wind conditions, or heats up by direct incident shortwave radiation) introduce a temperature bias. The thermal adjustment of the sensor can thus lead to changes in measurements, known as

thermal drift: the recorded temperature changes while the object's temperature remains the same (Ribeiro-Gomes et al., 2017; Malbéteau et al., 2018; Dugdale et al., 2019a; Aragon et al., 2020). Furthermore, the ever-changing micro-meteorological conditions under a drone prevent the perpetuation of a thermal equilibrium and hamper accurate radiometric measurements.

The FLIR Tau2 sensor performs an internal calibration, the flat field correction (FFC), to correct for non-uniformities by lens distortions and variations in the thermal pixel-to-pixel sensitivity. FFC is performed using the shutter at power up, when the camera changes temperature, and periodically during operation. The shutter is considered to be a uniform temperature source for each pixel and is used to update the offset correction coefficients. This internal calibration leads to in-flight temperature jumps that are accounted for in a post-processing step, called drift compensation. The occurrence of the FFC events is used to calculate linearly backwards an offset value for each frame (Teax, personal communication). Usually, this is done automatically by the ThermalViewer software but in our case, the reduced framerate resulted in the loss of several frames containing the FFC occurrence metadata entry. A drawback of the system one should be aware of. However, we identified the frames following the internal calibration and implemented the drift compensation ourselves (Figure 2.2b). To find the temperature jumps within the images, we used a threshold of 2 K differences in the mean temperature of the overlapping part in consecutive image pairs. The temperature jumps are clearly visible in the histogram time series (Figure 2.2a) and we found this threshold to match the temperature jumps best. The overlap was defined as the bounding box of matching keypoints detected in successive images using the Oriented FAST and Rotated BRIEF (ORB) algorithm (Rublee et al., 2011) implemented in the scikit-image python library (Van Der Walt et al., 2014).

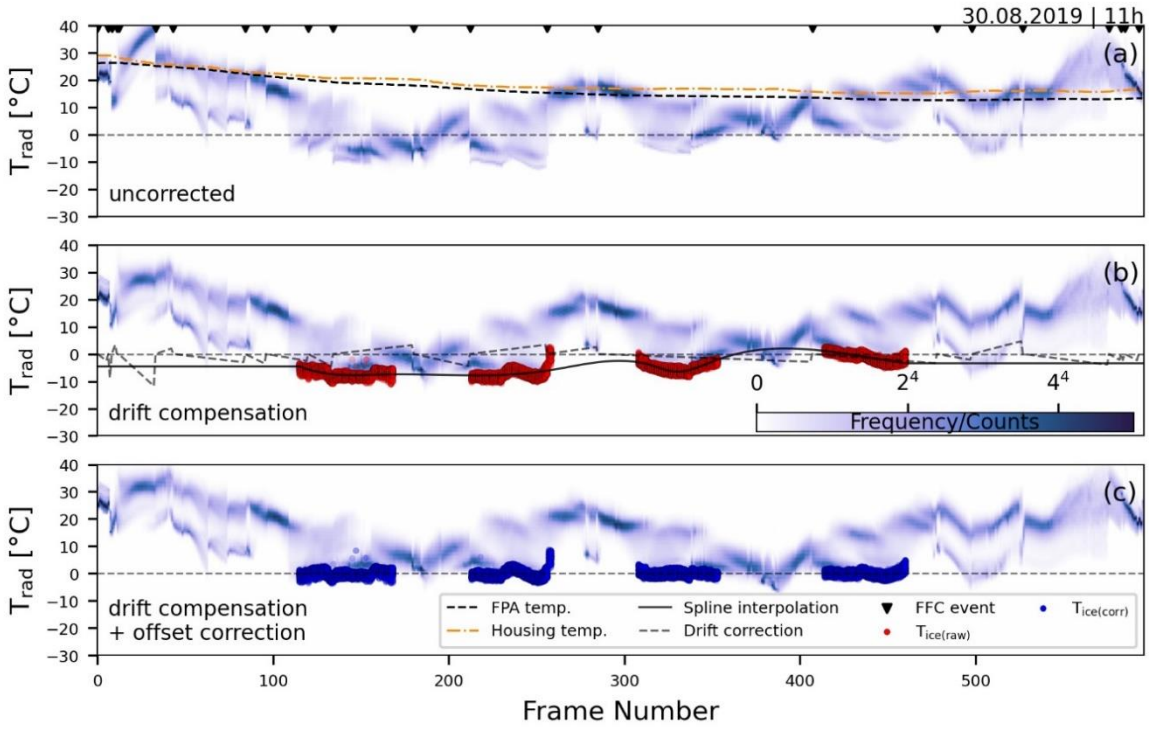

Figure 2.2. Thermal correction and calibration using bare ice temperatures on 2019-08-30 at 11:00 local time. Histogram time series, each vertical stripe shows the frequency of measured temperatures of one thermal infrared image. (a) Raw at-sensor (brightness) temperature with detected flat field correction events (black triangles). The temperatures of the focal plane array (FPA) and housing case returned by the sensor are shown in orange and bold black dashed line. (b) Drift compensated temperatures with ice surface temperatures (red dots) and thermal drift correction offset (dashed line). The black line shows the spline interpolation of the measured ice surface temperatures with the edges set to a constant value. (c) Offset corrected temperatures, each frame based on the spline interpolation that the ice surface temperatures are at 0 °C.

Despite the successful detection of FFC events and applied drift compensation during postprocessing of the temperature data, we still observed bare-ice surfaces with considerable temperature deviations from 0 °C, the expected temperature for a melting ice surface. Furthermore, the remaining temperature bias appears to be not constant with time (Figure 2.2b). Therefore, we applied a further calibration step that employs the ice surface as a reference. The air temperature during the day of measurements was well above 0 °C and the ice surface, where visible was melting. Therefore we assume the LST of the ice surface to be at 0 °C. The extraction of the ice surface was done by a color-based segmentation algorithm using k-means clustering (Pedregosa et al., 2011) and subsequently manually confirmed, similar to the approach of Aubry-Wake et al. (2015). We then interpolated the ice temperatures using splines and calculated an offset correction for each frame, in a manner that the LST of the ice will be 0 °C (Figure 2.2c). The drift and offset were similar for most flights, but the evening flights showed less variation in the ice temperatures. However, for large ice temperature variations, the spline interpolation may not capture the temperature offset as shown in Figure 2.2c (frame ~250). The correction and calibration procedure was applied for each flight.

2.3.3 Orthomosaic generation (photogrammetry)

Each flight yielded around 600 thermal infrared frames (Figure 2.2), of which around 400 have been used to generate orthomosaic maps and 200 were omitted as they recorded the take-off and landing of the UAV. The diurnal variation of the surface temperature and relatively low contrast of thermal images led to spatiotemporal variations in the reconstruction of the 3D point clouds. Instead of additional point cloud alignment (Rusinkiewicz and Levoy, 2001), we orthorectified the thermal images using the same digital surface model (DSM) obtained from simultaneously recorded optical images. Therefore, we identified and marked all GCPs in both the optical and thermal images prior to the photogrammetric processing to improve the image alignment and improving the calculation of the camera calibration parameters (Cook, 2017). As the footprint of the images is relatively large with respect to our area of interest, the 6 GCPs were visible in almost all thermal images. The generated DSM from the optical images was then used as the basis for the thermal image orthorectification. The overlapping parts were reduced by a weighted average during the orthomosaic generation. Agisoft Metashape software offers several options on how to handle overlap areas and we found the default setting to produce the most reasonable results.

2.3.4 Land surface temperature (LST)

The temperature measured by the sensor, the brightness temperature, is influenced by (1) the upward-directed path radiance, (2) the radiation emitted by the surface towards the sensor and (3) the reflected portion of the incoming atmospheric longwave radiation. Due to the low flight elevation of 80 m above ground we neglect the path radiance. The reflected portion of incoming atmospheric longwave radiation (3) was taken from the downward thermal flux of ERA5 Land hourly reanalysis data (Muñoz Sabater, 2019) with respect to the time of flight. The large footprint of the reanalysis data (0.1° × 0.1°) compared to the small test site (~150 m × 350 m) might introduce additional uncertainties. However, the influence on the LST is small, as the magnitude of the reflected radiation is also very small. The retrieval of the LST (2) is then a function of the emissivity of the surface material and the atmospheric transmissivity between the ground and the sensor. We assume the transmissivity to be negligible under the meteorological conditions and flight altitude (Kraaijenbrink et al., 2018; Malbéteau et al., 2018). Following Stefan-Boltzmann law we calculated the LST using:

$$LST = \sqrt[4]{\frac{\sigma T_{rad}^4 - (1-\varepsilon)\cdot LW\downarrow}{\sigma\varepsilon}} \qquad \text{Eq. 2.1,}$$

where σ is the Stefan-Boltzmann constant ($5.67 \times 10^8\ \mathrm{Wm^{-2}K^{-4}}$), ε the emissivity of the surface type (debris=0.94, rough ice=0.97) (Rounce and McKinney, 2014; Aubry-Wake et al., 2015), and $LW\downarrow$ the incoming longwave radiation ($\mathrm{Wm^{-2}}$). Some authors point out the relevance of atmospheric transmissivity (Torres-Rua, 2017; Herreid, 2021), while others neglect it due to low UAV flight

elevations above the ground surface (D. G. Sullivan et al., 2007; Hill-Butler, 2014). We think radiation attenuated by water vapour in the atmosphere between the sensor and ground would be spatially uniform and thus compensated by our calibration procedure. To assign emissivity values across the glacier surface, we distinguished between ice and debris using a supervised random forest classification with manually created training data (Breiman, 2001). By comparison with the optical imagery and according to the algorithm's mean prediction error, we found the best classification results when the temperature differences between ice and debris were the largest, at 15 h. Data from this flight were used to classify the thermal imagery.

2.3.5 Surface energy balance model

Thermal energy fluxes at the earth's surface are described in the surface energy balance approach used here. For a layer of supraglacial debris, the rate of change of heat stored in the debris (ΔS) must balance all incoming and outgoing energy fluxes (all fluxes have units of Wm^{-2} and are positive when directed towards the debris layer):

$$\Delta S = SW + LW + LE + H + G \qquad \text{Eq. 2.2,}$$

where *SW* and *LW* are the net shortwave and longwave radiation fluxes, *H* and *LE* are the sensible and latent heat fluxes, and *G* is the conductive heat flux from the debris into the underlying ice. The parameters used in the surface energy balance are listed in Table 2.1.

Table 2.1 Parameters used in the surface energy balance model

Model parameter	Symbol	Unit	Value
Debris albedo	α_d	-	0.30
Ice albedo	α_i	-	0.64
Debris emissivity	ε_d	-	0.94
Ice emissivity	ε_i	-	0.97
Effective thermal conductivity	k	W m^{-1} K^{-1}	0.96
Surface roughness length	z_0	m	0.016
Measurement height air temperature	z_t	m	2
Measurement height wind speed	z_u	m	10
Debris density	ρ_d	kg m^{-3}	1496
Debris specific heat capacity	c_d	J kg^{-1} K^{-1}	948
Specific heat capacity of dry air	c_a	J kg^{-1} K^{-1}	1010
Standard sea-level pressure	P_0	Pa	101325
Air density at sea-level elevation	ρ_{air}	kg m^{-3}	1.29

The net shortwave radiation is a function of the albedo and the amount of incoming solar radiation. We assumed a constant debris surface albedo of 0.3 (Rounce and McKinney, 2014; Schauwecker et al., 2015). Computation of the insolation at the time of the UAV flights was done

using a python implementation of the R package 'insol' (Corripio, 2003). The model determines the solar geometry (Iqbal, 1983) and estimates the atmospheric transmissivities (Bird and Hulstrom, 1981) based on a digital elevation model, which in our case was generated from the optical UAV images. Atmospheric attenuation was calculated using the relative humidity and air temperature, from ERA5 Land hourly reanalysis data at each time of flight (Muñoz Sabater, 2019). We also accounted for cast shadows by the surrounding topography, based on a 0.5-m resolution digital elevation model with a larger footprint (Swisstopo, 2010).

Net longwave radiation results from the difference between incoming longwave radiation ($LW\downarrow$) and outgoing longwave radiation ($LW\uparrow$). $LW\downarrow$ is the same as in Eq. 2.1 and based on ERA5 Land data (see section 0). $LW\uparrow$ is a function of the LST and the surface emissivity (see section 0) and calculated following Stefan-Boltzmann's law $LW\uparrow = \varepsilon\sigma LST^4$. The latent heat flux (LE) is assumed to be 0, as the debris surfaces were dry during the UAV flights.

The sensible heat flux H was estimated using the bulk aerodynamic approach assuming a neutral atmosphere (Nicholson and Benn, 2006; Steiner et al., 2018; Nakawo and Young, 1982; Rounce and McKinney, 2014):

$$H = \rho_{air} \frac{P}{P_0} c_a C_{bt} u (T_{air} - LST) \qquad \text{Eq. 2.3,}$$

where ρ_{air} is the air density at sea level pressure (kg m^{-3}), P_0 is atmospheric pressure at sea level (Pa) and P atmospheric pressure at site elevation (Pa), calculated following Iqbal (1983), c_a is the specific heat capacity of air ($J^{-1}kg^{-1}K^{-1}$) (Brock et al., 2010; Barry et al., 2021), u the wind speed (ms^{-1}), T_{air} the air temperature and C_{bt} the bulk transfer coefficient given as:

$$C_{bt} = \frac{k_*^2}{\ln(\frac{z_u}{z_0}) \ln(\frac{z_t}{z_0})} \qquad \text{Eq. 2.4,}$$

where k_* is the Kármán constant (0.41), z_0 is the surface roughness length (Rounce and McKinney, 2014; Stewart et al., 2021) and z_u and z_t are the measuring height (m) for wind speed and air temperature. The meteorological input data u and T_{air} were taken from ERA5 Land hourly reanalysis data (Muñoz Sabater, 2019).

The conductive heat transfer through the layer of debris and into the ice can be described by Fourier's law assuming a homogeneous layer of debris:

$$G = -k \frac{\partial T}{\partial z} \approx -k \frac{LST - T_{di}}{d} \qquad \text{Eq. 2.5,}$$

where $\frac{\partial T}{\partial z}$ is the temperature gradient in the debris layer and k the effective thermal conductivity ($\mathrm{W\ m^{-1}K^{-1}}$). We assume a linear temperature gradient in the debris layer and thus $\frac{\partial T}{\partial z}$ to be equal to the difference between the LST and the temperature of the debris-ice interface (T_{di}), which we assume to be at the melting point 0 °C. The assumption of a linear temperature gradient applies only approximately and for thin debris thicknesses (<10 cm) (Conway and Rasmussen, 2000; Nicholson and Benn, 2006; Rounce and McKinney, 2014). The average diurnal temperature profile through a layer of debris can be considered linear but at sub-daily time intervals, the profile varies in its degree of linearity (Reid and Brock, 2010). We will come back to this point in the discussion.

Solving the surface energy balance at sub-daily time intervals requires knowledge of the energy flux due to the change of heat stored in the layer of debris (ΔS) (Brock et al., 2010).

$$\Delta S = \rho_d c_d \frac{\partial \overline{T}_d}{\partial t} d \qquad \text{Eq. 2.6,}$$

where ρ_d is the debris density ($\mathrm{kg\ m^{-3}}$), c_d is the specific heat capacity of debris ($\mathrm{J\ kg^{-1}K^{-1}}$), d the debris thickness (m) and $\frac{\partial \overline{T}_d}{\partial t}$ the average rate of mean debris temperature change ($\mathrm{K\ s^{-1}}$) with $\overline{T_d}$ as the mean debris temperature, $(LST + T_{di})/2$, and t the time. Our sub-daily multitemporal LST measurements allow us to estimate temporal changes in LST, but these are very sensitive to uncertainties in the LST measurements (see section 2.3.2). To avoid such issues, we rely on the diurnal temperature cycle and fitted a linearized harmonic sine function (Shumway and Stoffer, 2016) to the temperature data of each pixel. The first derivative with respect to time of this function is the warming/cooling rate and can be used to calculate the change in the heat storage term.

2.3.6 Debris thickness estimation

As both the stored heat flux (ΔS) and the conductive heat flux (G) in the surface energy balance model (SEBM) are a function of the debris thickness, the surface energy balance model (section 2.3.5) can be described by a quadratic equation in form of:

$$d^2 \left(-p_d\, c_d \frac{\partial \overline{T}_d}{\partial t} \right) + d(SW + LW + H) - k(LST - T_{di}) = 0 \qquad \text{Eq. 2.7,}$$

Solving for debris thickness was done using the quadratic formula:

$$d = \frac{-b + \sqrt{b^2 - 4ac}}{2a} \qquad \text{Eq. 2.8,}$$

with $a = -\rho_d c_d \frac{\partial \overline{T}_d}{\partial t}$, $b = S + L + H$ and $c = -k(LST - T_{di})$. Note that the quadratic equation has mathematically two solutions whereas only one is physically plausible.

In addition to the SEBM approach, we also estimated debris thickness for each LST map using a rational curve (McCarthy, 2019; Boxall et al., 2021) of the form

$$d = \frac{LST}{c_1 + c_2 LST} \quad \text{Eq. 2.9,}$$

where c_1 and c_2 are empirically derived coefficients by a least squares regression.

To evaluate the performance of the two approaches for predicting debris thickness, we used the RMSE between the predicted and the observed debris thickness at the sites surveyed in the field (section 2.3.1). To account for the accuracy of the handheld GPS device, we used the mean variable values within a 2-m-radius buffered region around the GPS coordinate. Sites for which the SEBM approach did not yield a real and positive number were excluded from the comparison. We discuss the causes for these unphysical solutions in detail in section 2.5.1. To evaluate the least squares regression of the rational curve we divided the observed debris thickness data into a testing (n=45) and training (n=45) dataset. The training dataset has been used to derive the model coefficients c_1 and c_2 while the testing dataset was used to compare the modelled debris thickness estimates with the field observations.

2.4 Results

2.4.1 Land surface temperature and its diurnal variation

The LST changes over the day in a cyclic manner (early morning cool – afternoon hot – evening cool) and consequently the ability to estimate debris thickness using LST changes accordingly (Figure 2.3). Unlike satellite-derived LST observations, our diurnal LST measurements allow us to show how this relationship changes throughout the day.

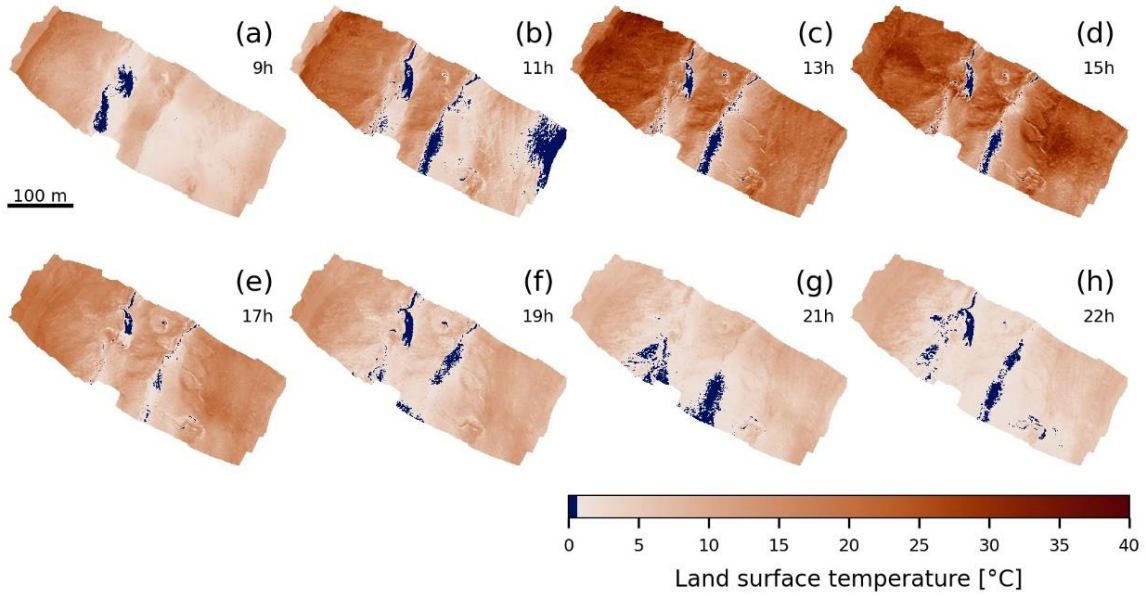

Figure 2.3. Spatiotemporal distribution of the land surface temperature (LST). The panels (a-h) show the 8 individual flights describing a large fraction of the diurnal land surface temperature variation. The maps have a spatial resolution of 15 cm and are colorized in dark blue for LST < 0.5 °C. Due to the residual uncertainties of the LST, ice surface geometries appear inconsistent with time. The southeast region of the panel (b) (11 h) shows an unreasonable cold temperature due to a failed calibration.

LST and debris thickness are generally positively correlated, but the suitability of a linear model to describe the relationship varies throughout the day with better correlation for cooler temperatures in the evening hours (Figure 2.4f-h). In the afternoon hours when the debris surface reaches its maximum diurnal temperature, the relationship between debris thickness and LST shows its non-linear nature (Figure 2.4c-e). Additionally, we observe the influence of the terrain aspect: east and south-facing slopes heat up earlier compared to west and north-facing slopes Figure 2.4a, b) (Crameri et al., 2020).

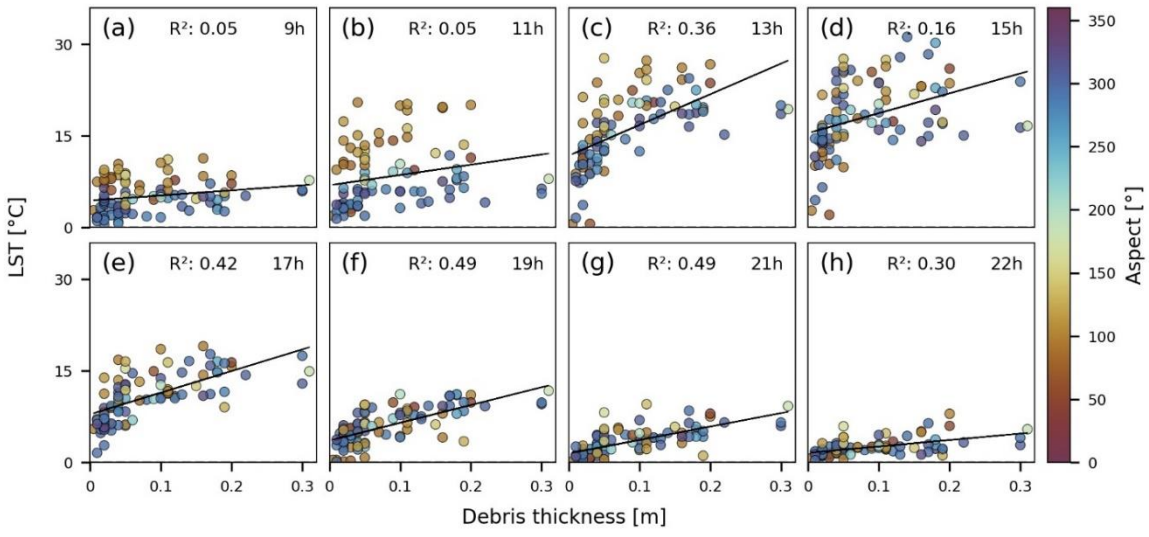

Figure 2.4. The temporal variation of the land surface temperature (LST) against in-situ measured debris thickness. Panels (a-h) show the arithmetic mean land surface temperature of a 2 m buffered region around the GPS coordinates of debris thickness measurements colorized for terrain aspect with 0/360 ° facing north. The LST of the warming phases (a-d) is stronger influenced by the aspect than the cooling phases (e-h). The non-linear nature of the relationship between the LST and debris thickness is noticeably pronounced for higher LST (c-e) while the correlation for low LST appears more linear (f-h).

The effect of the terrain aspect is not evident during the cooling phase in the afternoon and evening. The spatial and temporal variability of the LST (Figure 2.3) shows that at all flight times, surface temperatures are higher at the edges of the glacier (NW and SE) and lower in the central part of the test area. This pattern corresponds to high debris thicknesses at the glacier margins and thin debris thicknesses or no debris occurrence in the middle part. The mean LST of the debris cover follows the expected pathway of a diurnal temperature cycle (Table 2.2).

Table 2.2. Mean LST and standard deviation (1σ) of the debris and ice surface type.

Local flight time (h)	Mean ± 1σ (debris) °C	Mean ± 1σ (ice) °C
09 h	7.28 ± 4.60	1.71 ± 1.43
11 h	10.68 ± 7.69	0.87 ± 1.87
13 h	19.52 ± 7.13	1.43 ± 2.87
15 h	21.44 ± 6.16	1.51 ± 2.32
17 h	13.31 ± 4.46	2.26 ± 2.84
19 h	8.10 ± 3.76	1.16 ± 1.56
21 h	5.31 ± 2.80	1.31 ± 1.56
22 h	4.59 ± 2.99	0.72 ± 0.77

While the general spatial and temporal pattern of LST seems to be reasonable, some areas of concern exist locally. First, the southeastern region of the 11 h flight shows an unreasonable cold temperature patch, which most likely does not represent the actual LST at that time. Instead, we suspect that this artefact corresponds to an uncorrected bias of the thermal correction and calibration process. We will come back to this point in the discussion. Second, the 15 h flight shows a centrally located, transverse-oriented strip of higher LST, which seems to follow the flight path of the UAV. The directional temperature mismatch could be related to an oblique viewing angle of the sensor as the nadir alignment was set up manually and the angle of observation might partly control the amount of radiation received by the sensor and thus the temperature measurement (Norman and Becker, 1995).

In the absence of any other means to assess the precision of the LST values, we suggest that the variability of the bare ice surface temperatures, which ought to be at 0°C, might indicate the bias and precision of the LST. The LST values of ice surface temperatures vary by several degrees with a standard deviation of up to 2.87 °C (Table 2.2). Mean ice LST range between 0.72 and 2.26 °C throughout the day (Table 2.2). Field observations show that ice cliffs on TNG are often sprinkled

with small rocks and/or a thin layer of dust, which might influence the ice LST towards warmer temperatures.

Based on the LST measurements, we estimated the diurnal variation of the depth-integrated mean debris temperature. The pixel-wise fitted harmonic sine functions allow us to estimate the spatially distributed warming and cooling rates, as the first derivative with respect to time. The RMSE of the fit (*mean* ± *1σ*) is 1.51 ± 0.54 °C. The spatial distribution of the RMSE (Figure 2.5b) is relatively continuous but shows variability where the before mentioned local LST discrepancies occur. Figure 2.5a shows that, depending on the aspect, at 13 h and 15 h the debris surface reaches its maximum LST and consequently the temperature change rate converges to zero.

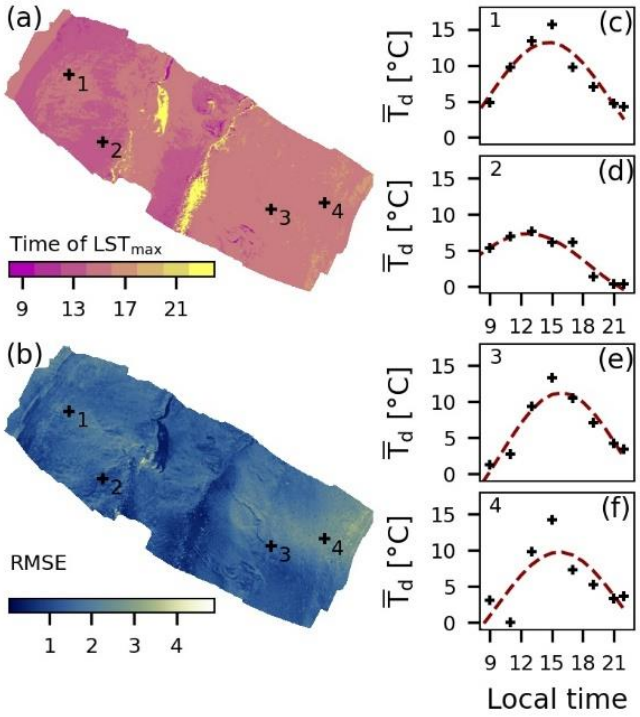

Figure 2.5. Sinusoidal regression of mean debris temperature ($\overline{T}_d$), estimated from LST (Eq. 2.6) for each pixel. (a) The panel shows the time at which $\overline{T}_d$ reaches its maximum diurnal temperature and thereby emphasizes the effect of the terrain aspect. (b) The RMSE of the regression for each pixel. The south-eastern region with larger errors is due to the anomalies in the LST at 11 h, see text for details. The spatial mean of the RMSE is 1.51 °C and the standard deviation is 0.54 °C. The panels (c-f) are example points of the sine function used to derive the warming/ cooling rate in each pixel. Locations of the examples are indicated in panels (a) and (b).

2.4.2 Surface energy balance modelling

To solve the surface energy balance (Eq. 2.2) we determined the LST-independent energy flux component *SW* and the LST-dependent components *LW*, *H*, ΔS and *G* based on the UAV-derived LST maps shown in Figure 2.3. In Figure 2.6, we show the diurnal variation of each component, evaluated at all locations where we obtained debris thickness measurements.

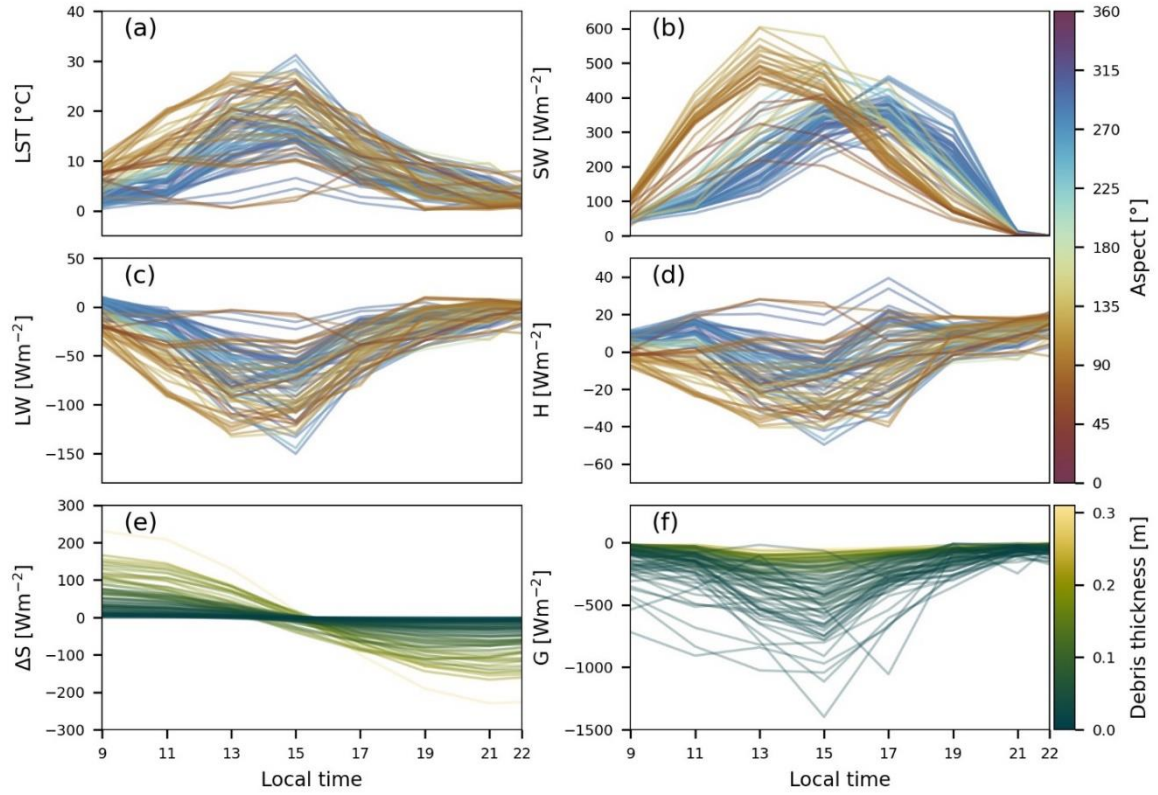

Figure 2.6. Energy fluxes at debris thickness measurement locations. Diurnal variations of (a) land surface temperature, LST, (b) net shortwave radiation, *SW*, (c) net longwave radiation, *LW*, and (d) sensible heat flux, *H*, with lines colorized by terrain aspect with 0/360 ° facing north. Diurnal variations of (e) the change in heat storage, Δ*S*, and (f) the conductive heat flux, *G*, with lines colorized by debris thickness measured in the field. Note that only *SW* (b) is independent of LST, whereas data in panels (c-f) are a function of LST.

East and south-facing slopes receive their maximum net shortwave radiation (*SW*) prior to the west and north-facing slopes (Figure 2.6b), which explains their earlier increase in LST (Figure 2.6a). By 15 h, all sites attained the daily maximum LST and cool down from then on. Despite the remaining differences in *SW*, no more aspect-related differences in LST can be observed. All the remaining SEBM components are a function of the LST and thus also show an aspect dependency before 15 h. The net longwave component (*LW*) expectedly mirrors the LST (Figure 2.6c). The sensible heat flux (*H*), calculated using the bulk approach (Eq. 2.3), attains only low flux values close to 0, which is likely related to the low wind velocities (<1 ms^{-1}) obtained from reanalysis data (Table 2.3). The rate of change in heat storage within the debris (Δ*S*) and the conductive heat flux (*G*) are, besides the LST, a function of the debris thickness (Eq. 2.6, Figure 2.6e, f). Whereas Δ*S* attains the largest magnitudes in the morning and evening hours and where the debris is thick, the opposite is true for *G*, which is largest at 15h and where the debris is thin.

Table 2.3. ERA5 Land hourly reanalysis data on 30.08.2019 interpolated at Tsijiore-Nouve Glacier, Switzerland (46.01° N, 7.46° E)

Local flight time (h)	Incoming longwave radiation, $LW\downarrow$ (W m^{-2})	Wind speed, u (m s^{-1})	Air temperature, T_a (°C)
09 h	311.03	0.35	6.64
11 h	304.38	0.45	10.29
13 h	304.05	0.48	11.69
15 h	307.31	0.85	12.09
17 h	308.26	0.87	10.24
19 h	307.46	0.41	8.98
21 h	306.71	0.46	7.74
22 h	306.19	0.60	7.20

2.4.3 Debris thickness estimates from SEBM

The SEBM-derived predictions of debris thickness (Figure 2.7) show a general pattern that matches observations in the field and the pattern of measured LST. Predicted debris thicknesses generally range between 0 and 30 cm. Given the chosen input parameters, Eq. 2.8 cannot be solved for all pixels in the first half of the day (9 h to 15 h) (Figure 2.7a-d).

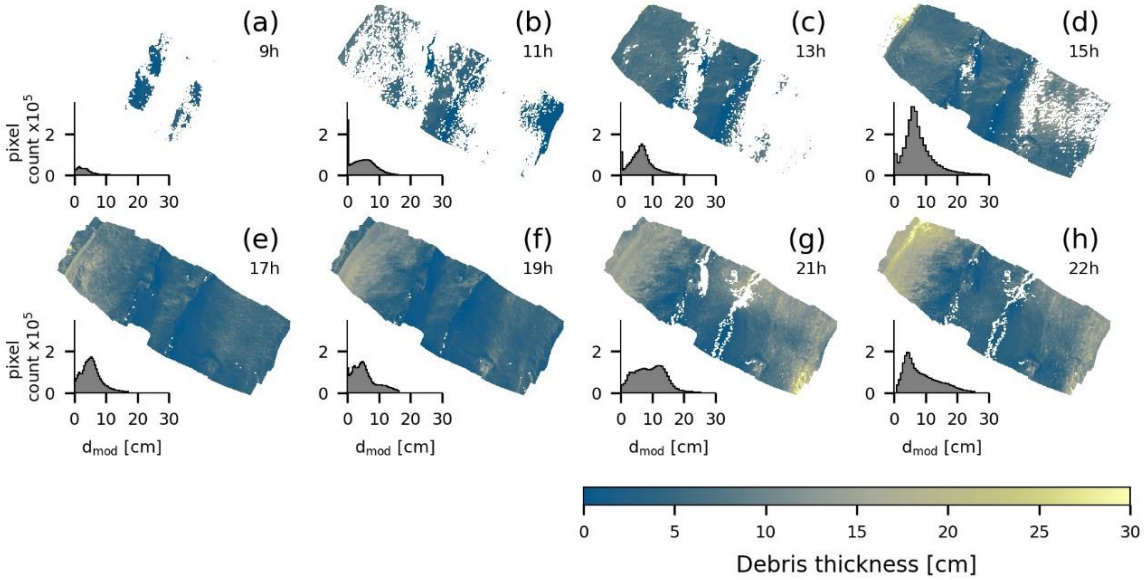

Figure 2.7. Estimated debris thicknesses for each flight time. White regions show regions where the surface energy balance model has no valid solution for debris thickness due to high uncertainties in the land surface temperature and reanalysis data. The histograms show the distribution of the predicted debris thicknesses displayed in the maps.

At these times the quantities of the surface energy balance components and the relatively low LST, lead to a negative term under the root in Eq. 2.8, and thus to no valid solution. Predictions of thicker (>10 cm) debris are primarily found in the afternoon and evening hours (17 h to 22 h) and the pattern of thin debris (<10 cm) predictions, primarily in the central part of the glacier, is relatively consistent in time.

Comparing the predictions to field observations (Figure 2.8) shows that the accuracy of the prediction remains comparable throughout the day with an RMSE of 6 to 8 cm. For most of the flights, we find a positive correlation between the predictions and observations, even if they do not follow the 1:1 line. During the warming phase of the day, when the aspect has a strong influence on LST (Figure 2.4a-c), the associated debris predictions do not show an aspect-related pattern. In contrast, debris thickness predictions based on the afternoon flights at 17 h and 19 h, seem to correlate with aspect whereas the LST data does not.

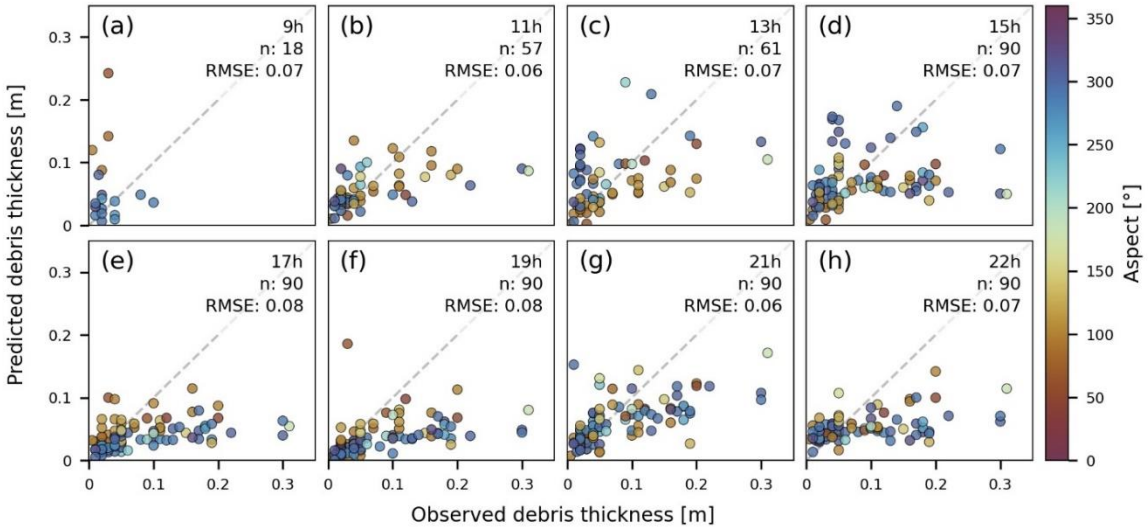

Figure 2.8. Comparison of modelled and observed debris thickness for each flight time (a-h) with RMSE values (m) for model evaluation. Sample points are colorized by terrain aspect and the grey dashed line shows the 1:1 line. RMSE for flights (a, b and c) is based on a reduced sample number.

Absolute values of predicted thin debris cover are less sensitive to the time of the day, compared to thick debris. Figure 9a shows the variation of the predicted thicknesses with time along the profile introduced in Figure 2.1b as the mean value $\pm 1\sigma$. The spatial variability of the standard deviation is shown in Figure 2.9d. As the SEBM does not yield a valid solution for all times of the day, Figure 2.9e additionally shows the number of valid predictions in time. Towards the glacier edges where the debris is greater than 10 cm, the spread in the standard deviation increases, compared to the central part, showing that the prediction of thick debris cover varies stronger in time than for thin debris cover.

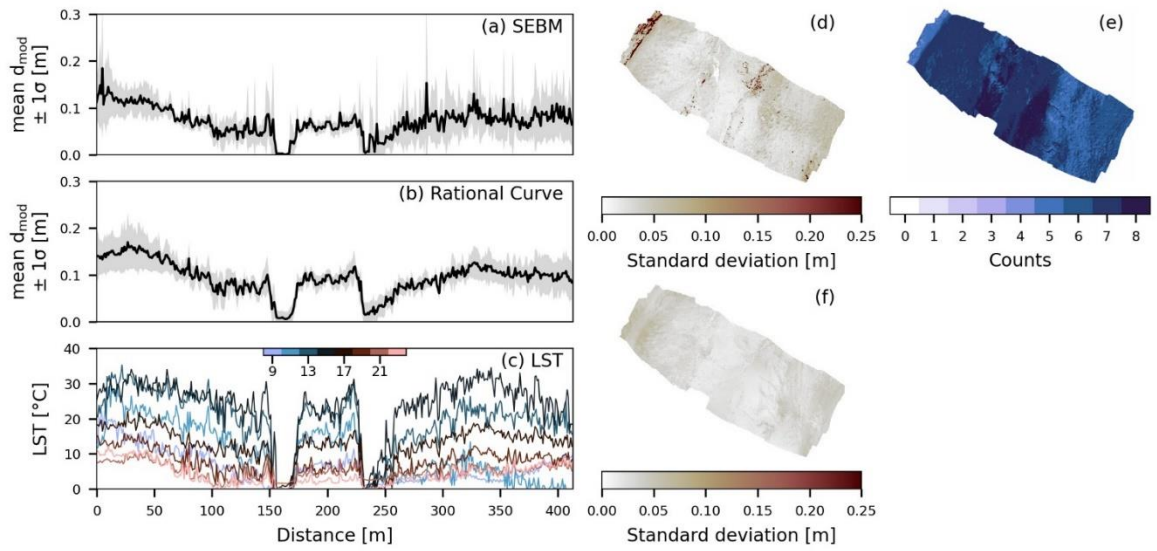

Figure 2.9. Diurnal mean ± 1σ debris thickness predictions along the profile line shown in Figure 1. (a) The predictions using the surface energy balance model (SEBM) show a larger spread of the standard deviation (grey) towards the edges and smaller towards the central part corresponding to regions of ticker and thinner debris cover. Panel (b) shows the results of the rational curve extrapolation approach. A smaller spread indicates greater consistency in the prediction over the day. (c) The diurnal variability of the land surface temperature along the profile line. Panel (d, f) shows the spatial variation of the standard deviation and (e) the number of valid solutions in the SEBM approach.

2.4.4 Debris thickness estimates by extrapolating a rational curve

The debris thickness maps created by the extrapolation approach using a rational curve result in slightly thicker predictions than following the SEBM approach (Figure 2.10). The general pattern of the spatial debris thickness distribution follows the field observations and the pattern of measured LST, similar to the results of the SEBM approach. The modelled debris thicknesses vary between 0 cm and 30 cm, but with early flights at 9 h and 11 h lacking predictions greater than 10 cm (Figure 2.10a, b).

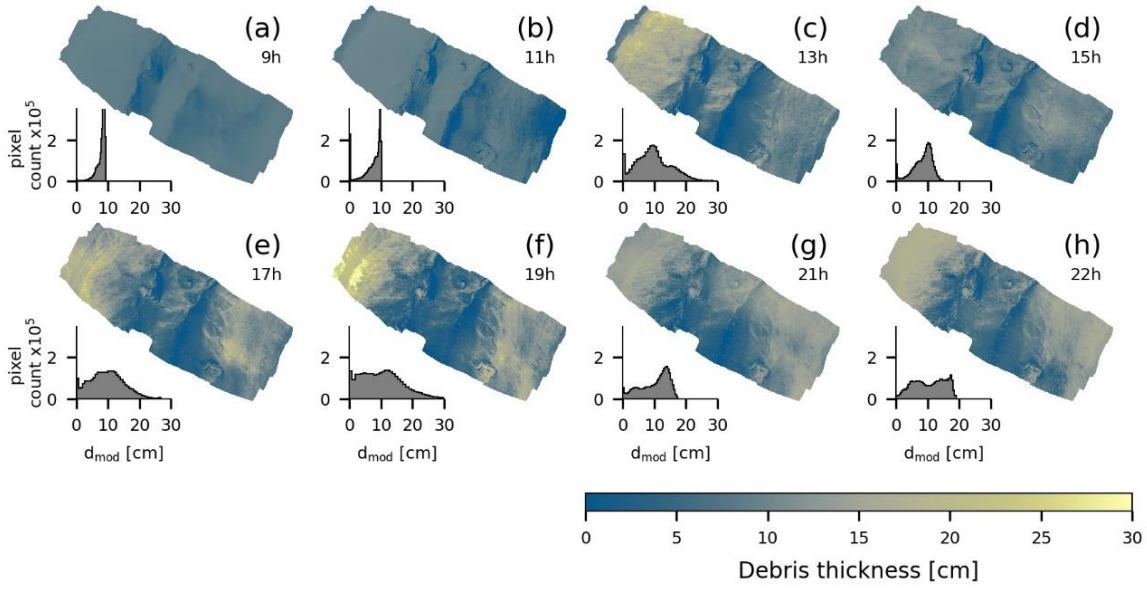

Figure 2.10. Estimated debris thickness using a rational function for each flight time. The histograms show the distribution of the predicted debris thicknesses displayed in the maps.

We divided (Pedregosa et al., 2011) the dataset of n = 90 samples into a training (n = 45) and testing (n = 45) dataset. Figure 2.11 shows training and testing data for each flight time including the coefficients c_1 and c_2, derived by least squares regression of Eq. 2.9 and the RMSE between the predictions and the observations of the testing data (Figure 2.11). Similar to the SEBM, the RMSE ranges between 6 cm and 8 cm, but debris thicknesses > 10 cm are better represented in the extrapolation approach and thus follow more closely the 1:1 line. At 9 h, 11 h and 15 h the RMSE is highest at 8 cm and the shape of the curve already shows that the model does not represent the data well. The aspect dependency of the LST at these times (Figure 2.4, a,b) was not considered as an additional parameter for the regression and thus, results in a curve that does not represent the shape of the data well (Figure 2.11a,b). The afternoon flights between 17 h and 22 h have the lowest RMSE with 6-7 cm.

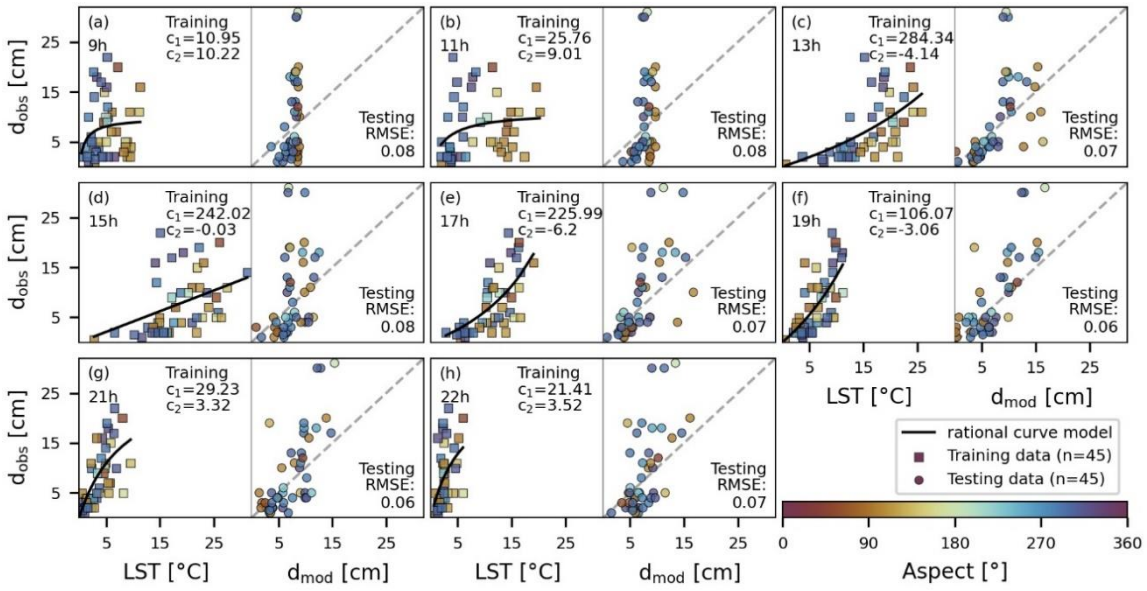

Figure 2.11. Least squares regression of a rational function of 50 % of the debris thickness measurements (n=45) with the arithmetic mean land surface temperature of a 2 m buffered region around the GPS coordinates of debris thickness measurement locations (training data) (a-h). The adjacent panels show the comparison of modelled and observed debris thickness of the other 50 % (n=45) with RMSE values to evaluate the prediction (testing data). Sample points are colorized by terrain aspect.

The diurnal stability in predicting debris thickness (Figure 2.9) shows that thin debris cover, as found in the central part of the profile line, remains stable throughout the day and is thus comparable to the results of the SEBM approach. For thicker debris the spread of the standard deviation is higher, showing that predicting thick debris cover depends more on the time of the day than thin debris. Even though the range of the RMSE throughout the day remains comparable to the SEBM results, for some flights (e.g., 19 h) the average prediction accuracy improves by about 2 cm.

2.5 Discussion

2.5.1 Predicted versus observed debris thickness

Debris thickness predictions with the SEBM approach yielded mixed results. The fact that the modelled debris thickness does not vary in unreasonable ways across the glacier surface, but in a systematic pattern, shows that mapping high-resolution debris thickness with UAVs has some potential. During most of the flights, we observe a general positive correlation between the modelled and observed debris thickness (Figure 2.8b-h). The overall relationship between higher surface temperature and thicker debris that is evident in the input data (Figure 2.4) can be reproduced. However, given the chosen parameters, we are unable to obtain a non-biased match between the observed and modelled debris thickness. The SEBM approach mostly underestimates debris

thickness at all flight times compared to field measurements. For thick debris cover, this underestimation is more pronounced than for thin debris (<10 cm).

Over the course of the day, the RMSEs between observed and predicted debris thicknesses range from 6 to 8 cm. For many pixels in the flights at 9 h, 11 h, and 13 h and some pixels at 15 h (Figure 2.7 a-d) the quadratic equation (Eq. 2.7) has no real solution, and the SEB cannot be solved for debris thickness. The reason for this is a negative term in the square root of Eq. 2.8, which occurs if $b^2 < 4ac$. Recall that b accounts for the radiative and sensible heat fluxes (SW+LW+H), whereas a and c are the conductive heat flux and the storage term, respectively. As long as LST > 0 °C, c is always negative. The inequality condition above can thus only occur if also a is negative, which is only possible when the debris is heating up, in our case until about 15 h (Figure 2.5a, Figure 2.6e). That explains, why many pixels in the morning flights have no debris thickness solution. Furthermore, at 9 h, the term b^2 is rather small, mostly because of low SW values. However, at 11 h and,13 h southeast-exposed pixels receive higher SW (Figure 2.6b), which causes b to increase, making the inequality condition less likely. The most likely reason for no physical solution to Eq. 2.7 is inaccurate values of LST and reanalysis-derived variables. Mostly during the morning, even small deviations from true values are sufficient to find no physically meaningful debris thickness solution. For thin debris (< 2cm), G is very sensitive to uncertainties in LST and leads to large negative numbers. This is a major drawback of the SEB approach, and it highlights the sensitivity of the approach to uncertainties in the input data. We note that these uncertainties prevail, even if a solution is found. However, compared to the ground observations of debris thickness the model predictions show a positive correlation.

As a result of spatially incomplete debris thickness maps, the number of sample points to evaluate the quality of the prediction is reduced (see low 'n' in Figure 2.8a-c) and should be kept in mind when comparing the RMSE with respect to the time of the day. Previous studies did not face this issue, in part because ΔS was incorporated as a fraction of the conductive heat flux G, which is always negative (Foster et al., 2012; Schauwecker et al., 2015). Comparison of ΔS and G for the sites where we measured debris thickness shows that such an assumption appears to be invalid for most times of the day (Figure 2.5). By estimating ΔS using the warming/cooling rate from multitemporal LST measurements, we can better account for this energy balance component, but these estimates are also prone to uncertainties in LST. In general, however, the magnitude and distribution of SW, LW and ΔS for most of the sample locations compare well to values determined by Brock et al. (2010) with an automatic weather station (AWS) at the Miage Glacier at comparable latitude, time of the year, and elevation (500 m difference).

Debris thickness predictions below ~10 cm seem to correlate reasonably well with field observations, whereas predictions of thicker debris cover are generally too low (Figure 2.8). This

may indicate that uncertainties in parameters that are unlikely to vary spatially or as a function of debris thickness are not particularly relevant. To further test this hypothesis, we performed sensitivity tests of SEBM-derived debris thickness estimates to variations in the input parameters air temperature, wind speed, thermal conductivity, albedo, and surface roughness length (Figure 2.12). Variations of the parameters air temperature, albedo, and surface roughness length across value ranges commonly found in the literature (Brock et al., 2000; Foster et al., 2012; Schauwecker et al., 2015; Shaw et al., 2016; Miles et al., 2017) result in generally small variations of the mean debris thickness (averaged across the entire studied surface). In consequence, the impact on the RMSE when evaluated against our field observations of debris thickness is also small. Only the flights at 9 h, 11 h, and 13 h show more significant variations in the RMSE, but these correspond to simultaneously low coverage of valid predictions and thus only small numbers of sample points to estimate the RMSE (Figure 2.9).

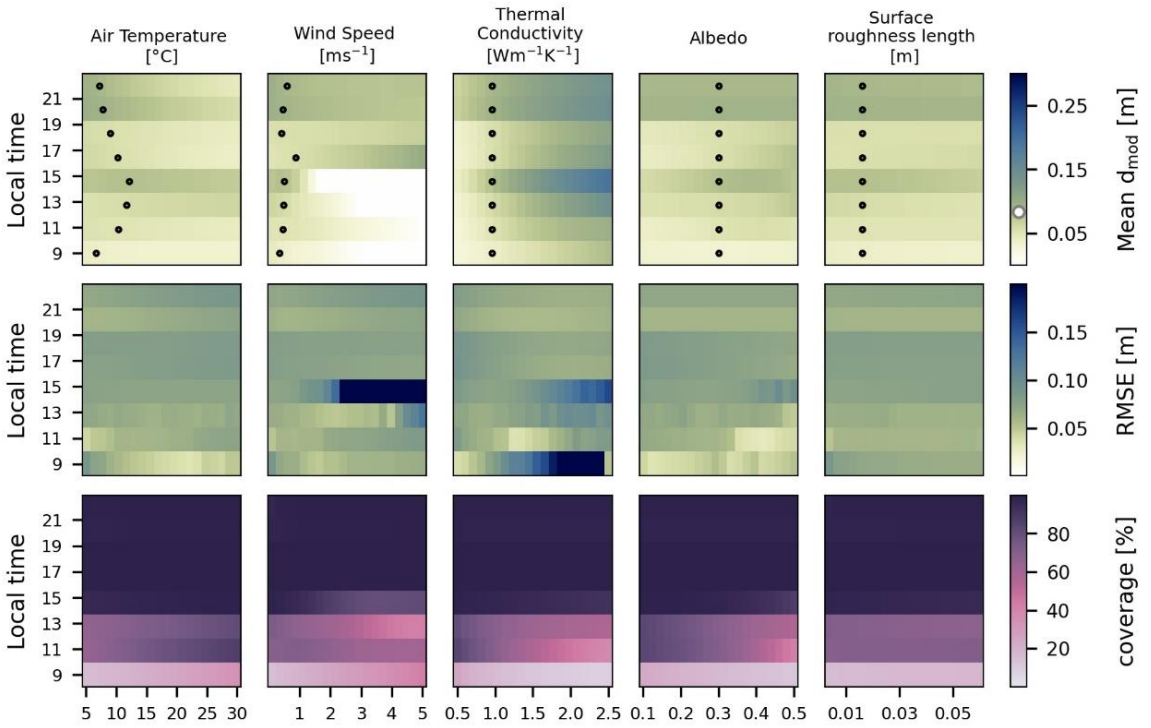

Figure 2.12. Sensitivity of debris thickness prediction using a surface energy balance model (SEBM) to the parameters air temperature, wind speed, effective thermal conductivity, albedo and surface roughness length. For each flight time, each parameter was varied across a range of values and debris thickness maps were created. Each column shows colorized (1) the modelled mean debris thickness averaged over all pixels in the test area, (2) the RMSE between the observed and predicted debris thicknesses and (3) the coverage of valid predictions as the surface energy balance model cannot always be solved. The white dot in modelled mean debris thickness shows the mean debris thickness observed in the field.

The same is essentially true for wind speed, which is a notoriously difficult parameter to constrain in any surface energy balance model (Schauwecker et al., 2015; Stewart et al., 2021) and

is a strong control of the sensible heat flux (Eq. 2.3). ERA5-derived wind speed during the time of our experiment is relatively low at <1 m s^{-1}, whereas wind speeds of ~2-4 m s^{-1} are not uncommon in the vicinity of glaciers (e.g., Oerlemans and Greuell, 1986; Brock et al., 2010; Steiner et al., 2018). During a different visit to the TNG in 2021, we operated a small AWS for a full day and obtained wind speeds of 2.5-4 m s^{-1}, which were higher than ERA5-derived wind speeds of 0.5-2 m s^{-1} for the same day. Although we don't know what the actual wind speed was during our experiment in 2019, increasing the wind speed and solving for debris thickness has a minor effect on flights from 17 h onwards, whereas for earlier flights, the coverage quickly drops to low values. This is related to the fact that larger negative H values reduce b (i.e., the sum of the radiative and sensible heat fluxes, $SW+LW+H$), thereby increasing the likelihood to obtain a negative term in the square root of Eq. 2.8. Similar effects also account for changes in coverage for the other parameters. We thus emphasize that changes in RMSE during flights until about 15 h that are associated with changes in coverage do not necessarily indicate better model performance. The high sensitivity of the SEBM approach to uncertainties in LST and the reanalysis data reduces the suitability to reliably estimate debris thickness.

The only tested parameter that has a more pronounced effect on the mean debris thickness and RMSE without changing the coverage is the thermal conductivity (k) through its influence on the conductive heat flux, G. Higher k values result in greater energy losses to the ice and a higher debris thickness for the same LST. A similar effect has been achieved by Rounce and McKinney (2014) by introducing a factor to account for the non-linearity of the temperature profile in the debris cover. (Bird and Hulstrom, 1981)

It should also be noted that the effective thermal conductivity k is likely to vary spatially, as thick debris cover can hold more moisture, which thus leads to higher values of k (Steiner, 2021). Additionally, a thin debris cover composed of smaller grain sizes may have different pore space than a layer of thick debris cover consisting of larger grain sizes. The bulk debris-void space and thus the effective conductivity could vary with debris thickness, too. Because the effective thermal conductivity of a debris layer and its spatial variability is a rather complex quantity that is not easily measured, this parameter could be used as a free parameter to tune the debris thickness map against field observations.

Debris thickness predictions using least squares regression of a rational curve yield RMSE values between 6 and 8 cm, similar to the results of the SEBM approach. The pattern of spatially distributed debris thickness estimates (Figure 2.10) follows the expected spatial pattern of the LST for each time of the day. The range of predicted debris thicknesses corresponds to the field observations with values similar to the SEBM approach, between 0 cm and 30 cm. As the LST varies throughout the day, the suitability of the rational curve regression to estimate debris thickness varies

too. For instance, at 9 h and 11 h, LST depends strongly on the terrain aspect and thus the results are biased towards the aspect (Figure 2.11a,b). Nevertheless, at 13 h the RMSE between observations and predictions (Figure 2.11c, testing data) is still 7 cm. This suggests that during the times when the debris is heating up, the regression of a rational curve would benefit from taking the terrain aspect into account, i.e., by fitting a parametric surface to the data. In addition, the strongly non-linear relationship between LST and debris thickness at 9 h and 11 h limits predicted debris thicknesses to <10 cm. The predictions at these flight times show unrealistic uniform values in the same regions at which the SEBM approach cannot be solved. This supports the SEBM approach and indicates that the LST at this time is too low to relate it to debris thickness. When the debris is cooling down in the evening (Figure 2.11e-h), the aspect has a minor effect, and the curve appears to satisfy the available data. When LST is low (morning and evening), the relationship between LST and debris thickness seems to be almost linear, and a simple linear regression is expected to result in comparable accuracy. This agrees with the findings of Boxall et al. (2021), based on satellite-derived LST.

2.5.2 Opportunities and limits of UAV-derived LST for debris thickness mapping

High-resolution studies can improve our understanding of processes that move and distribute debris on glacier surfaces (Westoby et al., 2020). Spatiotemporal debris thickness estimates using UAV-derived thermal images have the potential to serve as a new approach to quantify how debris is mobilised across the surface of the glacier over short times scales. The detailed representation of surface features, such as ice cliffs, large boulders (Figure 2.13), or surface ponds makes UAV-derived LST measurements a valuable tool for debris cover research.

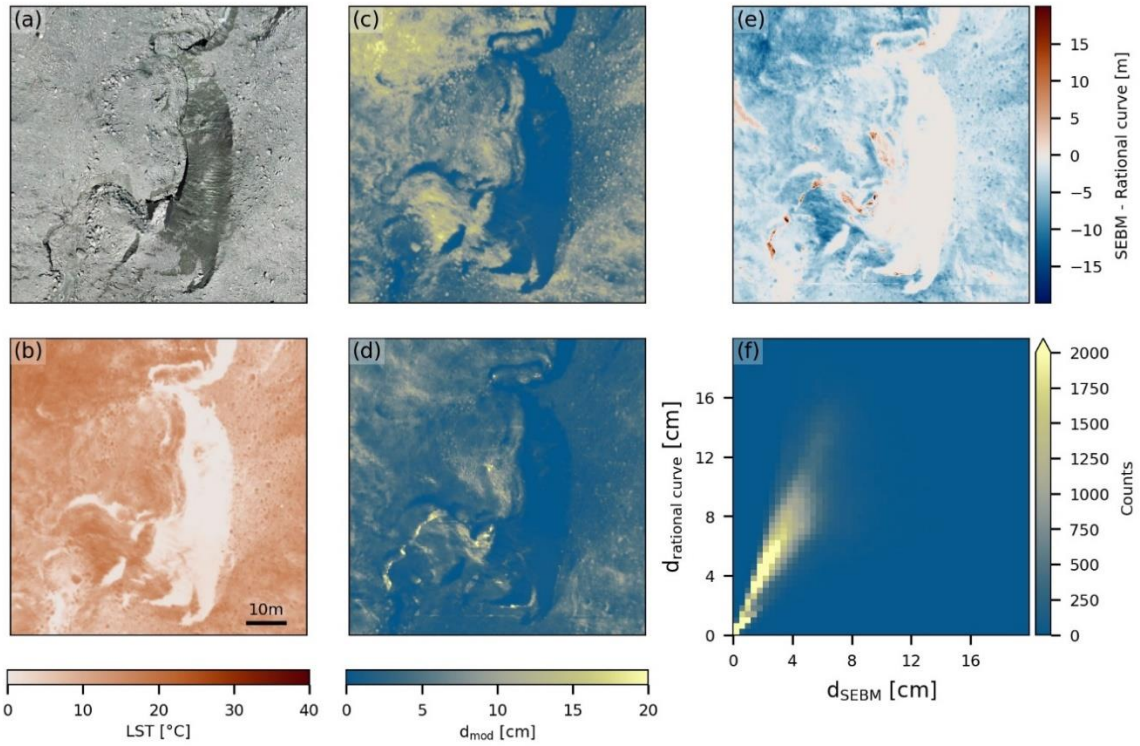

Figure 2.13. High-resolution subsection of the unpiloted aerial vehicle imagery (UAV) with debris cover, large boulders and ice cliff. The panels show (a) the RGB image, (b) the land surface temperature at 15 h, (c) debris thickness prediction using the rational curve approach and (d) debris thickness prediction by solving the surface energy balance model. The difference map (e) and 2d histogram (f) show how the model predictions compare spatially.

So far, the conversion of LST to debris thickness in high resolution was only studied using ground-based oblique viewing angles (Herreid, 2021) using empirical equations. However, challenges in this approach include (1) the area covered by the field of view, (2) the variable path radiance and (3) the viewing angle that controls the amount of radiation received by the sensor. UAV offers opportunities to overcome these issues, but also face challenges that we discuss here. These challenges stem from the specifics of image acquisition, limited battery lifetime, post-processing requirements, and the conversion of the brightness temperature to LST.

All high-resolution studies, including ours, have so far used uncooled microbolometers, a sensor type that requires thermal equilibrium between the sensor device and the environment for accurate measurements (Budzier and Gerlach, 2015). As these conditions are difficult to achieve and maintain in high mountain settings, the obtained thermal infrared images require calibration and correction. The ambient temperature difference between the ground and the flight elevation requires the sensor device to thermally adjust after take-off, which thus introduces a measurement bias that varies with time (Figure 2.2a). While this effect is primarily relevant for UAV applications, the maintenance of stable environmental conditions (e.g., changing wind speeds) cannot be guaranteed even for ground-based measurements and temporal variance of the measurement bias should be

considered. While the sensor device cools down after take-off due to flight altitude, direct incident shortwave radiation may cause the device to heat up (Dugdale et al., 2019). The change in the measurement bias with time, the thermal drift, is partially balanced by the internal in-flight calibration of uncooled microbolometers (Mesas-Carrascosa et al., 2018), leading to recurring systematic jumps in the measured temperature (Figure 2.2) that can be compensated for in a postprocessing step (see section 2.3.2). Long flight times, slow flight speeds and no direct shortwave radiation would thus minimize the effect of thermal drift but would likely not substitute for additional calibration.

The thermal correction during post-processing in our case included (1) recovering the occurrence of flat field correction (FFC) events that were "lost" by the reduced sampling rate, (2) identifying and correcting the thermal drift, and (3) correcting the residual measurement bias using bare ice surfaces. During all flight times, thermal drift corrected for by FFC events was rather large and resulted in changes by up to ~8 K over 50 frames (Figure 2.2a). With a frame rate of 1/s, this means a thermal drift of up to 0.16 K s^{-1}. Assuming that the thermal drift is indeed linear with time, the in-flight FFC or, as in our case, post-processing identification of FFC is relatively straightforward, due to the step change in LST across an FFC event. Figure 2a also shows the internal housing temperature and the temperature of the focal plane array, as recorded by the thermal sensor. The rapid decline, in the beginning, shows the thermal adjustment due to the vertical temperature gradient between the ground and flight elevation. While UAVs with larger battery capacity might offset this effect to some extent, our setup was limited at that point.

To convert the brightness temperature to LST, we accounted for the reflected portion of the incoming longwave radiation and surface-type emissivity but neglected the path radiance between the sensor and the ground. As the elevation of the UAV above ground does not change significantly throughout the flight, the potential measurement bias of longwave radiation emitted by atmospheric water vapour content is minimized and assumed to be constant. Our 'bulk' calibration approach using spline interpolation of measured ice surface temperatures compensates for the systematic temporal variability of the measurement bias (Figure 2.2b) introduced by (1) thermal adjustment after take-off, (2) fluctuations of atmospheric conditions by wind or incident direct shortwave radiation or (3) longwave radiation emitted from atmospheric water vapour content or the surrounding terrain (Aubry-Wake et al., 2015; Aragon et al., 2020; Herreid, 2021).

Because of the need to calibrate all thermal images, the requirement of spatially well-distributed reference temperatures is the main drawback of the proposed method. In our case, bare ice surfaces were present in the central part but not at the glacier's sides. Two image regions are found to be severely erroneous, an anomalously low-temperature patch on the eastern edge at 11 h and a warm temperature stripe in the centre that seems to follow the flight path of the UAV at 15 h

(Figure 2.3b,d). We think the cold region at 11 h could be due to a failed drift compensation, as the spline interpolation assumes a constant correction value before the first and after the last occurrence of bare ice in the thermal images. The warm temperature strip could be related to an oblique viewing angle of the sensor during that flight, as the sensor alignment was done manually (Sobrino and Cuenca, 1999; Byerlay et al., 2020; FLIR, 2020).

So far, we discussed the challenges and needs to derive glacier surface LST. Provided the measurements obtained in our experiment, we also observed differences in the resulting debris thickness that we derived from the SEBM and the rational curve approaches. The SEBM approach requires meteorological input data, assumptions on debris properties (in space and time) and substantial simplifications of SEB components. Because the conservation of energy represents a balance among all energy fluxes, it follows that any simplification in one component will have a quantitative effect on the others (Price, 1985). However, when comparing the diurnal variation of the energy flux components with measured quantities in a comparable setting regarding location, time, and debris thickness (Brock et al., 2010), we find good agreement in magnitude and distribution for net shortwave, net longwave and change in heat storage and the conductive heat flux (Figure 2.6). The possibility to estimate sub-daily surface energy balance components improves our understanding of ΔS. Repeated LST measurements might additionally increase understanding of the spatial variability of debris properties (e.g., thermal conductivity, debris density or specific heat capacity) by quantifying the thermal inertia.

The accuracy of predicting debris thickness using a SEBM and empirically using a rational curve yielded comparable results with RMSEs of 6-8 cm depending on the time of the day. Both methods yield a terrain aspect bias. The SEBM approach compensates for the terrain effect to some degree as the amount of incident shortwave radiation is a function of aspect, too. The terrain bias in the early flights using the rational curve approach is more pronounced as it is only based on the LST. However, as this approach is less sensitive to uncertainties in LST, we recommend the rational curve approach to estimate debris thickness as long as enough debris thickness measurements are available. Steep moraines of debris or hummocky-shaped debris-covered surfaces are likely to introduce bias via mixed-pixel effects, when predicting debris thickness using coarse spatial resolution LST from remote sensing data, especially in the case of empirically derived debris thicknesses. For example, the time of overpass of the Landsat satellite is typically between 10 h to 11 h locally, a time when debris cover is still heating up. Therefore, the effect of aspect on satellite-derived LST debris thickness estimates should be studied in more detail.

2.6 Conclusions

In our experiment, we mapped supraglacial debris cover using high-resolution UAV-derived LST measurements at various times of the day and using two common approaches to create debris

thickness maps: a surface energy balance model approach and a simple extrapolation approach using a rational curve that relies on field measurements. We conclude that:

1. Measuring the LST from a UAV using an uncooled microbolometer requires temperature calibration that varies with time. Here we determine an offset correction value for each thermal infrared frame by interpolating splines of spatially well-distributed bare ice surfaces, assuming the ice to be at melting point of 0 °C. This bulk correction compensates for several sources of uncertainties but requires the presence of bare ice surfaces.
2. Quantifying the surface energy balance components based on the UAV-derived LST measurements led to debris thicknesses predictions with an RMSE of 6-8 cm, depending on the time of the day. Debris thicknesses were underestimated at all flight times. Measuring the diurnal variability of LST allowed us to extend the commonly used surface energy balance approach by quantifying the rate of change of heat storage.
3. The non-linearity of the relationship between LST and debris thickness increases with LST. Choosing the best empirical function for predicting debris thickness thus depends on the time of the day. Morning conditions yield a strong terrain aspect bias, which is better accounted for in the SEBM approach. When the LST reaches its diurnal maximum, here at 13 h or 15 h, the non-linearity is most evident. Towards the evening the relationship between debris thickness and LST appears almost linear and aspect plays a minor role.
4. Practical considerations for quantifying supraglacial debris cover using UAV-derived LST comprise LST calibration, choosing the model based on the time of the day and debris thickness measurements for evaluation. In our case, the ultra-lightweight UAV set-up was suitable for remote high mountain field work but had a significant drawback due to the limited battery capacity, resulting in short flight times of 10 to 15 minutes and small spatial coverage. Consequently, the thermal adjustment of the device led to strong thermal drift and thus to many in-flight calibration events that had to be considered. Maximizing the flight time by using a larger UAV could offset this effect to some degree. The measurement bias varies with time and spatially well-distributed reference temperatures should be used for calibration.

3 Land surface temperature trends derived from Landsat imagery in the Swiss Alps

Deniz Tobias Gök[1], Dirk Scherler[1,2], Hendrik Wulf[3]

[1] GFZ German Research Centre for Geosciences; D-14473 Potsdam, Germany.
[2] Institute of Geographical Sciences, Freie Universität Berlin; D-14195 Berlin, Germany.
[3] Remote Sensing Laboratories, University of Zurich; CH-8057 Zurich, Switzerland.

In Review: EGUsphere [preprint], https://doi.org/10.5194/egusphere-2024-1228, 2024

Abstract

The warming of high mountain regions caused by climate change is leading to glacier retreat, decreasing snow cover, and thawing permafrost, which has far-reaching effects on ecosystems and societies. Landsat Collection 2 provides multi-decadal land surface temperature (LST) data, principally suited for large-scale monitoring at high spatial resolution. In this study, we assess the potential to extract LST trends using Landsat 5, 7, and 8 time series. We conduct a comprehensive comparison of both LST and LST trends with data from 119 ground stations of the IMIS network, located at high elevations in the Swiss Alps. The direct comparison of Landsat and IMIS LST yields robust satellite data with a mean accuracy and precision of 0.26 K and 4.68 K, respectively. For LST trends derived from a 22.6-year record length, as imposed by the IMIS data, we obtain a mean accuracy and precision of -0.02 K yr^{-1} and 0.13 K yr^{-1}, respectively. However, we find that Landsat-LST trends are biased due to unstable diurnal acquisition times, especially for Landsat 5 and 7. Consequently, LST trend maps derived from the 38.5-year Landsat data exhibit systematic variations with topographic slope and aspect that we attribute to changes in direct shortwave radiation between different acquisition times. We discuss the origin of the magnitude and spatial variation of the LST trend bias in comparison with modelled changes in direct shortwave radiation and propose a simple approach to estimate the LST trend bias. After correcting for the LST trend bias, remaining LST trend values average between 0.07 and 0.10 K yr^{-1}. Further, the comparison of Landsat- and IMIS-derived LST trends suggests the existence of a clear-sky bias, with an average value of 0.027 K yr^{-1}. Despite these challenges, we conclude that Landsat LST data offer valuable high-resolution records of spatial and temporal LST variations in mountainous terrain. In particular, changes in the mountain cryosphere such as glacier retreat, glacier debris cover evolution and changes in snow cover, are preserved in the LST trends and potentially contribute to improved prediction of permafrost temperatures with large spatial coverage. Our study highlights the significance of understanding and addressing biases in LST trends for reliable monitoring in such challenging terrains.

3.1 Introduction

The Earth's surface temperature, at the land-atmosphere interface, is a key parameter of the surface energy budget and influences a range of biological, chemical, and physical processes within the critical zone (e.g., Brantley et al., 2007). It reflects both climate change and land surface processes and is defined as an essential climate variable by the World Meteorological Organisation (Bojinski et al., 2014). Increasing surface temperature is expected to have a severe adverse impact on ecosystems, human health, and infrastructure (IPCC, 2023). With time, surface warming propagates to greater depths, resulting in additional changes. High mountain regions that often host glaciers, snow cover, and permafrost, are particularly sensitive to increasing temperatures. Where mean annual ground temperatures rise to above 0°C, permafrost thaws, thereby destabilizing steep hillslopes (Gruber and Haeberli, 2007; Huggel, 2009; Allen et al., 2009). Indeed, increased rockfall activity and several recent significant slope failures in the European Alps (Gruber et al., 2004; Harris et al., 2009; Walter et al., 2020) have been linked to permafrost thaw. Such catastrophic events pose serious hazards to both people and infrastructure in numerous mountain ranges on Earth. Monitoring Earth's surface temperature and its spatiotemporal variation, therefore, significantly contributes to the improved prediction of the impacts of Global Warming. Ground-based instrumental monitoring of the surface temperature, however, is laborious and difficult to implement over large regions and in remote mountainous areas with steep hillslopes. Therefore, the spatial coverage of station-based surface temperature data is limited, especially when it comes to long-term records.

Satellite platforms equipped with thermal infrared sensors, allow measuring the land surface temperature (LST) at a range of spatial and temporal resolutions and have long been used in a variety of research fields (Li et al., 2013, Hulley et al., 2019, Reiners et al., 2023; Li et al., 2023). Temporal LST analysis for climate change studies or environmental monitoring requires multi-decadal time series data, which often encounters the challenge of maintaining the temporal coherence of the thermal data (Kuenzer and Dech, 2013). Many LST studies rely on data from the Moderate Resolution Imaging Spectroradiometer (MODIS) sensor onboard the Terra and Aqua satellites (Reiners et al., 2023). MODIS LST records are temporally consistent (Hulley and Hook, 2011) and LST trends have been recently derived globally (Sobrino et al., 2020). However, the relatively coarse spatial resolution of the thermal bands (1000 m) restricts the applicability of MODIS LST in high mountainous regions, where the steep terrain results in large spatial gradients in surface temperatures. In addition to altitudinal gradients in temperature, due to the decreasing air temperature, temperature variations also exist in response to variable exposition to the sun.

As the robustness of trends increases with longer time series, LST records from the Advanced Very-High-Resolution Radiometer (AVHRR) and the Landsat Program, are particularly useful for this purpose (Prata, 1994; Gutman and Masek, 2012). Both suffer, although in different manner, from

orbital drift effects, causing the acquisition time to vary over time (Julien and Sobrino, 2022, Zhang and Roy, 2016). Orbital drift corrections for AVHRR LST time series are continuously developed (e.g., Gutman et al., 1999; Mao and Treadon, 2013; Dech et al., 2021, Julien and Sobrino, 2022), as the daily temporal resolution allows unique insights into long-term dynamics of LST. Landsat, with its lower temporal but higher spatial resolution, has so far been underutilized for time series analysis (Fu and Weng, 2015). The recently released Landsat Collection 2, with improved radiometric calibration and geolocation information (Crawford et al., 2023), provides consistently generated LST data (Malakar, 2018). Landsat-derived LST time series therefore present a unique opportunity to explore the dynamics of high mountain landscapes in response to climate change and human land cover modifications.

For instance, recently published LST trends of glacier surfaces in High Mountain Asia show enhanced surface warming trends due to supraglacial debris cover and its expansion (Ren et al., 2024). Spatial patterns in LST trends are also expected in areas of seasonal snow cover. Especially at altitudes near the 0 °C isotherm, small changes in air temperature can have a significant impact on snow cover (Pepin and Lundquist et al., 2008). Observations show that in the European Alps snow cover declines in extent, duration and depth (Matiu et al., 2021) with vegetation expanding into higher elevations and thus changing the surface albedo (Rumpf et al., 2022). Furthermore, because mountain permafrost temperatures vary in response to changes in air temperature and snow cover (Smith et al., 2022), spatial patterns in LST and LST trends have the potential to inform about expected spatial variations in permafrost temperature, depth and extent. Despite sufficiently long records and the high spatial resolution of Landsat observations, deriving LST trends is complicated as acquisition times have changed by up to 1 h (Roy et al., 2020), due to orbit changes over the last decades (Zhang and Roy, 2016).

Here, we explore the opportunities of monitoring LST trends in steep mountainous regions using Landsat Collection 2. We first assessed the reliability of Landsat-derived LST and LST trends by comparison with ground observations from the Intercantonal Measurement and Information System (IMIS) network, which provides comparable radiometric surface temperatures at high-elevation sites across the Swiss Alps (Figure 3.1). We then calculated spatially distributed LST trends and identify a spatially variable bias that we associate with orbital drift of the satellites. We analyse the magnitude and spatial variation of this bias and present a simple approach to correct for it. Additionally, we address issues related to the clear-sky bias and explore opportunities and limitations for studying cryosphere changes using the corrected Landsat LST trends.

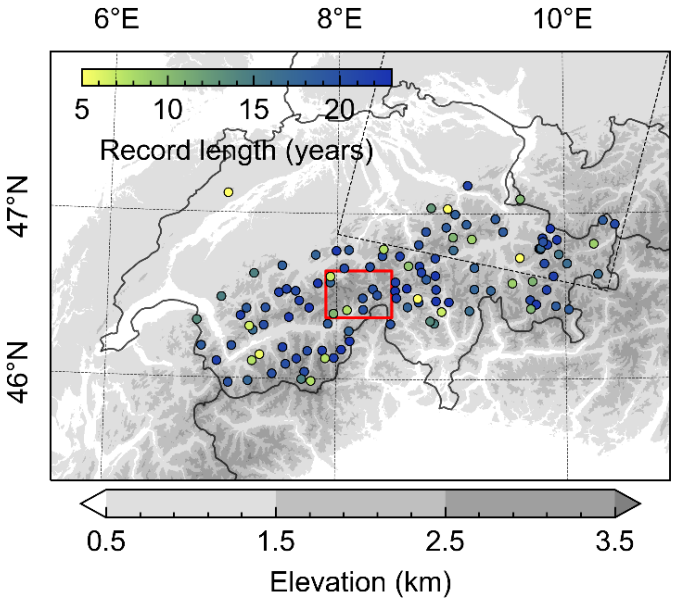

Figure 3.1. Intercantonal Measurement and Information System (IMIS) network of automated weather stations distributed across the Swiss Alps. The station data provide radiometric surface temperatures at 30-minute intervals with varying time spans, indicated by inset color. The red rectangle identifies the upper Rhone Valley shown in Figure 3.7. The black dashed rectangle indicates the Landsat footprint at path 194 and row 27, referred to in Figure 3.2.

3.2 Materials and Methods

3.2.1 Landsat-derived LST

Landsat Collection 2 (C2) - Level-2 Science Products provide multi-decadal observational remote sensing data that is geometrically and radiometrically consistent and has harmonized quality assessment bands (Dwyer et al., 2018). We used the Google Earth Engisne (GEE) to analyze LST data (Malakar et al., 2018) from Landsat 5 Thematic Mapper (TM), Landsat 7 Enhanced Thematic Mapper Plus (ETM+) and Landsat 8 Thermal Infrared Sensor (TIR) (hereafter LT05, LE07, LC08) covering a timespan from 1984 to 2022. The native spatial resolutions of LT05 (120 m), LE07 (60 m) and LC08 (100 m) have been resampled in Collection 2 to 30 m, which is the spatial resolution that we used in our study.

The Landsat C2 LST calculation is based on the single-channel algorithm (Malakar et al., 2018) that relies only on one thermal infrared band and which has been widely used to retrieve LST from Landsat data (Jiménez-Muñoz and Sobrino, 2003; Cook et al., 2014). The conversion of at-sensor radiometric temperature to LST requires an atmospheric correction and knowledge of the surface emissivity. The atmospheric correction in the Landsat C2 LST calculation is based on the total column water vapor derived from NCEP atmospheric reanalysis data (Kalnay et al., 1996). Mean emissivity estimates over the time period 2000-2008 are based on the Advanced Spaceborne Thermal Emission and Reflection Radiometer Global Emissivity Dataset (ASTER GED) (Hulley et al., 2015)

and temporally adjusted using Landsat-derived NDVI and NDSI (Normalized difference snow index). Inspection of the ASTER GED reveals several artifacts, which appear to align with artefacts in the Landsat LST data. To avoid erroneous LST data and mask out clouds in the Landsat images, we applied several filters and masks that we describe in more detail in section 2.3.

The scene acquisition time of Landsat for the Swiss Alps lies mostly between 09:30 and 10:30 UTC. Figure 3.2 shows the acquisition times from the different Landsat sensors during the study period. Whereas LC08 has a relatively stable acquisition time, LE07 shows slightly continuous drift before and strong drift after about 2018, due to depleted onboard fuel resources (Qiu et al., 2021). LT05 on the other hand shows both sporadic and continuous orbit changes that lead to significant variations in acquisition time (Zhang and Roy, 2016). Although orbit variations are often due to sporadic orbit keeping maneuvers, a gradual increase in overpass times is evident too (Roy et al., 2020). When fitting a linear model to all satellites together (but excluding LE07 data after 2018 due to strong orbital decay), the acquisition time has increased approximately from 9:29 in 1984 to 10:16 in 2022 (Figure 3.2, dotted line). We expect that LST trends derived from the 38.5-year time series are likely biased by the progressively delayed acquisition times, probably towards more positive values, due to gradual warming of the land surface in the morning. Because different acquisition times also lead to geometric changes in the sun-target-sensor configuration, this bias may additionally vary with slope and aspect of the topography. We describe our approach to analyze this issue in section 2.4.

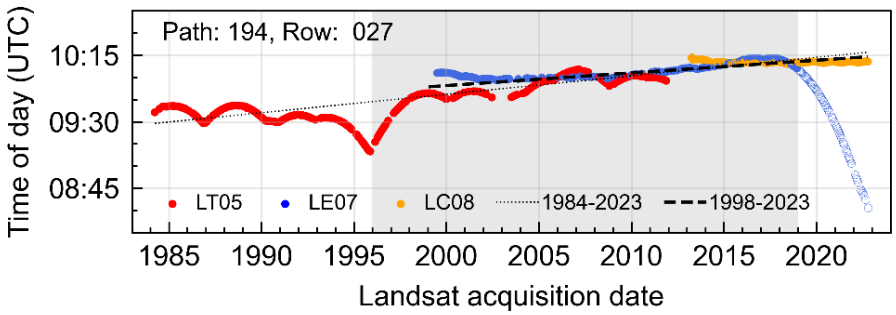

Figure 3.2. Acquisition times (UTC) of Landsat LT05 (red), LE07 (blue), and LC08 (orange) at path 194 and row 027. LE07's noticeable orbital drift after 2018 (hollow blue circles), causes a significant shift in revisit timing and has been excluded from the analysis. Linear regression lines (dotted and dashed) depict acquisition time trends, with and without abrupt LT05 orbit changes prior to 2000. The gray-shaded area indicates the time period for which IMIS station data exists, although with variable record length.

3.2.2 IMIS-derived LST

We evaluated the Landsat-derived LST data by comparing them with in situ surface temperature measurements from automated weather stations of the IMIS network. The IMIS network was set up by the Swiss Federal Institute for Snow and Avalanche Research (SLF) and consists of

186 stations distributed across the Swiss Alps. We used a subset of 119 stations (Table B 1) that record radiometric surface temperature in 30 min intervals. The record length per station varies, with the longest record covering a period from 1996 to 2019 (Figure 3.1). The IMIS stations are located between 1258 m and 2953 m elevation above sea level and are usually installed on flat to gentle sloping ground. As the stations are primarily used for snow monitoring, the reported surface temperature is calibrated using an emissivity of 0.98 (for snow), which may thus introduce a bias towards colder temperatures during snow-free conditions. Because the transition between snow-covered and snow-free conditions cannot be unambiguously determined based on the IMIS data alone, and because of unknown actual emissivity values of the ground surface, we refrained from efforts to correct this bias. For a surface temperature of 15 °C, a change in emissivity of 0.01 would result in a temperature change of 0.73 K (Kuenzer and Dech, 2013). This bias decreases for lower LST values. Despite potential measurement deviations under snow-free conditions, the IMIS stations measure radiometric surface temperatures and are thus well suited to compare with Landsat derived LST. Additionally, the high temporal resolution of the IMIS data allows to compare LST clear-sky and cloudy-sky conditions using the Landsat overpass times. We expect the large difference in spatial resolution to introduce additional uncertainty as Landsat most likely provides a mixed-pixel signal of varying LSTs, compared to the IMIS data

3.2.3 LST processing and trend estimation

For the studied period and the chosen Landsat sensors, we obtained for each 30-m pixel in the co-registered image collection several hundred LST observations scattered across different times of a year. We used a harmonic model including a linear trend (Eq. 3.1) to perform an ordinary least squares regression (Shumway and Stoffer, 2016; Fu and Weng, 2015) on the LST time series data in order to estimate (1) the mean annual LST (MALST), (2) the annual LST amplitude, (3) the long-term LST trend and (4) the phase shift:

$$LST_t = \beta_0 + \beta_1 t + A\cos(2\pi\omega t - \varphi) \quad \text{Eq. 3.1,}$$

where β_0 is the mean annual LST (K), β_1 is the slope (K yr^{-1}) of the linear trend, t is the time in years, A is the amplitude (K), ω is the frequency (equal to one for one cycle per year) and φ is the phase. The harmonic term can be decomposed into a sine and a cosine term, and thus Eq. 3.1 is linearized to:

$$LST_t = \beta_0 + \beta_1 t + \beta_2 cos(2\pi\omega t) + \beta_3 sin(2\pi\omega t) \quad \text{Eq. 3.2,}$$

where β_2 and β_3 are the newly introduced coefficients that are equal to $A\cos(\varphi)$ and $A\sin(\varphi)$, respectively. GEE allows ordinary least squares regression of Eq. 3.2 and thus the determination of the four coefficients β_0 to β_3. We acknowledge that LST time series may contain abrupt changes due

to land cover change, for example, which may not be well captured by a linear model (Zhu and Woodcock, 2012). Different approaches have been proposed to detect such changes and simultaneously obtain trend values (see the recent review by Li et al., 2022). However, the change detection approaches currently available in GEE are more limited (Kennedy et al., 2010; Zhu and Woodcock, 2012) and as we will show later, the segmentation of the time series affects our ability to account for LST trend bias due to orbital drift.

Prior to fitting Eq. 3.2 to the Landsat LST data, we implemented filters to mask (1) cloud-contaminated pixels and (2) duplicate LST observations with the same date that result from along-track overlapping Landsat scenes. Cloud masking was done using the Landsat C2 Pixel Quality Assessment Band (QA) cloud flag (Dwyer et al., 2018; Zhu and Woodcock, 2012). Although the cloud flag of the QA band provides good accuracy (Foga et al., 2017), bright surfaces such as snow and ice in high mountain settings, can still be challenging. Predominantly in LT05 data, we find extremely cold LST values, which are likely clouds that were not captured by the cloud detection algorithm. To overcome this issue, we applied an additional filter that masks outliers, by applying a threshold to the residuals between modeled and observed LST. We first calculated the β coefficients on the cloud-filtered data, including potential outliers missed by the QA cloud flag, and then uploaded them to GEE. In a second step, we predicted for each Landsat acquisition time the corresponding LST using the uploaded β coefficients (Eq. 2) and applied a threshold of +/-30 K to the residuals to mask extreme LST values that might otherwise bias the LST trend (cf., Weng and Fu, 2014). The procedure was applied to the complete Landsat time series data. Figure 3.3. Time series of Landsat LT05 (red), LE07 (blue) and LC08 (orange)-derived Land Surface Temperature (LST) at location 47.17° N, 9.15° E (IMIS station AMD2). The harmonic model (solid sinusoidal line) was derived by least squared regression including linear trend component (dashed line). Outliers (hollow circles) were detected by applying a threshold of 30 K to the (b) residuals and removed from further analysis. Panel (c) and (d) show the distribution of the LST and residuals respectively.shows an exemplary LST time series from each sensor, the harmonic model with linear trend, the residuals, and the filtered outliers at the location of IMIS station AMD2. Identical figures from all IMIS locations can be found in the supplement file B (Gök et al., 2022).

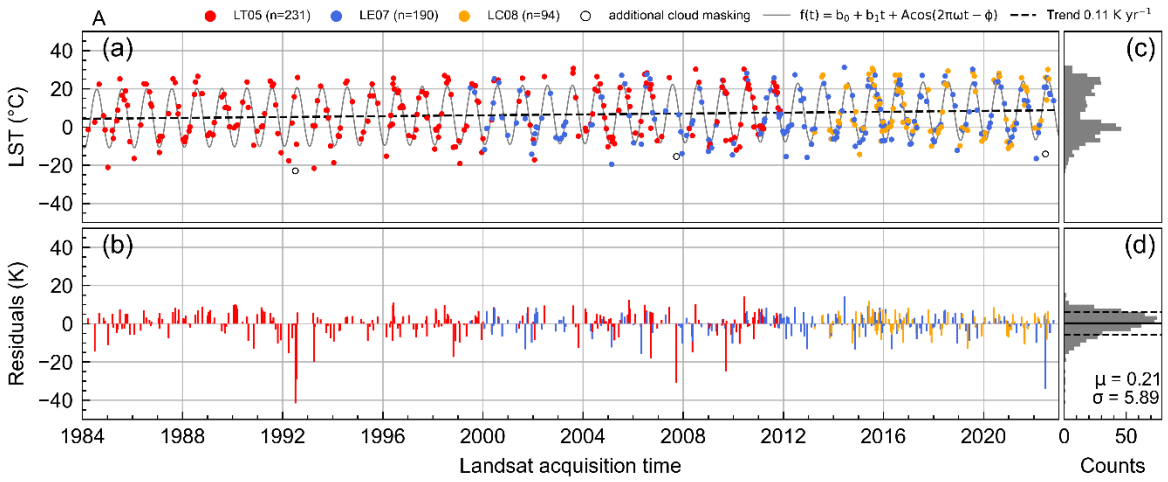

Figure 3.3. Time series of Landsat LT05 (red), LE07 (blue) and LC08 (orange)-derived Land Surface Temperature (LST) at location 47.17° N, 9.15° E (IMIS station AMD2). The harmonic model (solid sinusoidal line) was derived by least squared regression including linear trend component (dashed line). Outliers (hollow circles) were detected by applying a threshold of 30 K to the (b) residuals and removed from further analysis. Panel (c) and (d) show the distribution of the LST and residuals respectively.

To assess the reliability of the Landsat-derived LSTs and LST trends, we compared them with LST data derived from the IMIS network. We first extracted the Landsat LST time series at the locations of the IMIS stations. As IMIS records are only available in 30-minute intervals, we linearly interpolated LSTs at the Landsat acquisition times to obtain comparable LST time series of equal length. Based on Eq. 2, we derived the mean annual LST, the LST amplitude, the phase of the harmonic oscillation, and LST trends for both datasets. We further assessed the sensitivity of LST trends to the LT05, LE07, and LC08 sensors by comparing data from each sensor with the corresponding IMIS LST data, where the observation periods overlap. Because the temporal overlap of the individual Landsat sensors and the IMIS data varies, this comparison also results in different record lengths.

We used student's t-test to draw statistical inference for the regression slope and evaluate the significance of LST trends (Muro et al., 2018). Pixels with non-significant trends (p-values < 0.05) were flagged. Note that the comparison of LST trends between Landsat and IMIS data, as well as the spatial analysis of LST trends in relation to the LST trend bias is based on all trend data and does not require statistical significance of trend values.

3.2.4 LST trend bias analysis

We expect the LST trend to be biased due to the variations in acquisition time caused by orbital change of the satellites (Figure 3.2). Within the 47 minutes time difference in image acquisition between the beginning and the end of the 38.5-year Landsat observation period, the sun's position and thus also the solar zenith angle changes notably, modifying the amount of incoming

shortwave radiation received by the surface. In mountainous terrain with variably steep and exposed topography, we expect this effect to be spatially non-uniform. Based on the fitted linear model of the acquisition time, we analyzed changes in the incoming direct solar radiation (ΔSin) for the Swiss Alps using the "insol" functional library (Corripio, 2003). We studied the relationship of LST trends and ΔSin with topography by aggregating mean values for 2° slope and 10° aspect sections derived from the 10-m resolution Copernicus digital elevation model (Copernicus DEM, 2022). Prior to averaging LST trends we excluded glaciers and recently deglaciated areas using a mask based on glacier outlines from the Randolph Glacier Inventory V6 (RGI Consortium, 2017), which we expanded by 10 pixels in the 30-m resolution LST trend images. Additionally, we excluded all regions below 1700 m elevation, which are likely influenced by anthropogenic land cover changes (Rumpf et al., 2022).

3.2.5 Validation metrics

The LST data used in this study, obtained from the Landsat C2 archive, is based on three different sensors (LT05, LE07 and LC08) and auxiliary datasets such as the ASTER GED and NCEP reanalysis data. Since all these datasets have their limitations, it is important to validate LST data to ensure its accuracy and reliability. We compared the Landsat-derived LST with in situ LST measurements from the IMIS stations at the Landsat acquisition time. We followed the "Land Surface Temperature Product Validation Best Practice Protocol" (Guillevic et al., 2018) by using metrics of accuracy, precision and uncertainty for reporting LST validation results. The accuracy (μ), as a measure of the systematic error/bias, is given by the arithmetic mean of the difference between the satellite derived LST and the in situ measured reference LST (ΔLST_{ref}). The precision (σ) describes the spread of the LST around the expected value (ΔLST_{ref}) and can be approximated by the standard deviation. The uncertainty is given by the Root Mean Square Error (RMSE) and describes the dispersion of the LST values. Because the accuracy and precision of LST data can be strongly affected by outliers, we also report the median of the ΔLST_{ref} for the accuracy and the median absolute deviation of the residuals for the precision as additional validation metrics (Guillevic et al., 2018). We apply these validation metrics to both the LST data and the LST trends. We emphasize that in our study the term "validation" may be slightly misleading as it suggests that the ground-based IMIS measurements provide the correct LST values. However, we note that even the IMIS data is most likely biased during snow-free conditions (see section 2.2) and subject to measurement uncertainties. In addition, the different footprint of the ground- (~10 cm) and space-borne (~10-100 m) measurements allow for deviations due to spatial heterogeneity in LST. We will come back to this issue in our discussion. Nevertheless, we argue that the comparison of these data sets is a valuable effort and that consistency between both temperature measurements provides confidence.

3.3 Results

3.3.1 LST comparison

For comparing Landsat-derived LST with ground-based LST from the IMIS network, we interpolated IMIS LST's at the Landsat acquisition time. In total 44981 Landsat observations are available for comparison with IMIS observations. The LST data from all three Landsat sensors are scattered about the 1:1 line in comparison with the IMIS data (Figure 3.4 a-d). At around 0°C IMIS LST, the spread in Landsat-derived LST is the highest, which is likely related to differences in spatial resolution and the presence or absence of snow cover in the different measurement areas. It furthermore appears that LSTs derived from each Landsat sensor tend to be slightly warmer for LSTs above 0 °C compared to those below 0 °C. Mean- and median-based metrics of accuracy (μ), precision (σ) and uncertainty (RMSE) between Landsat and IMIS LST for each sensor and the entire time series, as shown in Figure 3.4 and Table 3.1. The accuracy (μ) ranges from +0.05 K (LC08) to +0.45 K (LE07) and indicates a slight positive bias. The precision (σ) ranges from 4.09 K (LE07) to 6.13 K (LT05). Considering data from all three sensors together (Figure 3.4d), the accuracy is +0.26 K, the precision is 4.69 K and the uncertainty is 4.7 K (Table 3.1). Considering median values, the precision improves but the accuracy deteriorates.

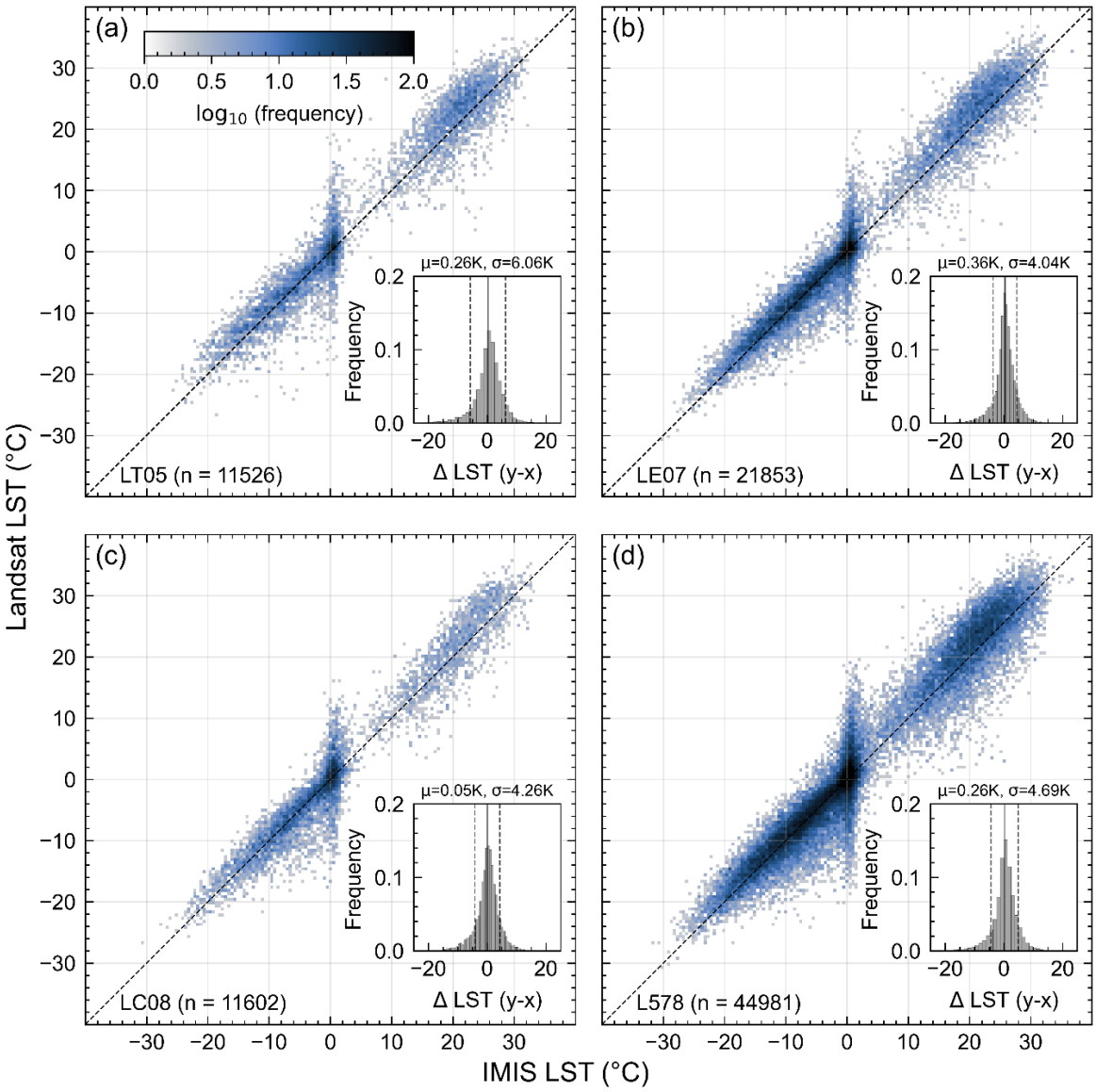

Figure 3.4. Comparison of Landsat-derived Land Surface Temperature (LST) with IMIS LST for sensors (a) Thematic Mapper (LT05), (b) Enhanced Thematic Mapper Plus (LE07), (c) Thermal Infrared Sensor (LC08) and (d) LT05, LE07, and LC08 together (L578). Colors denote the number of data points by decadal logarithm. Inset figures show histograms of LST residuals: ΔLST = Landsat LST-IMIS LST.

Table 3.1. Validation metrics of Landsat-derived LST in comparison with IMIS-derived LST.

Quantity	Symbol	Unit	LT05	LE07	LC08	L578
Accuracy (mean/median)	μ	K	0.26/0.72	0.36/0.5	0.05/0.31	0.26/0.5
Precision (mean/median)	σ	K	6.06/2.47	4.04/1.70	4.26/2.05	4.69/2.01
Uncertainty (RMSE)	RMSE	K	6.07	4.06	4.26	4.7
Sample number	n	-	11526	21853	11602	44981

3.3.2 LST trend comparison

We also compared Landsat-derived LST trends with trends derived from IMIS LST data interpolated at Landsat observation times, for each sensor as well as the complete time series (Figure 3.5, Table 3.2). We excluded stations with record lengths of less than 5 years. Short time series result from different temporal overlaps between the IMIS records and Landsat sensors, in particular LT05 and LC08 (Figure 3.5 a, c). These show large scatter about the 1:1 line compared to trends derived from longer time series, resulting in relatively large uncertainties (Table 3.2). Therefore, amongst the different sensors, LE07 provides the most reliable results (Figure 3.5), with better accuracy and precision (Table 3.2), due to the large temporal overlap with the IMIS data. Consequently, our comparison of trends derived from all sensors with IMIS-derived LST trends (Figure 3.5d) is primarily dominated by LE07. Considering data from all three sensors together, the accuracy is -0.02 K yr^{-1} and the precision is 0.13 K yr^{-1}, improving considerably when referring to median values.

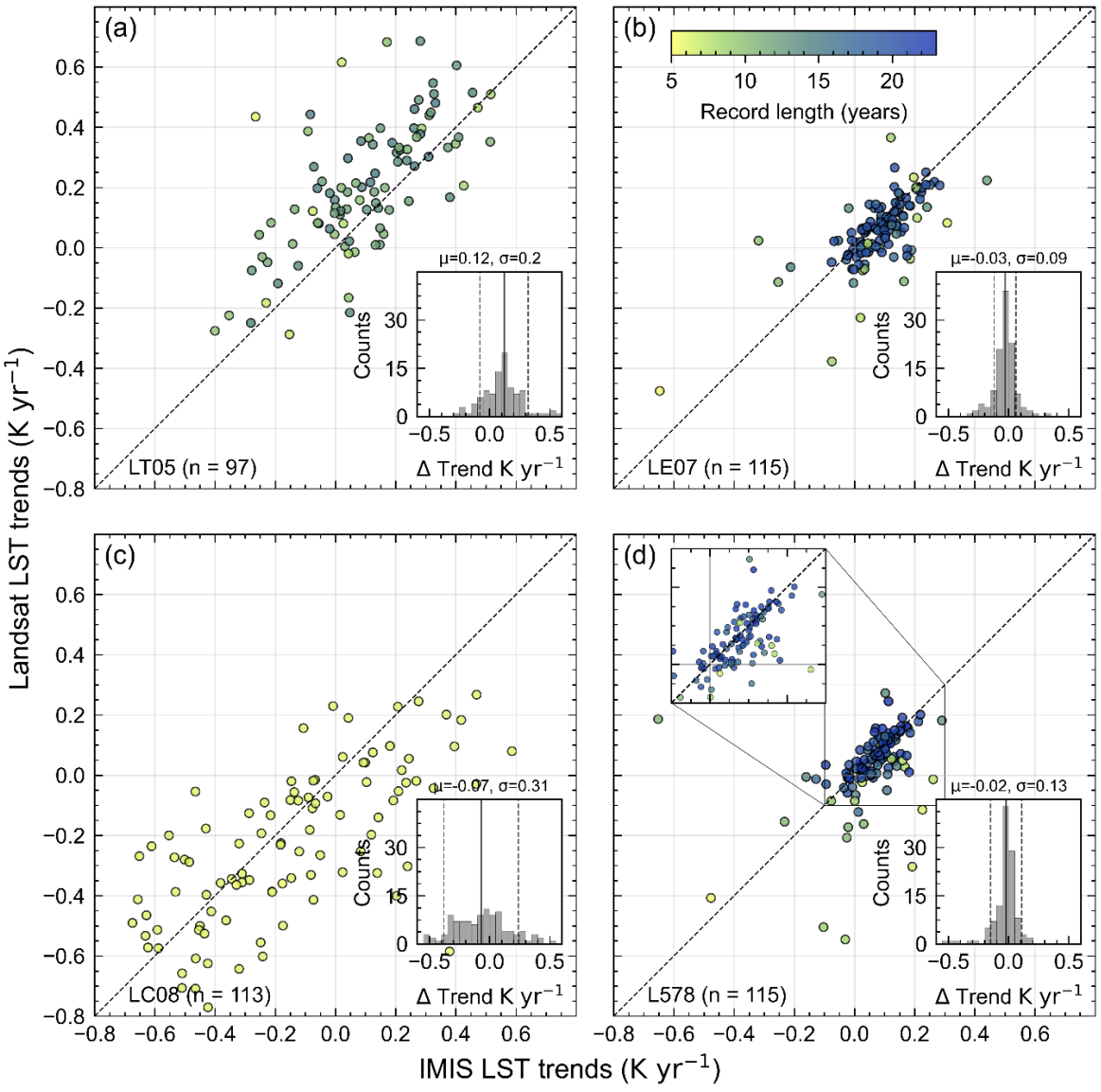

Figure 3.5. Comparison of Landsat-derived Land Surface Temperature (LST) trends with IMIS LST trends for sensors (a) Thematic Mapper (LT05), (b) Enhanced Thematic Mapper Plus (LE07), (c) Thermal Infrared Sensor (LC08) and (d) LT05, LE07, and LC08 together (L578). Stations with a record length (marker color) of less than five years have been omitted. Trend residuals (Landsat LST trends – IMIS LST trends) together with the accuracy (μ) and precision (σ) values are shown in the inset histograms. Note the strong impact of record length on the comparison of LST trends.

Table 3.2. Validation metrics of Landsat-derived LST trends in comparisons with IMIS-derived LST trends.

Quantity	Symbol	Unit	LT05	LE07	LC08	L578
Accuracy (mean/median)	μ	Kyr^{-1}	0.12/ 0.11	-0.03/ -0.02	-0.07/ -0.06	-0.02/ -0.01
Precision (mean/median)	σ	Kyr^{-1}	0.20/ 0.13	0.09/ 0.05	0.31/ 0.19	0.13/ 0.04
Uncertainty (RMSE)	RMSE	Kyr^{-1}	0.23	0.10	0.31	0.13
Sample number	n	-	97	115	113	115

3.3.3 Spatiotemporal variations of LST

We applied Eq. 3.2 to the Landsat LST time series (LT05, LE07 and LC08) across Switzerland using GEE. The model results are presented as maps of the mean annual land surface temperature (MALST), the LST amplitude, the phase of the harmonic oscillation and the LST trend in Figure 3.6, with a focus on the upper Rhone Valley shown in Figure 3.7. The presented MALST values are for the year 2000 and range from -25°C to +25°C. We observe consistently the highest MALST values at low elevations and the lowest at high elevations, where snow- and ice-covered areas range from 0°C to -20°C. As seen in the detailed map in Figure 3.7a, MALST values show reasonable spatial variations with terrain aspect and no significant processing artefacts are present. East-facing slopes consistently display higher MALST compared to west-facing ones, which aligns with expectations due to the late morning overpass of the Landsat satellites Figure 3.7a). Data gaps, which are in Figure 3.6 most evident in southern Germany, are due to data gaps in the ASTER GED data and consistent across all variables. LST amplitude values range between 3 and 25 K (Figure 3.6b), with the lowest values where snow or ice cover is present all year round. High amplitude values are found in regions with seasonal snow cover that also heat up during the summer (Figure 3.7b). The phase of the harmonic oscillation (Figure 3.7c), shows spatial variations in seasonal shifts, which we report as the day of the year with the highest (peak) temperature in the annual LST cycle. The phase values display an altitudinal gradient (Figure 3.6c) with a slight aspect dependence (Figure 3.7c).

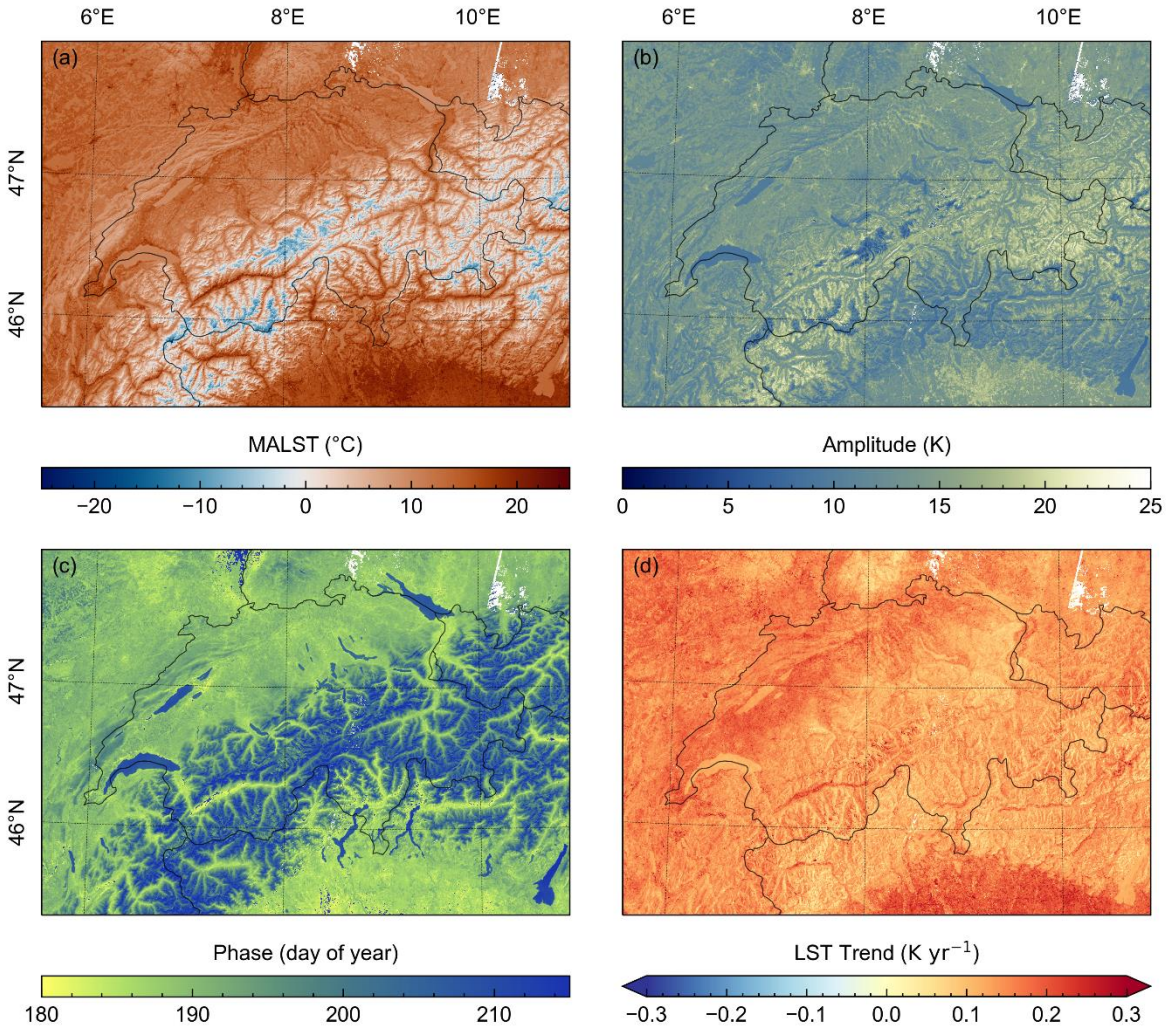

Figure 3.6. Landsat land surface temperature (LST) time series derived (a) mean annual LST (MALST), (b) LST amplitude and (c) phase of the harmonic oscillation and (d) LST trend across Switzerland and adjacent areas.

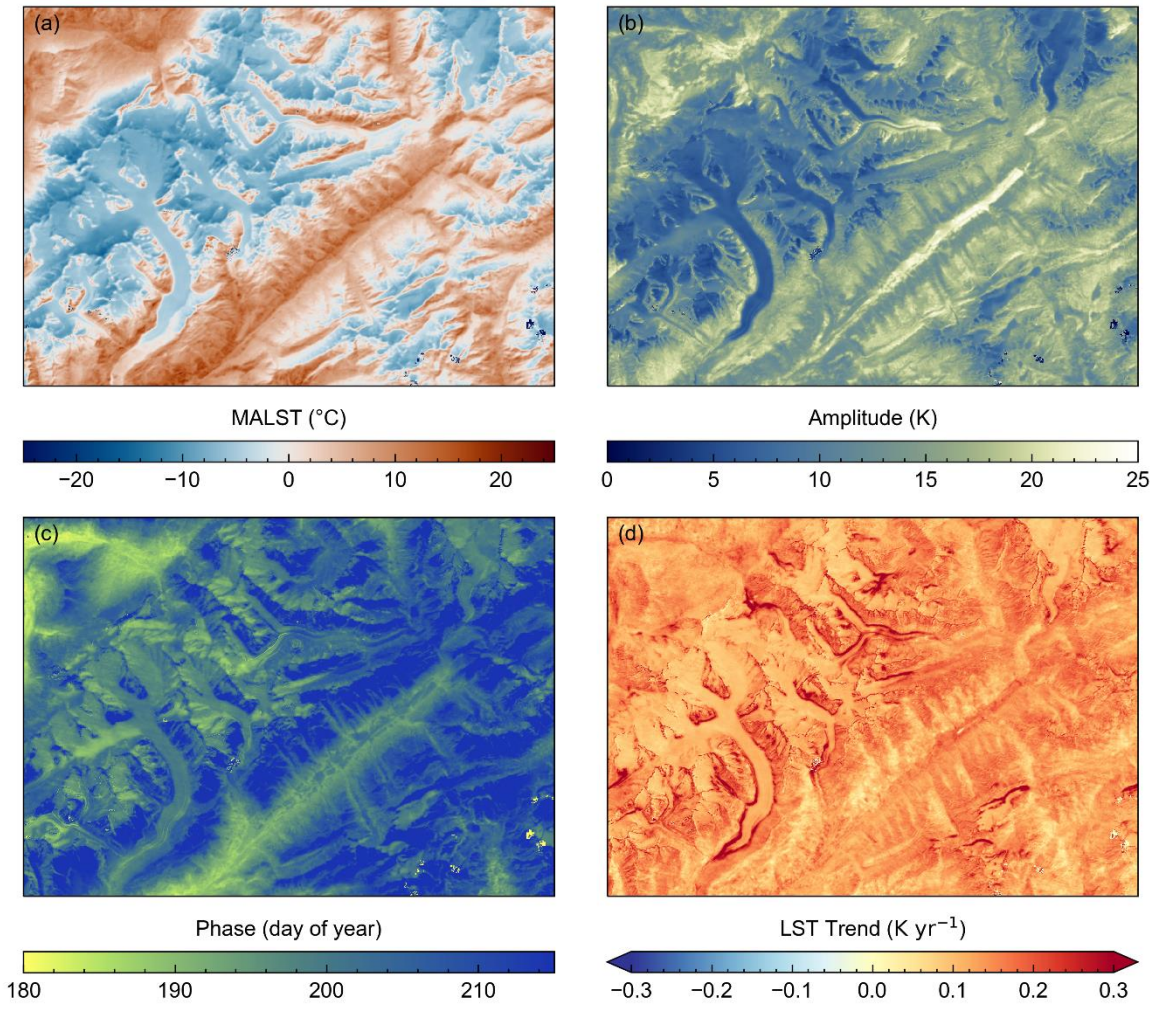

Figure 3.7. Landsat land surface temperature (LST) time series derived (a) mean annual LST (MALST), (b) LST amplitude, (c) phase of the harmonic oscillation and (d) LST trend, across the upper Rhone Valley.

Averaged across the entire study area, the mean LST trend is 0.14 K yr^{-1} with the 5th and 95th percentile of 0.08 K yr^{-1} and 0.21 K yr^{-1}, respectively. (Figure 3.6d). Areas with high population density often appear to exhibit trend values exceeding 0.2 K yr^{-1}. Notably, the highest trend values are observed in areas where retreating glaciers expose sediment or bedrock (Figure 3.7d). Compared to the MALST, LST amplitude and the phase of the harmonic oscillation, the LST trend values display more artefacts. Subtle but systematic across-track jumps in LST trends are visible in the northeast of the map in Figure 3.6d. These artefacts align with the Landsat orbit and variations in the number of observations due to overlapping scenes from adjacent orbital tracks (Figure B 1). Similarly, the post-2003 Landsat LE07 scan line corrector failure induces across-track stripes in the number of LST observations that also appear in some parts of the LST trend maps (only faintly visible on some glacier surfaces in Figure 3.7d). These patterns in LST trend values are consistent with the sensitivity to record length we observed in our comparison of Landsat- and IMIS-derived LST trends (section 3.3.2). We further discuss this point in section 4.1. Finally, LST trends in the detailed map

display an aspect dependency, with generally lower values at east-facing and higher values at west-facing slopes (Figure 3.7d). Regions with flat topography, as in the foreland, wide valleys, or lakes show more continuous trend values. We suspect that this effect is related to the shift towards later acquisition times and thus to variations in the solar zenith angle over the 38.5 years Landsat record. In the following section we examine this trend bias in more detail using IMIS station data.

3.3.4 LST trend bias

To estimate the LST trend bias in flat to gently sloping terrain, we used LST data from the IMIS stations. The daily LST differences (ΔLST) at 9:29 h and 10:16 h UTC across all 119 IMIS stations, derived from linear interpolation of the 30-minute interval raw data, show a bimodal distribution (Figure 3.8), which we separated using bimodal Gaussian regression. During melting periods, snow surfaces remain locked at the melting point and ΔLST values are essentially zero (blue curve). The remaining ΔLST values are normally distributed (red curve) with a mean ΔLST of 1.72 K and a standard deviation of 0.93 K. Over a 38.5-year period, this suggests an average LST trend bias of 0.045 K yr^{-1} for flat to gently sloping terrain.

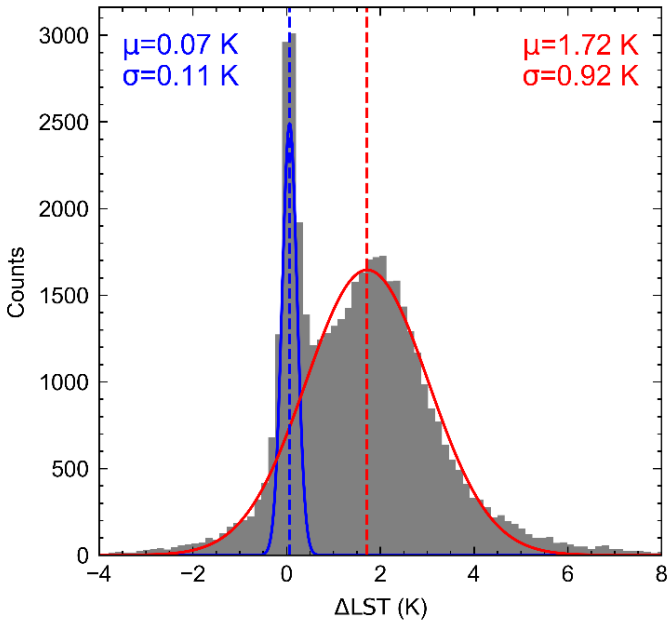

Figure 3.8. Bimodal distribution of IMIS-derived land surface temperature differences (ΔLST) of daily LST interpolated at 9:29 h and 10:16 h. Mean (μ) and standard deviation (σ) were obtained from bimodal gaussian regression. Over the 38.5-year time period, a mean ΔLST of 1.72 K may thus explain 0.045 Kyr^{-1} of the LST trend bias over flat and gentle sloping terrain where IMIS stations are typically located.

The influence of topographic slope and aspect on the LST trends is shown by aggregated mean values for 2° slope and 10° aspect bins in Figure 3.9c. For slope angles above ~10° LST trends

are generally lower on east-facing slopes whereas they are higher on west-facing slopes. Mean LST trend values for slope angles above 75° are noisy due to very few samples (pixels) and have been excluded from analysis. We compared this pattern with modeled differences in incoming solar radiation between 9:29 h and 10:16 h (ΔSin) for the 1st of all months of the year using terrain parameters from the DEM of our study area. In Figure 3.9d we show the pattern for July, which turned out to resemble the LST trend pattern the most, although differences in ΔSin patterns between May and September are generally small.

Overall, we find large similarities in the general pattern of how mean LST trends and ΔSin vary with slope and aspect (Figure 3.9c, d; note that one colorbar is diverging while the other is continuous). Specifically, the cross sections shown for slope angles of 30° and 50° (Figure 3.9e, f), highlight the sinusoidal variation of LST trend and ΔSin with aspect. We observe that the maximum and minimum values of LST trends for a given slope appear progressively translated to lower aspect values for slopes >30°. This pattern is absent in the ΔSin values. As expected, LST trend and ΔSin variations with aspect are low for slope angles <10°. However, whereas the average ΔSin value for any given slope and across all aspects is relatively similar, this is not the case for LST trends. There, we observe higher trend values for small slope angles when averaged across all aspects, compared to higher slope angles.

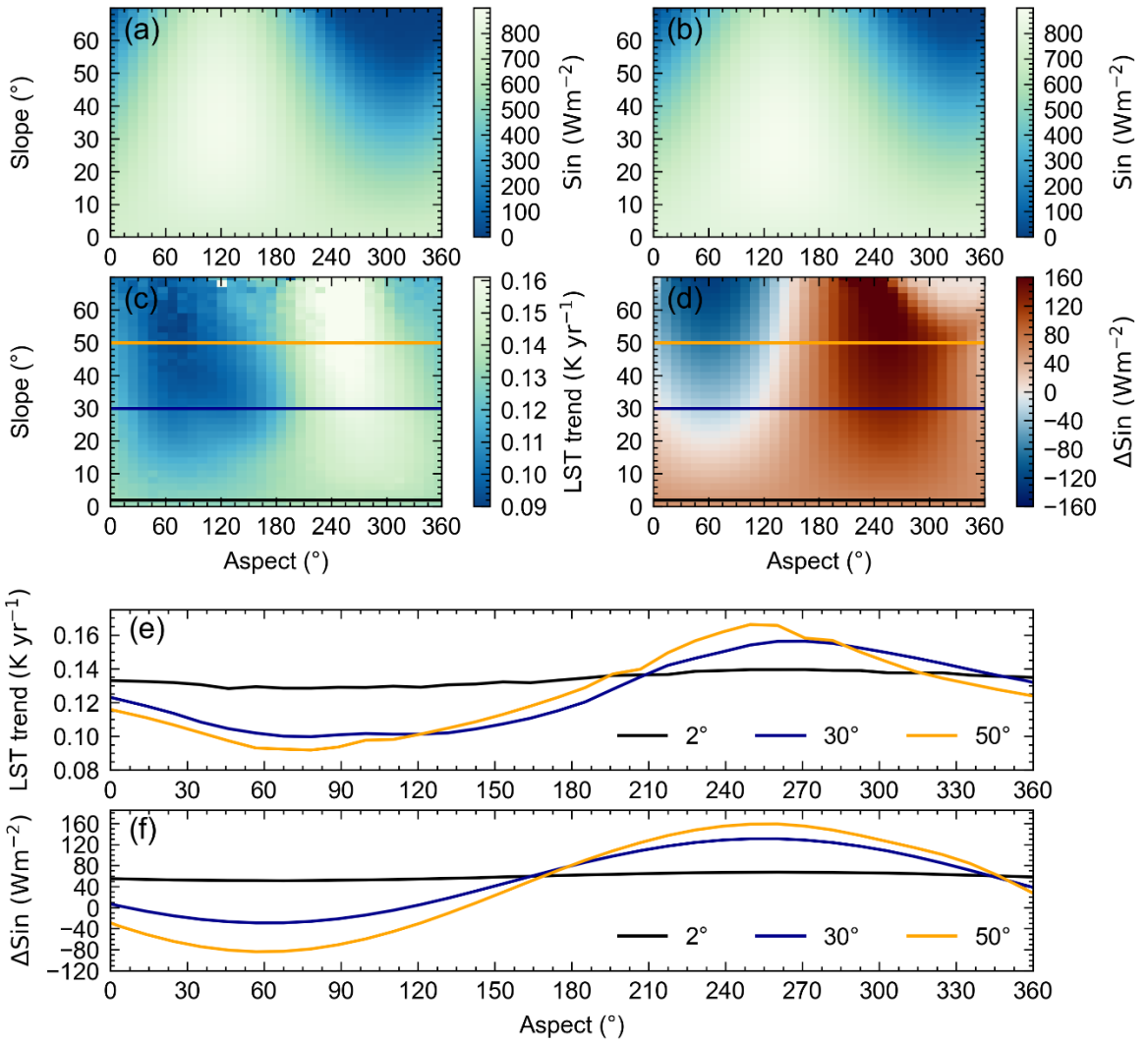

Figure 3.9. Incoming shortwave radiation at 9:29 h (a) and 10:16 h (b), land surface temperature (LST) trend (c) and shortwave radiation difference between both times (ΔSin) (d) across Switzerland, excluding glaciers and all regions below 1700 m. Values are averaged for 2° slope and 15° aspect bins. Cross-sections of 30° and 50° slope angles show a similar sinusoidal pattern between mean LST trend (e) and mean ΔSin (f), indicating LST trends biased by orbital drift.

3.4 Discussion

3.4.1 Uncertainties related to LST and LST trends

Our comparison of Landsat-derived and in situ-measured IMIS LSTs has shown good agreement with a mean accuracy of 0.26 K for the combined Landsat sensors (Figure 3.6, Table 3.1). We observed no significant deviations in accuracy for the individual sensors, but the number of data points vary due to different temporal overlap of IMIS records and Landsat sensors. The slight positive bias of Landsat-derived LSTs greater than 0 °C, compared to those measured from the IMIS stations, is likely due to inaccurate IMIS LST data during snow-free conditions. The radiometric temperature measurements at the IMIS stations are based on a constant emissivity value of 0.98 for snow, resulting

in biased temperatures for snow-free conditions. This explanation is consistent with greater accuracy at negative IMIS-derived LSTs, which often fall together with snow cover. The relatively large precision value of 4.69 K is likely in part due to the scatter around 0 °C, which is not necessarily a faulty or inaccurate measurement but rather caused by mixed-pixel effects due to the large resolution differences between IMIS and Landsat. During snowmelt periods, the IMIS sensor records ~0°C LST as long as snow persists under the sensor. Simultaneously, however, the larger footprint (60-100 m) of the Landsat measurement may record a mixed signal in the wider area around the IMIS station, potentially ranging from snow-free patches in sun-exposed areas to non-melting snow cover in shadows. By excluding data where IMIS LST is between -3.5 °C and +3.5 °C, the precision and uncertainty for L578 reduces to 4.37 and 4.38, respectively. Despite the relatively large uncertainty and a slight warm temperature bias, we find that the comparison of almost 4.5 × 104 LST measurements shows good agreement. We note, however, that the IMIS network's spatial distribution does not fully represent the topographic complexity encountered in high mountains, as the stations are mostly installed on flat to gentle sloping surfaces below 3000 m elevation.

The robustness of LST trends varies among Landsat sensors due to different temporal overlaps with the IMIS station data (Figure 3.2). Using LST data from all three sensors, the temporal overlap with IMIS LST data covers a record length of 22.6 years. Trends with such large temporal overlap are aligned well about the 1:1 line with a mean accuracy of -0.02 Kyr^{-1}, based on the residuals. However, this comparison is dominated by LE07, which has the longest overlap in the observation period (Figure 3.2). Although we are unable to evaluate LST trends from LT05 and LC08 based on long time series, our comparison together with the precious comparison of Landsat-derived and IMIS-derived LSTs for the different sensors provides confidence that LST trends derived from different Landsat sensors, spanning 38.5 years in total, are robust.

Besides the record length, the total number of LST observations also plays an important role to derive robust LST trends. Although the Landsat archive covers four decades of LST observations, its temporal resolution of 16-day revisit interval is rather low. In addition, cloud cover renders many scenes unusable, highlighting the need for reliable cloud masking. This raises two problems, especially for mountainous terrain. First, frequent cloud cover leads to inevitable data gaps; and second, cloud detection algorithms are prone to failure over bright surfaces like snow and ice, which are common at high elevations. Our filter procedure, which is based on an initial LST model and thresholding the model-observation residuals in a second step, provides a way to detect unreasonably high or low LST values by taking the existing seasonal trend into account. We found that this filter more often removes unreasonable cold LSTs, which are likely misclassified clouds, rather than warm LSTs. Yet, it is also possible that the Landsat cloud flag might have classified bright surfaces as clouds, resulting in the possible removal of valid LST observations. A robust and reliable cloud detection algorithm is currently the only practical way to minimize such problems.

The number of observations in the LST time series vary not only due to clouds, but also due to other systematic factors. Substantial spatial differences in LST counts arise from partial overlapping of adjacent Landsat paths (Figure B 1b), which tends to increase towards the poles. In our study area, these overlaps yield approximately twice as many observations for a third of the area. Furthermore, the Landsat 7 scan line corrector failure further reduces data availability at smaller spatial scales. MALST, amplitude and phase derived from LST time series seem to be generally unaffected by the variable number of observations as no large-scale patterns following the mentioned limitations can be observed (Figure 3.6a, b, c). However, the LST trend is more sensitive to the number of observations and subtle artefacts in some regions can be identified that align with the flight path of the satellite (Figure 3.6d). In some regions faint stripes can be seen that correspond to the Landsat 7 scan line failure and thus reduced data availability. We assessed the robustness of LST trend calculations with respect to the number of observations through a systematic Monte Carlo simulation. By iteratively reducing the time series size (n=100) and performing repeated trend analyses (1000 repetitions), we quantified the impact of data reduction on trend stability. Each value of the 1000 repetition was compared to the LST trend of the full time series (difference) and summarized as the mean and standard deviation. We chose the Landsat LST time series at the IMIS location of OFE2, comprising 1009 observations with a LST trend of 0.11 Kyr^{-1}, as an illustrative test site. The analysis revealed that although mean LST trend value remains stable across sample sizes, the standard deviation, which represents the precision, varies more strongly. For common sample sizes of around 750 LST observations over the 38-year period, the 1-sigma value is 0.01.

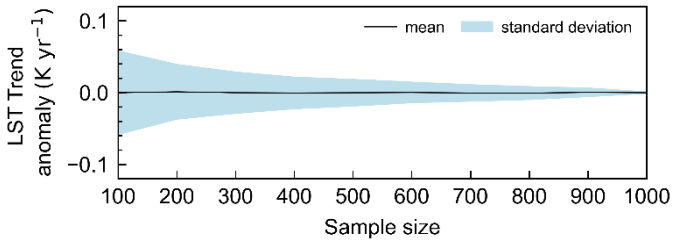

Figure 3.10. Sensitivity Analysis of land surface temperature (LST) trend stability. LST trend anomaly shows the difference of LST trend derived from full time series and repeated LST trend calculations (1000 repetitions) with iteratively reduced sample sizes (n=100). Results are given as mean and standard deviation.

3.4.2 Clear-sky bias

LST measurements based on thermal infrared remote sensing are biased towards clear-sky conditions (Ermida et al., 2019). The effect of such a bias on LST trends has not yet received much attention. A recent study indicated no discernible impact of clear-sky bias on LST trends (Good et al., 2022) by comparing satellite-derived LST with 2-meter air temperatures under clear-sky and all-sky conditions. Further, Zhao et al. (2021) compared mean annual LST trends with trends in clear-sky day occurrence and did not identify a clear correlation for daytime LST but emphasized the

challenges arising from changing surface conditions in the analysis. The Landsat data provides us with the timing of cloud cover and thus allows us to estimate the impact of cloud cover on LST trends at the IMIS locations. We compared IMIS LST trends derived during Landsat overpass days for both clear-sky and all-weather conditions and found that on average LST trends during clear-sky conditions are 0.027 Kyr^{-1} warmer than during all-weather conditions (Figure 3.11a). We note however that the spread in the data is relatively large and we are reluctant to generalize this finding. Nevertheless, this exercise suggests that for our study area an additional uncertainty of ~0.03 K yr^{-1} is associated for comparison between clear-sky and all-weather conditions.

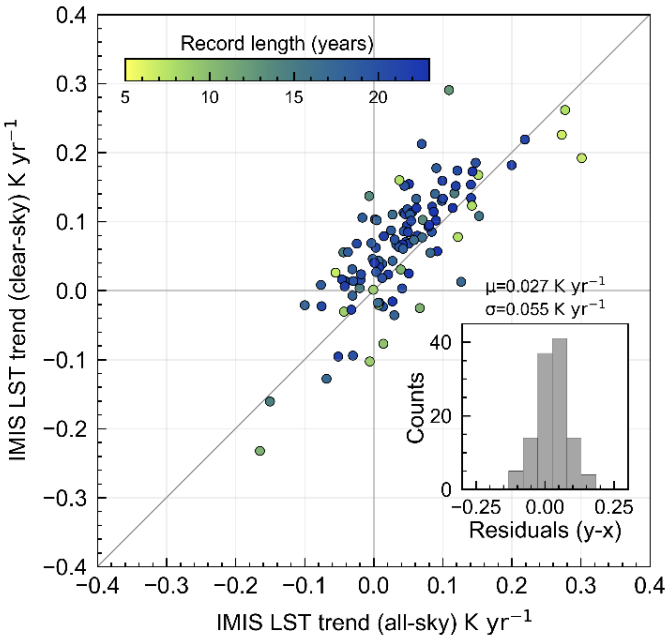

Figure 3.11. Relationship between IMIS land surface temperature (LST) trends during clear-sky and during all-weather conditions. LST data were interpolated at Landsat overpass times.

3.4.3 LST trend bias due to changing acquisition times

Our analysis of changes in IMIS LST during 9:29 h and 10:16 h UTC (Figure 3.8) and the spatial patterns of Landsat-derived LST trends with slope and aspect (Figure 3.9) suggest the existence of an LST trend bias due to changing acquisition times. A linear fit of the acquisition times of all three sensors together does obviously not cover all the individual variations in orbit position. However, the close similarity of the slope and aspect dependency in LST trends and ΔSin suggests that this approach appears to recover the first-order bias reasonably well. The dominant process that influences diurnal variations in LST during clear-sky conditions is the incoming solar radiation (Ghausi et al., 2023). Surfaces that are exposed to direct solar radiation receive particularly high amounts of energy and are thus prone to heating up quickly during the morning hours, especially during the summer months. The additional radiation flux received during the 47-minute time window peaks for surfaces that are oriented orthogonal to the sun position, at an aspect value of approximately

130°, whereas the LST trend and ΔSin peaks at approximately 75° and 255° respectively (Figure 3.9a, b). Instead, our results suggest that, rather than the total amount of energy received, the spatial pattern in LST trend is more strongly controlled by the relative changes in direct solar radiation (ΔSin) during the 47-minute time window, with positive and negative peaks at approximately westerly- and easterly-exposed surfaces, respectively. As a result, the greatest temperature changes occur where surfaces have an orientation that results in a switch between sun-exposure and shadow during the 47-minute time window. Observed differences in the slope-aspect dependence of ΔSin and LST trends (Figure 3.9 a, b) are probably related to actual LST trends that are unrelated to slope and aspect.

Possibly the simplest way to deal with the LST trend bias due to changing acquisition times would be to choose an observation time period in which the orbital drift was minimal, such as 1998-2018, or by neglecting Landsat 5 data altogether and Landsat 7 after 2018 (Figure 3.3). We tested this shorter time period (Figure B 2-4) and obtained LST trend values that were considerably noisier and more strongly affected by artefacts seemingly related to the number of observations (see section 3.4.1). We attribute this lower signal-to-noise ratio to the shorter observation time period, which also happened to be a limiting factor in our comparison with IMIS-derived trend values (Figure 3.5). Previous studies concerned with the removal of the influence of orbital satellite drift on LST data – mostly for NOAA-AVHRR – employed different techniques (e.g., Julien and Sobrino, 2012) that are, however, difficult to implement for Landsat, due to substantially fewer observations and more heterogeneous terrain. In addition, correcting each observation to a consistent time before fitting Eq. 3.2 is prone to unquantified errors and spurious trends (Julien and Sobrino, 2012), and difficult to implement in GEE. We thus tested another possible approach, which is to estimate the LST trend bias after the fitting, based on the strong observed terrain influence (Figure 3.9). This approach is probably less accurate as it neglects potential influences of different ground surface materials, but it is easier to implement. To do so, we first smoothed the map of mean ΔSin for slope and aspect using local linear regression and normalized the values by the standard score. We then scaled the normalized model to approximate the observed LST trend pattern as a function of slope and aspect by least squares regression. Finally, we used the mean amount of surface warming (0.045 Kyr^{-1}) within the 47-minutes time window for flat and gentle sloping terrain from the IMIS stations (Figure 3.8) to align the model data for slope angles less than 10° (Figure 3.12).

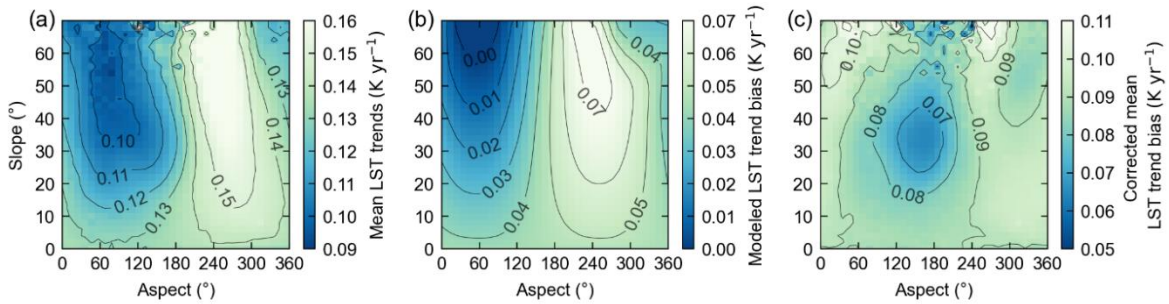

Figure 3.12. Mean LST trends (a), modeled LST trend bias (b) and corrected mean LST trends (c) for 2° slope and 10° aspect angles.

The modeled LST trend bias ranges between approximately 0 and 0.07 Kyr^{-1}, depending on slope and aspect. After removing the estimated bias, the remaining LST trends (Figure 3.12c) still show some residual pattern that follows the topography, with about 0.02 Kyr^{-1} lower trend values centered on ~160° aspect and ~35° slope. The slope-aspect position of this residual LST trend feature is similar to the position of the highest Sin values in Figure 3.9a & b. If there would be an additional influence of the additional Sin, received during the 47-minutes time period, we would expect LST trend values to be higher on surfaces approximately orthogonal to the sun vector, not lower, as suggested by the observations. Therefore, it presently remains unclear, whether the residual LST trend feature is due to the LST trend bias and an inadequate correction, or possibly related to other processes. Applying the LST trend bias correction to the LST trends (Figure 3.13) derived from GEE results in overall lower trend values and less spatial differences in LST trends with respect to aspect. Insignificant ($p>0.05$) LST trends, determined by a t-test, were masked out from the map. For all of Switzerland, the spatially-averaged ($\pm 1\sigma$) Landsat-derived clear-sky LST trend for the time period 1984-2022, is 0.1 ± 0.05 K yr^{-1}. Across the Swiss Alps LST trend values mostly range from 0.07 - 0.09 Kyr^{-1}, with higher trend values in populated valley bottoms, like the Rhone Valley in southern Switzerland, and lower trend values over vegetated hillslopes at higher elevations. Further spatial variations that are still present after the bias correction appear to be related to differences as well as changes in land cover types (such as glacier retreat, see Figure 3.7d) and warrant further detailed inspection, which is beyond the scope of this study.

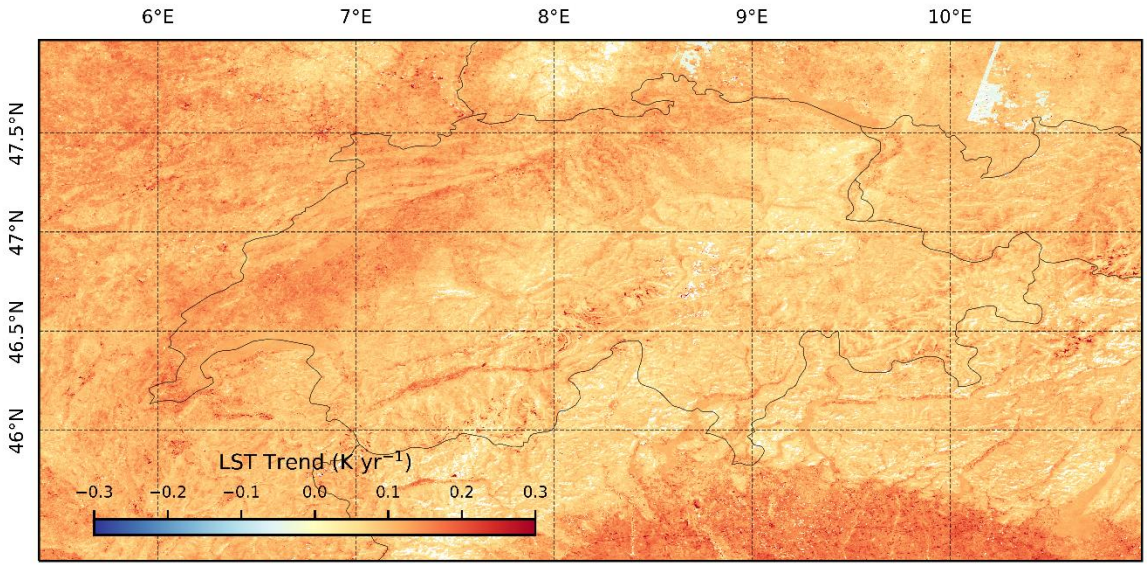

Figure 3.13. Corrected land surface temperature (LST) trends of the Swiss Alps. Significance was estimated using a t-test and only significant ($p < 0.05$) LST trends are shown in the map.

3.4.4 Prospects for studying changes of the cryosphere

Based on the corrected LST trend map, the spatially-averaged (±1σ) Landsat-derived clear-sky LST trend for all of Switzerland and for the time period 1984-2022, is 0.1 ± 0.05 K yr^{-1}. Insignificant ($p>0.05$) LST trends, determined by a t-test, were masked out and not considered. Most LST trend values range from 0.07 to 0.09 K yr^{-1}, with higher trends in populated valley bottoms like the Rhone Valley and lower trends over vegetated hillslopes at higher elevations (Figure 3.7). A detailed analysis of LST trend variations with respect to different land cover types and properties as well as their change is beyond the scope of this study. However, we here briefly present examples of how changes in the mountain cryosphere map into spatial patterns of LST trends at high spatial resolution. For instance, the rapid changes of mountain glaciers correlate well with patterns observed in the LST trends. Figure 3.14 shows as an example the Unteraar Glacier, where by far the highest LST trends occur along the glacier margin due to ice retreat and exposure of bedrock. Additionally, high LST trends are associated with the expansion of supraglacial debris, which is well shown on the southern branch of the Unteraar Glacier, and the disappearance of clean ice in the lower few kilometers of the glacier. In contrast, LST trends are lower in magnitude and spatially more homogenous in the accumulation zone, which experiences minimal changes in surface type.

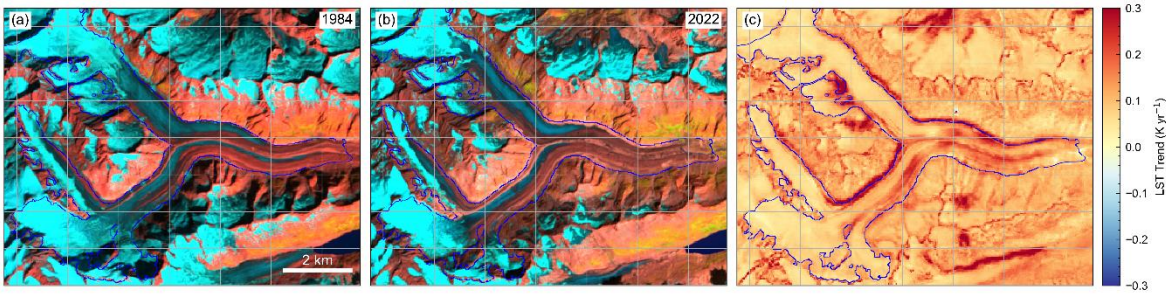

Figure 3.14. Changes of the Unteraar Glacier, Switzerland, evidenced by late summer Landsat scenes from (a) 1984 and (b) 2022, and by (c) land surface temperature (LST) trends. The satellite images show false color composites using the shortwave infrared 1, near infrared and red bands as red, green and blue channels. The blue line in all panels indicates the outline of the Unteraar Glacier based on the Randolph Glacier Inventory (RGI Consortium, 2017).

How changes in snow cover influence LST trends would require a detailed analysis with respect to snow extent, duration, depth and seasonality, which is beyond the scope of this study. However, in order to assess the first order sensitivity of LST trends to potential changes in snow cover, we spatially averaged LST trends for 100 m elevation bins and 1 °C MALST bins across the study area (Figure 3.1), excluding glaciers and glacier retreat zones (see section 3.2.4). Based on a previous global scale study of air temperatures we expect the highest positive temperature trends at altitudes where the MALST is between -10 and +5 °C, due to reduced snow cover and increased absorption of solar radiation (Pepin & Lundquist, 2008). Observed mean LST trends at elevations where MALST is between -10 °C and 0 °C are among the highest trend values, consistent with an influence of snow cover on LST trends (Figure 3.15). In fact, LST trend magnitudes display a systematic pattern with MALST and elevation that merit more detailed examination. We note that MALST differences of up to ~20 K at similar elevation, are easily explained by different aspects, that is, exposure to the sun (see Figure 3.7a), which may coincide with different long-term trends in snow cover duration. Although dominantly negative mean annual snow depth trends, derived from the IMIS stations by linear regression of annual mean snow depths further supports the effect of snow decline on LST trends, we did not find a clear correlation between LST trends and mean annual snow depth trends (Figure 3.15b). In addition, we do observe mostly positive trends in the number of snow-free days per year (Figure 3.15c), and these trends appear to increase in elevation. It is reasonable to assume that LST trends are higher where changes in snow cover are associated with more snow-free days, and that LST trends are likely smaller where snow depth declines but the surface remains nevertheless mostly snow covered, similar as in glacier accumulation zones. However, a clear correlation between trends in the number of snow free days and LST are not obvious, which could be related to the rather short record length of the IMIS stations and significant year-to-year variability in snow depth and cover.

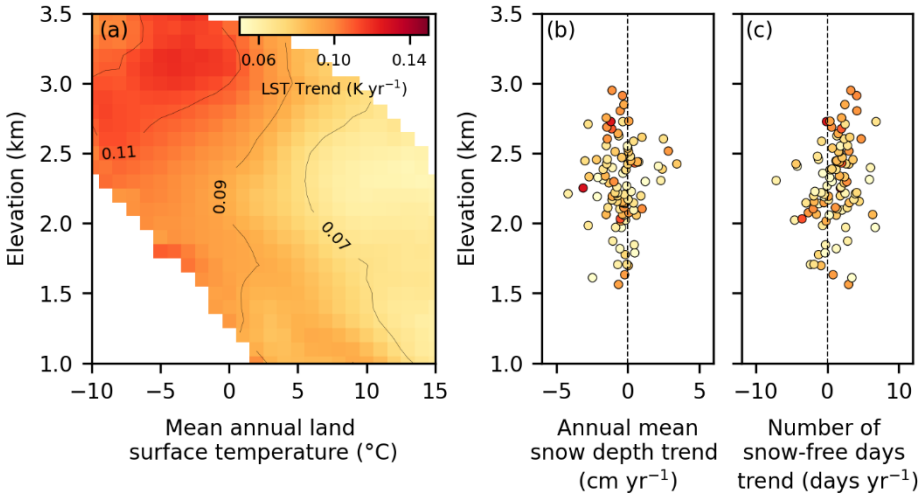

Figure 3.15. Relationship between (a) mean land surface temperature (LST) trends for 100 m elevation bins and 1 °C mean annual land surface temperature (MALST) bins, (b) annual mean snow depth trends and (c) trend in number of annual snow-free days at the IMIS stations with more than 10 years record length.

3.5 Conclusions

Our study has shown that Landsat-derived Land Surface Temperature (LST) since 1984 offer opportunities to study the spatial variability of LST in complex topography at high spatial resolution. Our comparison with ground observations from the IMIS network provides confidence in the remote sensing derived LST data and LST trends, despite challenges due to differences in spatial resolution. The analysis of Landsat C2 LST time series, using harmonic regression including a linear component, exploits the periodic nature of the intra-annual LST variation and yields maps of the mean annual LST (MALST), the annual amplitude, the timing of the harmonic oscillation (phase), and the long-term LST trend. We observe reasonable spatial patterns with elevation, slope and aspect that allow identifying the influence of surface orientation or type (e.g., glacier surfaces) on annual LST variations. However, all LST time series components (i.e., MALST, amplitude, phase, trend) presented in this study are based on LST at around ~10 h UTC and thus must be interpreted accordingly. In principle, the Landsat archive provides a sufficiently long time series to obtain LST trends, as shown from our comparison with IMIS LST data. LST trend values obtained from Landsat and the IMIS network converge for record lengths >15 years, whereas shorter records exhibit considerably more noise. However, our analysis of the slope-aspect dependence of LST trends strongly suggests that trend values are biased due to the long-term orbit changes that cause spurious LST trends. As orbit variations are not uniform with time and sensor, a temporal coherence correction is challenging. Assuming a long-term linear change in acquisition time, we have shown that the change in incident solar radiation can explain, at least in large parts, the spatial slope-aspect patterns of Landsat derived ‘apparent’ LST trends. By modeling and removing the LST trend bias due to

changing acquisition time, we obtain a spatially-averaged (±1σ) Landsat-derived clear-sky LST trend for the time period 1984-2022 of 0.1 ± 0.05 K yr^{-1}. The corrected LST trends respond to changes in the mountain cryosphere such as glacier retreat and debris cover evolution, snow decline and can potentially contribute to an improved prediction of permafrost temperatures, as surface temperatures propagate into greater depth. Further analysis is needed to disentangle the effect of land cover and land cover changes on the observed LST trends.

4 Landsat-derived land surface temperature trends and land cover changes in the European Alps

Deniz Tobias Gök[1], Dirk Scherler[1,2], Hendrick Wulf[3]

[1] GFZ German Research Centre for Geosciences; D-14473 Potsdam, Germany.
[2] Institute of Geographical Sciences, Freie Universität Berlin; D-14195 Berlin, Germany.
[3] Remote Sensing Laboratories, University of Zurich; CH-8057 Zurich, Switzerland.

Prepared for submission.

Abstract

High mountain areas are highly sensitive to climate change and respond to increasing atmospheric temperatures by extensive degradation of the mountain cryosphere, which includes snow cover, glaciers, and permafrost. These processes are related to changes in land surface temperature (LST) and can affect hillslope stability, ecology, and societies, making their monitoring and detection at large spatial scales crucial for mitigation efforts. Landsat-derived high-resolution land surface temperature (LST) time series allows the derivation of long-term LST trends over large spatial scales that reflect climate change and surface processes. In this study, we derived Landsat LST trends of the European Alps (1984-2022), corrected for the LST trend bias induced by changing acquisition times. We used binary masks derived from published datasets to assess the impact of land cover type and specific land cover changes on LST trends. Our findings reveal positive LST trends across the European Alps, with a spatial mean of 0.09 K yr^{-1}. However, LST trends vary significantly across different land cover types and land cover changes. For instance, the highest LST trends were observed for urbanised area while the lowest LST trends were found in area of forrest gain. The timing of land cover changes, such as deforestation, also influences LST trends. Factors such as the uncertainties in land cover or land cover change masks, exposition or elevation contribute to the relatively large variability in derived LST trends. Relatively homogenous surfaces like water and upper glacier zones exhibit less variability. We observe significant altitudinal differences in LST trends that we relate to changes in snow and ice cover. Regions of significant summer snow cover loss, show LST trends that gradually increase with elevation. This has implications for permafrost research, as decreasing snow cover amplifies LST trends, propagates into the depths and increases permafrost temperatures. Despite relatively large root mean square error (RMSE) values ranging from 4 K to 6.1 K, a simple harmonic model incorporating a linear trend effectively captures the influence of land cover and land cover changes on LST trends.

4.1 Introduction

Global warming affects various environments in mountainous landscapes as glaciers retreat, snow cover decreases and permafrost thaws (Beniston et al., 2018; Hock et al., 2019; Biskaborn et al., 2019). Since the 1980s, the average air temperatures in the European Alps (Figure 4.1) have increased by 0.05 K yr^{-1} (Nigrelli & Chiarle, 2023) and seasonal snow cover extent, duration, and thickness have decreased remarkably since then (Klein et al., 2016; Marty et al., 2017; Matiu et al., 2021). Observed environmental changes include increased rockfall activity (Harris et al., 2009; Huggel et al., 2012; Kos et al., 2016; Grämiger et al., 2018; Hartmeyer et al., 2020), shifts in plant species distributions to higher elevations, and alterations in downstream discharge patterns (Huss et al., 2017; Adler et al., 2022), all of which have direct implications for human livelihoods and the economy (Huggel, 2009; Deline et al., 2009; Keiler et al., 2010; Hock et al., 2019). While warming is driven by air temperature, many processes in alpine environments are driven by ground temperature (Haberkorn et al., 2021), which depends on air temperature and surface conditions (Jin and Dickson, 2010). Snow cover, for example, shields the ground from warm atmospheric temperatures during summer (Smith et al., 2022), and any change in snow cover affects the heat flux into the ground. Therefore, temporal changes in ground temperatures are controlled by atmospheric warming and changes in surface properties. However, direct observations of how different ground properties or land cover (LC) types and their changes affect ground warming are rare (Zhou and Wang, 2010; Fu and Weng, 2016; Muro et al., 2018).

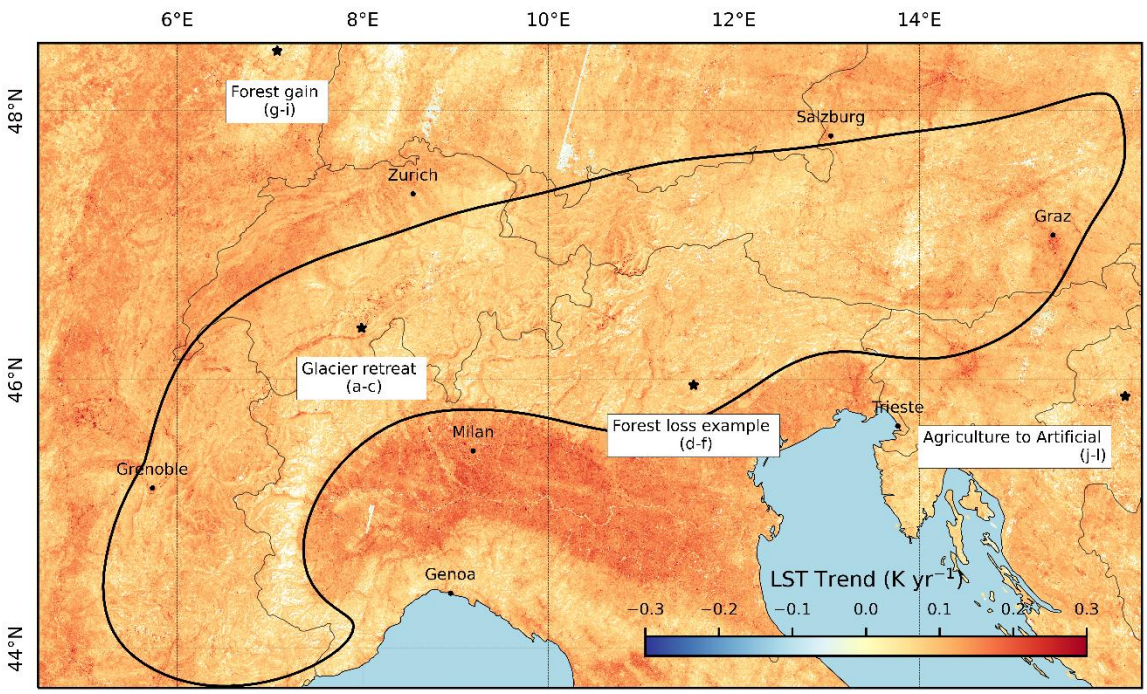

Figure 4.1: Land surface temperature (LST) trends with marked study area of the European Alps (black solid line) and example locations of selected land cover changes shown in Figure 2. Insignificant LST trends are masked out (p-values<0.005)

The land surface is the interface between the air and the ground, and quantifying temporal changes, or trends, in land surface temperature (LST) can provide valuable constraints on the evolution of ground temperatures. LST is imaged globally by various satellite systems (Li et al., 2023). However, previous studies of LST trends have mainly focused on the Moderate Resolution Imaging Spectroradiometer (MODIS) and the Advanced Very High-Resolution Radiometer (AVHRR) data because of their high frequency and relatively long time series (Lui et al., 2019; Ma et al., 2020; Waring et al.,2023). However, steep altitudinal temperature gradients of LST and ground properties in mountainous landscapes pose challenges to quantifying LST trends with both systems due to their relatively low spatial resolution of ~1 km. In addition, the large swath width of MODIS introduces a thermal anisotropy bias (Ermida et al., 2017) that varies with topography. For AVHRR, harmonizing LST data from 14 satellite platforms involves considerable challenges due to orbital drift effects (Dech et al., 2021; Julien and Sobrino, 2022; Ma et al., 2020).

The Landsat satellites have been providing long records of LST observations in narrow swaths with a resolution of 60-120 m since the early1980s, but with an interval of 16 days per sensor, depending on cloud cover (Weng and Fu, 2014). Additionally, while Landsat Collection 2 offers optimized LST data for time series analysis across all sensors (Malakar et al., 2023), an orbital drift of certain satellites has resulted in shifts in overpass times by nearly one hour over the past 40 years (Zhang and Roy, 2016). In a recent study from Switzerland, Gök et al. (2024) reported good agreement in LST and its trends compared to ground LST data from high-altitude stations, and they

provided an approach to correct for long-term orbital drift effects. The high-resolution maps reveal steep gradients in LST trends that are clearly related to changes in land cover, such as glacier retreat, forest cover loss and gain, or urbanization (Figure 4.2). Because different land cover types exhibit different energy exchanges with the atmosphere, LST trends are expected to vary with both land cover and land cover changes, irrespective of their natural and anthropogenic origin (Hulley et al., 2019).

Here, we present an analysis of Landsat-derived LST trends across the European Alps (Figure 4.1), focusing on the influence of surface conditions. Specifically, we examined magnitudes of LST trends in selected categories of land cover types and commonly observed changes between land cover types. Because changes in land cover are often abrupt rather than continuous, whereas LST trends are generally modelled linearly, we also studied the influence of the timing of land cover change on LST trends.

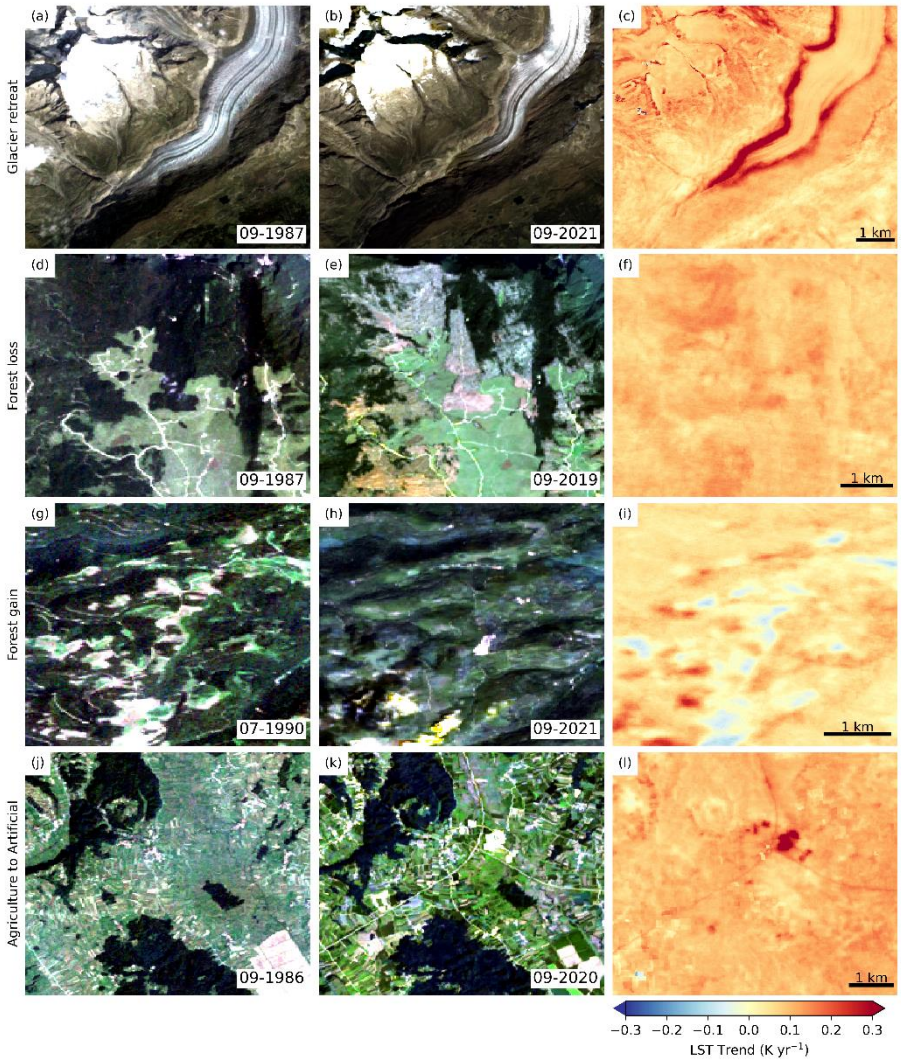

Figure 4.2: Selected Landsat scenes of land cover changes (left and middle column) and corresponding land surface temperature trends (right column) from the time period 1984-2022 (Gök

et al., 2024). Examples from the European Alps and surrounding areas show (a-c) glacier retreat, (d-f) forest loss, (g-i) forest gain and (j-l) agricultural use to artificial surfaces.

4.2 Materials and Methods

4.2.1 Landsat-derived LST trends

We determined LST trends from combined Landsat TM, ETM+ and TIRS across the European Alps using Google Earth Engine (GEE), and employing the procedure described in detail by Gök et al. (2024) (Figure 4.1). LST trends were calculated by fitting a harmonic model, including a linear trend component, to 38.5 years of Landsat Collection 2 (C2) LST data:

$$LST_t = \beta_0 + \beta_1 t + \beta_2 cos(2\pi\omega t) + \beta_3 sin(2\pi\omega t) \quad \text{Eq. 4.1,}$$

where β_0 is the mean annual LST (K), β_1 is the slope (K yr^{-1}) of the linear trend, β_2 and β_3 are the coefficients that are equal to $Acos(\varphi)$ and $Asin(\varphi)$, with A the amplitude (K) and φ is the phase, t is the time in years, and ω is the frequency (equal to one for one cycle per year). The harmonic model accounts for the cyclic inter-annual variability of LST and ensures that the linear trends yield robust results.

Before applying Eq. 4.1 to the Landsat LST data, we filtered out cloud-contaminated pixels and duplicate observations resulting from along-track overlapping scenes. Although the Landsat C2 cloud flag in the Pixel Quality Assessment Band detects most cloudy pixels, some remain unrecognized over bright surfaces like snow and ice. We implemented an additional cloud filter in GEE by obtaining a first estimate of the parameters $\beta_{0\text{-}3}$ by fitting Eq. 4.1 to the LST data. We then uploaded these parameters as images to GEE to estimate the LST and then applied a threshold of +/- 30 K to the residuals between the estimated and observed LST.

Changes in the orbits of the Landsat satellites influence the LST observations and introduce a bias in the derived trends (Gök et al., 2024). Linear regression of daily acquisition times between 1984 and 2022 suggests a 47-minute shift over the entire time period, influencing incident solar radiation. High temporal resolution LST data from alpine weather stations indicate that this delay induces a warming trend of 0.045 K yr^{-1} over relatively flat terrain. However, higher and lower mean warming rates can be observed on steeper terrain as a function of terrain slope and aspect. This terrain-dependent LST trend bias can be reasonably well recovered by modelling relative changes in direct solar radiation over the 47-minute window (Gök et al., 2024). Although this approach does not account for all variations in orbit position, it captures a significant portion of the LST trend bias (Gök et al., 2024). From the corrected LST trend map, we masked out all pixels with non-significant LST trends based on a student's test ($p<0.05$).

4.2.2 Analysis

We assess LST trend magnitudes across different land cover categories by comparing trends among distinct land covers and common land cover changes using binary masks. The masks were generated from multiple auxiliary datasets to delineate areas with temporal persistent land cover types and those undergoing selected transitions during the study period (Table 4.1). These masks were then applied to extract LST trend values and distributions shown as boxplots with key statistical metrics. Most land cover changes involve abrupt transitions such as forest loss or the conversion from agriculture to artificial surfaces in urbanised areas. It is clear that such abrupt changes are not adequately captured by the linear trend model (Eq. 4.1) and are expected to result in relatively high root mean square error (RMSE) values. We thus also evaluated the performance of the harmonic model to fit the data by analyzing the RMSE for each LC and LC change category.

Table 4.1: Summary characteristics of land cover and land cover change categories in the European Alps

Land cover/ land cover change category*	Area (km^2)	Mean LST trend ($K\ yr^{-1}$)	25th percentile elevation (m)	50th percentile elevation (m)	75th percentile elevation (m)
Upper glacier zones	238	0.07	3199	3367	3570
Persistent snow cover	256	0.07	2932	3107	3277
Forest gain	598	0.07	703	1001	1259
Grassland	28108	0.08	1486	1827	2082
Forest cover	35288	0.08	761	1042	1319
Lower glacier zones	705	0.09	2672	2856	3014
Forest to Agriculture	537	0.09	674	908	1155
Bare rock	12734	0.1	2330	2580	2784
Agriculture	34051	0.1	399	609	875
Forest to Artificial	149	0.11	569	990	1391
Summer snow (decreasing)	1329	0.11	2387	2583	2762
Lakes	1973	0.11	193	368	423
Forest loss	3522	0.12	773	1059	1342
Artificial	7293	0.13	306	446	640
Agriculture to Artificial	602	0.13	324	487	711
Glacier retreat zones	74	0.18	2333	2566	2741

*Categories are sorted by mean LST trend magnitudes

4.2.3 CORINE Land Cover Datasets

The “Coordination of Information on the Environment” (CORINE) land cover datasets provide an inventory of thematic classes of land cover and land use (LC) across Europe at 100 m spatial resolution (Büttner, 2014). We used the LC datasets from 2000, 2006, 2012 and 2018, as they provide complete coverage across the entire study area. The 5 CORINE LC classes comprise a total of over 44 subclasses. To simplify and focus on large-scale LST trend magnitudes, we aggregated certain subclasses (Table 4.1) into the broader categories: (1) artificial surfaces, (2) agricultural surfaces, (3) forests, (4) grasslands, and (5) bare rock surfaces. We generated binary masks for each category and time and distinguished between areas of persistent LC and changing LC. We defined persistent LC by unchanged LC categories in all four years. For changing LC, we focused on shifts from (1) agricultural to artificial, (2) forest to artificial, and (3) forest to agricultural use. Transitions were determined by the first LC type present in 2000 and 2006 and the second in 2012 and 2018. For these categories, the change from one LC category to the other thus occurred between 2006 and 2012, which is in the third quarter of the time period for which LST trends were obtained. Finally, the created binary masks were resampled to match Landsat’s spatial resolution.

4.2.4 Forest cover

In addition to the CORINE land cover category "forest," we incorporated the updated Global Forest Change (GFC) dataset (Hansen et al., 2013) to delineate tree cover and tree cover change. This dataset, derived from Landsat imagery time series analysis, offers global forest extent and change information. It includes canopy cover data for the year 2000, represented as canopy closure for all vegetation taller than 5m, a binary mask indicating forest loss from 2000 to 2023, another binary mask showing forest gain (the inverse of loss), and the year of forest loss events from 2000 to 2023. Forest gain data covers the period from 2000 to 2012 (Global Forest Change Update, 2023). "Forest loss" and "forest gain" here denote changes in tree cover rather than land use. Given our focus on the influence of land cover change on LST trends, we refined the forest loss mask by excluding pixels experiencing forest loss events after 2019 (Figure 4.5). Additionally, we generated a binary mask for "persistent" forest cover, defined by canopy closure exceeding 85% in 2000 and no forest loss events during the study period.

4.2.5 Snow cover

Snow cover modifies the heat transfer from the atmosphere into the ground, affecting land surface temperature. Since snow cover decreases in extent, thickness and duration, long-term LST trends are expected to increase accordingly. To assess the impact of snow cover and its changes on LST trends, we created binary masks of two key areas: (1) regions experiencing significant declines in summer snow cover and (2) areas characterized by near year-round snow cover without glaciation

that we term ‘persistent’ snow cover. We used published trends of summer snow cover in non-glaciated, non-forest regions of the European Alps (Rumpf et al., 2022). These trends were derived using the Kendall’s rank correlation coefficient on Landsat-derived normalized difference snow index data, with a threshold of 0.4. Negative values (-1 to 0) indicate decreasing snow cover, while positive values (0 to 1) denote increasing snow cover. Our binary mask for summer snow decline focuses on significant (p-value<0.0001) negative trends.

For the second binary mask, we used Landsat-derived annual snow cover frequency of the European Alps between 1984 and 2022. The snow cover frequency represents the ratio of all classified snow cover observations to all cloud-free observations. The snow cover classification is based on a decision tree that distinguishes between snow, clouds, vegetation, water, and soil/urban (Wulf et al., 2020). In particular, it considers snow in forests and snow in shadows, which is a common feature in alpine terrain. As regions with full-year snow cover are usually glaciated, we focused on non-glaciated pixels with an annual snow cover frequency greater than 85%.

4.2.6 Glaciers

Glaciers are dynamic features in high mountain landscapes, with distinct surface cover differences that may lead to varying LST trends. To account for these differences, we categorized glaciers into three zones: (1) high, (2) low, and (3) retreat. The high and low zones are meant to approximate the accumulation and ablation areas, which are difficult to delineate in detail due to missing information. Based on the Randolph Glacier Inventory (RGI) version 7 dataset (RGI v.7.0, 2023), we defined these zones for glaciers larger than 1 km^2, using surface elevations from a 10-meter resolution digital elevation model (DEM; Copernicus DEM, 2022). For each analysed glacier, we defined binary masks for both the high and low zones based on the 100^{th}-75^{th} and 50^{th}-5^{th} elevation percentiles, respectively. To account for glacier shrinkage since the generation of the outline and erroneous pixels in the rasterised masks, we applied binary pixel erosion with a squared 4-pixel kernel from the Python scikit-image library (Van der Walt et al., 2014). Glacier retreat zones were identified by generating binary masks for regions below the 5^{th} elevation percentile for each glacier. These masks were then expanded using pixel dilation and subtracted from the unmodified mask. Figure 4.3 shows an example of the approximated glacier regions at Great Aletsch Glacier in Switzerland.

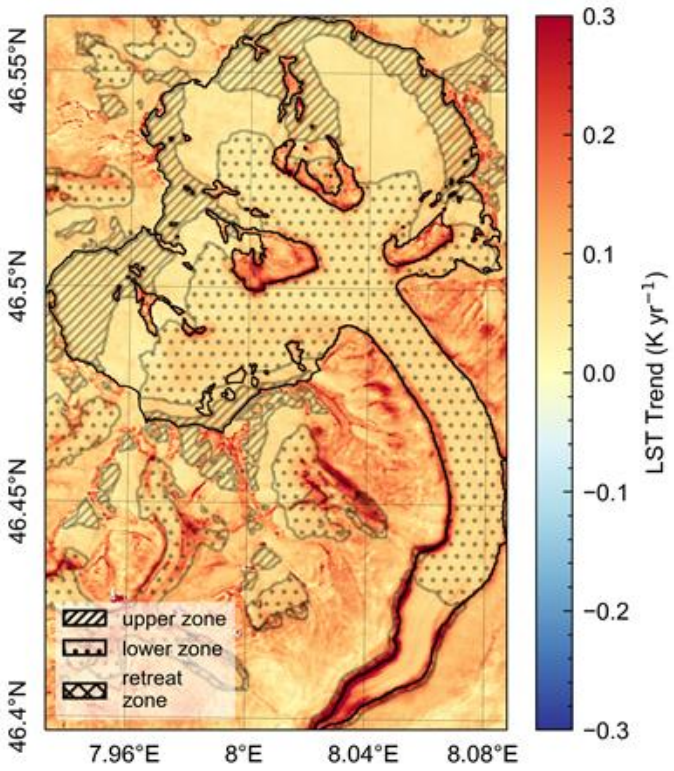

Figure 4.3: Land surface temperature (LST) trends of Great Aletsch glacier in the Swiss Alps. Indicated are the glacier outline from the Randolph Glacier Inventory (RGI) version 7 and the three analysed zones (upper, lower, and retreat). Binary masks of these glacier zones were computed for each glacier in the European Alps.

4.2.7 Water surfaces

Water surface temperatures are less variable than land surface temperatures due to the higher heat capacity of water and the mixing of surface with deeper water. Therefore, long-term trends of water surface temperatures are often used as climate change indicators (e.g., Hansen et al., 2010). As water surfaces are often large and homogenous, with well-known emissivity, they lend themselves to satellite-derived sea or lake surface temperature monitoring and inter-comparison across sensors with different spatial resolutions (García, 2020). We created binary masks for both sea and lake surfaces. The sea surface area within our study region is limited to the northern part of the Adriatic and Ligurian Seas and was delineated using the DEM. The lake mask was derived from the HydroLakes database (Messager et al., 2016), excluding lakes smaller than one square kilometre in area. To address potential inaccuracies in delineation or lake area changes, we excluded shoreline regions using pixel erosion with a 4x4 pixel kernel.

4.3 Results

The mean LST trend averaged across all land cover categories in the European Alps is 0.09 K yr^{-1} with a standard deviation of 0.04 K yr^{-1} (black horizontal lines in Figure 4.4). The mean LST

trends for the analysed persistent surfaces (Figure 4.4 a) range notably from 0.07 K yr^{-1} for the upper glacier zones to 0.13 K yr^{-1} for artificial surfaces. Most of these land cover types are normally distributed with varying spreads. The widest spreads are observed for artificial surfaces, agricultural surfaces, and lower glacier zones, while water surfaces have notably smaller variability (Figure C 2). Lower glacier zones, which approximate the ablation area of glaciers, exhibit skewness towards higher trend values, likely due to variations of seasonal snow cover and the influence of supraglacial debris cover on LST. The LST trend distributions of regions with persistent snow cover and the upper glacier zones show similar magnitudes and spreads, with some skewness observed in snow-covered regions, possibly due to occasional snow-free periods during the year.

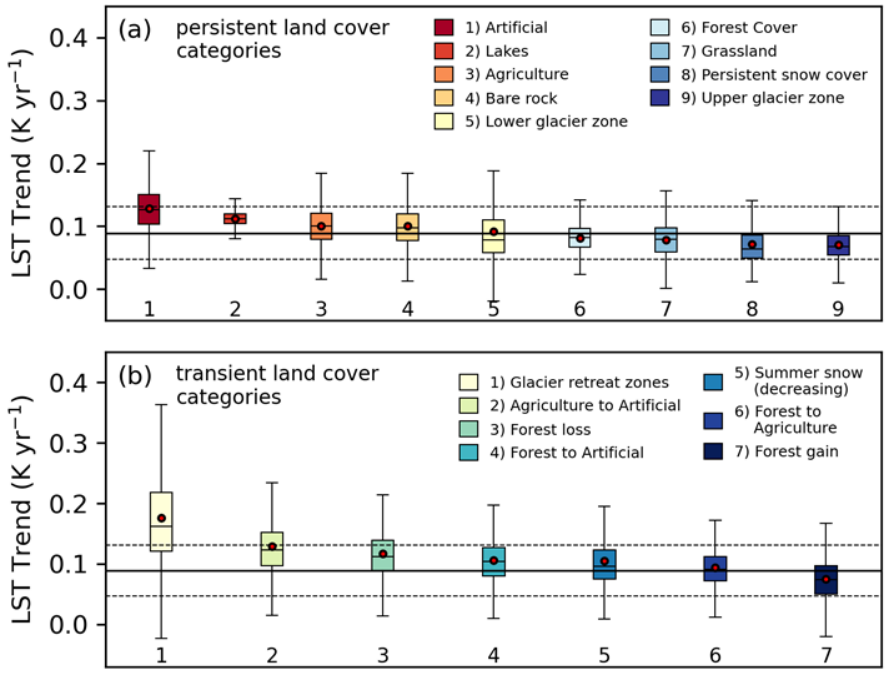

Figure 4.4: Distributions of land surface temperature (LST) trends for various land cover categories. Boxplots for (a) persistent surfaces and (b) transient surfaces show the mean (red dot), median (black line), interquartile range and minimum and maximum values, excluding outliers. The solid and dashed lines show mean and standard deviation of 0.09 ± 0.04 K yr-1 of LST trends averaged across the European Alps.

Most land cover changes lead to higher LST warming rates than the average trend we observe across the European Alps (Figure 4.4 b). The impact of these changes on LST trends depends on the magnitude of change in surface properties, such as emissivity and albedo (Figure 4.2), as well as the timing of these changes (Figure 4.5). The largest LST trends are observed at glacier margins where ice retreat exposes bedrock surfaces (Figure 4.3). The lowest warming rates are found in regions that experienced forest gain. In some cases, afforestation can even cause surface cooling (Figure 4.2 i), although this appears to be an exception. The trend values for transient surfaces are mostly normally distributed, except for glacier retreat zones and areas transitioning from forest cover to artificial surfaces, which are skewed towards higher LST trends.

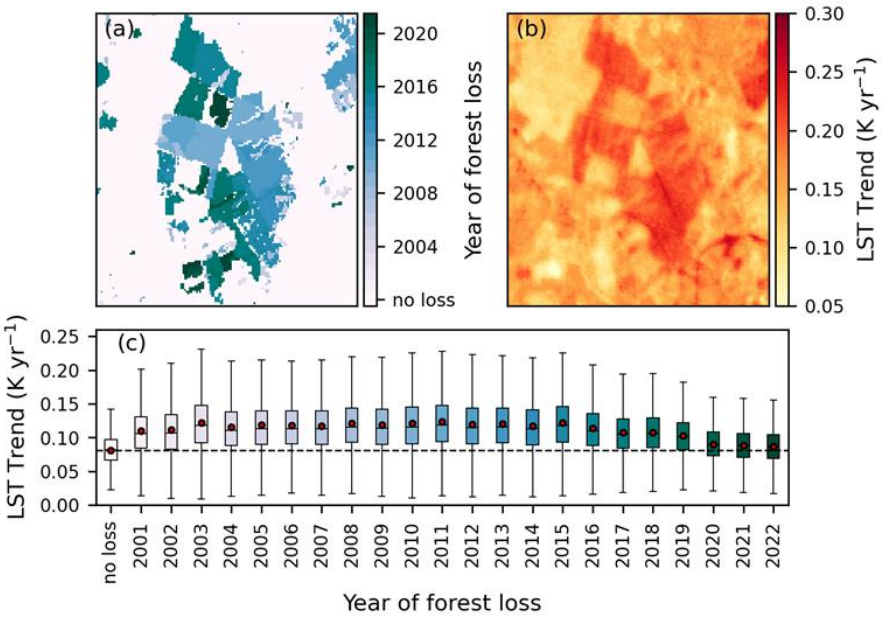

Figure 4.5: Influence of deforestation on land surface temperature (LST) trends at example site (47.50° N, 5.92° W). Deforestation timing (a) aligns with observed LST trends (b). Forest loss after 2019 has minimal LST impact. Boxplots (c) show LST trend values specific to regions experiencing forest loss across the European Alps.

The large variability in LST trends for persistent and transient land cover categories can be partly explained by variations in trends with elevation (Figure C 1). Mean LST trends for 100 m elevation bands and a minimum area of 5 km^2 show mixed results (Figure 4.6). At high elevations, above 2000 m, LST trends of bare rock surfaces vary with elevation, equally reflected by aggregated regions that experience significant summer snow loss (Figure 4.6). Lower glacier zones show an inverse pattern with higher LST trends at lower elevations, possibly related to the emergence of debris cover and/or overlap with the retreat zone. LST trends of upper glacier zones and persistently snow-covered regions that are not glaciated do not show such variability.

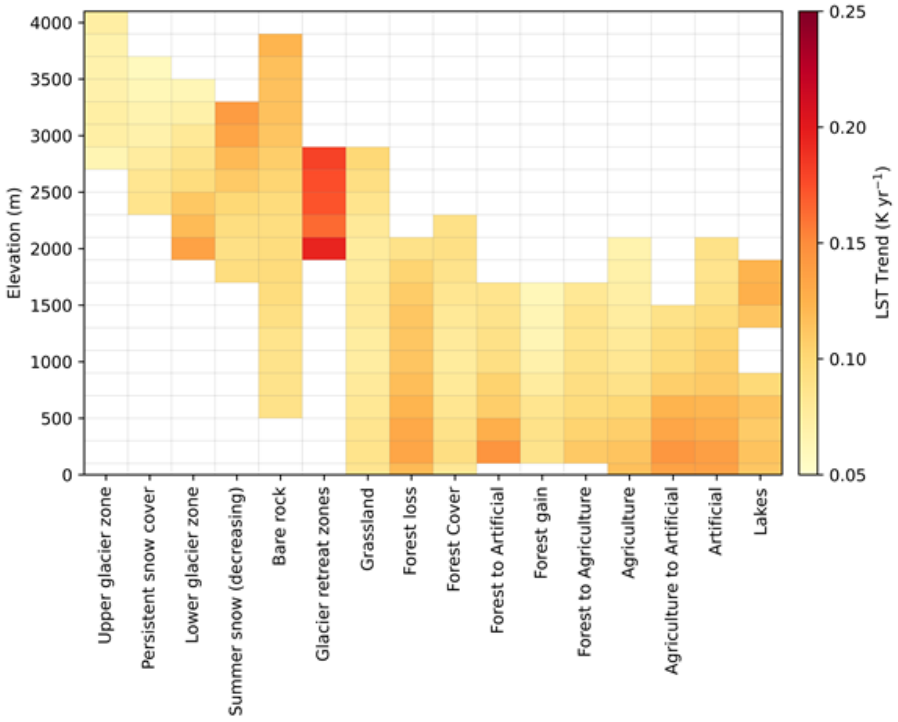

Figure 4.6: Mean land surface temperature trends (K yr^{-1}) across 100 m elevation bands for each land cover or land cover change category. Land cover category bins comprising areas less than 5 km^2 have been omitted.

At lower elevations, below 2000 m, LST trends show mixed elevational patterns. Grasslands, forest cover, and regions transitioning from forest to agricultural use are consistently warming with elevation at a rate of 0.08 to 0.09 K yr^{-1}. Artificial surfaces or regions that transition to artificial surfaces are warming faster at elevations below 800 m, but LST trends are not increasing gradually with elevation. Conversely, lake surface temperature trends are higher at elevations above 1000 m than at lower elevations.

Spatially averaged RMSE values for all land cover categories range from 3.5 K for lakes to 6.1 K for regions of summer snow decline (Figure 4.7). The variability in mean RMSE values across land cover categories differs between persistent and transient categories. The linearly-trending harmonic model performs better for water and persistently snow-covered or ice-covered surfaces than for other LC categories, although the standard deviation of the RMSE values within each category is relatively large. RMSE for most transient categories range around 5 K to 5.5 K, with the exception of regions experiencing significant summer snow decline. The harmonic model performs best for water and persistently snow-covered or ice-covered surfaces, compared to the other land cover categories.

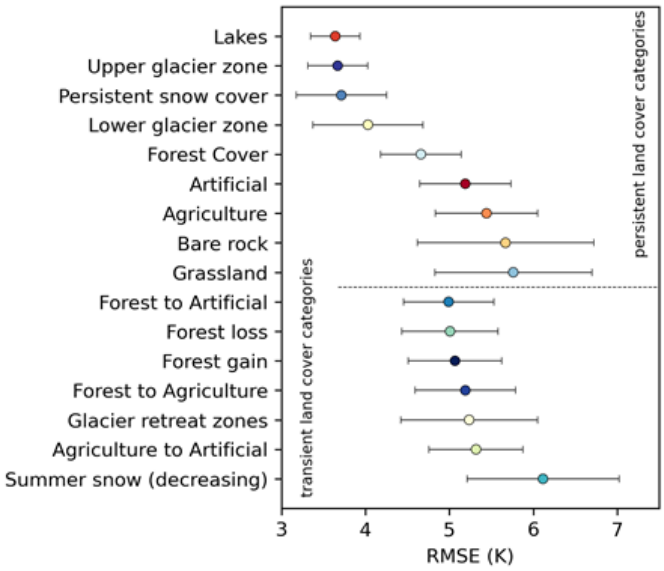

Figure 4.7: Mean and standard deviation of RMSE values of the harmonic model for persistent and transient land cover categories, averaged across the European Alps.

4.4 Discussion

The persistent (Figure 4.4 a) and transient (Figure 4.4 b) land cover categories both show significant deviations from the alpine-wide mean LST trend of 0.09 ± 0.04 K yr^{-1}, with variability influenced by elevation-dependent trends (Figure 4.6). While the persistent land cover categories are assumed to remain unchanged, transient land covers experienced gradual or abrupt alterations in surface properties, affecting the surface energy and water balance and thereby impacting the LST (Mauder et al., 2020). However, possible changes in the apparently "persistent" land cover categories may be hidden by inaccuracies or temporal inconsistencies in some of the land cover masks. For instance, undetected land cover changes before 2000 that would influence the LST trend are possible due to temporal limitations in the CORINE dataset. Also, the spatial resolution of 100 m may hide small-scale land cover changes. For instance, artificial surfaces, with a mean LST trend of 0.13 K yr^{-1}, could be affected by increased human activities, such as driving cars, and general urban densification that amplifies the urban heat island effect and impact LST trends (Guo et al., 2015; Levermore et al., 2018; Lui et al., 2022). Similarly, agricultural surfaces undergo changes in crop types over time, potentially leading to undetected alterations in surface properties, too.

The variability in LST trends among land cover categories (Figure 4.4) is partially attributed to variations in trends with elevation (Figure 4.6). The elevation dependency observed in bare rock surfaces is likely influenced by the gradual reduction in summer snow cover extent (Beaumet et al., 2021). This effect is further pronounced in regions above 1700 m that experience a significant loss of summer snow cover (Figure 4.6). Several studies have discussed the snow/ice albedo feedback and other mechanisms as possible causes for elevation-dependent warming (Pepin and Lundquist,

2008; Rangwalla and Miller, 2012; Ceppi et al., 2012; Mountain Research Initiative EDW Working Group, 2015). However, recent findings highlight that annual air temperature trends are independent of elevation (Nigrelli & Chiarle, 2023). For the Swiss Alps, Rottler et al. (2019) argued that the snow/ice albedo feedback has a small effect on air temperature warming rates compared to elevation differences of incoming solar radiation and weather patterns. However, these studies refer to air temperature trends, and our results for regions with declining summer snow clearly show that LST trends increase with elevation. Observed upward greening of the Alps (Rumpf et al., 2022) could further enhance these elevation differences in LST trends. In contrast, despite being at similar elevations, lower glacier zones show an inverse elevation-dependence pattern, with higher trend values observed at lower elevations. Many of these areas are glacier ablation zones, which are progressively covered by supraglacial debris (Fleischer et al., 2021; Scherler et al., 2018), potentially leading to higher LST trends.

There is no variability in mean LST trends with elevation for bare rock, grassland, and forest cover located below 2000 m. These land cover categories comprise large areas (Table 4.1) of relatively homogenous surface cover and show very similar LST trends around 0.08 K yr^{-1} (Figure 4.6). Conversely, lakes found at comparable elevations and also persistent through time show a higher mean LST trend of 0.11 K yr^{-1} with increased trends for lakes above 1000 m elevation (Figure C 3). This could be attributed to reduced freezing frequency and snow cover at high elevations, potentially leading to increasing LST trends (Christianson et al., 2021; Schneider et al., 2009). Upper glacier zones are most likely unaffected by decreasing snow cover or inaccuracies in land cover masks, and they tend to be spatially relatively homogeneous. Their LST trends show no relationship with elevation (Figure 4.6). Interestingly, sea surface temperature (SST) trends in the northern Mediterranean Sea (Figure C 2) are with 0.05 ± 0.2 K yr^{-1}, quite similar to LST trends of the upper glacier zone category (0.07 ± 0.03 K yr^{-1}), despite substantial differences in elevation.

Most of the selected land cover transitions have, on average, higher LST trends than the Alps-wide mean (Figure 4.4 b). Land cover changes are modifications of ground properties such as albedo, emissivity, surface roughness, heat capacity or thermal conductivity, directly influencing LST. Hence, the overall effect of land cover changes on LST trends depends on the magnitude of change in the physical properties of the previous and current land cover type. Most prominently, this can be observed at retreating glacier margins (Figure 4.2 c), where newly exposed sediment or bedrock leads to exceptionally high LST trends. However, these regions cover a very small area (Table 4.1) with a presumably small impact on the regional climate. LST trends of land cover transitions towards artificial surfaces are comparable to those of persistent artificial surfaces in magnitude and elevational pattern (Figure 4.6). Assuming unchanged artificial surfaces, this suggests that the mechanisms driving high trends in urban areas prevail in the effect of land cover transition. Note that

all transient land cover categories are based on the CORINE dataset and that we only consider changes that occurred between 2006 and 2012.

Forest loss can lead to surface warming due to reduced evapotranspiration or to surface cooling due to increased albedo and, thereby, reduced absorption of solar radiation (Pielke et al., 2011; Perguini et al., 2017). We found that forest loss regions are warming at relatively high rates, with a mean LST trend of 0.12 K yr^{-1}. This aligns with previous studies reporting a positive surface warming effect following forest loss in mid-latitudes (Alkama and Cescatti, 2016; Prevedello et al., 2019). Our results further show that the magnitude of the LST trends depends on the timing of forest loss (Figure 4.5), with negligible effects of forest loss that occurred after 2019. This result is consistent with a positive step change in the LST time series that we fit with a linearly-trending harmonic model, where step changes near the end or beginning of the record have the smallest effect on the trend. In contrast, warming rates in areas of forest gain are amongst the lowest, with a mean LST trend of 0.07 K yr^{-1}. This highlights the significant role of vegetation in mitigating future regional surface warming (Li et al., 2023; Alkama et al., 2022).

We derived LST trends using a harmonic model that included a linear trend component. Previous comparison with LST trends derived from high-elevation ground stations has shown robust Landsat LST trends with a mean accuracy of -0.02 K yr^{-1}, despite large differences in measurement footprint (Gök et al., 2024). Comparison of LST trends across diverse land covers with trends derived from other satellite platforms is difficult due to different sensor characteristics, record length, spatial and temporal resolution, viewing angle and acquisition time (Guillevic et al., 2018). However, for large homogenous surfaces, such as the northern Adriatic and Ligurian Seas, some of the restrictions are minimized, and MODIS-derived mean SST trends of 0.04 - 0.06 K yr^{-1} (Sakalli, 2017; Pastor et al., 2019; García-Monteiro et al., 2022) compare well to our Landsat derived mean SST trend of 0.05 K yr^{-1}. The harmonic model with linear trend is a simple but effective approach to obtaining robust LST trends over large spatial scales and is compatible with the cloud computing platform Google Earth Engine (Gorelick et al., 2017). However, not all of the LST variability is captured by the model, resulting in relatively large mean RMSE values of 3 K to 6.1 K (Figure 4.7) across the examined persistent and transient land cover categories. The best model performance with a mean RMSE of 3-4 K was observed for water bodies and snow/ice surfaces, while the remaining categories range from 5 K to 6 K. Water bodies, with their large heat capacity, are less sensitive to local weather conditions, resulting in reduced susceptibility to surface temperature fluctuations and thus lower RMSE values. Also, snow and ice surfaces may respond less sensitively to local weather conditions with an additional contribution of the zero-curtain effect that could lead to lower RMSE values. The remaining persistent land cover categories respond quickly to short-term weather-related variations in LST and, therefore, lead to a large RMSE. Additionally, land cover changes may even cause amplitude and phase shift changes, which the harmonic model does not account for. In particular,

adjusted models would be beneficial to better capture abrupt land cover changes, such as regions of forest loss or glacier retreat. Recent methods, such as Continuous Change Detection and Classification, have been proposed to detect break points in time series data (Li et al., 2022). While these approaches are promising, resulting LST trends would necessarily be based on shorter record lengths, which introduces more noise (Gök et al., 2024) and makes the comparison more complicated.

4.5 Conclusions

We analyzed LST trends across the European Alps from 1984 to 2022, focusing on persistent and transient land cover categories and their elevational variability. Additionally, we examined the impact of land cover change timing on LST trends. We conclude the following:

1. LST trends in the European Alps are generally positive and vary significantly with land cover and land cover changes.
2. The common land cover changes we analyzed yielded mean LST trends above the alpine mean LST trend of 0.09 K yr^{-1}, except in areas of forest gain, which exhibited lower LST trends. Moreover, the timing of land cover changes influences the magnitude of mean LST trends for transient LC categories, with changes occurring after 2019 showing minimal impact.
3. Elevational differences in LST trends depend on the land cover category. Increasing LST trends with elevation were observed for regions above 2000 m that are subject to decreasing extent of snow and ice cover. These regions are particularly threatened by permafrost loss as LST warming trends propagate into depth.
4. High RMSE values of 4 K to 6.1 K for most LC categories indicate that the harmonic model is not able to capture the large short-term variability of LST. Water and ice surfaces, which respond less to short-term weather fluctuations, yielded considerably lower RMSE values of around 3 K.

Despite the low temporal resolution of Landsat LST, we show that a simple harmonic model can capture the impact of land cover and land cover changes on LST trends. The high spatial resolution and long record length of Landsat LST observations make it unique for high mountain applications. Snow cover decline allows amplified heating of the ground, which likely affects the thermal state of permafrost. Therefore, spatially distributed long-term LST trends contribute to developing mountain permafrost models and complement borehole-based permafrost monitoring.

5 Synthesis and conclusions

The main objective of this thesis was to **evaluate the potential and limitations of remotely sensed Land Surface Temperature (LST) for detecting and analysing glacial landscape dynamics**. As atmospheric temperatures rise, high mountain landscapes become increasingly dynamic, experiencing declining snow cover, retreating glaciers, and thawing permafrost. Increased rockfall activity and catastrophic slope failures at high elevations have been related to climate change (Stoffel et al., 2024), as thawing permafrost (Gruber and Haeberli, 2007; Deline et al., 2021) and deglaciation (Ballantyne et al., 2014; Wetterauer et al., 2022) contribute to the destabilisation of mountain hillslopes. Deposited onto glacier surfaces, mountain glaciers become increasingly covered by a layer of supraglacial debris (Fleischer et al., 2021; Scherler et al., 2018), which modifies their response to climate change (Scherler et al., 2011). Large-scale monitoring and analysis techniques are crucial as these landscape changes pose significant threats to communities in and near mountainous regions. They help to address recent threats from slope instability and improve our understanding of the long-term evolution of glacial landscapes. Declining ice cover and thawing permafrost in temperature-sensitive glacial landscapes are accompanied by changes in LST. Therefore, LST is a key variable for studying the link between warming climate and landscape changes at various spatial and temporal scales.

In this thesis, I used LST derived from two sensor systems: (1) in very high spatial resolution from a UAV and (2) multidecadal time series derived from Landsat satellites 5, 7 and 8. The very high-resolution LST was used to estimate the spatially distributed debris cover thickness of a debris-covered glacier surface. The LST time series was processed using the cloud-computing platform Google Earth Engine to analyze trends and identify patterns in the Landsat LST data across the European Alps. In this final Chapter, I synthesise the conclusions drawn from the individual studies concerning the overarching objective of this thesis:

1) *How can high-resolution LST from UAVs provide insights into the evolution of debris-covered glaciers?*
2) *How can the extensive Landsat Collection 2 LST archive be used to detect changes in glacial landscapes?*
3) *How do LST trends vary with changes in land cover and elevation?*

In my first study, I conducted a field experiment to measure a significant fraction of the diurnal temperature cycle of a debris-covered glacier section in Switzerland and estimated spatially distributed debris thickness using two distinct approaches. I repeatedly recorded very high-resolution LST using a lightweight UAV with a thermal infrared sensor (uncooled microbolometer). At the time of the study, existing methods for estimating debris thickness had only been tested using satellite-

derived LST data, which are limited by several factors such as (1) the coarse spatial resolution, (2) lack of meteorological data, (3) uncertainties in model input parameters such as debris thermal properties or (4) LST acquisition times at fixed times. However, data availability, scalability, accuracy, and the physical relationship between LST and debris thickness (Mihalcea et al., 2008) are good arguments for improving and extending existing approaches (McCarthy et al., 2018). Thermal methods, independent of in-situ measurements in principle, allow debris thickness estimation at large spatial scales and in remote areas (Schauwecker et al., 2015) up to 0.5 m thickness (Rounce et al., 2021). Current thermal infrared approaches in this regard solve the surface energy balance equation for debris thickness (Foster et al., 2012). As many components in the SEB are a function of LST, very high-resolution LST can significantly reduce uncertainties in the approximation of these components. While I focused on the link between LST and debris cover thickness, very high-resolution LST data benefit many research disciplines, such as agricultural science applications or vegetation monitoring (Li et al., 2023). One of the key advantages is the ability to monitor the temporal evolution of LST at arbitrarily short time scales (Sismanidis et al., 2021). This allows for studying thermal properties, such as thermal inertia and conductivity of a substrate, and facilitates relating these measurements to satellite-derived data, which are limited to fixed overpass times.

Very high-resolution debris cover thickness maps allow us to correct satellite-derived debris cover thickness maps and quantify the mixed-pixel effect from spatially heterogeneous debris cover thicknesses. Repeated field campaigns further allow monitoring of the evolution of supraglacial debris cover over short time scales, thus filling a gap in the temporal resolutions provided by satellite overpasses (e.g., Landsat 16 days) or data gaps generated by cloud cover (Wang et al., 2024). The study demonstrates that the time of day significantly influences debris thickness estimates in the SEB model and the regression approach. This finding is essential for interpreting satellite-derived debris thickness estimates obtained at fixed acquisition times, offering a unique opportunity to calibrate these satellite-derived estimates. As the nonlinearity in the relationship between LST and debris thickness increases with LST, selecting appropriate empirical models to predict LST depends on the acquisition time. In the SEB approach, the sub-daily LST measurements allowed the quantification of the SEB components throughout the day, including the rate of change in heat storage, which remains unknown with satellite-derived LST but is a significant component of the SEB.

However, despite the opportunities to bridge the gap between spatial and temporal scales, some practical considerations must be taken into account. The sensor type used in this study requires thermal equilibrium between the device and the environment for accurate measurements, which is challenging to maintain in high mountain settings, and additional shielding may be beneficial. I calibrated the LST observations using delineated ice cliffs on the glacier section, assuming they were at the melting point. The variability of temperatures derived from these ice cliff surfaces was relatively large, and their uneven spatial distribution led to calibrated LST with significant residual

uncertainties. Combined with uncertainties from coarse resolution reanalysis data, this resulted in debris thickness estimates with relatively large RMSE values. However, debris thickness estimates from a recent comparable study (Messmer and Groos, 2024) yielded much lower RMSE values using meteorological data from a nearby weather station and a thermally adjusted sensor.

In my second study, I accessed patterns and trends in Landsat-derived LST data of the Swiss Alps using least squares regression of a harmonic model, including a linear trend component. Given the sensitivity of the mountain cryosphere to climate change, LST is a crucial variable for monitoring warming and surface processes related to changes in the surface energy balance (Westermann et al., 2011). For instance, snow and ice cover loss allows increased temperature propagation into greater depths, increasing permafrost temperatures and contributing to permafrost thaw (Smith et al., 2022). Since permafrost occurrence in mountainous regions is often discontinuous or sporadic (Kenner et al., 2019), monitoring permafrost using borehole temperature measurements cannot adequately cover large areas. Permafrost occurrence is influenced by the ground surface temperature, which is determined by the surface energy balance. Satellite-derived LST, therefore, may be essential for detecting changes in glacial landscapes and estimating how temperature propagates into the ground (Bartsch et al., 2023). Although several studies have highlighted the suitability of LST time series for climate change studies and environmental monitoring (e.g. Sobrino et al., 2020), commonly used sensors often do not fulfil the required criteria to analyse changes in high mountain landscapes (Zhao et al., 2021). In fact, only the Landsat satellites provide sufficient high spatial resolution and record length to account for the large spatiotemporal variability of LST in steep mountain landscapes.

Direct comparison of Landsat LST and LST trends with in-situ measured LST at the time of Landsat overpass yielded good results with mean accuracies of 0.26 K and -0.02 K yr^{-1}, respectively. While the validation of LST and LST trends provide a promising foundation for using Landsat LST in alpine settings, the robustness of the derived trends depends on the number of available observations. Chapter 2 shows that although the temporal resolution of Landsat is relatively low at 16 days, the record length of almost four decades is sufficient to derive robust long-term LST trends. Systematic orbit-related data scarcity and regions of frequent cloud cover can affect the robustness of LST trends, indicated by slight along-track artefacts over large areas. This circumstance will diminish with ongoing Landsat observations.

A significant issue with Landsat observations is the changing acquisition times caused by orbit changes (Zhang et al., 2016; Qiu et al., 2021). Sporadic and continuous orbit changes, particularly in Landsat 5 and 7, have caused variations in acquisition times of up to one hour. This temporal inconsistency in LST leads to a bias in LST trends that needs correction. Although the usage of Landsat LST has a long scientific tradition (Price, 1984), the issue of long-term trend bias has not yet been addressed in the literature. The LST trend bias is most strongly in regions transitioning from

shadowed to sunlit slopes within the 47 minutes of linear change in the overpass times. Although the simple correction method proposed addresses continuous changes in acquisition time, the remaining residuals indicate a need for future efforts to correct Landsat LST observations before trend calculation, accounting for LST variability due to sporadic orbit changes. However, direct correction of LST observations is not straightforward as LST from other sensors is often not comparable. Despite the limitations of the proposed topography-based trend correction, the corrected LST trend exhibits considerably less variation with slope and aspect. Further validation of the corrected LST trends is needed to evaluate if the remaining residuals are a signal of insufficient correction or a natural pattern that indicates aspect-dependent LST warming in the Alps.

Concerning changes in the mountain cryosphere, the corrected LST trends respond to changes in snow and ice cover. Glacier changes, such as retreat zones and the evolution of supraglacial debris cover, are well preserved in the LST trends. The effect of the decline in snow depth on LST trends is more complicated to disentangle as snow depth varies strongly in space and time (Matiu et al., 2021). The data from the IMIS network did not reveal a clear correlation between the mean annual snow depth trends and the Landsat LST trends, possibly because of significant differences in spatial resolution and the limited record length of snow depth time series. However, it is notable that snow depth trends mostly show a negative trend, while both the trend in the annual number of snow-free days and the LST trends exhibit positive trends. Kenner et al. (2024) recently demonstrated a strong correlation between mountain permafrost loss and the elevation rise of the zero-degree isotherm, aligning with increased air temperature trends around the zero-degree isotherm (Pepin and Lundquist, 2008). Across the Swiss Alps, the strongest mean LST trends, as discussed in Chapter 3, are observed where the mean annual land surface temperature (MALST) is between -5 and 0°C. This highlights the importance of analyzing Landsat LST time series data, including MALST and trends, to identify areas susceptible to permafrost loss, as permafrost temperatures are closely linked to air temperature and snow cover (Etzelmüller et al., 2023).

Land cover, such as snow, not only influences temperature propagation into depth (Magnin et al., 2023) but also the local and regional climate, as the surface energy budget depends on the ground's biophysical properties and its changes (Pielke et al., 2005). In Chapter 4, I compared LST trends of persistent and transient land cover categories in the European Alps and assessed their elevational differences using several auxiliary datasets. I demonstrated that LST trends significantly vary with land cover and land cover changes. As shown for the Swiss Alps in Chapter 3, the highest LST trends across the entire European Alps are found where snow and ice cover decline. While the total area of glacier retreat zones is relatively small, the area experiencing snow cover loss is extensive. Monitoring these regions is therefore relevant for identifying areas of risk from permafrost thaw related natural hazards and understanding changes in the local climate. Various recent studies have explored elevation-dependent warming (EDW) in high mountain landscapes. While there is

agreement that no consistent EDW profile exists globally (Pepin et al., 2022), warming trends at different elevations vary due to diverse causes and feedback mechanisms. In the Swiss Alps, these include elevation-sensitive responses to changes in weather-type frequencies and differences in radiation linked to variable atmospheric composition with elevation (Rottler et al., 2019). However, unlike air temperature, the snow/ice albedo effect significantly impacts the LST trends. Averaged across the European Alps, mean LST trends in regions with significant snow cover loss (Rumpf et al., 2022) increase with elevation, while upper glacier zones at similar elevations do not show this elevational pattern. Some land cover changes, such as snow decline or vegetation growth, are expected to occur gradually over long periods, while others happen abruptly. In the LST time series, these abrupt land cover changes may be reflected as step changes rather than gradual transitions. Although these changes are still captured in LST trends, the harmonic model with a linear trend is not equally effective in accurately deriving LST trends.

Future studies could benefit from adjusting the model for specific land cover types and changes. For snow decline, this could involve accounting for the zero-curtain effect in the annual LST cyclicity, while for abrupt land cover changes, determining temporal breakpoints would be an option. For example, the Continuous Change Detection and Classification algorithm can detect breaks in time series and calculating trends for continuous segments has been recently suggested (Li et al., 2022). However, shortening the time series to accommodate these breaks might result in less robust trends, as long time series are required for deriving reliable LST trends.

In this thesis, I used LST with unprecedented high spatial resolution to evaluate the limits and opportunities in detecting and analyzing the dynamics of glacial landscapes. LST provides independent temperature data that complements in situ and reanalysis data and is closely linked to near-surface air temperature. The LST data from both sensor types used in this thesis contribute to a better understanding of climate-sensitive landscape processes in high mountains, such as the evolution of debris-covered glaciers, the decline of snow and ice cover, and the associated warming of mountain permafrost. Despite the limitations of Landsat satellites, such as low temporal resolution and LST trend bias, this work is the first to quantify LST trends across the European Alps, revealing a spatially averaged mean of 0.09 K yr^{-1}. The high spatial resolution of LST trends helps identify regions prone to hazardous slope failures related to thawing permafrost. As a continuation of this work, the corrected LST trends are currently being used as input for the numerical modeling of permafrost temperatures at depth (Scherler et al., 2024).

6 References

Adler, C., Palazzi, E., Kulonen, A., Balsiger, J., Colangeli, G., Cripe, D., Forsythe, N., Goss-Durant, G., Guigoz, Y., Krauer, J., Payne, D., Pepin, N., Peralvo, M., Romero, J. L., Sayre, R., Shahgedanova, M., Weingartner, R., & Zebisch, M. (2018). Monitoring Mountains in a Changing world: New horizons for the Global Network for Observations and Information on Mountain Environments (GEO-GNOME). Mountain Research and Development, 38(3), 265–269. https://doi.org/10.1659/mrd-journal-d-8-00065.1

Adler, C., Wester, P., Huggel, C., Insarov, G. E., Morecroft, M. D., Muccione, V., & Prakash, A. (2022). Cross-Chapter Paper 5: Mountains. In: Climate Change 2022: Impacts, Adaptation, and Vulnerability. Contribution of Working Group II to the Sixth Assessment Report of the Intergovernmental Panel on Climate Change. https://doi.org/10.1017/9781009325844.022.

Ali, E., Cramer, W., Carnicer, J., Georgopoulou, E., Hilmi, N. J. M., Cozannet, G. L., & Lionello, P. (2022). Cross-Chapter Paper 4: Mediterranean Region. In Climate Change 2022: Impacts, Adaptation, and Vulnerability. (Contribution of Working Group II to the Sixth Assessment Report of the Intergovernmental Panel on Climate Change [H.-O. Pörtner, D.C. Roberts, M. Tignor, E.S. Poloczanska, K. Mintenbeck, A. Alegría, M. Craig, S. Langsdorf, S. Löschke, V. Möller, A. Okem, B. Rama (eds.)]., pp. 2233–2272). Cambridge University Press, Cambridge. https://doi.org/10.1017/9781009325844.021.

Alkama, R., & Cescatti, A. (2016). Biophysical climate impacts of recent changes in global forest cover. Science, 351(6273), 600–604. https://doi.org/10.1126/science.aac8083

Alkama, R., Forzieri, G., Duveiller, G., Grassi, G., Liang, S., & Cescatti, A. (2022). Vegetation-based climate mitigation in a warmer and greener World. Nature Communications, 13(1). https://doi.org/10.1038/s41467-022-28305-9

Allen, S. K., Gruber, S., & Owens, I. F. (2009). Exploring steep bedrock permafrost and its relationship with recent slope failures in the Southern Alps of New Zealand. Permafrost and Periglacial Processes, 20(4), 345–356. https://doi.org/10.1002/ppp.658Alley, R., & Jentoft-Nilsen, M. (1999). Algorithm Theoretical Basis Document for: Brightness Temperature. Et Propulsion Lab., California Inst. Of Tech., Pasadena, CA.

Anderson, L. S., & Anderson, R. S. (2018). Debris thickness patterns on debris-covered glaciers. Geomorphology, 311, 1–12. https://doi.org/10.1016/j.geomorph.2018.03.014

Anderson, L. S., Armstrong, W. H., Anderson, R. S., Scherler, D., & Petersen, E. (2021). The Causes of Debris-Covered Glacier thinning: Evidence for the importance of ice dynamics from Kennicott Glacier, Alaska. Frontiers in Earth Science, 9. https://doi.org/10.3389/feart.2021.680995

Anderson, M. C., Norman, J. M., Mecikalski, J. R., Otkin, J. A., & Kustas, W. P. (2007). A climatological study of evapotranspiration and moisture stress across the continental United States based on thermal remote sensing: 1. Model formulation. Journal of Geophysical Research, 112(D10). https://doi.org/10.1029/2006jd007506

Aragon, B., Johansen, K., Parkes, S., Malbeteau, Y., Al-Mashharawi, S., Al-Amoudi, T., Andrade, C. F., Turner, D., Lucieer, A., & McCabe, M. F. (2020). A calibration procedure for field and UAV-Based uncooled thermal infrared instruments. Sensors, 20(11), 3316. https://doi.org/10.3390/s20113316

Aubry-Wake, C., Baraer, M., McKenzie, J. M., Mark, B. G., Wigmore, O., Hellström, R. Å., Lautz, L., & Somers, L. (2015). Measuring glacier surface temperatures with ground-based thermal infrared imaging. Geophysical Research Letters, 42(20), 8489–8497. https://doi.org/10.1002/2015gl065321

Aubry-Wake, C., Zéphir, D., Baraer, M., McKenzie, J. M., & Mark, B. G. (2017). Importance of longwave emissions from adjacent terrain on patterns of tropical glacier melt and recession. Journal of Glaciology/Journal of Glaciology, 64(243), 49–60. https://doi.org/10.1017/jog.2017.85

Ballantyne, C. K. (2002). Paraglacial geomorphology. Quaternary Science Reviews, 21(18–19), 1935–2017. https://doi.org/10.1016/s0277-3791(02)00005-7

Ballantyne, C. K., Sandeman, G. F., Stone, J. O., & Wilson, P. (2014). Rock-slope failure following Late Pleistocene deglaciation on tectonically stable mountainous terrain. Quaternary Science Reviews, 86, 144–157. https://doi.org/10.1016/j.quascirev.2013.12.021

Barnett, T. P., Adam, J. C., & Lettenmaier, D. P. (2005). Potential impacts of a warming climate on water availability in snow-dominated regions. Nature, 438(7066), 303–309. https://doi.org/10.1038/nature04141

Barry, R., Chorley, R., Barry, R. G., & Chorley, L. R. (2003). Atmosphere, weather and climate. Routledge.

Barsi, J., Barker, J., & Schott, J. (2004). An Atmospheric Correction Parameter Calculator for a single thermal band earth-sensing instrument. Proc. IEEE Int. Geosci. Remote Sens. Symp. (IGARSS). https://doi.org/10.1109/igarss.2003.1294665

Bartsch, A., Strozzi, T., & Nitze, I. (2023). Permafrost Monitoring from Space. Surveys in Geophysics, 44(5), 1579–1613. https://doi.org/10.1007/s10712-023-09770-3

Bartsch, A., Strozzi, T., & Nitze, I. (2023). Permafrost Monitoring from Space. Surveys in Geophysics, 44(5), 1579–1613. https://doi.org/10.1007/s10712-023-09770-3

Beaumet, J., Ménégoz, M., Morin, S., Gallée, H., Fettweis, X., Six, D., Vincent, C., Wilhelm, B., & Anquetin, S. (2021). Twentieth century temperature and snow cover changes in the French Alps. Regional Environmental Change, 21(4). https://doi.org/10.1007/s10113-021-01830-x

Bechtel, B. (2015). A new global climatology of annual land surface temperature. Remote Sensing, 7(3), 2850–2870. https://doi.org/10.3390/rs70302850

Begert, M., & Frei, C. (2018). Long-term area-mean temperature series for Switzerland—Combining homogenized station data and high resolution grid data. International Journal of Climatology, 38(6), 2792–2807. https://doi.org/10.1002/joc.5460

Beniston, M., Díaz, H. F., & Bradley, R. S. (1997). Climatic change at high elevation sites: an overview. Climatic Change, 36(3/4), 233–251. https://doi.org/10.1023/a:1005380714349

Beniston, M., Farinotti, D., Stoffel, M., Andreassen, L. M., Coppola, E., Eckert, N., Fantini, A., Giacona, F., Hauck, C., Huss, M., Huwald, H., Lehning, M., López-Moreno, J. I., Magnusson, J., Marty, C., Morán-Tejéda, E., Morin, S., Naaim, M., Provenzale, A., . . . Vincent, C. (2018). The European mountain cryosphere: a review of its current state, trends, and future challenges. □the □Cryosphere, 12(2), 759–794. https://doi.org/10.5194/tc-12-759-2018

Benn, D., & Evans, D. J. A. (2014). Glaciers and Glaciation, 2nd edition. In Routledge eBooks. https://doi.org/10.4324/9780203785010

Benn, D., Bolch, T., Hands, K., Gulley, J., Luckman, A., Nicholson, L., Quincey, D., Thompson, S., Toumi, R., & Wiseman, S. (2012). Response of debris-covered glaciers in the Mount Everest region to recent warming, and implications for outburst flood hazards. Earth-science Reviews, 114(1–2), 156–174. https://doi.org/10.1016/j.earscirev.2012.03.008

Bhambri, R., Bolch, T., Chaujar, R. K., & Kulshreshtha, S. C. (2011). Glacier changes in the Garhwal Himalaya, India, from 1968 to 2006 based on remote sensing. Journal of Glaciology/Journal of Glaciology, 57(203), 543–556. https://doi.org/10.3189/002214311796905604

Bird, R. E., & Hulstrom, R. L. (1981). Simplified clear sky model for direct and diffuse insolation on horizontal surfaces. https://doi.org/10.2172/6510849

Biskaborn, B. K., Smith, S. L., Noetzli, J., Matthes, H., Vieira, G., Streletskiy, D. A., Schoeneich, P., Romanovsky, V. E., Lewkowicz, A. G., Abramov, A., Allard, M., Boike, J., Cable, W., Christiansen, H. H., Delaloye, R., Diekmann, B., Drozdov, D., Etzelmüller, B., Grosse, G., . . . Lantuit, H. (2019). Permafrost is warming at a global scale. Nature Communications, 10(1). https://doi.org/10.1038/s41467-018-08240-4

Bliss, A., Hock, R., & Radić, V. (2014). Global response of glacier runoff to twenty-first century climate change. Journal of Geophysical Research. Earth Surface, 119(4), 717–730. https://doi.org/10.1002/2013jf002931

Bojinski, S., Verstraete, M. M., Peterson, T. C., Richter, C., Simmons, A. J., & Zemp, M. (2014). The concept of essential climate variables in support of climate research, applications, and policy. Bulletin of the American Meteorological Society, 95(9), 1431–1443. https://doi.org/10.1175/bams-d-13-00047.1

Bolch, T., Kulkarni, A., Kääb, A., Huggel, C., Paul, F., Cogley, J. G., Frey, H., Kargel, J. S., Fujita, K., Scheel, M., Bajracharya, S., & Stoffel, M. (2012). The state and fate of Himalayan glaciers. Science, 336(6079), 310–314. https://doi.org/10.1126/science.1215828

Boxall, K., Willis, I., Giese, A., & Liu, Q. (2021). Quantifying patterns of supraglacial debris thickness and their glaciological controls in high mountain Asia. Frontiers in Earth Science, 9. https://doi.org/10.3389/feart.2021.657440

Brantley, S. L., Goldhaber, M. B., and Ragnarsdottir, K.: Crossing disciplines and scales to understand the critical zone, Elements, 3, 307–314, https://doi.org/10.2113/gselements.3.5.307, 2007.

Breiman, L. (2001). Random forests. Machine Learning, 45(1), 5–32. https://doi.org/10.1023/a:1010933404324

Brock, B. W., Mihalcea, C., Kirkbride, M. P., Diolaiuti, G., Cutler, M. E. J., & Smiraglia, C. (2010). Meteorology and surface energy fluxes in the 2005–2007 ablation seasons at the Miage debris-covered glacier, Mont Blanc Massif, Italian Alps. Journal of Geophysical Research, 115(D9). https://doi.org/10.1029/2009jd013224

Brock, B. W., Willis, I. C., & Sharp, M. J. (2000). Measurement and parameterization of albedo variations at Haut Glacier d'Arolla, Switzerland. Journal of Glaciology/Journal of Glaciology, 46(155), 675–688. https://doi.org/10.3189/172756500781832675

Brown, R., & Mote, P. W. (2009). The response of northern hemisphere snow cover to a changing climate*. Journal of Climate, 22(8), 2124–2145. https://doi.org/10.1175/2008jcli2665.1

Budzier, H., & Gerlach, G. (2015). Calibration of uncooled thermal infrared cameras. Journal of Sensors and Sensor Systems, 4(1), 187–197. https://doi.org/10.5194/jsss-4-187-2015

Büttner, G. (2014). CORINE Land cover and land cover change products. In Remote sensing and digital image processing (pp. 55–74). https://doi.org/10.1007/978-94-007-7969-3_5

Byerlay, R. A., Coates, C., Aliabadi, A. A., & Kevan, P. G. (2020). In situ calibration of an uncooled thermal camera for the accurate quantification of flower and stem surface temperatures. Thermochimica Acta, 693, 178779. https://doi.org/10.1016/j.tca.2020.178779

Casey, K. S., & Cornillon, P. (2001). Global and regional sea surface temperature trends. Journal of Climate, 14(18), 3801–3818. https://doi.org/10.1175/1520-0442(2001)014

Ceppi, P., Scherrer, S. C., Fischer, A. M., & Appenzeller, C. (2010). Revisiting Swiss temperature trends 1959–2008. International Journal of Climatology, 32(2), 203–213. https://doi.org/10.1002/joc.2260

Christianson, K. R., Loria, K. A., Blanken, P. D., Caine, N., & Johnson, P. T. J. (2021). On thin ice: Linking elevation and long-term losses of lake ice cover. Limnology and Oceanography Letters, 6(2), 77–84. https://doi.org/10.1002/lol2.10181

Clague, J. J., Huggel, C., Korup, O., & McGuire, B. (2012). Climate change and hazardous processes in high mountains. Revista De La Asociación Geológica Argentina, 69(3), 328–338. https://doi.org/10.5167/uzh-77920

Coe, J. A., Bessette-Kirton, E. K., & Geertsema, M. (2017). Increasing rock-avalanche size and mobility in Glacier Bay National Park and Preserve, Alaska detected from 1984 to 2016 Landsat imagery. Landslides, 15(3), 393–407. https://doi.org/10.1007/s10346-017-0879-7

Consortium CCI LST - European Space Agency. (2023). CCI Land Surface Temperature: Algorithm Development Plan. In https://climate.esa.int/de/projekte/land-surface-temperature/ (WP2.1 – DEL-D2.4).

Conway, H., & Rasmussen, L. A. (2000). Summer temperature profiles within supraglacial debris on Khumbu Glacier, Nepal (No. 89–98). IAHS-AISH Publication.

Cook, K. L. (2017). An evaluation of the effectiveness of low-cost UAVs and structure from motion for geomorphic change detection. Geomorphology, 278, 195–208. https://doi.org/10.1016/j.geomorph.2016.11.009

Cook, M., Schott, J. R., Mandel, J., & Raqueno, N. G. (2014). Development of an Operational Calibration Methodology for the Landsat Thermal Data Archive and Initial Testing of the Atmospheric Compensation Component of a Land Surface Temperature (LST) Product from the Archive. Remote Sensing, 6(11), 11244–11266. https://doi.org/10.3390/rs61111244Copernicus DEM: COP-DEM_EEA-10-INSP. (2022). [Dataset]. European Space Agency. https://doi.org/10.5270/esa-c5d3d65

Corripio, J. G. (2003). Vectorial algebra algorithms for calculating terrain parameters from DEMs and solar radiation modelling in mountainous terrain. International Journal of Geographical Information Science, 17(1), 1–23. https://doi.org/10.1080/713811744

Crameri, F., Shephard, G. E., & Heron, P. J. (2020). The misuse of colour in science communication. Nature Communications, 11(1). https://doi.org/10.1038/s41467-020-19160-7

Crawford, C. J., Roy, D. P., Arab, S., Barnes, C., Vermote, E., Hulley, G., Gerace, A., Choate, M., Engebretson, C., Micijevic, E., Schmidt, G., Anderson, C., Anderson, M., Bouchard, M., Cook, B., Dittmeier, R., Howard, D., Jenkerson, C., Kim, M., . . . Zahn, S. (2023). The 50-year Landsat collection 2 archive. Science of Remote Sensing, 8, 100103. https://doi.org/10.1016/j.srs.2023.100103

Dech, S., Holzwarth, S., Asam, S., Andresen, T., Bachmann, M., Boettcher, M., Dietz, A., Eisfelder, C., Frey, C., Gesell, G., Geßner, U., Hirner, A., Hofmann, M., Kirches, G., Klein, D., Klein, I., Kraus, T., Krause, D., Plank, S., . . . Kuenzer, C. (2021). Potential and Challenges of Harmonizing 40 years of AVHRR Data: The TIMELINE Experience. Remote Sensing, 13(18), 3618. https://doi.org/10.3390/rs13183618

Dedieu, J., Lessard-Fontaine, A., Ravazzani, G., Cremonese, E., Shalpykova, G., & Beniston, M. (2014). Shifting mountain snow patterns in a changing climate from remote sensing retrieval. Science of the Total Environment, 493, 1267–1279. https://doi.org/10.1016/j.scitotenv.2014.04.078

Deline, P. (2009). Interactions between rock avalanches and glaciers in the Mont Blanc massif during the late Holocene. Quaternary Science Reviews, 28(11–12), 1070–1083. https://doi.org/10.1016/j.quascirev.2008.09.025

Deline, P., Gruber, S., Amann, F., Bodin, X., Delaloye, R., Failletaz, J., Fischer, L., Geertsema, M., Giardino, M., Hasler, A., Kirkbride, M., Krautblatter, M., Magnin, F., McColl, S., Ravanel, L., Schoeneich, P., & Weber, S. (2021). Ice loss from glaciers and permafrost and related slope instability in high-mountain regions. In Elsevier eBooks (pp. 501–540). https://doi.org/10.1016/b978-0-12-817129-5.00015-9

Deline, P., Gruber, S., Delaloye, R., Fischer, L., Geertsema, M., Giardino, M., Hasler, A., Kirkbride, M. P., Krautblatter, M., Magnin, F., McColl, S. T., Ravanel, L., & Schoeneich, P. (2015). Ice loss and slope stability in High-Mountain regions. In Elsevier eBooks (pp. 521–561). https://doi.org/10.1016/b978-0-12-394849-6.00015-9

Díaz, H. F., & Bradley, R. S. (1997). Temperature variations during the last century at high elevation sites. Climatic Change, 36(3/4), 253–279. https://doi.org/10.1023/a:1005335731187

Dousset, B., & Gourmelon, F. (2003). Satellite multi-sensor data analysis of urban surface temperatures and landcover. ISPRS Journal of Photogrammetry and Remote Sensing, 58(1–2), 43–54. https://doi.org/10.1016/s0924-2716(03)00016-9

Draebing, D. (2021). Identification of rock and fracture kinematics in high alpine rockwalls under the influence of elevation. Earth Surface Dynamics, 9(4), 977–994. https://doi.org/10.5194/esurf-9-977-2021

Draebing, D., & Krautblatter, M. (2019). The efficacy of frost weathering processes in alpine rockwalls. Geophysical Research Letters, 46(12), 6516–6524. https://doi.org/10.1029/2019gl081981

Draebing, D., Krautblatter, M., & Hoffmann, T. (2017). Thermo-cryogenic controls of fracture kinematics in permafrost rockwalls. Geophysical Research Letters, 44(8), 3535–3544. https://doi.org/10.1002/2016gl072050

Dugdale, S. J., Kelleher, C. A., Malcolm, I. A., Caldwell, S., & Hannah, D. M. (2019). Assessing the potential of drone-based thermal infrared imagery for quantifying river temperature heterogeneity. Hydrological Processes, 33(7), 1152–1163. https://doi.org/10.1002/hyp.13395

Duveiller, G., Hooker, J., & Cescatti, A. (2018). The mark of vegetation change on Earth's surface energy balance. Nature Communications, 9(1). https://doi.org/10.1038/s41467-017-02810-8

Dwyer, J. L., Roy, D. P., Sauer, B., Jenkerson, C. B., Zhang, H. K., and Lymburner, L.: Analysis Ready Data: Enabling analysis of the Landsat Archive, Remote Sensing, 10, 1363, https://doi.org/10.3390/rs10091363, 2018.

Elsen, P. R., & Tingley, M. W. (2015). Global mountain topography and the fate of montane species under climate change. Nature Climate Change, 5(8), 772–776. https://doi.org/10.1038/nclimate2656

Eppes, M. C., & Keanini, R. (2017). Mechanical weathering and rock erosion by climate-dependent subcritical craking. Reviews of Geophysics, 55(2), 470–508. https://doi.org/10.1002/2017rg000557

Eppes, M. C., Magi, B., Hallet, B., Delmelle, E., Mackenzie-Helnwein, P., Warren, K., & Swami, S. (2016). Deciphering the role of solar-induced thermal stresses in rock weathering. The Geological Society of America Bulletin/Geological Society of America Bulletin, 128(9–10), 1315–1338. https://doi.org/10.1130/b31422.1

Ermida, S. L., DaCamara, C. C., Trigo, I. F., Pires, A., Ghent, D., & Remedios, J. J. (2017). Modelling directional effects on remotely sensed land surface temperature. Remote Sensing of Environment, 190, 56–69. https://doi.org/10.1016/j.rse.2016.12.008

Ermida, S. L., Trigo, I. F., DaCamara, C. C., Jiménez, C., and Prigent, C.: Quantifying the Clear-Sky bias of satellite land surface temperature using Microwave-Based estimates, Journal of Geophysical Research. Atmospheres, 124, 844–857, https://doi.org/10.1029/2018jd029354, 2019.

Etzelmüller, B., Guglielmin, M., Hauck, C., Hilbich, C., Hoelzle, M., Isaksen, K., Noetzli, J., Oliva, M., & Ramos, M. (2020). Twenty years of European mountain permafrost dynamics—the PACE legacy. Environmental Research Letters, 15(10), 104070. https://doi.org/10.1088/1748-9326/abae9d

Etzelmüller, B., Isaksen, K., Czekirda, J., Westermann, S., Hilbich, C., & Hauck, C. (2023). Rapid warming and degradation of mountain permafrost in Norway and Iceland. The Cryosphere, 17(12), 5477–5497. https://doi.org/10.5194/tc-17-5477-2023

Evans, Stephen G., and John J. Clague. (1999). Rock avalanches on glaciers in the Coast and St. Elias Mountains, British Columbia. Proceedings of the 13th annual vancouver geotechnical society symposium, vancouver.

Farinotti, D., Immerzeel, W. W., De Kok, R., Quincey, D. J., & Dehecq, A. (2020). Manifestations and mechanisms of the Karakoram glacier Anomaly. Nature Geoscience, 13(1), 8–16. https://doi.org/10.1038/s41561-019-0513-5

Fleischer, F., Otto, J., Junker, R. R., & Hölbling, D. (2021). Evolution of debris cover on glaciers of the Eastern Alps, Austria, between 1996 and 2015. Earth Surface Processes and Landforms, 46(9), 1673–1691. https://doi.org/10.1002/esp.5065

FLIR – UAS Radiometric Temperature Measurements. (2020). Retrieved April 26, 2022, from https://www.flir.com/discover/suas/uas-radiometric-temperature-measurements/

Foga, S., Scaramuzza, P., Guo, S., Zhu, Z., Dilley, R. D., Beckmann, T., Schmidt, G. L., Dwyer, J. L., Hughes, M. J., and Laue, B.: Cloud detection algorithm comparison and validation for operational Landsat data products, Remote Sensing of Environment, 194, 379–390, https://doi.org/10.1016/j.rse.2017.03.026, 2017.

Foster, L., Brock, B., Cutler, M., & Diotri, F. (2012). A physically based method for estimating supraglacial debris thickness from thermal band remote-sensing data. Journal of Glaciology/Journal of Glaciology, 58(210), 677–691. https://doi.org/10.3189/2012jog11j194

Friedl, M. (2002). Forward and inverse modeling of land surface energy balance using surface temperature measurements. Remote Sensing of Environment, 79(2–3), 344–354. https://doi.org/10.1016/s0034-4257(01)00284-x

Fu, N. P., & Weng, N. Q. (2015). Temporal dynamics of land surface temperature from Landsat TIR Time Series images. IEEE Geoscience and Remote Sensing Letters, 12(10), 2175–2179. https://doi.org/10.1109/lgrs.2015.2455019

Fu, P., & Weng, Q. (2016). A time series analysis of urbanization induced land use and land cover change and its impact on land surface temperature with Landsat imagery. Remote Sensing of Environment, 175, 205–214. https://doi.org/10.1016/j.rse.2015.12.040

Fu, P., & Weng, Q. (2016). Consistent land surface temperature data generation from irregularly spaced Landsat imagery. Remote Sensing of Environment, 184, 175–187. https://doi.org/10.1016/j.rse.2016.06.019

García, M. J. L. (2020). SST comparison of AVHRR and MODIS time series in the Western Mediterranean Sea. Remote Sensing, 12(14), 2241. https://doi.org/10.3390/rs12142241

García-Monteiro, S., Sobrino, J. A., Julien, Y., Sòria, G., & Skoković, D. (2022). Surface Temperature trends in the Mediterranean Sea from MODIS data during years 2003–2019. Regional Studies in Marine Science, 49, 102086. https://doi.org/10.1016/j.rsma.2021.102086

Gardelle, J., Berthier, E., & Arnaud, Y. (2012). Slight mass gain of Karakoram glaciers in the early twenty-first century. Nature Geoscience, 5(5), 322–325. https://doi.org/10.1038/ngeo1450

Ghausi, S. A., Tian, Y., Zehe, E., and Kleidon, A.: Radiative controls by clouds and thermodynamics shape surface temperatures and turbulent fluxes over land, Proceedings of the National Academy of Sciences of the United States of America, 120, https://doi.org/10.1073/pnas.2220400120, 2023.

Gibson, M. J., Glasser, N. F., Quincey, D. J., Mayer, C., Rowan, A. V., & Irvine-Fynn, T. D. (2017). Temporal variations in supraglacial debris distribution on Baltoro Glacier, Karakoram between 2001 and 2012. Geomorphology, 295, 572–585. https://doi.org/10.1016/j.geomorph.2017.08.012

Glasser, N. F., Holt, T. O., Evans, Z. D., Davies, B. J., Pelto, M., & Harrison, S. (2016). Recent spatial and temporal variations in debris cover on Patagonian glaciers. Geomorphology, 273, 202–216. https://doi.org/10.1016/j.geomorph.2016.07.036

Glen, J. (1997). W. S. B. Paterson 1994. The physics of glaciers. 3rd edition. Oxford, etc., Pergamon, 480 pp. ISBN 0-08037945 1. Hardback. £70; 0-O8O37944 3, Flexieover. £25. Journal of Glaciology/Journal of Glaciology, 43(145), 594. https://doi.org/10.3189/s002214300003522x

Global Forest Change Update. (2023). Usage Notes. Retrieved April 11, 2024, from https://storage.googleapis.com/earthenginepartners-hansen/GFC-2023-v1.11/download.html.

Gök, D. T., Scherler, D., & Anderson, L. S. (2022). High-resolution debris cover mapping using UAV-derived thermal imagery [Dataset]. GFZ Data Service. https://doi.org/10.5880/GFZ.3.3.2022.003

Gök, D. T., Scherler, D., & Wulf, H. (2024). Land surface temperature trends derived from Landsat imagery in the Swiss Alps. EGUsphere [Preprint]. https://doi.org/10.5194/egusphere-2024-1228

Good, E. (2016). An in situ-based analysis of the relationship between land surface "skin" and screen-level air temperatures. Journal of Geophysical Research. Atmospheres, 121(15), 8801–8819. https://doi.org/10.1002/2016jd025318

Good, E., Aldred, F., Jimenez, C., Veal, K. L., & Jiménez, C. (2022). An Analysis of the Stability and Trends in the LST_cci Land Surface Temperature Datasets Over Europe. Earth and Space Science, 9(9). https://doi.org/10.1029/2022ea002317

Gorelick, N., Hancher, M., Dixon, M., Ilyushchenko, S., Thau, D., & Moore, R. (2017). Google Earth Engine: Planetary-scale geospatial analysis for everyone. Remote Sensing of Environment, 202, 18–27. https://doi.org/10.1016/j.rse.2017.06.031

Grämiger, L. M., Moore, J. R., Gischig, V. S., & Loew, S. (2018). Thermomechanical stresses drive damage of Alpine Valley rock walls during repeat glacial cycles. Journal of Geophysical Research. Earth Surface, 123(10), 2620–2646. https://doi.org/10.1029/2018jf004626

Gruber, S., & Haeberli, W. (2007). Permafrost in steep bedrock slopes and its temperature-related destabilization following climate change. Journal of Geophysical Research, 112(F2). https://doi.org/10.1029/2006jf000547

Gruber, S., Hoelzle, M., & Haeberli, W. (2004). Rock-wall temperatures in the Alps: modelling their topographic distribution and regional differences. Permafrost and Periglacial Processes, 15(3), 299–307. https://doi.org/10.1002/ppp.501

Guillevic, P., Göttsche, F., Nickeson, J., Hulley, G., Ghent, D., Yu, Y., Trigo, I. F., Hook, S. J., Sobrino, J. A., Remedios, J. J., Román, M. O., & Camacho, F. (2018). Land Surface Temperature Product Validation Best Practice Protocol: Good Practices for Satellite-Derived Land Product Validation. In Land Product Validation Subgroup (WGCV/CEOS). https://doi.org/10.5067/doc/ceoswgcv/lpv/lst.001

Guo, G., Wu, Z., Xiao, R., Chen, Y., Liu, X., & Zhang, X. (2015). Impacts of urban biophysical composition on land surface temperature in urban heat island clusters. Landscape and Urban Planning, 135, 1–10. https://doi.org/10.1016/j.landurbplan.2014.11.007

Gutman, G., & Masek, J. G. (2012). Long-term time series of the Earth's land-surface observations from space. International Journal of Remote Sensing, 33(15), 4700–4719. https://doi.org/10.1080/01431161.2011.638341

Gutman, G. G. (1999). On the use of long-term global data of land reflectances and vegetation indices derived from the advanced very high resolution radiometer. Journal of Geophysical Research, 104(D6), 6241–6255. https://doi.org/10.1029/1998jd200106

Gutman, G. G. (1999a). On the monitoring of land surface temperatures with the NOAA/AVHRR: Removing the effect of satellite orbit drift. International Journal of Remote Sensing, 20(17), 3407–3413. https://doi.org/10.1080/014311699211435

Haberkorn, A., Kenner, R., Noetzli, J., & Phillips, M. (2021). Changes in ground temperature and dynamics in mountain permafrost in the Swiss Alps. Frontiers in Earth Science, 9. https://doi.org/10.3389/feart.2021.626686

Haeberli, W., & Beniston, M. (2021). Icy mountains in a warming world: Revisiting science from the end of the 1990s in the early 2020s. Ambio, 50(6), 1130–1132. https://doi.org/10.1007/s13280-021-01513-1

Haeberli, W., Noetzli, J., & Mühll, D. V. (2023). Using Borehole Temperatures for Knowledge Transfer about Mountain Permafrost: The Example of the 35-year Time Series at Murtèl-Corvatsch (Swiss Alps). Revue De Géographie Alpine/Revue De GéOgraphie Alpine, 111–2. https://doi.org/10.4000/rga.11950

Hallet, B. (1996). Glacial quarrying: a simple theoretical model. Annals of Glaciology, 22, 1–8. https://doi.org/10.3189/1996aog22-1-1-8

Hallet, B., Walder, J. S., & Stubbs, C. W. (1991). Weathering by segregation ice growth in microcracks at sustained subzero temperatures: Verification from an experimental study using acoustic emissions. Permafrost and Periglacial Processes, 2(4), 283–300. https://doi.org/10.1002/ppp.3430020404

Hansen, M. C., Potapov, P., Moore, R., Hancher, M., Turubanova, S., Tyukavina, A., Thau, D., Stehman, S. V., Goetz, S. J., Loveland, T. R., Kommareddy, A., Egorov, A., Chini, L. P., Justice, C. O., & Townshend, J. R. G. (2013). High-Resolution Global Maps of 21st-Century Forest cover change. Science, 342(6160), 850–853. https://doi.org/10.1126/science.1244693

Harris, C., Arenson, L. U., Christiansen, H. H., Etzelmüller, B., Frauenfelder, R., Gruber, S., Haeberli, W., Hauck, C., Hölzle, M., Humlum, O., Isaksen, K., Kääb, A., Kern-Lütschg, M. A., Lehning, M., Matsuoka, N., Murton, J. B., Nötzli, J., Phillips, M., Ross, N., . . . Mühll, D. V. (2009). Permafrost and climate in Europe: Monitoring and modelling thermal, geomorphological and geotechnical responses. Earth-science Reviews, 92(3–4), 117–171. https://doi.org/10.1016/j.earscirev.2008.12.002

Hartmann, D. (1994). The energy Balance of the surface. In Global Physical Climatology (pp. 81–114). International Geophysics, Academic Press. https://doi.org/10.1016/s0074-6142(08)60561-6

Hartmeyer, I., Delleske, R., Keuschnig, M., Krautblatter, M., Lang, A., Schrott, L., & Otto, J. (2020a). Current glacier recession causes significant rockfall increase: the immediate paraglacial response of deglaciating cirque walls. Earth Surface Dynamics, 8(3), 729–751. https://doi.org/10.5194/esurf-8-729-2020

Hartmeyer, I., Keuschnig, M., Delleske, R., Krautblatter, M., Lang, A., Schrott, L., Prasicek, G., & Otto, J. (2020b). A 6-year lidar survey reveals enhanced rockwall retreat and modified rockfall magnitudes/frequencies in deglaciating cirques. Earth Surface Dynamics, 8(3), 753–768. https://doi.org/10.5194/esurf-8-753-2020

Hasler, A., Geertsema, M., Foord, V., Gruber, S., & Noetzli, J. (2015). The influence of surface characteristics, topography and continentality on mountain permafrost in British Columbia. The Cryosphere, 9(3), 1025–1038. https://doi.org/10.5194/tc-9-1025-2015

Heinemann, S., Siegmann, B., Thonfeld, F., Muro, J., Jedmowski, C., Kemna, A., Kraska, T., Muller, O., Schultz, J., Udelhoven, T., Wilke, N., & Rascher, U. (2020). Land Surface Temperature Retrieval for Agricultural Areas Using a Novel UAV Platform Equipped with a Thermal Infrared and Multispectral Sensor. Remote Sensing, 12(7), 1075. https://doi.org/10.3390/rs12071075

Herman, F., De Doncker, F., Delaney, I., Prasicek, G., & Koppes, M. (2021). The impact of glaciers on mountain erosion. Nature Reviews. Earth & Environment, 2(6), 422–435. https://doi.org/10.1038/s43017-021-00165-9

Herreid, S. (2021). What can thermal imagery tell us about glacier melt below rock debris? Frontiers in Earth Science, 9. https://doi.org/10.3389/feart.2021.681059

Herreid, S., & Pellicciotti, F. (2020). The state of rock debris covering Earth's glaciers. Nature Geoscience, 13(9), 621–627. https://doi.org/10.1038/s41561-020-0615-0

Hill-Butler, C. (2014). Thermal infrared remote sensing: sensors, methods, applications, edited by C. Kuenzer. International Journal of Remote Sensing, 35(13), 5289–5290. https://doi.org/10.1080/01431161.2014.928448

Hock, R., & Huss, M. (2021). Glaciers and climate change. In Elsevier eBooks (pp. 157–176). https://doi.org/10.1016/b978-0-12-821575-3.00009-8

Hock, R., Golam, R., Jackson, M., Kääb, A., Kang, S., Kutuzov, S., Federation, R., Milner, A. M., Molau, U., Morin, S., Orlove, B., Allen, S., Arenson, L. U., Banerjee, S., Barr, I., Bórquez, R., Carey, M., Cogley, G., Fischlin, A., . . . Weyer, N. (2022). High mountain areas. In Cambridge University Press eBooks (pp. 131–202). https://doi.org/10.1017/9781009157964.004

Holzman, M., Rivas, R., & Piccolo, M. (2014). Estimating soil moisture and the relationship with crop yield using surface temperature and vegetation index. International Journal of Applied Earth Observation and Geoinformation, 28, 181–192. https://doi.org/10.1016/j.jag.2013.12.006

Hopkinson, C., Barlow, J., Demuth, M., & Pomeroy, J. (2010). Mapping changing temperature patterns over a glacial moraine using oblique thermal imagery and lidar. Canadian Journal of Remote Sensing, 36(sup2), S257–S265. https://doi.org/10.5589/m10-053

Huang, L., Li, Z., Tian, B. S., Han, H. D., Liu, Y. Q., Zhou, J. M., & Chen, Q. (2017). Estimation of supraglacial debris thickness using a novel target decomposition on L-band polarimetric SAR images in the Tianshan Mountains. Journal of Geophysical Research. Earth Surface, 122(4), 925–940. https://doi.org/10.1002/2016jf004102

Huggel, C. (2009). Recent extreme slope failures in glacial environments: effects of thermal perturbation. Quaternary Science Reviews, 28(11–12), 1119–1130. https://doi.org/10.1016/j.quascirev.2008.06.007

Huggel, C., Allen, S., Deline, P., Fischer, L., Noetzli, J., & Ravanel, L. (2012). Ice thawing, mountains falling—are alpine rock slope failures increasing? Geology Today, 28(3), 98–104. https://doi.org/10.1111/j.1365-2451.2012.00836.x

Hugonnet, R., McNabb, R., Berthier, É., Menounos, B., Nuth, C., Girod, L., Farinotti, D., Huss, M., Dussaillant, I., Brun, F., & Kääb, A. (2021). Accelerated global glacier mass loss in the early twenty-first century. Nature, 592(7856), 726–731. https://doi.org/10.1038/s41586-021-03436-z

Hulley, G. C., & Hook, S. J. (2011). Generating consistent land surface temperature and emissivity products between ASTER and MODIS data for earth science research. IEEE Transactions on Geoscience and Remote Sensing, 49(4), 1304–1315. https://doi.org/10.1109/tgrs.2010.2063034

Hulley, G. C., Dousset, B., & Kahn, B. H. (2020). Rising trends in heatwave metrics across Southern California. Earth's Future, 8(7). https://doi.org/10.1029/2020ef001480

Hulley, G. C., Ghent, D., Göttsche, F. M., Guillevic, P. C., Mildrexler, D. J., & Coll, C. (2019). Land surface temperature. In Elsevier eBooks (pp. 57–127). https://doi.org/10.1016/b978-0-12-814458-9.00003-4

Hulley, G. C., Hook, S. J., Abbott, E., Malakar, N., Islam, T., & Abrams, M. (2015). The ASTER Global Emissivity Dataset (ASTER GED): Mapping Earth's emissivity at 100 meter spatial scale. Geophysical Research Letters, 42(19), 7966–7976. https://doi.org/10.1002/2015gl065564

Hulley, G. C., Malakar, N. K., Islam, T., & Freepartner, R. J. (2018). NASA's MODIS and VIIRS Land Surface Temperature and Emissivity Products: A Long-Term and Consistent Earth System Data Record. IEEE Journal of Selected Topics in Applied Earth Observations and Remote Sensing, 11(2), 522–535. https://doi.org/10.1109/jstars.2017.2779330

Huss, M., Bookhagen, B., Huggel, C., Jacobsen, D., Bradley, R. S., Clague, J. J., Vuille, M., Buytaert, W., Cayan, D. R., Greenwood, G. B., Mark, B. G., Milner, A. M., Weingartner, R., & Winder, M. (2017). Toward mountains without permanent snow and ice. Earth's Future, 5(5), 418–435. https://doi.org/10.1002/2016ef000514

IPCC, 2022: Climate Change 2022 – Impacts, adaptation and vulnerability (By [H.-O. Pörtner, D.C. Roberts, M. Tignor, E.S. Poloczanska, K. Mintenbeck, a. Alegría, M. Craig, S. Langsdorf, S. Löschke, V. Möller, a. Okem, B. Rama (Eds.)]). (2023). Cambridge University Press. https://doi.org/10.1017/9781009325844

Iqbal, M. (1983). An introduction to solar radiation. In Elsevier eBooks. https://doi.org/10.1016/b978-0-12-373750-2.x5001-0

Irvine-Fynn, T. D. L., Porter, P. R., Rowan, A. V., Quincey, D. J., Gibson, M. J., Bridge, J. W., Watson, C. S., Hubbard, A., & Glasser, N. F. (2017). Supraglacial ponds regulate runoff from Himalayan Debris-Covered glaciers. Geophysical Research Letters, 44(23). https://doi.org/10.1002/2017gl075398

Ivy-Ochs, S., Kerschner, H., Maisch, M., Christl, M., Kubik, P. W., & Schlüchter, C. (2009). Latest Pleistocene and Holocene glacier variations in the European Alps. Quaternary Science Reviews, 28(21–22), 2137–2149. https://doi.org/10.1016/j.quascirev.2009.03.009

Jackson, R. D., Idso, S. B., Reginato, R. J., & Pinter, P. J. (1981). Canopy temperature as a crop water stress indicator. Water Resources Research, 17(4), 1133–1138. https://doi.org/10.1029/wr017i004p01133

Jiménez-Muñoz, J. C., & Sobrino, J. A. (2003). A generalized single-channel method for retrieving land surface temperature from remote sensing data. Journal of Geophysical Research, 108(D22). https://doi.org/10.1029/2003jd003480

Jin, J., & Dickinson, R. E. (2010). Land surface skin temperature climatology: benefitting from the strengths of satellite observations. Environmental Research Letters, 5(4), 044004. https://doi.org/10.1088/1748-9326/5/4/044004

Jin, M., & Treadon, R. E. (2003). Correcting the orbit drift effect on AVHRR land surface skin temperature measurements. International Journal of Remote Sensing, 24(22), 4543–4558. https://doi.org/10.1080/0143116031000095943

Julien, Y., & Sobrino, J. A. (2012). Correcting AVHRR Long Term Data Record V3 estimated LST from orbital drift effects. Remote Sensing of Environment, 123, 207–219. https://doi.org/10.1016/j.rse.2012.03.016

Julien, Y. and Sobrino, J. A.: Toward a reliable correction of NOAA AVHRR orbital drift, Frontiers in Remote Sensing, 3, https://doi.org/10.3389/frsen.2022.851933, 2022.

Julien, Y., & Sobrino, J. A. (2022b). Toward a reliable correction of NOAA AVHRR orbital drift. Frontiers in Remote Sensing, 3. https://doi.org/10.3389/frsen.2022.851933

Kalnay, E., Kanamitsu, M., Kistler, R., Collins, W. G., Deaven, D. G., Gandin, L. S., Iredell, M., Saha, S., White, G. H., Woollen, J. S., Zhu, Y., Chelliah, M., Ebisuzaki, W., Higgins, W., Janowiak, J. E., Mo, K. C., Ropelewski, C. F., Wang, J., Leetmaa, A., Reynolds, R. W., Jenne, R. L., and Joseph, D.: The NCEP/NCAR 40-Year Reanalysis Project, Bulletin of the American Meteorological Society, 77, 437–471, https://doi.org/10.1175/1520-0477(1996)077, 1996.

Kaser, G., Großhauser, M., & Marzeion, B. (2010). Contribution potential of glaciers to water availability in different climate regimes. Proceedings of the National Academy of Sciences of the United States of America, 107(47), 20223–20227. https://doi.org/10.1073/pnas.1008162107

Kaushik, S., Singh, T., Bhardwaj, A., Joshi, P. K., & Dietz, A. J. (2022). Automated delineation of supraglacial debris cover using deep learning and multisource remote sensing data. Remote Sensing, 14(6), 1352. https://doi.org/10.3390/rs14061352

Keiler, M., Knight, J., & Harrison, S. (2010). Climate change and geomorphological hazards in the eastern European Alps. Philosophical Transactions - Royal Society. Mathematical, Physical and Engineering Sciences/Philosophical Transactions - Royal Society. Mathematical, Physical and Engineering Sciences, 368(1919), 2461–2479. https://doi.org/10.1098/rsta.2010.0047

Kennedy, R. E., Yang, Z., & Cohen, W. B. (2010). Detecting trends in forest disturbance and recovery using yearly Landsat time series: 1. LandTrendr — Temporal segmentation algorithms. Remote Sensing of Environment, 114(12), 2897–2910. https://doi.org/10.1016/j.rse.2010.07.008

Kenner, R., & Magnusson, J. (2016). Estimating the effect of different influencing factors on rock glacier development in two regions in the Swiss Alps. Permafrost and Periglacial Processes, 28(1), 195–208. https://doi.org/10.1002/ppp.1910

Kenner, R., Noetzli, J., Bazargan, M., & Scherrer, S. C. (2024). Response of alpine ground temperatures to a rising atmospheric 0 °C isotherm in the period 1955–2021. Science of the Total Environment, 171446. https://doi.org/10.1016/j.scitotenv.2024.171446

Kenner, R., Noetzli, J., Hoelzle, M., Raetzo, H., & Phillips, M. (2019). Distinguishing ice-rich and ice-poor permafrost to map ground temperatures and ground ice occurrence in the Swiss Alps. The Cryosphere, 13(7), 1925–1941. https://doi.org/10.5194/tc-13-1925-2019

Kirkbride, M. P. (1993). The temporal significance of transitions from melting to calving termini at glaciers in the central Southern Alps of New Zealand. Holocene, 3(3), 232–240. https://doi.org/10.1177/095968369300300305

Kirkbride, M. P., & Deline, P. (2013). The formation of supraglacial debris covers by primary dispersal from transverse englacial debris bands. Earth Surface Processes and Landforms, 38(15), 1779–1792. https://doi.org/10.1002/esp.3416

Kos, A., Amann, F., Strozzi, T., Delaloye, R., Von Ruette, J., & Springman, S. M. (2016). Contemporary glacier retreat triggers a rapid landslide response, Great Aletsch Glacier, Switzerland. Geophysical Research Letters, 43(24). https://doi.org/10.1002/2016gl071708

Kraaijenbrink, P. D. A., Shea, J. M., Litt, M., Steiner, J. F., Treichler, D., Koch, I., & Immerzeel, W. W. (2018). Mapping surface temperatures on a Debris-Covered glacier with an unmanned aerial vehicle. Frontiers in Earth Science, 6. https://doi.org/10.3389/feart.2018.00064

Kraaijenbrink, P. D. A., Stigter, E. E., Yao, T., & Immerzeel, W. W. (2021). Climate change decisive for Asia's snow meltwater supply. Nature Climate Change, 11(7), 591–597. https://doi.org/10.1038/s41558-021-01074-x

Kraaijenbrink, P., Bierkens, M., Lutz, A., & Immerzeel, W. (2017). Impact of a global temperature rise of 1.5 degrees Celsius on Asia's glaciers. Nature, 549(7671), 257–260. https://doi.org/10.1038/nature23878

Krautblatter, M., & Leith, K. (2015). Glacier- and permafrost-related slope instabilities. In Cambridge University Press eBooks (pp. 147–165). https://doi.org/10.1017/cbo9781107588653.009

Krautblatter, M., Funk, D., & Günzel, F. K. (2013). Why permafrost rocks become unstable: a rock–ice-mechanical model in time and space. Earth Surface Processes and Landforms, 38(8), 876–887. https://doi.org/10.1002/esp.3374

Krautblatter, M., Weber, S., Dietze, M., Keuschnig, M., Stockinger, G., Brückner, L., Beutel, J., Figl, T., Trepmann, C., Hofmann, R., Rau, M., Pfluger, F., Barbosa Mejia, L., and Siegert, F. (2024). The 2023 Fluchthorn massive permafrost rock slope failure analysed, EGU General Assembly 2024, Vienna, Austria, 14–19 Apr 2024, EGU24-20989, https://doi.org/10.5194/egusphere-egu24-20989

Kuenzer, C., & Dech, S. (2013). Thermal infrared remote sensing: Sensors, Methods, Applications. Springer Science & Business Media.

Levermore, G., Parkinson, J., Lee, K., Laycock, P. J., & Lindley, S. (2018). The increasing trend of the urban heat island intensity. Urban Climate, 24, 360–368. https://doi.org/10.1016/j.uclim.2017.02.004

Li, J., Li, Z., Wu, H., & You, N. (2022). Trend, seasonality, and abrupt change detection method for land surface temperature time-series analysis: Evaluation and improvement. Remote Sensing of Environment, 280, 113222. https://doi.org/10.1016/j.rse.2022.113222

Li, Y., Li, Z., Wu, H., Zhou, C., Li, X., Leng, P., Yang, P., Wu, W., Tang, R., Shang, G., & Ma, L. (2023). Biophysical impacts of earth greening can substantially mitigate regional land surface temperature warming. Nature Communications, 14(1). https://doi.org/10.1038/s41467-023-35799-4

Li, Y., Zhao, M., Motesharrei, S., Mu, Q., Kalnay, E., & Li, S. (2015). Local cooling and warming effects of forests based on satellite observations. Nature Communications, 6(1). https://doi.org/10.1038/ncomms7603

Li, Z., Wu, H., Duan, S., Zhao, W., Ren, H., Li, X., Leng, P., Tang, R., Ye, X., Zhu, J., Sun, Y., Si, M., Liu, M., Li, J., Zhang, X., Shang, G., Tang, B., Yan, G., and Zhou, C.: Satellite Remote sensing of global land surface temperature: definition, methods, products, and applications, Reviews of Geophysics, 61, https://doi.org/10.1029/2022rg000777, 2023.

Li, Z., Wu, H., Duan, S., Zhao, W., Ren, H., Li, X., Leng, P., Tang, R., Ye, X., Zhu, J., Sun, Y., Si, M., Liu, M., Li, J., Zhang, X., Shang, G., Tang, B., Yan, G., & Zhou, C. (2023). Satellite Remote sensing of global land surface temperature: definition, methods, products, and applications. Reviews of Geophysics, 61(1). https://doi.org/10.1029/2022rg000777

Li, Z., Tang, B., Wu, H., Ren, H., Yan, G., Wan, Z., Trigo, I. F., & Sobrino, J. A. (2013b). Satellite-derived land surface temperature: Current status and perspectives. Remote Sensing of Environment, 131, 14–37. https://doi.org/10.1016/j.rse.2012.12.008

Liu, Z., Zhan, W., Bechtel, B., Voogt, J. A., Lai, J., Chakraborty, T., Wang, Z., Li, M., Huang, F., & Lee, X. (2022). Surface warming in global cities is substantially more rapid than in rural background areas. Communications Earth & Environment, 3(1). https://doi.org/10.1038/s43247-022-00539-x

Lui, X., Tang, B., Yan, G., Li, Z., & Liang, S. (2019). Retrieval of Global Orbit Drift Corrected Land Surface Temperature from Long-term AVHRR Data. Remote Sensing, 11(23), 2843. https://doi.org/10.3390/rs11232843

Ma, J., Zhou, J., Göttsche, F., Liang, S., Wang, S., & Li, M. (2020). A global long-term (1981–2000) land surface temperature product for NOAA AVHRR. Earth System Science Data, 12(4), 3247–3268. https://doi.org/10.5194/essd-12-3247-2020

Mair, D., Lechmann, A., Delunel, R., Yeşilyurt, S., Tikhomirov, D., Vockenhuber, C., Christl, M., Akçar, N., & Schlunegger, F. (2020). The role of frost cracking in local denudation of steep Alpine rockwalls over millennia (Eiger, Switzerland). Earth Surface Dynamics, 8(3), 637–659. https://doi.org/10.5194/esurf-8-637-2020

Malakar, N. K., Hulley, G. C., Hook, S. J., Laraby, K., Cook, M., & Schott, J. R. (2018). An Operational Land Surface Temperature Product for Landsat Thermal Data: Methodology and Validation. IEEE Transactions on Geoscience and Remote Sensing, 56(10), 5717–5735. https://doi.org/10.1109/tgrs.2018.2824828

Malbéteau, Y., Parkes, S., Aragon, B., Rosas, J., & McCabe, M. F. (2018). Capturing the diurnal cycle of land surface temperature using an unmanned aerial vehicle. Remote Sensing, 10(9), 1407. https://doi.org/10.3390/rs10091407

Matiu, M., Crespi, A., Bertoldi, G., Carmagnola, C. M., Marty, C., Morin, S., Schöner, W., Berro, D. C., Chiogna, G., De Gregorio, L., Kotlarski, S., Majone, B., Resch, G., Terzago, S., Valt, M., Beozzo, W., Cianfarra, P., Gouttevin, I., Marcolini, G., . . . Weilguni, V. (2021). Observed snow depth trends in the European Alps: 1971 to 2019. The Cryosphere, 15(3), 1343–1382. https://doi.org/10.5194/tc-15-1343-2021

Matsuoka, N., & Murton, J. B. (2008). Frost weathering: recent advances and future directions. Permafrost and Periglacial Processes, 19(2), 195–210. https://doi.org/10.1002/ppp.620

Mauder, M., Foken, T., & Cuxart, J. (2020). Surface-Energy-Balance Closure over Land: A Review. Boundary-layer Meteorology/Boundary - Layer Meteorology, 177(2–3), 395–426. https://doi.org/10.1007/s10546-020-00529-6

McCarthy, M. J. (2019). Quantifying supraglacial debris thickness at local to regional scales. https://doi.org/10.17863/cam.41172

McCarthy, M., Pritchard, H., Willis, I., & King, E. (2017). Ground-penetrating radar measurements of debris thickness on Lirung Glacier, Nepal. Journal of Glaciology/Journal of Glaciology, 63(239), 543–555. https://doi.org/10.1017/jog.2017.18

McDowell, G., Stevens, M., Lesnikowski, A., Huggel, C., Harden, A., DiBella, J., Morecroft, M., Kumar, P., Joe, E. T., & Bhatt, I. D. (2021). Closing the adaptation gap in Mountains. Mountain Research and Development, 41(3). https://doi.org/10.1659/mrd-journal-d-21-00033.1

McShane, R. R., Driscoll, K. P., & Sando, R. (2017). A review of surface energy balance models for estimating actual evapotranspiration with remote sensing at high spatiotemporal resolution over large extents. Scientific Investigations Report. https://doi.org/10.3133/sir20175087

Merchant, C. J., Matthiesen, S., Rayner, N. A., Remedios, J. J., Jones, P. D., Olesen, F., Trewin, B., Thorne, P. W., Auchmann, R., Corlett, G. K., Guillevic, P. C., & Hulley, G. C. (2013). The surface temperatures of Earth: steps towards integrated understanding of variability and change. Geoscientific Instrumentation, Methods and Data Systems, 2(2), 305–321. https://doi.org/10.5194/gi-2-305-2013

Mesas-Carrascosa, F., Pérez-Porras, F., De Larriva, J. E. M., Frau, C. M., Agüera-Vega, F., Carvajal-Ramírez, F., Martínez-Carricondo, P., & García-Ferrer, A. (2018). Drift correction of lightweight microbolometer thermal sensors On-Board unmanned aerial vehicles. Remote Sensing, 10(4), 615. https://doi.org/10.3390/rs10040615

Messager, M. L., Lehner, B., Grill, G., Nedeva, I., & Schmitt, O. (2016). Estimating the volume and age of water stored in global lakes using a geo-statistical approach. Nature Communications, 7(1). https://doi.org/10.1038/ncomms13603

Messmer, J., & Groos, A. R. (2024). A low-cost and open-source approach for supraglacial debris thickness mapping using UAV-based infrared thermography. □the □Cryosphere, 18(2), 719–746. https://doi.org/10.5194/tc-18-719-2024

Mihalcea, C., Brock, B., Diolaiuti, G., D'Agata, C., Citterio, M., Kirkbride, M., Cutler, M., & Smiraglia, C. (2008). Using ASTER satellite and ground-based surface temperature measurements to derive supraglacial debris cover and thickness patterns on Miage Glacier (Mont Blanc Massif, Italy). Cold Regions Science and Technology, 52(3), 341–354. https://doi.org/10.1016/j.coldregions.2007.03.004

Mildrexler, D. J., Zhao, M., & Running, S. W. (2011). A global comparison between station air temperatures and MODIS land surface temperatures reveals the cooling role of forests. Journal of Geophysical Research, 116(G3). https://doi.org/10.1029/2010jg001486

Miles, E. S., Steiner, J. F., & Brun, F. (2017). Highly variable aerodynamic roughness length (z0) for a hummocky debris-covered glacier. Journal of Geophysical Research. Atmospheres, 122(16), 8447–8466. https://doi.org/10.1002/2017jd026510

Miles, E. S., Steiner, J. F., Buri, P., Immerzeel, W. W., & Pellicciotti, F. (2022). Controls on the relative melt rates of debris-covered glacier surfaces. Environmental Research Letters, 17(6), 064004. https://doi.org/10.1088/1748-9326/ac6966

Miles, E. S., Willis, I., Buri, P., Steiner, J. F., Arnold, N. S., & Pellicciotti, F. (2017). Surface pond energy absorption across four Himalayan glaciers accounts for 1/8 of total catchment ice loss. Geophysical Research Letters, 45(19). https://doi.org/10.1029/2018gl079678

Mohan, M. M. P., Kanchirapuzha, R., & Varma, M. R. R. (2020). Review of approaches for the estimation of sensible heat flux in remote sensing-based evapotranspiration models. Journal of Applied Remote Sensing, 14(04). https://doi.org/10.1117/1.jrs.14.041501

Mountain Research Initiative EDW Working Group. (2015). Elevation-dependent warming in mountain regions of the world. Nature Climate Change, 5(5), 424–430. https://doi.org/10.1038/nclimate2563

Muro, J., Strauch, A., Heinemann, S., Steinbach, S., Thonfeld, F., Waske, B., & Diekkrüger, B. (2018). Land surface temperature trends as indicator of land use changes in wetlands. International Journal of Applied Earth Observation and Geoinformation, 70, 62–71. https://doi.org/10.1016/j.jag.2018.02.002

Nakawo, M., & Young, G. (1981). Field experiments to determine the effect of a debris layer on ablation of glacier ice. Annals of Glaciology, 2, 85–91. https://doi.org/10.3189/172756481794352432

Neteler, M., Roiz, D., Rocchini, D., Castellani, C., & Rizzoli, A. (2011). Terra and Aqua satellites track tiger mosquito invasion: modelling the potential distribution of Aedes albopictus in north-eastern Italy. International Journal of Health Geographics, 10(1), 49. https://doi.org/10.1186/1476-072x-10-49

Nicholson, L., & Benn, D. I. (2006). Calculating ice melt beneath a debris layer using meteorological data. Journal of Glaciology/Journal of Glaciology, 52(178), 463–470. https://doi.org/10.3189/172756506781828584

Nicholson, L., & Mertes, J. (2017). Thickness estimation of supraglacial debris above ice cliff exposures using a high-resolution digital surface model derived from terrestrial photography. Journal of Glaciology/Journal of Glaciology, 63(242), 989–998. https://doi.org/10.1017/jog.2017.68

Nigrelli, G., & Chiarle, M. (2023). 1991–2020 climate normal in the European Alps: focus on high-elevation environments. Journal of Mountain Science/Journal of Mountain Science, 20(8), 2149–2163. https://doi.org/10.1007/s11629-023-7951-7

Norman, J. M., & Becker, F. (1995). Terminology in thermal infrared remote sensing of natural surfaces. Agricultural and Forest Meteorology, 77(3–4), 153–166. https://doi.org/10.1016/0168-1923(95)02259-z

Notarnicola, C. (2020). Hotspots of snow cover changes in global mountain regions over 2000–2018. Remote Sensing of Environment, 243, 111781. https://doi.org/10.1016/j.rse.2020.111781

Oerlemans, J., & Greuell, W. (1986). Sensitivity studies with a mass balance model including temperature profile calculations inside the glacier. Zeitschrift Für Gletscherkunde Und Glazialgeologie, 22(2), 101–124. http://dspace.library.uu.nl/handle/1874/21035

Östrem, G. (1959). Ice Melting under a Thin Layer of Moraine, and the Existence of Ice Cores in Moraine Ridges. Geografiska Annaler, 41(4), 228–230. https://doi.org/10.1080/20014422.1959.11907953

Pastor, F., Valiente, J., & Palau, J. L. (2017). Sea surface temperature in the Mediterranean: Trends and spatial Patterns (1982–2016). Pure and Applied Geophysics, 175(11), 4017–4029. https://doi.org/10.1007/s00024-017-1739-z

Pedregosa, F., Varoquaux, G., Gramfort, A., Michel, V., Thirion, B., Grisel, O., Blondel, M., Prettenhofer, P., Weiss, R., Dubourg, V., Vanderplas, J., Passos, A., Cournapeau, D., Brucher, M., Perrot, M., & Duchesnay, É. (2011). Scikit-learn: Machine Learning in Python. Journal of Machine Learning Research. http://jmlr.org/papers/v12/pedregosa11a.html

Pellicciotti, F., Carenzo, M., Bordoy, R., & Stoffel, M. (2014). Changes in glaciers in the Swiss Alps and impact on basin hydrology: Current state of the art and future research. Science of the Total Environment, 493, 1152–1170. https://doi.org/10.1016/j.scitotenv.2014.04.022

Pellicciotti, F., Stephan, C., Miles, E., Herreid, S., Immerzeel, W. W., & Bolch, T. (2015). Mass-balance changes of the debris-covered glaciers in the Langtang Himal, Nepal, from 1974 to 1999. Journal of Glaciology/Journal of Glaciology, 61(226), 373–386. https://doi.org/10.3189/2015jog13j237

Pepin, N. C., & Lundquist, J. D. (2008). Temperature trends at high elevations: Patterns across the globe. Geophysical Research Letters, 35(14). https://doi.org/10.1029/2008gl034026

Pepin, N., Adler, C., Kotlarksi, S., & Palazzi, E. (2022). Mountains undergo enhanced impacts of climate change. Eos, 103. https://doi.org/10.1029/2022eo185278

Perugini, L., Caporaso, L., Marconi, S., Cescatti, A., Quesada, B., De Noblet-Ducoudré, N., House, J. I., & Arneth, A. (2017). Biophysical effects on temperature and precipitation due to land cover change. Environmental Research Letters, 12(5), 053002. https://doi.org/10.1088/1748-9326/aa6b3f

Pielke, R. A., Pitman, A. J., Niyogi, D., Mahmood, R., McAlpine, C., Hossain, F., Goldewijk, K. K., Nair, U. S., Betts, R., Fall, S., Reichstein, M., Kabat, P., & De Noblet, N. (2011). Land use/land cover changes and climate: modeling analysis and observational evidence. Wiley Interdisciplinary Reviews. Climate Change, 2(6), 828–850. https://doi.org/10.1002/wcc.144

Pinheiro, A., Mahoney, R., Privette, J., & Tucker, C. (2006). Development of a daily long term record of NOAA-14 AVHRR land surface temperature over Africa. Remote Sensing of Environment, 103(2), 153–164. https://doi.org/10.1016/j.rse.2006.03.009

Pitman, A. J., Avila, F. B., Abramowitz, G., Wang, Y., Phipps, S. J., & De Noblet-Ducoudré, N. (2011). Importance of background climate in determining impact of land-cover change on regional climate. Nature Climate Change, 1(9), 472–475. https://doi.org/10.1038/nclimate1294

Pongratz, J., Schwingshackl, C., Bultan, S., Obermeier, W. A., Havermann, F., & Guo, S. (2021). Land Use Effects on climate: current state, recent progress, and emerging topics. Current Climate Change Reports, 7(4), 99–120. https://doi.org/10.1007/s40641-021-00178-y

Prata, A. J.: Land surface temperatures derived from the advanced very high resolution radiometer and the along-track scanning radiometer: 2. Experimental results and validation of AVHRR algorithms, Journal of Geophysical Research, 99, 13025–13058, https://doi.org/10.1029/94jd00409, 1994.

Prevedello, J. A., Winck, G. R., De Moraes Weber, M., Nichols, E., & Sinervo, B. (2019). Impacts of forestation and deforestation on local temperature across the globe. PloS One, 14(3), e0213368. https://doi.org/10.1371/journal.pone.0213368

Price, J. C. (1984). Land surface temperature measurements from the split window channels of the NOAA 7 Advanced Very High Resolution Radiometer. Journal of Geophysical Research, 89(D5), 7231–7237. https://doi.org/10.1029/jd089id05p07231

Price, J. C. (1985). On the analysis of thermal infrared imagery: The limited utility of apparent thermal inertia. Remote Sensing of Environment, 18(1), 59–73. https://doi.org/10.1016/0034-4257(85)90038-0

Pulliainen, J., Luojus, K., Derksen, C., Mudryk, L., Lemmetyinen, J., Salminen, M., Ikonen, J., Takala, M., Cohen, J., Smolander, T., & Norberg, J. (2020). Patterns and trends of Northern Hemisphere snow mass from 1980 to 2018. Nature, 581(7808), 294–298. https://doi.org/10.1038/s41586-020-2258-0

Qiu, S., Zhu, Z., Shang, R., & Crawford, C. J. (2021). Can Landsat 7 preserve its science capability with a drifting orbit? Science of Remote Sensing, 4, 100026. https://doi.org/10.1016/j.srs.2021.100026

Radić, V., & Hock, R. (2011). Regionally differentiated contribution of mountain glaciers and ice caps to future sea-level rise. Nature Geoscience, 4(2), 91–94. https://doi.org/10.1038/ngeo1052

Rangwala, I., & Miller, J. R. (2012). Climate change in mountains: a review of elevation-dependent warming and its possible causes. Climatic Change, 114(3–4), 527–547. https://doi.org/10.1007/s10584-012-0419-3

Ravanel, L., Magnin, F., & Deline, P. (2017). Impacts of the 2003 and 2015 summer heatwaves on permafrost-affected rock-walls in the Mont Blanc massif. Science of the Total Environment, 609, 132–143. https://doi.org/10.1016/j.scitotenv.2017.07.055

Reid, T. D., & Brock, B. W. (2010). An energy-balance model for debris-covered glaciers including heat conduction through the debris layer. Journal of Glaciology/Journal of Glaciology, 56(199), 903–916. https://doi.org/10.3189/002214310794457218

Reiners, P., Sobrino, J., & Kuenzer, C. (2023). Satellite-Derived Land Surface Temperature Dynamics In the Context of Global Change—A Review. Remote Sensing, 15(7), 1857. https://doi.org/10.3390/rs15071857

Ren, S., Yao, T., Yang, W., Miles, E., Zhao, H., Zhu, M., and Li, S.: Changes in glacier surface temperature across the Third Pole from 2000 to 2021, Remote Sensing of Environment, 305, 114076, https://doi.org/10.1016/j.rse.2024.114076, 2024.

Reznichenko, N., Davies, T., Shulmeister, J., & McSaveney, M. (2010). Effects of debris on ice-surface melting rates: an experimental study. Journal of Glaciology/Journal of Glaciology, 56(197), 384–394. https://doi.org/10.3189/002214310792447725

RGI Consortium. (2023). Randolph Glacier Inventory: A Dataset of Global Glacier Outlines (Version 7) [Dataset]. National Snow and Ice Data Center. Boulder, Colorado USA. https://doi.org/10.5067/F6JMOVY5NAVZ

Ribeiro-Gomes, K., Hernández-López, D., Ortega, J. F., Ballesteros, R., Poblete, T., & Moreno, M. A. (2017). Uncooled thermal camera calibration and optimization of the photogrammetry process for UAV applications in agriculture. Sensors, 17(10), 2173. https://doi.org/10.3390/s17102173

Rottler, E., Kormann, C., Francke, T., & Bronstert, A. (2019). Elevation-dependent warming in the Swiss Alps 1981–2017: Features, forcings and feedbacks. International Journal of Climatology, 39(5), 2556–2568. https://doi.org/10.1002/joc.5970

Rounce, D. R., & McKinney, D. C. (2014). Debris thickness of glaciers in the Everest area (Nepal Himalaya) derived from satellite imagery using a nonlinear energy balance model. □the □Cryosphere, 8(4), 1317–1329. https://doi.org/10.5194/tc-8-1317-2014

Rounce, D. R., Hock, R., Maussion, F., Hugonnet, R., Kochtitzky, W., Huss, M., Berthier, E., Brinkerhoff, D., Compagno, L., Copland, L., Farinotti, D., Menounos, B., & McNabb, R. W. (2023). Global glacier change in the 21st century: Every increase in temperature matters. Science, 379(6627), 78–83. https://doi.org/10.1126/science.abo1324

Rounce, D. R., Hock, R., McNabb, R., Millan, R., Sommer, C., Braun, M., Malz, P., Maussion, F., Mouginot, J., Seehaus, T., & Shean, D. (2021). Distributed global debris thickness estimates reveal debris significantly impacts glacier mass balance. Geophysical Research Letters, 48(8). https://doi.org/10.1029/2020gl091311

Rounce, D. R., King, O., McCarthy, M., Shean, D. E., & Salerno, F. (2018). Quantifying debris thickness of Debris-Covered glaciers in the Everest region of Nepal through inversion of a subdebris melt model. Journal of Geophysical Research. Earth Surface, 123(5), 1094–1115. https://doi.org/10.1029/2017jf004395

Roy, D. P., Li, Z., Zhang, H. K., & Huang, H. (2020). A conterminous United States analysis of the impact of Landsat 5 orbit drift on the temporal consistency of Landsat 5 Thematic Mapper data. Remote Sensing of Environment, 240, 111701. https://doi.org/10.1016/j.rse.2020.111701

Rublee, E., Rabaud, V., Konolige, K., & Bradski, G. (2011). ORB: An efficient alternative to SIFT or SURF. Proceedings of the IEEE International Conference on Computer Vision. https://doi.org/10.1109/iccv.2011.6126544

Rumpf, S. B., Gravey, M., Broennimann, O., Luoto, M., Cianfrani, C., Mariéthoz, G., & Guisan, A. (2022). From white to green: Snow cover loss and increased vegetation productivity in the European Alps. Science, 376(6597), 1119–1122. https://doi.org/10.1126/science.abn6697

Rusinkiewicz, S., & Levoy, M. (2002). Efficient variants of the ICP algorithm. Proc. Int. Conf. 3-D Digit. Imaging Model. https://doi.org/10.1109/im.2001.924423

Sakallı, A. (2017). SEA SURFACE TEMPERATURE CHANGE IN THE MEDITERRANEAN SEA UNDER CLIMATE CHANGE: a LINEAR MODEL FOR SIMULATION OF THE SEA SURFACE TEMPERATURE UP TO 2100. Applied Ecology and Environmental Research, 15(1), 707–716. https://doi.org/10.15666/aeer/1501_707716

Schauwecker, S., Rohrer, M., Huggel, C., Kulkarni, A., Ramanathan, A., Salzmann, N., Stoffel, M., & Brock, B. (2015). Remotely sensed debris thickness mapping of Bara Shigri Glacier, Indian Himalaya. Journal of Glaciology/Journal of Glaciology, 61(228), 675–688. https://doi.org/10.3189/2015jog14j102

Scherler, D., Langer, M., Wulf, H., Gök, D., and Phillips, M. (2024). Simulating ground temperatures in mountainous terrain with remote sensing observations and modeling. EGU General Assembly 2024, Vienna, Austria, 14–19 Apr 2024, EGU24-14950, https://doi.org/10.5194/egusphere-egu24-14950.

Scherler, D., & Egholm, D. L. (2020). Production and transport of supraglacial debris: Insights from Cosmogenic 10BE and Numerical Modeling, Chhota Shigri Glacier, Indian Himalaya. Journal of Geophysical Research. Earth Surface, 125(10). https://doi.org/10.1029/2020jf005586

Scherler, D., Bookhagen, B., & Strecker, M. R. (2011a). Hillslope-glacier coupling: The interplay of topography and glacial dynamics in High Asia. Journal of Geophysical Research, 116(F2). https://doi.org/10.1029/2010jf001751

Scherler, D., Bookhagen, B., & Strecker, M. R. (2011b). Spatially variable response of Himalayan glaciers to climate change affected by debris cover. Nature Geoscience, 4(3), 156–159. https://doi.org/10.1038/ngeo1068

Scherler, D., Wulf, H., & Gorelick, N. (2018). Global Assessment of Supraglacial Debris-Cover Extents. Geophysical Research Letters, 45(21). https://doi.org/10.1029/2018gl080158

Schneider, D. P., Deser, C., Fasullo, J., & Trenberth, K. E. (2013). Climate data guide spurs discovery and understanding. Eos, 94(13), 121–122. https://doi.org/10.1002/2013eo130001

Schneider, P., & Hook, S. J. (2010). Space observations of inland water bodies show rapid surface warming since 1985. Geophysical Research Letters, 37(22). https://doi.org/10.1029/2010gl045059

Schneider, P., Hook, S. J., Radocinski, R. G., Corlett, G. K., Hulley, G., Schladow, S. G., & Steissberg, T. E. (2009). Satellite observations indicate rapid warming trend for lakes in California and Nevada. Geophysical Research Letters, 36(22). https://doi.org/10.1029/2009gl040846

Schwaab, J., Meier, R., Mussetti, G., Seneviratne, S., Bürgi, C., & Davin, E. L. (2021). The role of urban trees in reducing land surface temperatures in European cities. Nature Communications, 12(1). https://doi.org/10.1038/s41467-021-26768-w

Seidel, D. J., & Free, M. (2003). Comparison of Lower-Tropospheric Temperature Climatologies and Trends at Low and High Elevation Radiosonde Sites. In Advances in global change research (pp. 53–74). https://doi.org/10.1007/978-94-015-1252-7_4

Shaw, T. E., Brock, B. W., Fyffe, C. L., Pellicciotti, F., Rutter, N., & Diotri, F. (2016). Air temperature distribution and energy-balance modelling of a debris-covered glacier. Journal of Glaciology/Journal of Glaciology, 62(231), 185–198. https://doi.org/10.1017/jog.2016.31

Shugar, D. H., Jacquemart, M., Shean, D., Bhushan, S., Upadhyay, K., Sattar, A., Schwanghart, W., McBride, S., Van Wyk De Vries, M., Mergili, M., Emmer, A., Deschamps-Berger, C., McDonnell, M., Bhambri, R., Allen, S., Berthier, E., Carrivick, J. L., Clague, J. J., Dokukin, M., . . . Westoby, M. (2021). A massive rock and ice avalanche caused the 2021 disaster at Chamoli, Indian Himalaya. Science, 373(6552), 300–306. https://doi.org/10.1126/science.abh4455

Shukla, A., Gupta, R., & Arora, M. (2009). Estimation of debris cover and its temporal variation using optical satellite sensor data: a case study in Chenab basin, Himalaya. Journal of Glaciology/Journal of Glaciology, 55(191), 444–452. https://doi.org/10.3189/002214309788816632

Shumway, R. H., & Stoffer, D. S. (2011). Time Series Analysis and its applications. In Springer texts in statistics. https://doi.org/10.1007/978-1-4419-7865-3

Sismanidis, P., Bechtel, B., Keramitsoglou, I., Göttsche, F., & Kiranoudis, C. T. (2021). Satellite-derived quantification of the diurnal and annual dynamics of land surface temperature. Remote Sensing of Environment, 265, 112642. https://doi.org/10.1016/j.rse.2021.112642

Smith, S. L., O'Neill, H. B., Isaksen, K., Noetzli, J., & Romanovsky, V. E. (2022). The changing thermal state of permafrost. Nature Reviews. Earth & Environment, 3(1), 10–23. https://doi.org/10.1038/s43017-021-00240-1

Smith, T., & Bookhagen, B. (2018). Changes in seasonal snow water equivalent distribution in High Mountain Asia (1987 to 2009). Science Advances, 4(1). https://doi.org/10.1126/sciadv.1701550

Sobrino, J. A., & Cuenca, J. (1999). Angular variation of thermal infrared emissivity for some natural surfaces from experimental measurements. Applied Optics, 38(18), 3931. https://doi.org/10.1364/ao.38.003931

Sobrino, J. A., Julien, Y., & García-Monteiro, S. (2020). Surface Temperature of the Planet Earth from Satellite Data. Remote Sensing, 12(2), 218. https://doi.org/10.3390/rs12020218

Sobrino, J. A., Julien, Y., Atitar, M., & Nerry, F. (2008). NOAA-AVHRR Orbital drift correction from Solar Zenithal angle data. IEEE Transactions on Geoscience and Remote Sensing, 46(12), 4014–4019. https://doi.org/10.1109/tgrs.2008.2000798

Steiner, J. F., Kraaijenbrink, P. D. A., & Immerzeel, W. W. (2021). Distributed melt on a Debris-Covered glacier: field observations and melt modeling on the Lirung glacier in the Himalaya. Frontiers in Earth Science, 9. https://doi.org/10.3389/feart.2021.678375

Steiner, J. F., Litt, M., Stigter, E. E., Shea, J., Bierkens, M. F. P., & Immerzeel, W. W. (2018). The importance of turbulent fluxes in the surface energy balance of a Debris-Covered glacier in the Himalayas. Frontiers in Earth Science, 6. https://doi.org/10.3389/feart.2018.00144

Stewart, R. L., Westoby, M., Pellicciotti, F., Rowan, A., Swift, D., Brock, B., & Woodward, J. (2021). Using climate reanalysis data in conjunction with multi-temporal satellite thermal imagery to derive supraglacial debris thickness changes from energy-balance modelling. Journal of Glaciology/Journal of Glaciology, 67(262), 366–384. https://doi.org/10.1017/jog.2020.111

Stoffel, M., & Huggel, C. (2012). Effects of climate change on mass movements in mountain environments. Progress in Physical Geography, 36(3), 421–439. https://doi.org/10.1177/0309133312441010

Stoffel, M., Trappmann, D. G., Coullie, M. I., Cánovas, J. a. B., & Corona, C. (2024). Rockfall from an increasingly unstable mountain slope driven by climate warming. Nature Geoscience, 17(3), 249–254. https://doi.org/10.1038/s41561-024-01390-9

Stooksbury, D. E., Idso, C. D., & Hubbard, K. G. (1999). The effects of data gaps on the calculated monthly mean maximum and minimum temperatures in the continental United States: A Spatial and Temporal study. Journal of Climate, 12(5), 1524–1533. https://doi.org/10.1175/1520-0442(1999)012

Swisstopo. (n.d.). ALTI 3d DEM. Retrieved July 7, 2021, from https://www.swisstopo.admin.ch/de/geodata/height/alti3d.html#download

Taylor, C., Robinson, T., Dunning, S., Carr, J. R., & Westoby, M. (2023). Glacial lake outburst floods threaten millions globally. Nature Communications, 14(1). https://doi.org/10.1038/s41467-023-36033-x

Thornton, J., Snethlage, M. A., Sayre, R., Urbach, D., Viviroli, D., Ehrlich, D., Muccione, V., Wester, P., Insarov, G., & Adler, C. (2022). Human populations in the world's mountains: Spatio-temporal patterns and potential controls. PloS One, 17(7), e0271466. https://doi.org/10.1371/journal.pone.0271466

Tielidze, L. G., Bolch, T., Wheate, R. D., Kutuzov, S. S., Lavrentiev, I. I., & Zemp, M. (2020). Supra-glacial debris cover changes in the Greater Caucasus from 1986 to 2014. The Cryosphere, 14(2), 585–598. https://doi.org/10.5194/tc-14-585-2020

Torres-Rua, A. F. (2017). Vicarious calibration of SUAS microbolometer temperature imagery for estimation of radiometric land surface temperature. Sensors, 17(7), 1499. https://doi.org/10.3390/s17071499

Trewin, B. (2010). Exposure, instrumentation, and observing practice effects on land temperature measurements. Wiley Interdisciplinary Reviews. Climate Change, 1(4), 490–506. https://doi.org/10.1002/wcc.46

Van Der Walt, S., Schönberger, J. L., Nunez-Iglesias, J., Boulogne, F., Warner, J. D., Yager, N., Gouillart, E., & Yu, T. (2014). scikit-image: image processing in Python. PeerJ, 2, e453. https://doi.org/10.7717/peerj.453

Veh, G., Korup, O., & Walz, A. (2019). Hazard from Himalayan glacier lake outburst floods. Proceedings of the National Academy of Sciences of the United States of America, 117(2), 907–912. https://doi.org/10.1073/pnas.1914898117

Verbesselt, J., Hyndman, R. J., Newnham, G., & Culvenor, D. (2010). Detecting trend and seasonal changes in satellite image time series. Remote Sensing of Environment, 114(1), 106–115. https://doi.org/10.1016/j.rse.2009.08.014

Viviroli, D., Kummu, M., Meybeck, M., Kallio, M., & Wada, Y. (2020). Increasing dependence of lowland populations on mountain water resources. Nature Sustainability, 3(11), 917–928. https://doi.org/10.1038/s41893-020-0559-9

Walter, F., Amann, F., Kos, A., Kenner, R., Phillips, M., De Preux, A., Huss, M., Tognacca, C., Clinton, J., Diehl, T., & Bonanomi, Y. (2020). Direct observations of a three million cubic meter rock-slope collapse with almost immediate initiation of ensuing debris flows. Geomorphology, 351, 106933. https://doi.org/10.1016/j.geomorph.2019.106933

Wang, Q., Tang, Y., Tong, X., & Atkinson, P. M. (2024). Filling gaps in cloudy Landsat LST product by spatial-temporal fusion of multi-scale data. Remote Sensing of Environment, 306, 114142. https://doi.org/10.1016/j.rse.2024.114142

Waring, A. M., Ghent, D., Perry, M., Anand, J. S., Veal, K. L., & Remedios, J. (2023). Regional climate trend analyses for Aqua MODIS land surface temperatures. International Journal of Remote Sensing, 44(16), 4989–5032. https://doi.org/10.1080/01431161.2023.2240522

Weng, Q., & Fu, P. (2014). Modeling annual parameters of clear-sky land surface temperature variations and evaluating the impact of cloud cover using time series of Landsat TIR data. Remote Sensing of Environment, 140, 267–278. https://doi.org/10.1016/j.rse.2013.09.002

Westermann, S., Langer, M., & Boike, J. (2011). Spatial and temporal variations of summer surface temperatures of high-arctic tundra on Svalbard — Implications for MODIS LST based permafrost monitoring. Remote Sensing of Environment, 115(3), 908–922. https://doi.org/10.1016/j.rse.2010.11.018

Westoby, M. J., Rounce, D. R., Shaw, T. E., Fyffe, C. L., Moore, P. L., Stewart, R. L., & Brock, B. W. (2020). Geomorphological evolution of a debris-covered glacier surface. Earth Surface Processes and Landforms, 45(14), 3431–3448. https://doi.org/10.1002/esp.4973

Wetterauer, K., Scherler, D., Anderson, L. S., & Wittmann, H. (2022). Temporal evolution of headwall erosion rates derived from cosmogenic nuclide concentrations in the medial moraines of Glacier d'Otemma, Switzerland. Earth Surface Processes and Landforms, 47(10), 2437–2454. https://doi.org/10.1002/esp.5386

Woolway, R. I., Kraemer, B. M., Lenters, J. D., Merchant, C. J., O'Reilly, C. M., & Sharma, S. (2020). Global lake responses to climate change. Nature Reviews. Earth & Environment, 1(8), 388–403. https://doi.org/10.1038/s43017-020-0067-5

Wulf, H., Sassik, B., Milani, G., & Leiterer, R. (2020). High-resolution snow depth monitoring for entire mountain ranges. 2020 7th Swiss Conference on Data Science (SDS), 1–4. https://doi.org/10.1109/sds49233.2020.00008

Zemp, M., Gärtner-Roer, I., Frey, H., Nussbaumer, S. U., Hoelzle, M., Paul, F., Denzinger, F., Haeberli, W., Ahlstrøm, A. P., Anderson, B., Baroni, C., Cáceres, B. E., Casassa, G., Cobos, G., Dávila, L. R., Delgado Granados, H., Demuth, M. N., Espizua, L., Fischer, A., . . . Vincent, C. (2015). Historically unprecedented global glacier decline in the early 21st century. Journal of Glaciology, 61(228), 745–762. https://doi.org/10.3189/2015JoG15J017

Zemp, M., Huss, M., Eckert, N., Thibert, E., Paul, F., Nussbaumer, S. U., & Gärtner-Roer, I. (2020). Brief communication: Ad hoc estimation of glacier contributions to sea-level rise from the latest glaciological observations. The Cryosphere, 14(3), 1043–1050. https://doi.org/10.5194/tc-14-1043-2020

Zhang, H. K., & Roy, D. P. (2016). Landsat 5 Thematic Mapper reflectance and NDVI 27-year time series inconsistencies due to satellite orbit change. Remote Sensing of Environment, 186, 217–233. https://doi.org/10.1016/j.rse.2016.08.022

Zhang, T. (2005). Influence of the seasonal snow cover on the ground thermal regime: An overview. Reviews of Geophysics, 43(4). https://doi.org/10.1029/2004rg000157

Zhang, Y., Fujita, K., Liu, S., Liu, Q., & Nuimura, T. (2011). Distribution of debris thickness and its effect on ice melt at Hailuogou glacier, southeastern Tibetan Plateau, using in situ surveys and ASTER imagery. Journal of Glaciology/Journal of Glaciology, 57(206), 1147–1157. https://doi.org/10.3189/002214311798843331

Zhang, Y., Gao, T., Kang, S., Shangguan, D., & Luo, X. (2021). Albedo reduction as an important driver for glacier melting in Tibetan Plateau and its surrounding areas. Earth-science Reviews, 220, 103735. https://doi.org/10.1016/j.earscirev.2021.103735

Zhao, W., Yang, M., Chang, R., Zhan, Q., and Li, Z.-L.: Surface warming trend analysis based on MODIS/Terra Land surface temperature product at Gongga Mountain in the southeastern Tibetan Plateau, Journal of Geophysical Research. Atmospheres, 126, https://doi.org/10.1029/2020jd034205, 2021.

Zhou, X., & Wang, Y. (2010). Dynamics of land surface temperature in response to Land-USe/Cover change. Geographical Research, 49(1), 23–36. https://doi.org/10.1111/j.1745-5871.2010.00686.x

Zhu, Z. and Woodcock, C. E.: Object-based cloud and cloud shadow detection in Landsat imagery, Remote Sensing of Environment, 118, 83–94, https://doi.org/10.1016/j.rse.2011.10.028, 2012.

A. Appendix A

Supplementary information to Chapter 2

Supplement A1 is part of the data publication: High-resolution debris cover mapping using UAV-derived thermal imagery published at GFZ Data Services.

Gök, Deniz; Scherler, Dirk; Anderson, Leif S. (2022): High-resolution debris cover mapping using UAV-derived thermal imagery. GFZ Data Services. https://doi.org/10.5880/GFZ.3.3.2022.003

Appendix A 1. Surface energy balance model to calculate debris thickness. Functions to calculate surface energy balance components and solve for debris thickness. Python implementation of the R Package Insol from Javier G. Corripio (2003), available through GFZ Data Services (https://doi.org/10.1080/713811744)

```
def JD(d):
    """
    Convert a datetime object to a julian date.
    Parameters:
    d (datetime object)
    Returns:
    JulianDay (float)
    """
    seconds_per_day = 86400
    JulianDay = d.timestamp() / seconds_per_day + 2440587.5
    return JulianDay


def hourangle(jd, longitude, timezone):
    """
    Function for solar position calculation.
    Parameters:
    jd (float)
    longitude (float)
    timezone (int)
    Returns:
    omega_r (float)
    """
    hour = ((jd-np.floor(jd))*24+12) % 24
    time_offset=eqtime(jd)
    standard_meridian=timezone * 15
    delta_longitude_time=(longitude-standard_meridian)*24.0/360.0
    omega_r = np.pi * (
        ((hour + delta_longitude_time + time_offset / 60) / 12.0) - 1.0)
    return omega_r
```

```
def eqtime(jd):
    """
    Calculate the equation of time.
    Parameters:
    jd (float)
    Returns:
    EqTime_deg (float)
    """
    jdc = (jd - 2451545.0) / 36525.0
    sec = 21.448 - jdc * (46.8150 + jdc * (0.00059 - jdc * 0.001813))
    e0 = 23.0 + (26.0 + (sec / 60.0)) / 60.0
    oblcorr = e0 + 0.00256 * np.cos(np.deg2rad(125.04 - 1934.136 * jdc))
    l0 = 280.46646 + jdc * (36000.76983 + jdc * 0.0003032)
    l0 = (l0 - 360 * (l0 // 360)) % 360
    gmas = 357.52911 + jdc * (35999.05029 - 0.0001537 * jdc)
    gmas = np.deg2rad(gmas)
    ecc = 0.016708634 - jdc * (0.000042037 + 0.0000001267 * jdc)
    y = (np.tan(np.deg2rad(oblcorr) / 2)) ** 2
    rl0 = np.deg2rad(l0)
    EqTime = y * np.sin(2 * rl0) \
        - 2.0 * ecc * np.sin(gmas) \
        + 4.0 * ecc * y * np.sin(gmas) * np.cos(2 * rl0)\
        - 0.5 * y * y * np.sin(4 * rl0) \
        - 1.25 * ecc * ecc * np.sin(2 * gmas)
    EqTime_deg = np.rad2deg(EqTime) * 4
    return EqTime_deg
```

```
def sunr(jd):
    """
    Earth-Sun distance in unit AU.
    Parameters:
    jd (float)
    Returns:
    R (float)
    """
    # Julian Centuries (Meeus, Astronomical Algorithms 1999. (24.1))
    T = (jd - 2451545)/36525.0
    # mean obliquity of the ecliptic (21.2)
    epsilon = (23+26/60.0+21.448/3600.0) - (46.8150/3600.0)*T - (0.00059/3600.0)*T**2 +
(0.001813/3600.0)*Taa**3
    # mean anomaly of the Sun (24.3)
    M = 357.52910 + 35999.05030*T - 0.0001559*T**2 - 0.00000048*T**3
    # eccentricity of the Earth's orbit (24.4)
    e = 0.016708617 - 0.000042037*T - 0.0000001236*T**2
    # Sun's equation of center
    C = (1.914600 - 0.004817*T - 0.000014*T**2)*np.sin(np.radians(M)) + (0.019993 -
0.000101*T)*np.sin(2*np.radians(M)) +0.000290*np.sin(3*np.radians(M))
    # Sun's true anomaly
    v = M + C
    # Sun's Radius Vector (24.5)
    R = (1.000001018*(1-e**2))/(1 + e*np.cos(np.radians(v)))
    return R
```

```
def declination(jd):
    """
    Compute the declination of the sun on a given day.
    Parameters:
    jd (float)
    Returns:
    R (float)
    """
    jdc = (jd - 2451545.0) / 36525.0
    sec = 21.448 - jdc * (46.8150 + jdc * (0.00059 - jdc * .001813))
    e0 = 23.0 + (26.0 + (sec / 60.0)) / 60.0
    oblcorr = e0 + 0.00256 * np.cos(np.deg2rad(125.04 - 1934.136 * jdc))
    l0 = 280.46646 + jdc * (36000.76983 + jdc * 0.0003032)
    l0 = (l0 - 360 * (l0 // 360)) % 360
    gmas = 357.52911 + jdc * (35999.05029 - 0.0001537 * jdc)
    gmas = np.deg2rad(gmas)
    seqcent = np.sin(gmas) * (1.914602 - jdc * (0.004817 + 0.000014 * jdc)) + \
        np.sin(2 * gmas) * (0.019993 - 0.000101 * jdc) + np.sin(3 * gmas) * 0.000289
    suntl = l0 + seqcent
    sal = suntl - 0.00569 - 0.00478 * np.sin(np.deg2rad(125.04 - 1934.136 * jdc))
    delta = np.arcsin(np.sin(np.deg2rad(oblcorr)) * np.sin(np.deg2rad(sal)))
    delta_deg = np.rad2deg(delta)
    return delta_deg
```

```
def sunvector(jd,latitude,longitude,timezone):
    """
    Calulate unit vector in direction of sun from observer point
    Parameters:
    jd (float)
    latitude (float)
    longitude (float)
    timezone (int)
    Returns:
    sv (tuple)
    """
    omega=hourangle(jd,longitude,timezone)
    delta = np.radians(declination(jd))
    lat_rad = np.radians(latitude)
    svx = -np.sin(omega)*np.cos(delta)
    svy = np.sin(lat_rad)*np.cos(omega)*np.cos(delta)-np.cos(lat_rad)*np.sin(delta)
    svz = np.cos(lat_rad)*np.cos(omega)*np.cos(delta)+np.sin(lat_rad)*np.sin(delta)
    sv = (svx,svy,svz)
    return sv


def sunpos(sunv):
    """
    Azimith and zenith angles from unit vector to the sun from observer postion, Corripio
(2003)
    Parameters:
    sv (tuble)
    Returns:
    sp (tuple)
    """
    azimuth = np.degrees(np.pi - np.arctan2(sunv[0],sunv[1]))
    zenith = np.degrees(np.arccos(sunv[2]))
    sp = (azimuth,zenith)
    return sp
```

```
def gradient(grid, length_x, length_y=None):
    """
    Computes a unit vector normal to every grid cell in a digital elevation model (DEM).
    https://github.com/tomderuijter/python-dem-shadows
    Parameters:
    grid (2darray) #DEM
    Returns:
    grad (numpy.ndarray) #tensor
    """
    if length_y is None:
        length_y = length_x
    assert len(grid.shape) == 2, "Grid should be a matrix."
    grad = np.empty((*grid.shape, 3))
    grad[:] = np.nan
    grad[:-1, :-1, 0] = 0.5 * length_y * (
        grid[:-1, :-1] - grid[:-1, 1:] + grid[1:, :-1] - grid[1:, 1:]
    )
    grad[:-1, :-1, 1] = 0.5 * length_x * (
        grid[:-1, :-1] + grid[:-1, 1:] - grid[1:, :-1] - grid[1:, 1:]
    )
    grad[:-1, :-1, 2] = length_x * length_y
    # Copy last row and column
    grad[-1, :, :] = grad[-2, :, :]
    grad[:, -1, :] = grad[:, -2, :]
    area = np.sqrt(
        grad[:, :, 0] ** 2 +
        grad[:, :, 1] ** 2 +
        grad[:, :, 2] ** 2
    )
    for i in range(3):
        grad[:, :, i] /= area
    return grad
```

```
def check_gradient(grad):
    assert len(grad.shape) == 3 and grad.shape[2] == 3, \
        "Gradient should be a tensor with 3 layers."

def hill_shade(grad, sun_vector):
    """
    Compute the intensity of illumination on a surface given the sun position.
    Parameters:
    grad (numpy.ndarray) #tensor
    sun_vector (tuple)
    Returns:
    hsh (2darray)
    """
    check_gradient(grad)
    hsh = (
        grad[:, :, 0] * sun_vector[0] +
        grad[:, :, 1] * sun_vector[1] +
        grad[:, :, 2] * sun_vector[2]
    )
    hsh = (hsh + abs(hsh)) / 2.
    return hsh

def _normalize_sun_vector(sun_vector):
    normal_sun_vector = np.zeros(3)
    normal_sun_vector[2] = np.sqrt(sun_vector[0] ** 2 + sun_vector[1] ** 2)
    normal_sun_vector[0] = -sun_vector[0] * sun_vector[2] / normal_sun_vector[2]
    normal_sun_vector[1] = -sun_vector[1] * sun_vector[2] / normal_sun_vector[2]
    return normal_sun_vector
```

```
def _invert_sun_vector(sun_vector):
    return -sun_vector / max(abs(sun_vector[:2]))


def project_shadows(dem, sun_vector, dx, dy=None):
    """Cast shadows on the DEM from a given sun position."""
    if dy is None:
        dy = dx
    inverse_sun_vector = _invert_sun_vector(sun_vector)
    normal_sun_vector = _normalize_sun_vector(sun_vector)
    rows, cols = dem.shape
    z = dem.T
    # Determine sun direction.
    if sun_vector[0] < 0:
        # The sun shines from the West.
        start_col = 1
    else:
        # THe sun shines from the East.
        start_col = cols - 1
    if sun_vector[1] < 0:
        # The sun shines from the North.
        start_row = 1
    else:
        # The sun shines from the South.
        start_row = rows - 1
    in_sun = np.ones_like(z)
    # Project West-East
    row = start_row
    for col in range(cols):
        _cast_shadow(row, col, rows, cols, dx, in_sun, inverse_sun_vector,
                     normal_sun_vector, z)
    col = start_col # Project North-South
    for row in range(rows):
        _cast_shadow(row, col, rows, cols, dy, in_sun, inverse_sun_vector,
                     normal_sun_vector, z)
    return in_sun.T
```

```
#METEO
def relative_humidity(Tair_K, Tdew_K):
    """
    Calucates the relativity humidity [%] based on the dewpoint and air temperature [K]
    https://bmcnoldy.rsmas.miami.edu/Humidity.html, acessed   (Alduchov et al. 1996)
    Parameters:
    Tair_K (float)
    Tdew_K (float)
    Returns:
    rh (float)
    """
    c  = 243.04
    b  = 17.625
    rh = 100 * np.e**( (c * b * (Tdew_K - Tair_K))
    / ((c + Tair_K) * (c + Tdew_K)) )
    return rh

def z2p(z):
    """
    Computes air pressure (hPa) for a given altitude [m] according to the standart atmosphere
    Parameters:
    z (float)
    Returns:
    zp (float)
    """
    P0=101325 #air pressure sea level
    T0=288.15 #standart temperature
    Earth_G = 9.80665 # acceleration due to gravity (m s-2)
    EarthR = 6.3756766E6 # average earths radius (m)
    Md = 28.966 # Molecular weight of dry air
    R_star = 8.3145 # Universal gas constant J/molK
    stlapse = -0.0065 # standard lapse rate K/m
    H1 = (EarthR * z) /(EarthR + z)
    HB = 0.0
    zp = P0*(T0/(T0+stlapse*(H1-HB)))**((Earth_G*Md)/(R_star*stlapse*1000))
    zp = zp/100.0
    return(zp)
```

```
def SatPresWatVap(Ta):
    """
    Computes saturation pressure of water vapour in air [hPa] for  given air temperature [K]
    Lowe (1977)
    Parameters:
    Ta (float)
    Returns:
    watervaporpressure (float)
    """
    tempcl = Ta
    a0     = 6984.505294
    a1     = -188.9039310
    a2     = 2.133357675
    a3     = -1.288580973e-2
    a4     = 4.393587233e-5
    a5     = -8.023923082e-8
    a6     = 6.136820929e-11
    watervaporpressure =
a0+tempcl*(a1+tempcl*(a2+tempcl*(a3+tempcl*(a4+tempcl*(a5+tempcl*a6)))))
    return watervaporpressure
```

```
#ENERGY FLUXES AND DEBRIS THICKNESS
def insolation(zenith,jd,height,RH,tempK):
    """
    Computes direct and diffusive component of incoming shortwave radiation (Wm-2)
    without topographic effects
    Solar geometry is based von Iqbal (1983)
    Atmospheric transmissivity is based von Bird & Hulstrom (1981b)
    Parameters:
        zenith (float)
        jd (float)
        height (float)
        RH (float)
        tempK (float)
    Returns:
        radiation (tuple)
            In (float)
            Id (float)
    """
    O3 = 0.3
    visibility = 30
    alphag = 0.2
    Isc = 1361.8   # solar constant (Wm^(-2)) (1)
    theta = np.radians(zenith)
    ssctalb = 0.9  # single scattering albedo (aerosols)(Iqbal, 1983)
    Fc = 0.84      # ratio of forward to total energy scattered (Iqbal, 1983)
    Pz = z2p(height)
    Mr = 1.0/(np.cos(theta)+0.15*((93.885-zenith)**(-1.253)))
    Ma = Mr*Pz/1013.25
    wvap_s =  SatPresWatVap(tempK) #** Use Lowe(1977) Lowes polynomials for vapor pressure
    Wprec = 46.5*(RH/100.0)*wvap_s/tempK  #Prata 1996
    rho2 = (1/sunr(jd))**2
    #rho2 =eccentricity(jd,tz)
    #rho2=1 + 0.033*np.cos((2*np.pi*242)/365)
    TauR = np.exp((-.09030*(Ma**0.84) )*(1.0+Ma-(Ma**1.01)) )
    TauO = 1.0-( ( 0.1611*(O3*Mr)*(1.0+139.48*(O3*Mr))**(-0.3035) )-0.002715*(O3*Mr)*(
1.0+0.044*(O3*Mr)+0.0003*(O3*Mr)**2 )**(-1))
    TauG = np.exp(-0.0127*(Ma**0.26))
    TauW = 1.0-2.4959*(Wprec*Mr)*( (1.0+79.034*(Wprec*Mr))**0.6828 + 6.385*(Wprec*Mr) )**(-1)
    TauA = ( 0.97-1.265*(visibility**(-0.66)) )**(Ma**0.9)   #Machler, 1983
    TauTotal = TauR*TauO*TauG*TauW*TauA
```

```
    In = 0.9751*rho2*Isc*TauTotal

    tauaa = 1.0-(1.0-ssctalb)*(1.0-Ma+Ma**1.06)*(1.0-TauA)

    Idr = 0.79*rho2*Isc*np.cos(theta)*TauO*TauG*TauW*tauaa*0.5*(1.0-TauR)/(1.0-Ma+Ma**(1.02))

    tauas = (TauA)/tauaa

    Ida = 0.79*rho2*Isc*np.cos(theta)*TauO*TauG*TauW*tauaa*Fc*(1.0-tauas)/(1.0-Ma+Ma**1.02)

    alpha_atmos = 0.0685+(1.0-Fc)*(1.0-tauas)

    Idm = (In*np.cos(theta)+Idr+Ida)*alphag*alpha_atmos/(1.0-alphag*alpha_atmos)

    Id = Idr+Ida+Idm

    radiation = (In, Id)

    return radiation


def calc_sin(dt_object,latitude,longitude,timezone, dem, res, relhum, TairK,
shadow_surrounding=None):

    """

    Computes incident shortwave radiation for each pixel. Illumination intensity (hillshade)

    base on the DEM (or dem of surrounding terrain) determines how much radiation is received
by

    each pixel.

    Parameters:

        dt_object (datetime object)

        latitude (float)

        longitude (float)

        timezone (int)

        dem (numpy 2darray)

        res (float)

        relhum (float)

        TairK (float)

        shadow_surrounding (None or 2darray)

    Returns:

        Iglobal (2darray)
```

```
def calc_sin(dt_object,latitude,longitude,timezone, dem, res, relhum, TairK,
shadow_surrounding=None):
    """
    Computes incident shortwave radiation for each pixel. Illumination intensity (hillshade)
    base on the DEM (or dem of surrounding terrain) determines how much radiation is received
by
    each pixel.
    Parameters:
        dt_object (datetime object)
        latitude (float)
        longitude (float)
        timezone (int)
        dem (numpy 2darray)
        res (float)
        relhum (float)
        TairK (float)
        shadow_surrounding (None or 2darray)
    Returns:
        Iglobal (2darray)
  """
  jd = JD(dt_object)
  sv = sunvector(jd,latitude,longitude,timezone)
  zenith = sunpos(sv)[1]
  mean_elevation = np.nanmean(dem)
  cgr = gradient(dem, res, length_y=None)
  hsh = hill_shade(cgr,sv)
  hsh = (hsh+np.absolute(hsh))/2
  sh = project_shadows(dem, np.array(sv), res, dy=None)
  shade = hsh*sh
  #add shade from surrounding terrain
  if shadow_surrounding is not None:
    shade=shade*shadow_surrounding
  insol = insolation(zenith, jd, mean_elevation, relhum, TairK)
```

```
    insol = insolation(zenith, jd, mean_elevation, relhum, TairK)

    if zenith<90:
        direct = insol[0]
        diffuse = insol[1]
    else:
        direct = 0
        diffuse = 0

    print('Id: ', direct)
    print('In: ', diffuse)

    Iglobal = np.zeros(dem.shape)
    Iglobal = Iglobal + ( direct * shade + diffuse)

    return  Iglobal

def calc_lnet(lin, lout):
    """
    Computes net longwave radiation (Wm-2)
    Parameters:
    lin (float or 2darray)
    lout (loat or 2darray)
    Returns:
    lnet (float or 2darray)
    """
    lnet = lin-lout
    return lnet
```

```
def calc_snet(albedo, swin):
    """
    Computes net shortwave radiation (Wm-2) from albedo and incoming shortwave radiation (Wm-
2)
    Parameters:
    albedo (float or 2darray)
    swin (float or 2darray)
    Returns:
    lnet (loat or 2darray)
    """
    snet = (1-albedo)*swin
    return sent


def calc_lout(emissivity, lst):
    """
    Computes outgoinf longwave radiation (Wm-2) based on emssivity and land surface
temperature (K)
    Parameters:
    emissivity (float or 2darray)
    lst (float or 2darray)
    Returns:
    lout (loat or 2darray)
    """
    # convert C to K
    if np.nanmean(lst)<200:
        lst = lst+273.15
    Sboltzman_const=5.67e-08
    lout = Sboltzman_const * emissivity * (lst**4) # Stefan Boltzmann Law
    return lout
```

```
def calc_shf(TairK, lst, elevation, windspeed, zt, zu, roughness):
    """
    Computes sensible heat flux (Wm-2) based on land surface temperature (K), air temperature
(K)
    wind speed in (ms-1) and surface roughness length (m), Nicholson and Benn (2006)
    Parameters:
        TairK (float or 2darray)
        lst (float or 2darray)
        elevation (float)
        windspeed (float)
        zt (int)
        zu (int)
        roughness (float)
    Returns:
        H (float or 2darray)
    """
    karmans_const = 0.41 # Kármáns constant
    c_air = 1010 # specific heat capacity air (J kg-1 K-1)
    P0 = 101325 # air pressure at sealevel in (Pa)
    rho_sl = 1.29 # air density sealeavel (kgm-3)
    P = z2p(elevation)*100 # air pressure (Pa)
    rho_local = rho_sl *  (P/P0) # air density local (kgm-3)
    A = (karmans_const**2) / (np.log(zu / roughness)*np.log(zt / roughness)) # dimensionless
bulk transfer coefficient
    H = rho_local * c_air * windspeed * (TairK - lst) * A
    return H


def quadraticEq(a, b, c):
    """
    Quadratic formula, provides solution for quadratic equation
    """
    D = b**2 - (4*a*c)
    x0 = (-b + np.sqrt(D)) / (2*a)
    x1 = (-b - np.sqrt(D)) / (2*a)
    return x0, x1
```

```
def debristhickness_prediction(sw, lw, H, Ts, Ta, w_rate, params):
    '''
    Solves the surface energy balance for debris thickness. Net shortwave (Wm-2),
    net longwave (Wm-2), sensible heat flux (Wm-2), land surface temperature (K),
    warming rate (Ks-1) and air temperature (K) need to be determinded in advance.
    Additional parameters are stored in a dictionary.
    Assumes linear temperature gradient with the layer of debris.
    Parameters:
        sw (ndarray)
        lw (ndarray)
        H (ndarray)
        Ts (ndarray)
        Ta (ndarray)
        w_rate (ndarray)
        params (dictionary)
    Returns:
        x0 (ndarray)
    '''
    density_debris = params['density_d']
    heat_capacity_debris = params['c_d']
    thermal_conductivity = -params['k_eff']
    a = (density_debris * heat_capacity_debris * w_rate) * -1
    b = sw + lw + H
    c = thermal_conductivity * Ts
    x0, x1 = quadraticEq(a, b, c)
    return x0
```

B. Appendix B

Supplementary information to Chapter 3

Supplement B is part of the data publication: Landsat-derived spatiotemporal variations of land surface temperature published at GFZ Data Services.

Gök, Deniz; Scherler, Dirk; Wulf, Hendrik (2024): Landsat-derived spatiotemporal variations of land surface temperature. GFZ Data Services. https://doi.org/10.5880/GFZ.3.3.2023.005

Table B 1. IMIS station location information

	Station name	Altitude asl [m]	UTM X [m]	UTM Y [m]
1	ALI2	1708	345991.4	5150296
2	AMD2	1610	511131.2	5224159
3	ANV2	2640	386976.2	5116009
4	ANV3	2589	396189.7	5108387
5	ARO2	2847	379721.8	5098420
6	ARO3	2602	388832.8	5104766
7	ATT2	2550	366290.8	5107201
8	BED2	2450	462485.6	5153502
9	BED3	2101	463309.6	5148732
10	BEL2	2554	421135.1	5138430
11	BER2	2447	579087.3	5141292
12	BER3	2625	570353.9	5143446
13	BEV2	2512	564184.8	5154340
14	BOG2	2299	459332.9	5131272
15	BOR2	2517	431393.2	5126714
16	BOV2	2687	363466.1	5093869
17	CAM2	2216	478307.5	5145834
18	CAM3	2257	477657	5148264
19	CHA2	2218	358802.9	5137570
20	CMA2	2325	513987.1	5188164
21	CON2	2229	367068.1	5127688
22	CSL2	1455	350658.5	5219970
23	DAV2	2558	562645.2	5172030
24	DAV3	2455	559074.4	5181989
25	DAV4	2330	559897.1	5181482
26	DAV5	2315	560294.6	5182311
27	DIA2	2575	364694.4	5130440
28	DTR2	2057	489960.6	5154375
29	EGH2	2500	430199.5	5140760
30	ELA2	2726	554747.8	5160010
31	ELM2	2058	510390	5198018
32	ELS2	2143	395827.7	5153789
33	FAE2	1971	384581.5	5152971
34	FIR2	2111	428432.5	5168783
35	FIS2	2155	398191.8	5147287
36	FLU2	2394	572285.1	5178119
37	FNH2	2252	342643.5	5107258
38	FOU2	2800	350266.3	5092725
39	FRA2	2100	488700.6	5131639
40	FRA3	2170	486005.8	5133170
41	FUL2	2602	352598.8	5117452
42	FUS2	2390	470842.2	5142609
43	GAD2	2063	453975.6	5176914

44	GAN2	2710	404776	5142489
45	GLA2	1632	502857.4	5204790
46	GOM2	2439	441022.1	5141051
47	GOM3	2427	440793.5	5148686
48	GOR2	2953	405789.7	5093344
49	GRA2	1984	329450.2	5134886
50	GUT2	2115	445676.2	5169773
51	HTR2	2147	515666.3	5154555
52	HTR3	2200	526725.2	5153724
53	ILI2	2022	332383.7	5117602
54	JAU2	1707	367926.7	5165833
55	JUL2	2426	553143.2	5147447
56	KES2	2727	568762.4	5163472
57	KLO2	2147	566548	5195435
58	KLO3	2299	571040.2	5187947
59	LAG2	2730	557183.9	5144468
60	LAG3	2300	553615.4	5141454
61	LAU2	1970	375516.5	5142659
62	LHO2	2150	419074.7	5159345
63	LUK2	2555	483420.9	5161199
64	LUM2	2388	489412.1	5175346
65	MAE2	2162	419112.7	5163329
66	MEI2	2220	465702.8	5176788
67	MES2	2384	512319.2	5140061
68	MLB2	1974	546433.3	5215177
69	MTR2	1884	493666	5139465
70	MUN2	2205	417277	5131616
71	MUT2	2481	501332.7	5189469
72	NAR2	2077	489915.2	5146611
73	NAS2	2350	595764.9	5185375
74	NEN3	2203	371431.8	5111303
75	OBM2	2097	362791.1	5142460
76	OBW2	2432	447555.6	5154855
77	OBW3	2194	450475.1	5150679
78	OFE2	2359	598671.8	5165045
79	ORT2	1824	496843.9	5196062
80	OTT2	2017	389712.6	5155020
81	PAR2	2290	561357.7	5189001
82	PMA2	2429	541174.1	5158641
83	PUZ2	2196	489470.4	5163652
84	RGS3	1258	497783.8	5208576
85	RNZ2	2400	471460.4	5170291
86	ROA2	1875	423192.6	5180577
87	ROT3	2495	546177	5175684
88	SAA2	2480	413494.9	5113750
89	SAA3	2952	421307.8	5108716

90	SAA4	2680	415443.1	5108459
91	SCA2	2032	478436	5184418
92	SCA3	2338	483205.5	5193135
93	SCB2	1777	431558.5	5181038
94	SCH2	2332	410713.3	5158810
95	SHE2	1852	409293.9	5177937
96	SIM2	2450	498527.7	5145987
97	SLF2	1563	564714.6	5184707
98	SMN2	2512	601830.2	5201186
99	SPN2	2620	431958.6	5119919
100	SPN3	2424	426303.3	5114269
101	STH2	1791	386790.3	5170896
102	STN2	2914	403546	5113451
103	TAM2	2468	529737.8	5201723
104	TAM3	2166	534903.1	5193152
105	TIT2	2149	454926.7	5181554
106	TRU2	2459	391212.3	5136236
107	TUJ2	2262	478874.4	5170073
108	TUJ3	2211	480120.6	5165974
109	TUM2	2191	501638.8	5180835
110	URS2	2169	462756.9	5159362
111	VAL2	2268	470392	5155125
112	VDS2	2385	374327	5131066
113	VIN2	2729	609832	5198592
114	VLS2	2064	515698.1	5169004
115	WFJ2	2536	561721.8	5186551
116	YBR2	1701	486736	5209119
117	ZER2	2752	401535.2	5099521
118	ZER4	2408	399519.8	5094643
119	ZNZ2	2677	577893.8	5172077

Table B 2 shows the results of the harmonic regression of Landsat TM, ETM+ and TIRS observations at the IMIS stations. Landsat observations are filtered to match simultaneous IMIS LST record. The table contains information on the mean annual land surface temperature, MALST (K), the LST trends (K yr^{-1}), the Amplitude (K), the phase of the harmonic oscillation (-), the root mean square error (K) the number of LST observations, nobs and the record length, dt (years). The LST trends are shown in Figure 3.5.

Table B 2. Harmonic regression of combined Landsat 5, 7 and 8 LST time series at IMIS stations location.

Station	MALST [°C]	Trend [K yr^{-1}]	Amplitude [K]	Phase [-]	RMSE [K]	Number observations.	Record [years]
ALI2	9.554	-0.066	17.195	0.514	5.909	362	14.565
AMD2	6.271	0.115	15.647	0.500	6.166	316	21.355

ANV2	2.940	0.024	18.505	0.595	7.077	324	21.530
ANV3	4.582	0.035	20.261	0.519	7.103	352	21.465
ARO2	2.559	-0.008	16.286	0.605	6.946	301	19.997
ARO3	2.343	0.025	21.430	0.476	7.305	328	19.932
ATT2	1.689	-0.014	18.708	0.529	6.850	154	7.666
BED2	1.590	0.140	14.402	0.699	7.176	430	22.585
BED3	2.783	0.046	18.908	0.517	7.085	591	21.533
BEL2	6.969	-0.162	18.932	0.593	7.363	316	10.513
BER2	1.180	0.061	17.530	0.539	6.743	533	18.511
BER3	3.854	-0.003	18.718	0.571	7.421	480	18.508
BEV2	1.169	0.093	20.204	0.472	6.997	592	21.618
BOG2	7.908	-0.059	17.613	0.633	8.107	513	19.559
BOR2	0.104	0.041	15.364	0.565	6.124	455	17.656
BOV2	2.986	-0.039	18.534	0.494	6.335	257	17.478
CAM2	0.861	0.034	17.048	0.441	6.598	515	19.559
CAM3	21.723	-1.058	16.127	0.404	5.194	169	4.427
CHA2	4.346	0.052	16.370	0.569	5.904	505	21.615
CMA2	12.232	-0.545	16.789	0.531	6.867	154	8.630
CON2	4.422	0.003	17.314	0.614	7.220	306	16.537
CSL2	-42.166	2.872	16.946	0.478	3.318	34	1.183
DAV2	1.976	0.022	17.011	0.576	7.349	549	20.545
DAV3	1.832	0.156	17.435	0.581	7.635	509	20.523
DAV4	9.459	-0.122	17.971	0.547	7.690	403	17.060
DAV5	3.978	-0.013	18.980	0.388	6.142	372	17.060
DIA2	0.863	-0.115	12.412	0.529	6.117	135	6.527
DTR2	5.809	0.192	18.338	0.502	7.492	422	21.533
EGH2	4.263	0.054	18.046	0.626	7.570	232	7.710
ELA2	4.285	-0.173	17.047	0.510	7.484	288	10.691
ELM2	4.583	0.069	17.643	0.511	7.282	269	18.267
ELS2	7.847	-0.009	18.984	0.486	5.949	301	20.260
FAE2	5.326	0.018	17.334	0.493	6.299	341	21.552
FIR2	6.289	0.027	17.468	0.618	6.809	544	20.542
FIS2	2.565	0.046	17.487	0.408	5.795	324	21.618
FLU2	2.945	-0.050	18.198	0.472	6.201	390	15.639
FNH2	0.206	0.056	17.523	0.458	6.400	519	21.530
FOU2	-4.636	-0.030	13.622	0.383	4.849	387	19.622
FRA2	4.763	0.030	16.807	0.527	5.455	225	14.478
FRA3	7.309	0.273	13.758	0.444	6.429	258	13.558
FUL2	1.058	0.049	16.026	0.613	7.097	520	19.603
FUS2	3.560	-0.042	16.394	0.530	5.670	389	17.588
GAD2	3.527	0.107	17.559	0.524	6.445	508	20.216
GAN2	0.706	0.070	13.528	0.677	7.700	324	22.450
GLA2	5.765	0.157	17.851	0.507	5.393	323	18.267
GOM2	2.263	0.043	19.292	0.531	6.648	591	19.628
GOM3	2.108	0.178	17.801	0.551	7.372	473	19.496
GOR2	-2.186	0.027	18.218	0.503	6.953	255	7.710

GRA2	3.778	0.117	15.773	0.574	5.629	359	13.555
GUT2	5.062	0.120	18.166	0.484	7.117	514	19.581
HTR2	4.913	0.126	18.603	0.552	6.800	257	17.544
HTR3	1.723	0.084	17.998	0.446	6.441	274	17.544
ILI2	6.379	0.049	16.333	0.403	5.859	468	18.617
JAU2	10.147	-0.001	17.614	0.493	5.662	370	14.390
JUL2	2.766	0.066	18.554	0.520	7.504	548	20.764
KES2	-0.678	0.071	13.091	0.584	6.756	489	21.640
KLO2	4.246	0.154	19.005	0.520	7.324	577	22.604
KLO3	0.202	0.162	18.700	0.489	7.594	574	22.338
LAG2	0.509	0.162	17.323	0.543	8.068	537	22.341
LAG3	4.830	0.186	19.012	0.522	6.853	264	10.601
LAU2	7.414	-0.012	18.007	0.478	6.985	302	19.384
LHO2	4.384	0.136	19.744	0.460	7.338	459	17.478
LUK2	0.038	0.096	14.295	0.604	6.503	407	18.637
LUM2	-2.868	0.201	7.814	-0.002	3.198	32	20.917
MAE2	7.499	-0.024	17.111	0.536	7.426	223	6.790
MEI2	4.142	0.119	17.274	0.570	6.940	522	21.577
MES2	1.948	0.033	16.584	0.480	5.844	259	16.515
MLB2	4.516	-0.154	18.239	0.375	5.866	236	10.426
MTR2	13.971	-0.304	13.192	0.360	4.866	139	6.790
MUN2	8.930	0.073	20.209	0.450	6.951	514	18.508
MUT2	4.472	-0.207	16.048	0.539	7.743	195	10.601
NAR2	2.240	0.245	14.545	0.619	6.968	286	22.560
NAS2	15.398	-0.504	20.298	0.444	6.784	277	8.739
NEN3	10.569	-0.407	19.568	0.421	6.439	137	5.498
OBM2	3.670	0.053	16.886	0.517	5.870	460	18.508
OBW2	4.323	0.014	17.356	0.655	7.107	515	19.559
OBW3	1.128	0.083	18.593	0.503	6.979	549	19.584
OFE2	2.777	0.002	20.140	0.447	6.208	469	16.687
ORT2	10.037	0.019	15.632	0.473	6.028	425	18.505
OTT2	6.016	0.095	18.281	0.488	6.275	286	21.311
PAR2	0.785	0.144	18.428	0.481	7.480	543	21.418
PMA2	6.327	-0.085	17.551	0.476	7.242	261	8.674
PUZ2	1.294	0.127	18.277	0.464	6.500	408	22.366
RGS3	-10.627	1.145	17.193	0.186	5.575	54	1.645
RNZ2	1.515	-0.086	15.602	0.519	5.028	230	9.530
ROA2	7.255	0.144	16.898	0.527	6.980	519	22.431
ROT3	546.141	-28.842	14.991	-0.095	4.401	21	0.569
SAA2	6.014	0.006	19.051	0.449	6.541	562	21.621
SAA3	-4.999	0.034	15.983	0.436	5.353	602	21.621
SAA4	0.476	0.108	16.559	0.520	6.326	248	7.644
SCA2	-1.143	0.110	19.259	0.391	7.065	543	19.693
SCA3	0.392	0.148	15.260	0.587	7.620	438	19.759
SCB2	6.281	0.064	18.297	0.515	6.685	481	18.686
SCH2	4.304	0.011	16.438	0.587	6.734	338	22.450

SHE2	7.864	-0.007	17.052	0.540	6.031	251	17.610
SIM2	3.130	0.105	17.603	0.529	6.133	331	22.560
SLF2	7.063	0.149	21.042	0.210	7.061	567	21.418
SMN2	-0.205	0.005	18.780	0.470	7.751	465	18.508
SPN2	3.479	0.013	15.732	0.540	6.869	469	22.601
SPN3	-0.549	-0.011	14.615	0.479	5.525	500	22.560
STH2	6.630	0.021	17.801	0.481	5.391	262	18.223
STN2	-1.106	0.067	12.509	0.591	6.677	346	20.348
TAM2	-0.151	0.117	15.950	0.478	6.438	229	18.530
TAM3	3.406	0.124	18.633	0.411	6.152	262	18.642
TIT2	3.021	0.049	18.139	0.524	6.418	218	7.713
TRU2	2.627	0.023	17.253	0.622	7.808	341	22.253
TUJ2	5.824	0.064	18.297	0.596	7.808	513	21.577
TUJ3	1.814	0.010	18.565	0.463	6.338	578	21.465
TUM2	7.156	0.006	18.578	0.586	7.263	245	16.537
URS2	2.118	0.076	18.423	0.457	6.154	574	21.421
VAL2	7.587	0.107	16.276	0.601	7.445	530	22.560
VDS2	3.842	-0.008	18.223	0.615	7.214	317	20.173
VIN2	-1.768	0.088	16.622	0.402	6.974	448	20.613
VLS2	2.734	0.129	17.886	0.367	6.317	289	17.807
WFJ2	1.742	0.141	17.693	0.543	7.694	494	19.756
YBR2	4.026	0.181	18.930	0.417	5.421	321	12.550
ZER2	1.904	0.065	18.018	0.572	7.688	555	20.348
ZER4	4.091	-0.006	21.312	0.441	6.456	408	14.500
ZNZ2	-1.791	0.004	16.120	0.463	6.687	415	16.649

Table B 3 shows the results of the harmonic regression of the IMIS LST observations interpolated at the Landsat overpass time. The table contains information on the mean annual land surface temperature, MALST (K), the LST trends (K yr^{-1}), the Amplitude (K), the phase of the harmonic oscillation (-), the root mean square error (K) the number of LST observations, nobs and the record length, dt (years). The LST trends are shown in

Figure 3.5.

Table B 3. Harmonic regression of IMIS LST time series at IMIS station locations.

Station	MALST [°C]	Trend [K yr^{-1}]	Amplitude [K]	Phase [-]	RMSE [K]	Number observations.	Record [years]
ALI2	7.784	0.004	16.416	0.525	5.015	362	14.565
AMD2	5.779	0.122	15.054	0.488	5.331	317	21.355
ANV2	3.437	0.013	18.117	0.565	6.832	324	21.530
ANV3	2.700	0.016	18.008	0.473	5.533	352	21.465
ARO2	-1.163	0.062	13.235	0.482	5.780	301	19.997

ARO3	0.332	0.113	19.347	0.443	5.706	328	19.932
ATT2	-1.883	0.262	18.335	0.528	7.355	154	7.666
BED2	0.522	0.114	14.552	0.582	6.866	430	22.585
BED3	1.259	0.134	18.016	0.464	6.597	592	21.533
BEL2	3.821	0.031	17.649	0.520	6.602	316	10.513
BER2	0.834	0.130	16.570	0.527	6.306	534	18.511
BER3	4.128	0.039	17.683	0.553	6.095	481	18.508
BEV2	-0.096	0.069	18.890	0.429	6.281	592	21.618
BOG2	6.141	-0.023	16.942	0.565	6.844	514	19.559
BOR2	-0.591	0.043	13.454	0.574	6.086	455	17.656
BOV2	2.308	-0.007	18.655	0.446	6.448	257	17.478
CAM2	1.458	-0.017	16.859	0.427	5.749	518	19.559
CAM3	11.501	-0.493	17.046	0.352	6.249	169	4.427
CHA2	4.187	0.034	15.469	0.553	5.683	505	21.615
CMA2	4.155	-0.030	14.502	0.511	6.007	154	8.630
CON2	3.263	0.110	16.052	0.571	6.481	306	16.537
CSL2	-3.491	0.792	15.265	0.501	3.493	34	1.183
DAV2	1.238	0.003	15.490	0.564	6.898	549	20.545
DAV3	1.541	0.070	16.092	0.499	6.684	510	20.523
DAV4	4.682	0.013	17.665	0.448	6.448	403	17.060
DAV5	7.553	-0.128	19.666	0.422	6.586	372	17.060
DIA2	-3.705	0.226	11.198	0.487	5.582	135	6.527
DTR2	3.827	0.159	17.012	0.455	5.329	423	21.533
EGH2	2.556	0.123	17.026	0.573	6.990	232	7.710
ELA2	0.193	-0.021	14.346	0.385	5.854	288	10.691
ELM2	3.102	0.067	15.833	0.514	6.821	269	18.267
ELS2	7.419	-0.023	17.983	0.440	5.709	301	20.260
FAE2	6.103	0.023	15.598	0.528	5.448	341	21.552
FIR2	6.029	0.015	17.899	0.583	7.111	544	20.542
FIS2	4.323	0.006	18.328	0.443	6.464	324	21.618
FLU2	1.119	0.108	17.104	0.518	6.550	390	15.639
FNH2	-0.206	0.094	16.835	0.416	6.741	519	21.530
FOU2	-1.706	-0.094	10.925	0.350	5.554	387	19.622
FRA2	4.106	0.141	16.315	0.561	5.727	225	14.478
FRA3	11.955	0.102	14.622	0.485	7.707	258	13.558
FUL2	-1.351	0.085	13.757	0.633	7.046	520	19.603
FUS2	4.161	-0.036	17.267	0.565	5.969	389	17.588
GAD2	3.962	0.111	18.123	0.551	7.086	508	20.216
GAN2	-0.387	0.101	10.619	0.592	7.162	324	22.450
GLA2	5.325	0.177	17.010	0.528	5.811	323	18.267
GOM2	0.371	0.074	17.260	0.503	6.052	591	19.628
GOM3	2.437	0.213	17.498	0.559	6.744	474	19.496
GOR2	-3.914	0.168	16.661	0.448	6.733	255	7.710
GRA2	4.424	0.137	16.609	0.576	6.177	359	13.555
GUT2	4.763	0.118	17.106	0.466	6.290	515	19.581
HTR2	4.506	0.133	18.103	0.539	6.261	257	17.544

HTR3	3.709	0.043	18.044	0.435	5.777	275	17.544
ILI2	4.687	0.086	15.797	0.449	5.325	468	18.617
JAU2	7.862	0.055	16.641	0.532	5.317	370	14.390
JUL2	1.466	0.068	16.204	0.432	5.625	549	20.764
KES2	-2.268	0.154	12.787	0.492	6.043	490	21.640
KLO2	5.562	0.093	19.026	0.514	6.804	578	22.604
KLO3	0.075	0.173	16.702	0.441	6.666	575	22.338
LAG2	-0.209	0.154	18.785	0.608	8.913	539	22.341
LAG3	10.782	-0.652	17.624	0.175	7.531	264	10.601
LAU2	5.318	0.014	16.614	0.444	5.725	302	19.384
LHO2	3.779	0.140	19.225	0.430	6.602	460	17.478
LUK2	0.316	0.046	14.314	0.594	7.067	407	18.637
LUM2	-1.939	0.219	6.931	0.043	3.271	32	20.917
MAE2	5.482	0.026	14.316	0.515	5.634	223	6.790
MEI2	3.952	0.079	17.102	0.527	6.022	523	21.577
MES2	0.123	0.077	14.815	0.486	5.170	259	16.515
MLB2	5.127	-0.232	17.588	0.371	5.828	236	10.426
MTR2	7.767	0.192	18.346	0.325	6.603	139	6.790
MUN2	5.761	0.106	18.339	0.458	5.291	515	18.508
MUT2	1.203	-0.025	14.123	0.476	6.592	195	10.601
NAR2	5.929	0.113	16.004	0.672	6.221	287	22.560
NAS2	5.667	-0.103	19.186	0.357	5.961	277	8.739
NEN3	12.415	-0.477	19.002	0.384	6.142	137	5.498
OBM2	3.492	0.056	15.425	0.552	5.784	460	18.508
OBW2	3.562	0.027	17.304	0.568	6.889	515	19.559
OBW3	1.778	0.018	16.770	0.455	5.574	550	19.584
OFE2	3.975	-0.018	19.813	0.448	6.167	469	16.687
ORT2	6.829	0.031	16.602	0.513	6.096	425	18.505
OTT2	6.212	0.103	17.938	0.499	6.284	286	21.311
PAR2	1.060	0.152	16.686	0.460	6.710	544	21.418
PMA2	4.119	0.001	15.940	0.428	6.142	261	8.674
PUZ2	4.466	0.120	19.787	0.446	6.422	409	22.366
RGS3	-44.950	2.957	20.221	0.217	6.193	54	1.645
RNZ2	2.010	-0.077	16.313	0.501	6.165	230	9.530
ROA2	6.693	0.067	16.016	0.508	5.454	520	22.431
ROT3	1433.064	-75.143	25.284	-0.406	3.958	21	0.569
SAA2	7.678	-0.028	20.509	0.502	6.510	563	21.621
SAA3	1.716	-0.096	19.210	0.367	6.218	602	21.621
SAA4	0.381	0.078	16.439	0.509	6.563	248	7.644
SCA2	-0.283	0.063	18.982	0.366	6.825	544	19.693
SCA3	0.772	0.152	13.831	0.633	7.204	439	19.759
SCB2	5.514	0.069	17.198	0.515	5.865	482	18.686
SCH2	1.117	0.040	14.537	0.605	6.192	339	22.450
SHE2	8.795	-0.021	16.837	0.553	6.277	251	17.610
SIM2	3.095	0.119	17.587	0.568	6.573	331	22.560
SLF2	5.198	0.133	19.291	0.238	5.787	569	21.418

SMN2	-1.684	0.061	18.524	0.403	6.505	466	18.508
SPN2	2.304	0.057	15.339	0.457	5.607	470	22.601
SPN3	-1.168	-0.016	13.762	0.471	6.112	500	22.560
STH2	5.408	0.008	16.143	0.498	5.068	262	18.223
STN2	0.927	0.068	13.174	0.568	6.564	346	20.348
TAM2	-0.454	0.110	14.373	0.507	6.598	229	18.530
TAM3	1.001	0.087	17.351	0.345	6.235	262	18.642
TIT2	1.391	0.160	17.008	0.520	6.536	218	7.713
TRU2	2.230	0.025	16.013	0.607	6.958	342	22.253
TUJ2	5.983	0.085	16.237	0.578	6.003	514	21.577
TUJ3	-0.393	0.182	17.066	0.459	6.308	578	21.465
TUM2	5.695	0.073	17.602	0.489	6.272	245	16.537
URS2	3.479	0.079	17.768	0.419	5.570	575	21.421
VAL2	5.004	0.095	15.933	0.619	6.715	531	22.560
VDS2	3.512	0.024	16.686	0.611	6.946	317	20.173
VIN2	-1.018	0.101	17.319	0.368	7.302	449	20.613
VLS2	1.888	0.102	19.366	0.324	5.673	290	17.807
WFJ2	-0.467	0.185	15.542	0.460	6.568	495	19.756
YBR2	2.424	0.290	19.064	0.370	5.559	321	12.550
ZER2	-0.321	0.174	15.494	0.557	6.002	556	20.348
ZER4	6.566	-0.161	19.998	0.453	6.258	408	14.500
ZNZ2	-2.507	0.055	16.557	0.432	7.217	415	16.649

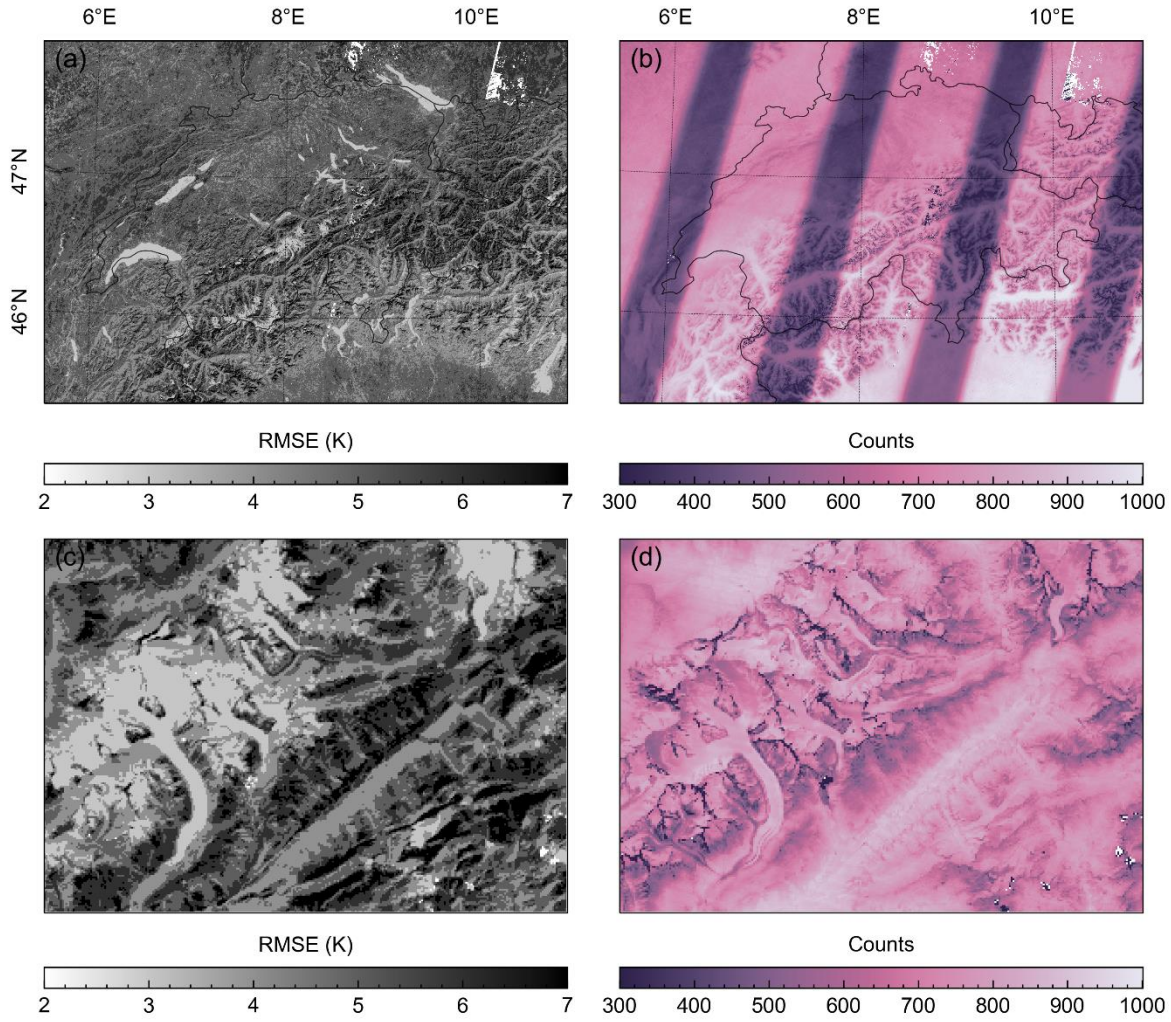

Figure B 1. Landsat land surface temperature (LST) time series derived (a) Root Mean Square error (RMSE) of the harmonic model, (b) counts of LST observations across Switzerland and across the upper Rhone Valley, respectively (c, d)

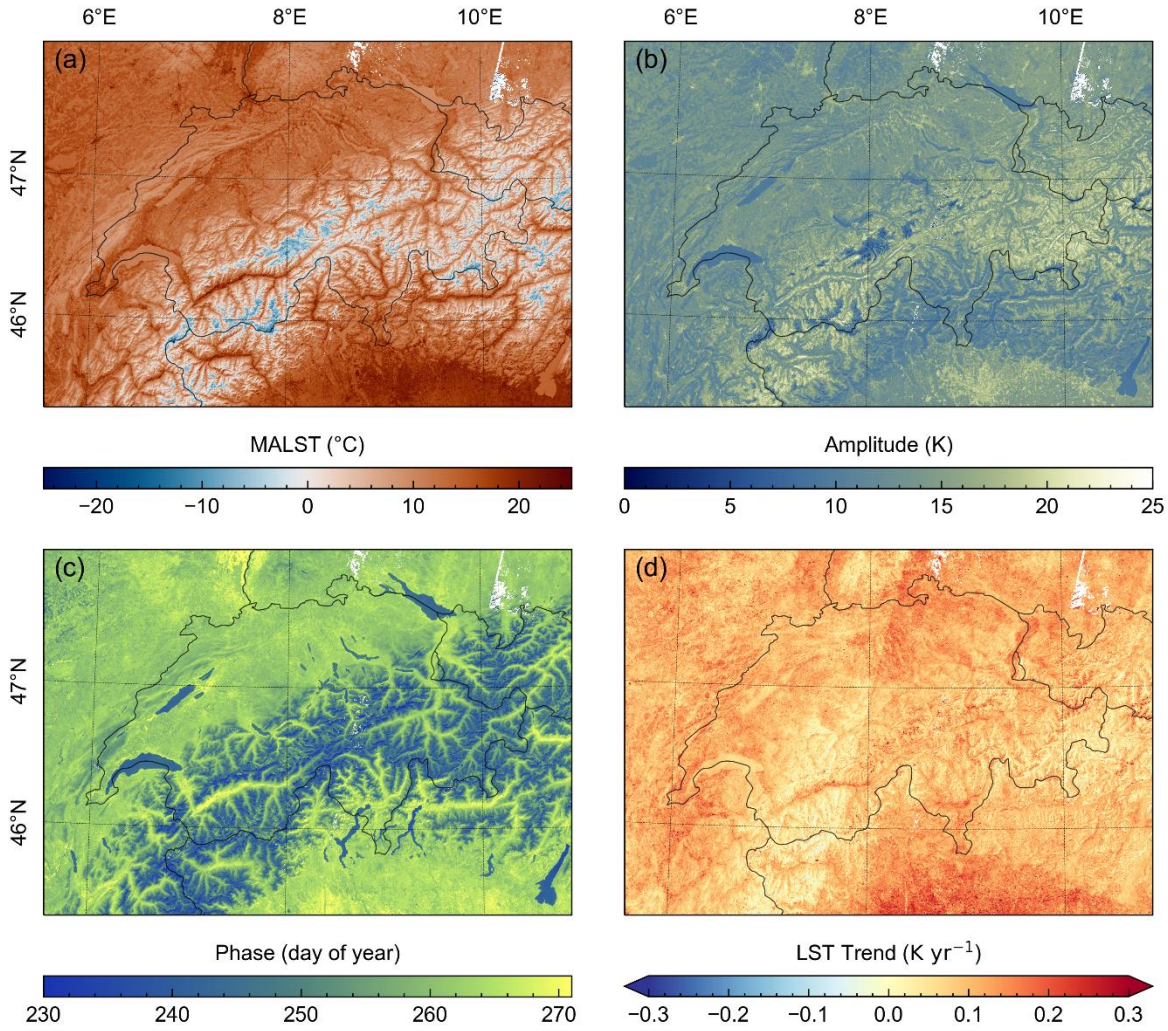

Figure B 2. Landsat land surface temperature (LST) time series (1998-2022) derived (a) mean annual LST (MALST), (b) LST amplitude and (c) phase of the harmonic oscillation and (d) LST trend across Switzerland and adjacent areas. The shorter time series excludes large proportion of orbital change affected Landsat 5 LST.

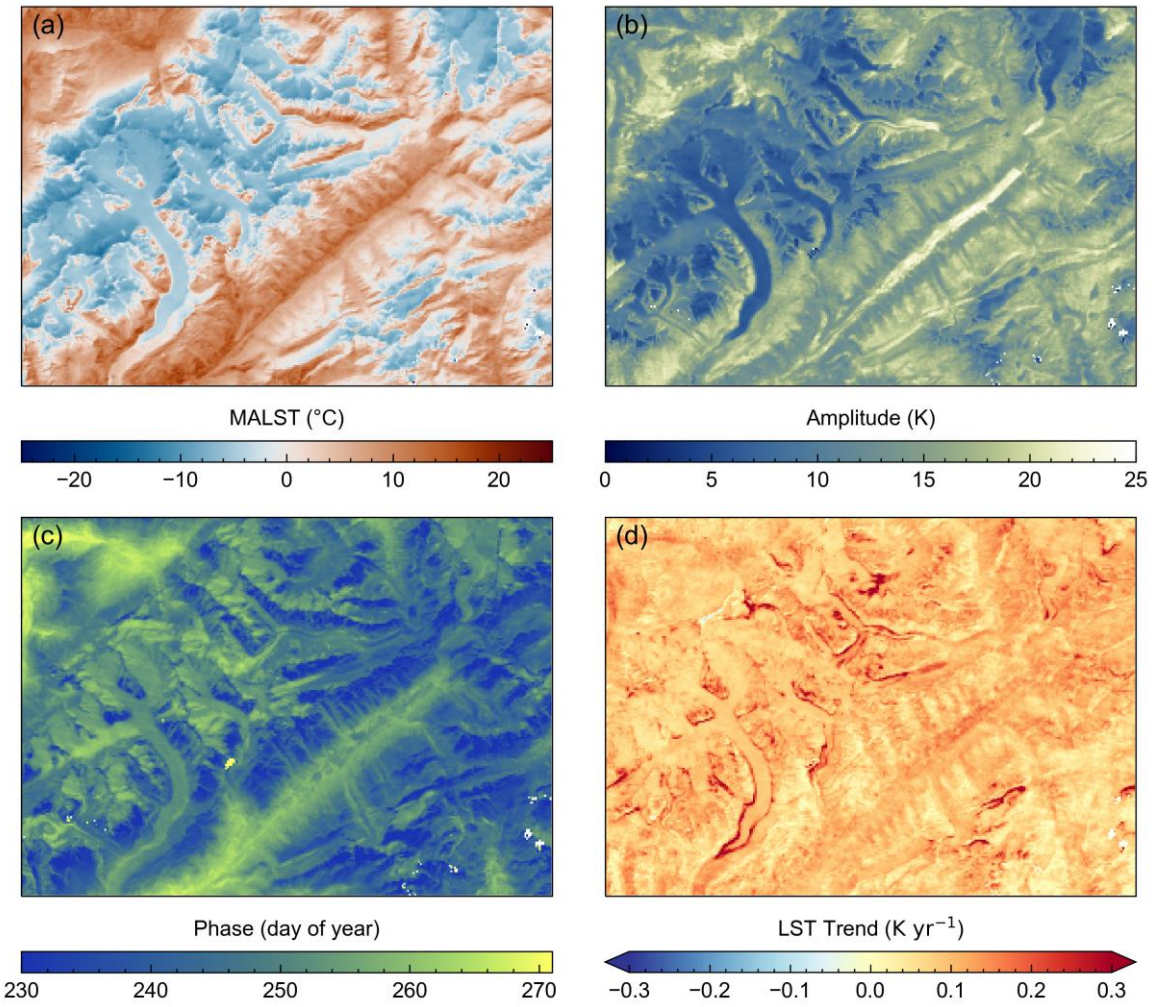

Figure B 3. Landsat land surface temperature (LST) time series (1998-2022) derived (a) mean annual LST (MALST), (b) LST amplitude, (c) phase of the harmonic oscillation and (d) LST trend, across the upper Rhone Valley. The shorter time series excludes large proportion of orbital change affected Landsat 5 LST.

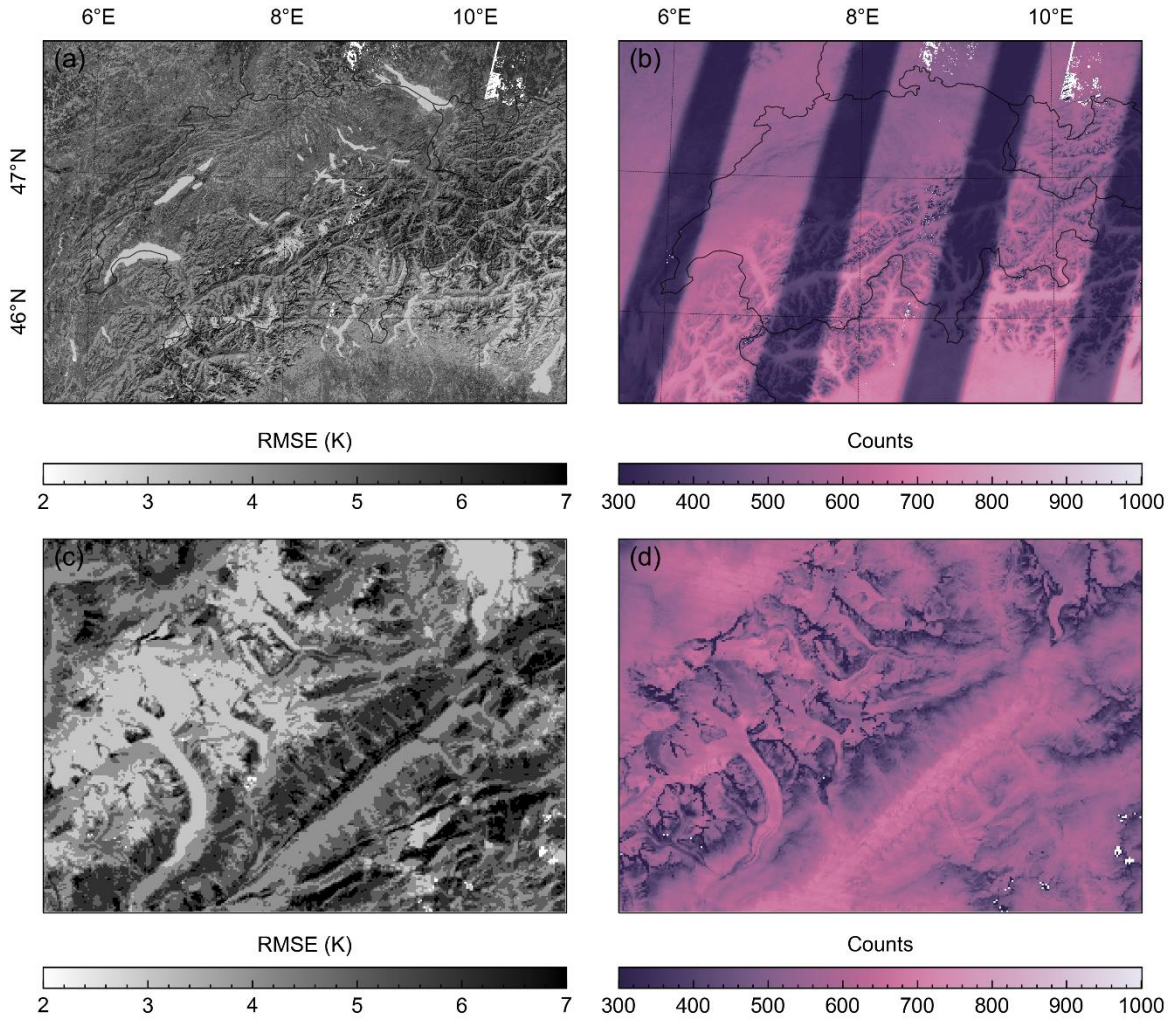

Figure B 4. Landsat land surface temperature (LST) time series (1998-2022) derived (a) Root Mean Square error (RMSE) of the harmonic model, (b) counts of LST observations across Switzerland and across the upper Rhone Valley, respectively (c, d). The shorter time series excludes large proportion of orbital change affected Landsat 5 LST.

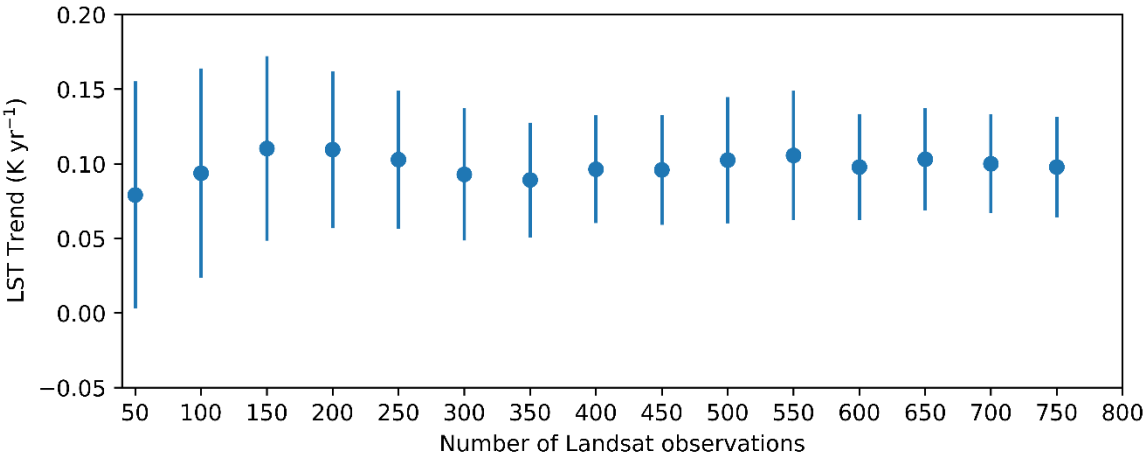

Figure B 5. Mean +- standard deviation of Landsat LST trends for n=50 number of observation bins.

C. Appendix C

Supplementary information to Chapter 4

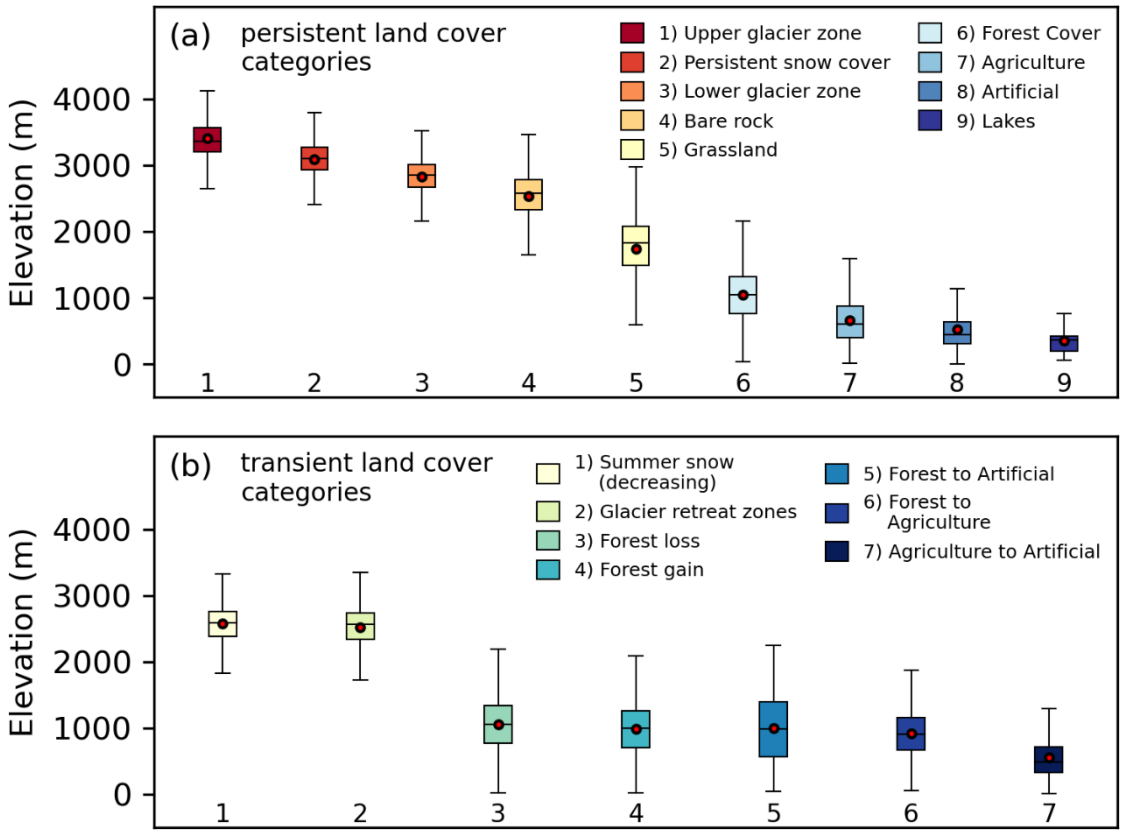

Figure C 1. Elevation for various land cover categories across the European Alps. Boxplots for (a) persistent surfaces and (b) transient surfaces show the mean (red dot), median (black line), the interquartile range and minimum and maximum values, excluding outliers.

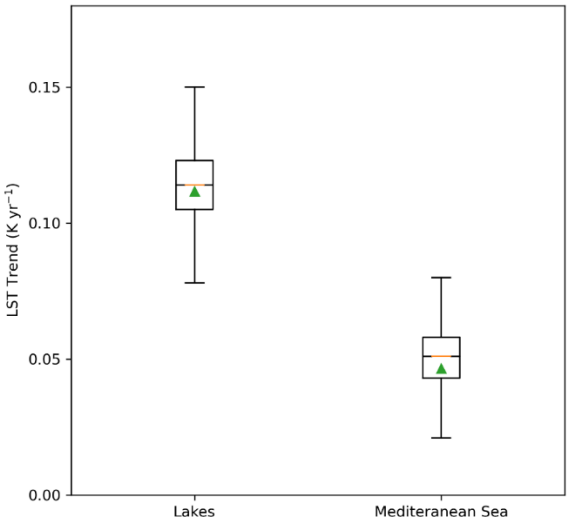

Figure C 2. Distributions of lake and sea surface temperature trends of combined lakes in the European Alps and the northern parts of the Ligurian and Adriatic Seas. The boxplots are showing the mean (red triangle), median (black line), the interquartile range (box) and minimum and maximum values, excluding outliers.

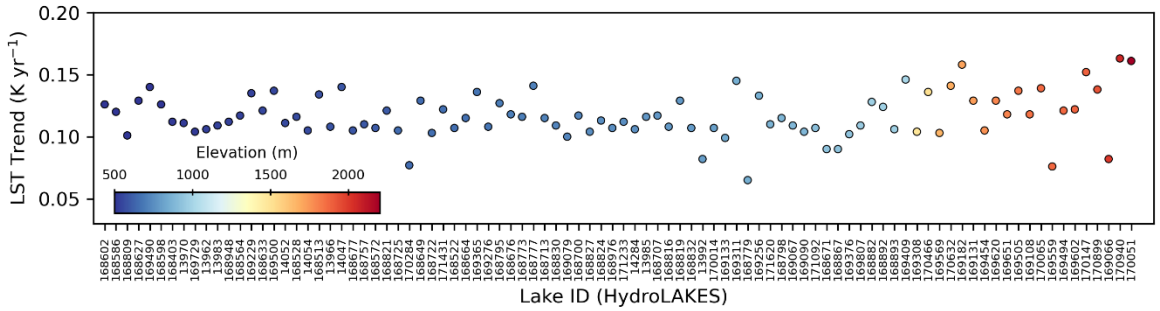

Figure C 3. Landsat derive lake surface temperature trends sorted by elevation. Lake IDs refer to nomenclature of the HydroLakes dataset (Messager et al., 2016)

Danksagung

Zuerst möchte ich meinem Supervisor Dirk Scherler danken, der mir die Mitarbeit im ERC-Projekt COLD am GFZ ermöglicht hat. Seine stets offene Tür, sein wissenschaftlicher Rat und seine konstruktive Kritik waren mir eine große Hilfe. Besonders dankbar bin ich ihm auch und vor allem auf persönlicher Ebene. Während für mich schwieriger Lebensumstände und während der Corona Pandemie, die uns allen viel abverlangt hat – war er mir eine außergewöhnliche und zuverlässige Unterstützung und Bezugsperson, die immer an mich geglaubt und mich motiviert hat die Promotion fortzuführen und nun auch abzuschließen. Ich danke dir aufrichtig für deine Geduld und dein Engagement.

Ein besonderer Dank geht an meine PhD-Kolleg*innen Katharina Wetterauer und Donovan Dennis, von denen ich viel gelernt habe und deren persönliche und professionelle Entwicklung ich beobachten und miterleben durfte. Die wunderbaren, herausfordernden und abenteuerlichen Feldarbeiten in den Alpen, zusammen mit Leif Anderson, waren überaus bereichernd und werden mir immer in Erinnerung bleiben.

Ich bin dankbar für die Gelegenheit, am Deutschen GeoForschungsZentrum in Potsdam zu forschen, und darüber viele interessante Menschen kennenzulernen, aus denen teilweise enge Freundschaften entstanden sind. Großer Dank geht an meine Kolleg*innen in der Sektion Geochemie der Erdoberfläche, die mir trotz meiner vielen Abwesenheiten stets mit Offenheit und Freundlichkeit begegnet sind. Großer Dank geht auch an Hendrik Wulf von der Uni Zürich für sein wissenschaftliches Feedback und sein offenes Ohr.

Die Promotion war für mich aus vielen Gründen eine große Herausforderung, und ich bin überaus dankbar für die Unterstützung und Begleitung einiger Menschen in meinem Leben. Ich danke Henriette Freckmann, die mich in besonderem Maße dazu motiviert hat, diesen Weg einzuschlagen und die für mich immer in Verbindung zu dieser Arbeit stehen wird. Ich danke Daniel Mohns und Marc Osterland, die mich bereits seit der Schulzeit begleiten und auf deren hands-on Unterstützung ich immer zählen konnte. Ich danke Soraya Kaiser, die mich ebenfalls schon lange begleitet, für den inhaltlichen und persönlichen Austausch unserer vielen Gemeinsamkeiten. Besonderer Dank geht an meine Mitbewohner*innen Hannah Nacken, Alice Fritze, Christoph Vizy, Kilian Bender, Lilith Kolling und Hecki für ihre Anteilnahme, Geduld und ihr Interesse an meiner Arbeit. Außerdem danke ich meiner Familie für die kontinuierliche Unterstützung und Anerkennung für meinen akademischen Werdegang mit all seinen Höhen und Tiefen.

Vielen Dank auch an die vielen Menschen, die hier nicht weiter namentlich erwähnt wurden für die Anteilnahme, Diskussionen, Ablenkung, Perspektivwechsel und Ermutigung.